NTNU – Trondheim
Norwegian University of
Science and Technology

Characterisation of the Magnetic Mineralogy, Properties and Magnetic Anomaly Responses of two Garnetiferous Peridotite Bodies in the WGR, Otrøya

Ground Magnetic Surveying, Sampling, Magnetic Characterisation and 2D Modelling

Emilie Kolstø Strømøy

Geology
Submission date: August 2014
Supervisor: Suzanne McEnroe, IGB

Norwegian University of Science and Technology
Department of Geology and Mineral Resources Engineering

Abstract

Information on magnetisation of earth’s crust comes from the study of magnetic anomalies measured at various elevations using ground, airborne and satellite data, as well as studies of deep-seated rocks exposed at the surface. In the Western Gneiss Region (WGR), western Norway, two well exposed bodies of garnetiferous peridotites lay on the island Otrøya. The WGR is a 25.000 km^2 window of Proterozoic Baltica continental crust exposed in the Scandinavian Caledonides, and is one of the largest exposures of deeply subducted rocks on earth. The two bodies exposed on Otrøya contain evidence of the early stability of Archean tectonometamorphic megacrystic mineral assemblages that include high P/T enstatites and majoritic garnet (presently exsolved into Proterozoic and Scandian tectonometamorphic assemblages) (Van Roermund, 2008). The magnetic properties and anomaly responses of these peridotites and their immediate enclosing bedrocks were investigated by sampling orientated blocks, conducting magnetic measurements in field and at lab, as well as conducting a ground magnetic survey. This provides us with information on the magnetic properties of deeply subducted mantle fragments, and adds to the knowledge of what is magnetic in the lower crust and lithospheric mantle.

The study of the two peridotite bodies at Otrøya displays several morphologies of magnetite, mostly displaying as discrete forms within seams and cracks, but also as well-defined rims around chromites. The remanent intensity and susceptibility of the rocks are low, however the remanent intensity is somewhat varying. The directions of remanent magnetisation within measured specimens are both negative and positive with positive directions commonly displaying the same direction as the ambient field as well as commonly carrying weaker intensities than the negative. All of the above could be indicative of several stages of magnetite creation, and/or several events of recording of natural remanent magnetisation. The immediate constricting bedrocks displayed substantially higher remanent and induced intensities. Within the measured specimens both intensities were varying with the remanence displaying the largest variance in addition to showing both positive and negative directions. This was reflected in the anomaly map created from the ground magnetic survey due to anomalies, both high and low, displaying within these bedrocks. However, the peridotites correlate with wide anomaly lows. With 2D modelling a magnetic profile over the area was investigated with susceptibility and geometry of the bodies as input parameters. It became evident that the susceptibility contrast of the peridotites and the constricting bedrocks, as well as their geometries, could create anomaly lows as displayed in the anomaly map. However, it could not explain the most negative anomaly responses – an indication on remanence being of importance.

Sammendrag

Studier av magnetiske anomalier målt på bakkenivå, fra flymålinger og fra satellittdata, samt studier av dyptliggende bergarter eksponert på jordoverflaten, gir informasjon om magnetisme i jordskorpen. Den vestre gneissregion (WGR), i Vest-Norge, er et vindu i de skandinaviske Kaledonidene, og eksponerer 25,000 km^2 med tidligere dyptliggende berg. Disse består av proterosoisk baltisk kontinentalskorpe, og er blant de største vinduene av dypt subduserte bergarter nå eksponert på jordoverflaten.

I den WGR befinner det seg blant annet to eksponerte peridotittkropper på øya Otrøya. Disse peridotittene inneholder bevis for tidlig stabilitet av arkeiske tektometamorfoiske megakrystiske mineralsammensetninger med høy P/T enstatitter og majoritiske granater (i dag eksolvert i proterosoiske og skandiske tektometamorfoiske sammensetninger) (Van Roermund, 2008). Ved grundmagnetisk undersøkelse, magnetisk måling i felt, og magnetiske laboratoriemålinger av orienterte steinprøver av disse peridotittene og dets rundtliggende grunnfjell, ble deres magnetiske egenskaper og anomaliresponser undersøkt. Ved å skaffe kunnskap om de magnetiske egenskapene til disse bergartene vil også de magnetiske egenskapene til dypt subduserte mantelfragmenter bli innhentet, og muligens bidra til kunnskap om hva som er magnetisk i den nedre skorpen og i den litosfæriske mantelen.

Studiet av de to peridotittkroppene på Otrøya viser flere morfologier av magnetitt, for det meste av diskrete former i sømmer og sprekker, men også som veldefinerte kanter rundt kromitter. Den remanente intensiteten og susceptibiliteten til peridotittene var lav, men med noe varians innenfor den remanente intensiteten. Blant peridotittsteinprøvene var retningen til den remanente magnetiseringen både negativ og positiv med positiv vanligvis i samme retning som det nåværende magnetiske felt, men ofte med svakere intensitet enn remanens med negativ retning. Alle nevnte observasjoner kan være indikasjoner på flere stadier av magnetittdannelse, og/eller flere NRM opptak. Det rundtliggende grunnfjellet viste vesentlig høyere remanent og indusert intensitet. Blant steinprøver av disse varierte begge intensiteter, men den remanente intensiteten viste størst variasjon i tillegg til og vise både positive og negative retninger. Dette illustreres i et anomalikart laget fra de grundmagnetiske undersøkelsene, hvor både positive og negative anomalier kan bli observert over det rundtliggende grunnfjellet. Peridotittene vises i anomalikartet som brede negative anomalier. Et magnetisk profil over området ble undersøkt ved 2D modellering, hvor susceptibilitet og geometri av peridotittene var inngangsparametere. Det fremkom at susceptibilitetskontrasten på peridotittene og det rundtliggende grunnfjellet, samt deres geometri, kan skape negative anomalier slik som observert på anomalikartet. Imidlertid kunne ikke de mest negative anomaliresponsene til peridotittene forklares med 2D modelleringen – en indikasjon på at remanens kan være en medvirkende faktor.

Acknowledgements

I would like to thank Suzanne McEnroe for taking me on as her master student, finding an interesting project, and for helping me and guiding me through the world of rock magnetism. You have always had my best interest at heart. I thank Christine Fichler for helping me with Oasis montaj and modelling in GEM-SYS, being an additional supervisor on my thesis, and giving me feedback on my work. Field work was supported by NFR project 222666 'Sources and nature of remanent magnetization and susceptibility: Keys to interpretation of magnetic anomalies over continental lithosphere'.

There were many people at my faculty that helped me. Gerd Inger Sætrom is kindly thanked for her support and guidance throughout the project. Knut Solem is thanked for helping me with general computer issues throughout 2013 and 2014. I thank Nathan Church for help with density and VSM measurements, as well as with discussions of results. I would like to thank Arild Monsøy and Kjetil Eriksen at “slipelaboratoriet” for helping me at short notice and letting me use their machines. I would also like to thank Gunnar Vistnes for helping and learning me the machines at the rock mechanics laboratory. Additionally, I would like to thank Stephen Lippard and Allan Krill for helping me find a suitable supervisor while I was away on exchange in Australia.

At NGU I wold like to thank Morgan Ganerød for help with the spinner magnetometer, and Odleiv Olesen and Jomar Gellein for providing me aeromagntic maps over Otrøya. Additionally, I would like to thank Margrét Traustadóttir which also helped me on VSM measurements, as well as the optical microscopy of my thin sections.

I would like to thank Silvana and Leo who drove me to my field sight, and Peter Robinson for bringing me back as well as giving me insight into the geology of Otrøya. I would like to thank all the people at Sandneset camping, especially Karin, Arnfinn, Liba, Max and Rhino who took me in and kept me companied, even though they were over twice my age. A special thanks to Aud and Arne which provided me with lunch and a good talk about everything and nothing after finding me measuring susceptibility of rocks in their garden.

And last of all I want to thank all of my friends and family which have listened when I have talked about my project, even though they had no idea what I was talking about. Especially Johanne S. Ness, Anine Andresen and Sofie Sjøli which has joined me the last weeks at the student office to keep me companied, and Anniken Mjøen Solli which had to stand my rambling throughout lunchtime at Café Sito for a whole year.

Contents

List of Figures

List of Tables

1 Introduction

1.1 Introduction to magnetism in the lithosphere

The geomagnetic field recorded at, or near the surface of the Earth, originates largely from dynamo effects in the core of the earth. In addition will the permanent (remanent) and the induced magnetisation of crustal rocks, and magnetic minerals, also contribute to the overall magnetic field (Reynolds, 2011). Studies have been done concerning the question of what exactly is magnetic in the lithospheric crust and the upper-most (solid) lithospheric mantle and the mantle itself (McEnroe et al., 2009a&b; Dunlop et al., 2010; Ferré et al., 2013 & 2014).

The magnetic contributions from the lithosphere is characterised by long-wavelength static or slowly varying anomalies (varying from that of the geomagnetic field), whilst the magnetic contribution originating from the outer core are characterised by even longer wavelengths. In the geomagnetic power spectrum (Figure 1.1-1) this transition from core-dominated processes to lithospheric-dominated processes can be seen at degree 13 as a change of slope, called the inflection point. Based on Mauersberger-Lowes spectrum this corresponds to a wavelength of approximately 3000km (see Figure 1.1-1).

High-amplitude magnetic anomalies on Earth are commonly arising from small scale features within the crust. These diminish in amplitude and extend in wavelength with depth (Reeves and Korhonen, 2007), and are commonly known to be explained by both remanent and induced magnetisation, whilst long wavelength magnetic anomalies (LWMA) are commonly thought of to be explained by induced magnetisation (McEnroe et al., 2009a).

1.1.1 The magnetic boundary and sources for LWMA

The Mohorovic discontinuity (Moho) is the boundary between the lithospheric crust and the lithospheric mantle (Figure 1.1-2). The position of the Moho can in terms of seismic waves be defined as the boundary where “crustal” p-wave velocities of less than 7km/sec shift into “mantle” velocities in the range of 7.7-8.4 km/sec (Wasilewski & Mayhew, 1992). The seismic Moho was defined as a magnetic boundary by Wasilewski et al. (1979), where contribution to LWMA only existed above the seismic Moho. Later Wasilewski and Mayhew (1992) revised this statement stating that a non-magnetic upper mantle below the seismic Moho and strongly magnetic mafic lithologies in the lower crust is the most viable model, but the seismic Moho would in general not necessarily be a magnetic boundary. This revision was largely based on the complex and variable nature of the seismic Moho.

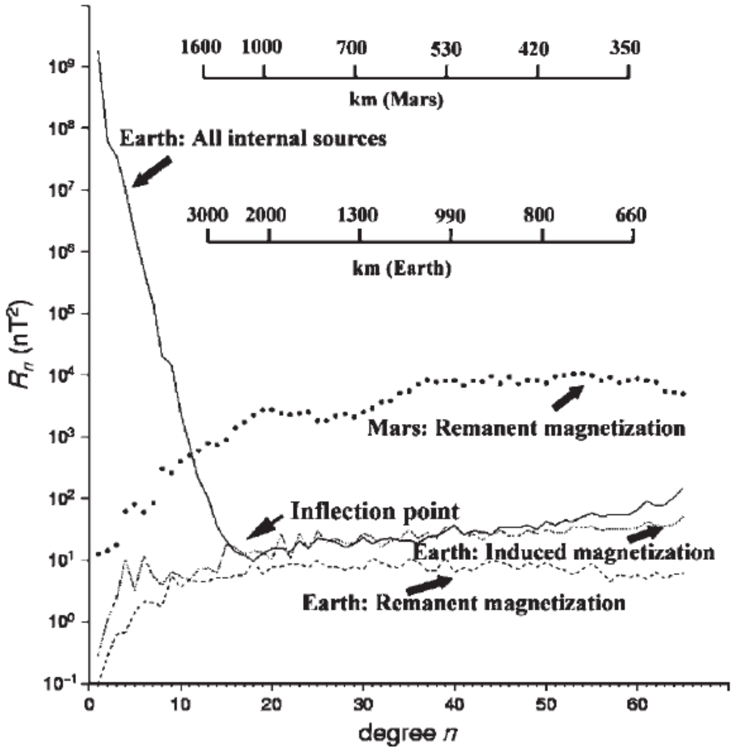

Figure 1.1-1: The inflection point in the terrestrial power spectra represents the sharp transition from core processes at low n to lithospheric processes at higher n. Rn is the mean square amplitude of the magnetic field over a sphere produced by harmonics of degree n. Data from Mars is also shown. After Purucker (2007).

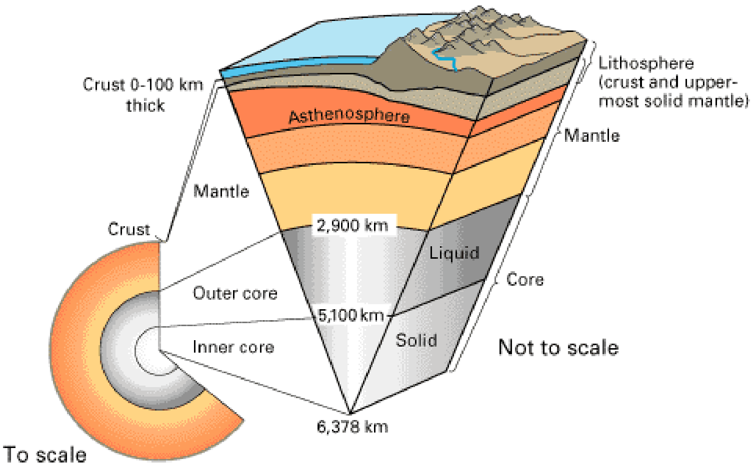

Figure 1.1-2: (Above) The Earth's interior and its respective thicknesses. After U. S. Geological Survey [USGS] (1999).

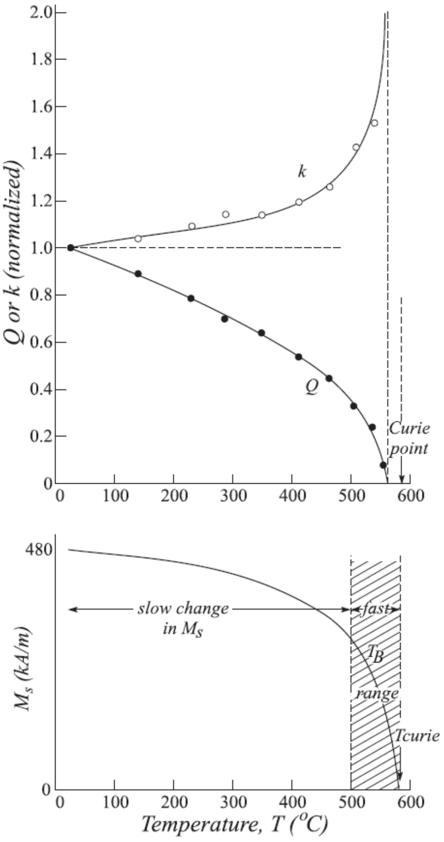

Figure 1.1-3: (Top right) Schematic diagram showing how susceptibility, k, increases and Q decreases for SD magnetite grains as temperature rises from 20°C to the blocking temperature T_B (where Q goes to zero, just below the Curie point). (Bottom right) Sketch showing how SD magnetite grains lose its magnetisation (M_s) when entering its blocking range (T_B). After Dunlop et al. (2010).

The origin of LWMA and its source has been described, among others, by Shive (1989) and Worm (1989) to largely be due to multi domain (MD) magnetite. Dunlop et al. (2010) agrees with this statement, and approaches the question of a magnetic boundary by looking at the limiting depth for magnetic sources based on the Curie point isotherm. With magnetite being the main contributor to the LWMA, with a Curie temperature (T_c) of 580°C, its isotherm and a magnetic boundary would be above 35 km depth at shield areas and shallower beneath mobile belts and active rifts. The T_c of magnetite is of now generally used as the magnetic boundary.

The statement of MD magnetite being the major contributor to LWMA was largely based on how magnetite acts according to its blocking temperature (T_B). For magnetite rocks, a typical range of blocking temperatures (T_B) would be 500-570°C (Dunlop et al., 2010). For MD magnetite, susceptibility values would be the same at all temperatures (T), whilst for T above 500°C its remanence would decrease by a factor of 2-3. For these conditions induced magnetisation would be three to five times as important as remanence when considering their respective contribution to LWMA.

In addition, Dunlop et al. (2010) argues that for single domain (SD) magnetite, induced magnetisation merges smoothly with thermo remanent magnetisation (TRM), when T is decreasing from T_B. At temperatures around T_B the induced magnetisation would, in general, become of similar importance to remanence for SD grains (Figure 1.1-3). Based on this Dunlop et al. (2010) concludes that at intermediate depths in the crust, where T is well below T_B and outside SD blocking range, remanence can play an important role for LWMA, if there is a reasonable SD magnetite content.

McEnroe and Brown (2000), on the other hand, found evidence for remanent magnetisation being essential in some observed LWMA. They observed high remanence values, high coercivities and Q values in slowly cooled igneous rocks containing members of the hematite-ilmenite solid solution series. This remanence arises from interfaces between canted antiferromagnetic hematite and paramagnetic ilmenite contact layers that attempt to reduce ionic charge imbalance (McEnroe et al., 2009a). This remanent magnetisation is called lamellar magnetism, and can, based on its intensity, dominate the induced magnetisation of a rock, giving the possibility for both negative and positive LWMA. McEnroe et al. (2009b) established that lamellar magnetism is not exotic, but a common cause of remanent magnetic anomalies.

Shive (1989) and Williams et al. (1985) also argues for the possibility of contribution of remanence in the lower crust, but then for viscous remanent magnetisation (VRM) required by magnetite. Though, Shive notes, VRM can only account for about an increase in 25% compared to the given induced magnetization at time of acquisition.

1.1.2 Magnetism in the lithospheric mantle and the crust

The question of where the source of the LWMA resides has also been highly debated. As pointed out, Wasilewski et al. (1987) and Wasilewski and Meyhew (1992) argued that the source resides inside the crust, whilst the lithospheric mantle is non-magnetic. Shive (1989) and Worm (1989) explained the LWMA largely to be due to MD magnetite, residing in the deep crust. Dunlop et al. (2010) agreed with this, and defined the magnetic boundary to be of the magnetite Curie isotherm.

Drawn on the basis of magnetite being the major contributor to LWMA, Shive (1989) and Williams et al. (1985) argued that the magnetisation measured in the lower crust is too weak to account for the observed magnetic anomalies. They state that even with VRM present in the lower crust, this remanence will not contribute significantly to LWMA. The relatively new discovery of lamellar magnetism described by McEnroe and Brown (2000) and McEnroe et al. (2009a, b) is a plausible explanation for this "missing magnetisation". McEnroe states that lamellae in the ilmenite-hematite system can have blocking temperatures above 580°C– indicating that lamellar magnetism of considerable strength may persist in the deep crust, contributing to LWMA. This also makes it necessary to reconsider the view of T_C of magnetite being the magnetic boundary. McEnroe et al. (2009b) are in addition putting constraints to the contribution to LWMA from SD magnetite by pointing out that fine-grained, SD magnetite, will coarsen and demagnetize under such conditions.

Ferré et al. (2013 & 2014), on the other hand, stated that the uppermost mantle could be magnetic due to magnetite. They base this largely on the existence of lithospheric mantle cooling below the Curie temperature for magnetite, especially for tectonic settings with depressed geotherms such as subduction zones, cratons, and for old oceanic lithosphere. In addition are some fine intergrowths such as hematite-maghemite/magnetite and the mantle mineral awaurite known to be extremely stable with T_B above 580°C. These could reside in the uppermost mantle, but according to Ferré et al. (2014) they are negligible concerning LWMA.

1.2 Further investigations of magnetism in the lithosphere

The existence of magnetic minerals in the lithospheric mantle, and their importance to LWMA e.g. compared to lamellar magnetism, needs to be further investigated. To investigate LWMA the most common approach is to use near-Earth satellites at altitudes of 350-750km (altitudes which generally is associated with the shortest wavelengths obtained for such anomalies). In November 2013 the European Space Agency launched the *Swarm* constellation of three satellites with the objective of resolving the lithospheric magnetic field with an exceptional accuracy. The mission of the satellites will be to bridge the spectral gap between satellite and airborne/marine magnetic surveys. To do this additional information on the magnetic character of deep crustal rocks needs to be obtained. In addition to satellite and airborne/marine magnetic surveys, information on magnetisation of Earth's crust comes from the study of anomalies measured at ground level (high amplitude magnetic anomalies), as well as studies of deep-seated rocks exposed at the surface. By investigating magnetic susceptibility, NRM and Q values, demagnetization behaviour, hysteresis, saturation and magnetic mineralogy of well exposed crustal sections of both metamorphic and deep crustal igneous rocks, a better understanding of the nature of magnetisation in the lower crust and lithospheric mantle can be obtained. LWMA, in the concern of induced and remanent magnetisation caused by magnetite and other magnetic minerals and intergrowths, especially for remanent magnetisation caused by VRM in magnetite, and remanence caused by lamellar magnetism, can in that way be further investigated.

1.2.1 The peridotites of Otrøya

Based on magnetic anomaly maps provided by NGU (personal communications) two peridotite bodies previously mapped in a simplified geological map over western Otrøya (Spengler, 2006, and references therein) are displayed within an area of green to blue colour, indicating anomaly lows in the anomaly map (Figure 1.2-1). Its immediate enclosing bedrocks, mostly consisting of gneiss rocks, display as yellow to red in the anomaly map, indicating normal values to anomaly highs.

These peridotites are of the Mg-Cr type garnet peridotites and display characteristic upper mantle mineral and whole rock chemistries (Carswell, 1968 as cited in Van Roermund, 2008) and isotopic ratios (Brueckner, 1977 as cited in Van Roermund, 2008) consistent with derivation from very highly depleted sub-continental lithospheric mantle (SCLM). The previous studies of the peridotite rocks of Otrøya gives estimated origin depths of at least mantle transition zone, evidence of at least three (ultra) high pressure temperature metamorphic events, firstly in the Archean (M1), in the Proterozoic (M2) and last in the Scandian (M3), and minerals containing evidence for all of the events mentioned above. This gives an exceptional opportunity to study the magnetic characters of large fragments of cratonic lithosphere, with a well-known history.

Due to the anomaly low observed over the peridotite bodies at Otrøya (Figure 1.2-1) the anomaly map raises the question of whether the peridotites can cause these magnetic anomalies. Peridotite rocks are usually described as weakly magnetic to paramagnetic, but the hydrothermal alteration process serpentinization, known to occur in peridotites, produces magnetite as a by-product. The peridotites at Otrøya are known to have undergone serpentinization. Can the anomaly low observed at Otrøya be due to magnetite produced by serpentinization of these peridotites, or by other minerals, processes, or the geometry of the bodies within the gneisses?

In this study a review of the extensive structural, mineralogical, geochronological, geochemistry and ultrahigh-pressure metamorphic petrology studies of these peridotite bodies, and the peridotites and rocks of the WGR, is presented. In addition, a review of geomagnetic theory, including earth magnetism, rock magnetism, types of magnetism and magnetic parameters, terrestrial magnetism as well as serpentinization is presented.

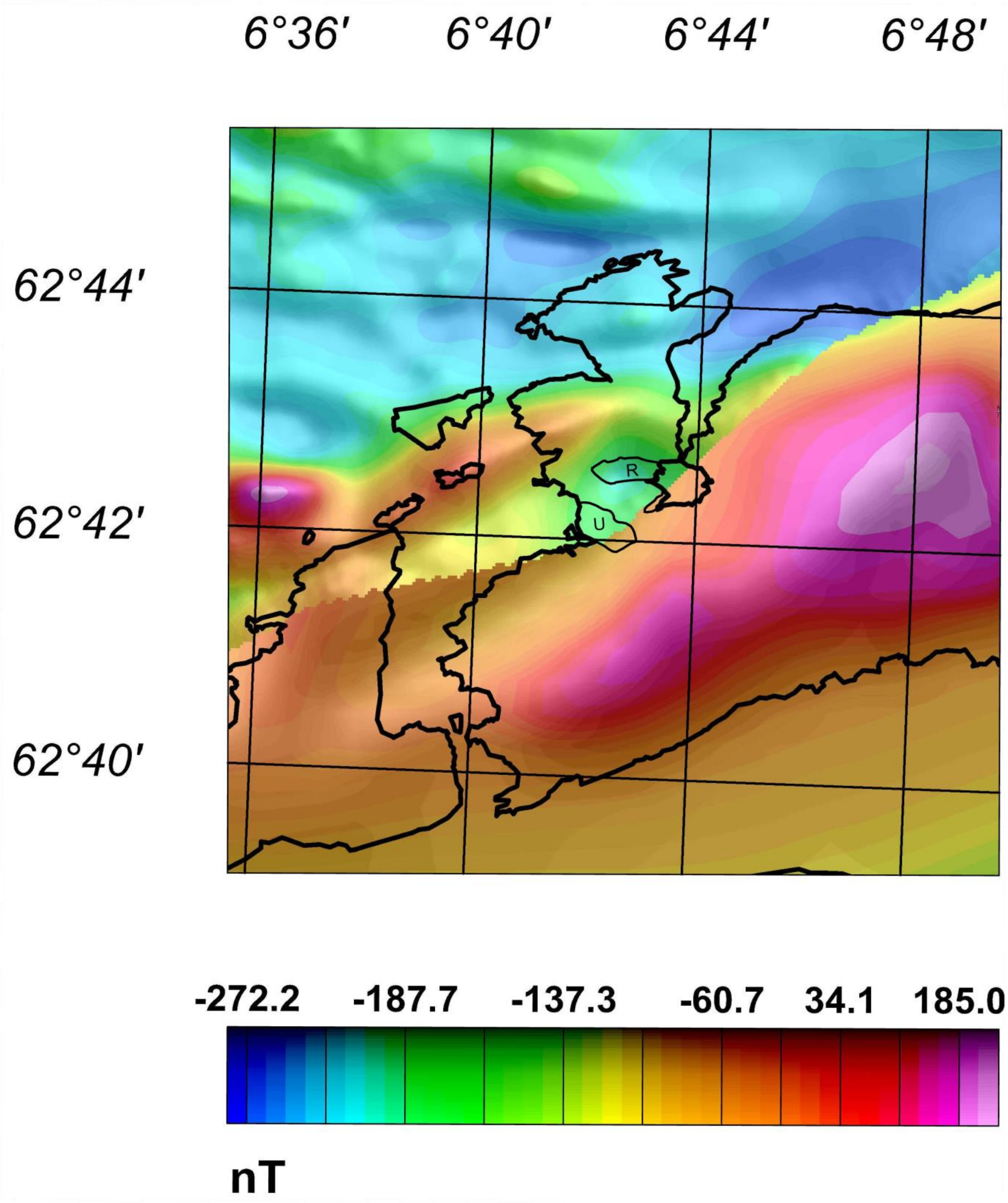

Figure 1.2-1: Peridotite bodies locations taken from the simplified geological map over Otrøya (Spengler, 2006 and references therein) superimposed an aeromagnetic map over western Otrøya provided by NGU (personal comunication). The two peridotite bodies, R=Raudhaugene and U=Ugelvik, can be viewed. Based on the aeromagnetic map the immediate enclosing bedrocks display higher anomalies (yellow to red) than these peridotite bodies (green to blue). Note that the aeromagnetic map consist of both new and old data put together. The border between new (upper part) and older (bottom part) is displayed as a sharp contrast in displayed anomaly values.

2 Aim of study

The aim of this study is to answer the following four questions concerning the peridotites of Otrøya:

1) What is magnetic in the peridotites and their immediate enclosing bedrocks?
2) What are the magnetic properties of the peridotites and their immediate enclosing bedrocks?
3) Can the peridotite bodies be viewed on a ground magnetic anomaly map, and can the anomalies be explained by the obtained properties?
4) Can the peridotite bodies be modelled based on geometry and susceptibility constraints provided by respectively literature and this study?

To investigate the magnetic mineral content of the peridotites, and to a minor degree the mineral content of its immediate enclosing bedrocks, thin sections from these rocks have been studied by optical microscopy and some selected thin sections by Scanning Electron Microscopy (SEM). Both, magnetic minerals and morphologies of the inhabitant magnetic minerals are described. On basis of these investigations the possible magnetic behaviour of these minerals is discussed.

To investigate the magnetic properties of the peridotites and its immediate enclosing bedrocks, samples of these rocks have been measured for NRM, susceptibility and hysteresis properties, and their magnetic properties have been presented. Further, the response of remanent intensity and induced magnetisation onto the total magnetic field has been investigated by evaluating the Q-value and the direction of the remanent intensities. Further investigations of the magnetic mineral content and how these tie in with the magnetic properties, have been evaluated. The degree of serpentinization and how this effects the peridotites with respect of density change and magnetic mineral content has to a certain degree been evaluated.

To investigate the response of the peridotites within the immediate constricting bedrocks a ground magnetic survey has been conducted. The magnetic data have been processed and an anomaly map has been created. The magnetic properties obtained have been evaluated on the basis of the magnetic anomaly response observed in the ground magnetic anomaly map.

To evaluate the response of the geometry and the susceptibility contrast between the peridotite bodies and their immediate enclosing gneisses, a 2D profile over the two bodies, based on constraints of structural data and geological maps, has been investigated. The main conclusion drawn from this investigation is that susceptibility contrast between the peridotite bodies and the constricting bedrocks is the main contributor to the anomalies created.

3 Location, Tectonics and Geological Setting

3.1 Location and Geomorphology: The Western Gneiss Region

The Western Gneiss Region (WGR) lies along the west coast of Norway, between Sogn and Nord-Trøndelag, and covers about 25.000 km^2 (location shown in Figure 3.1-1). The region consists mainly of Precambrian rocks, with varieties of granitic gneisses and migmatites often with lenses and layers of mica rich gneisses and amphibolites (Ramberg, Bryhni & Nøttvedt, 2007). The gneisses making up the crust of the northern WGR is dated to be originating from the 1.7 Ga to 1.5 Ga Gothian orogeny (Beyer et al., 2012), while the southern WGR is Sveconorwegian. The geological structures of the area are primarily acknowledged as the result of the formation of the Scandian Caledonides.

The WGR is the lowermost tectonic unit in the Scandian Caledonides. This is an 1800km long, linear, orogenic belt composed of nappe units (i.e. the lower, middle, upper and uppermost allochthons, Figure 3.1-2). These were assembled during the closure of the Iapetus Ocean during the 435-390 Ma Scandian Orogeny (Beyer et al., 2012 and references therein). During this collision the nappes were thrust and re-thrust towards the east or south-east (present coordinates), resulting in the western continent, Laurentia, overthrusting the crystalline, Precambrian, rocks of the eastern continent, Baltica (Beyer et al., 2012). The WGR is generally interpreted to originate from the western rim of the Baltic shield. The Precambrian rocks along this rim were in places subducted to great depths of at least 180-200km (Van Roermund, 2009). A sign of this deep subduction is the metamorphic facies observed in the area. The northern part of the WGR contains hundreds of bodies of High Pressure (HP) to Ultra High Pressure (UHP) eclogites and other eclogite facies rocks, including garnet peridotites (Beyer et al., 2012), indicating up to Ultra-High-Pressure-Metamorphism (UHPM), while the southern part indicate amphibolite to granulite metamorphic facies (Van Roermund, 2009). In Figure 3.1-1 this increase of temperature (and pressure) from the south-east (≤600°C) to the north-west (≥800°C) is shown. It should also be noted that most of the UHP eclogites are found near, or west of the 800°C isotherm.

The peridotites within the WGR have been vastly studied due to the question of how the peridotites were emplaced into the gneisses. Medaris Jr. (1984) represented two hypotheses about the placement of the peridotites into the crust of the WGR; the peridotites, with developed garnet, were tectonically emplaced from the mantle, or they were emplaced in the crust where it was serpentinized and metamorphosed along with the crustal rock. The former hypothesis is the most widely recognised today. Beyer et al. (2012) support this hypothesis and argue that the peridotites of the WGR were tectonically introduced as fragments of the subcontinental lithosphere beneath Laurentia. Their study (and references therein) shows that the bulk of the WGR gneisses were originally generated during the 1.7-1.5 Ga Gothian orogeny.

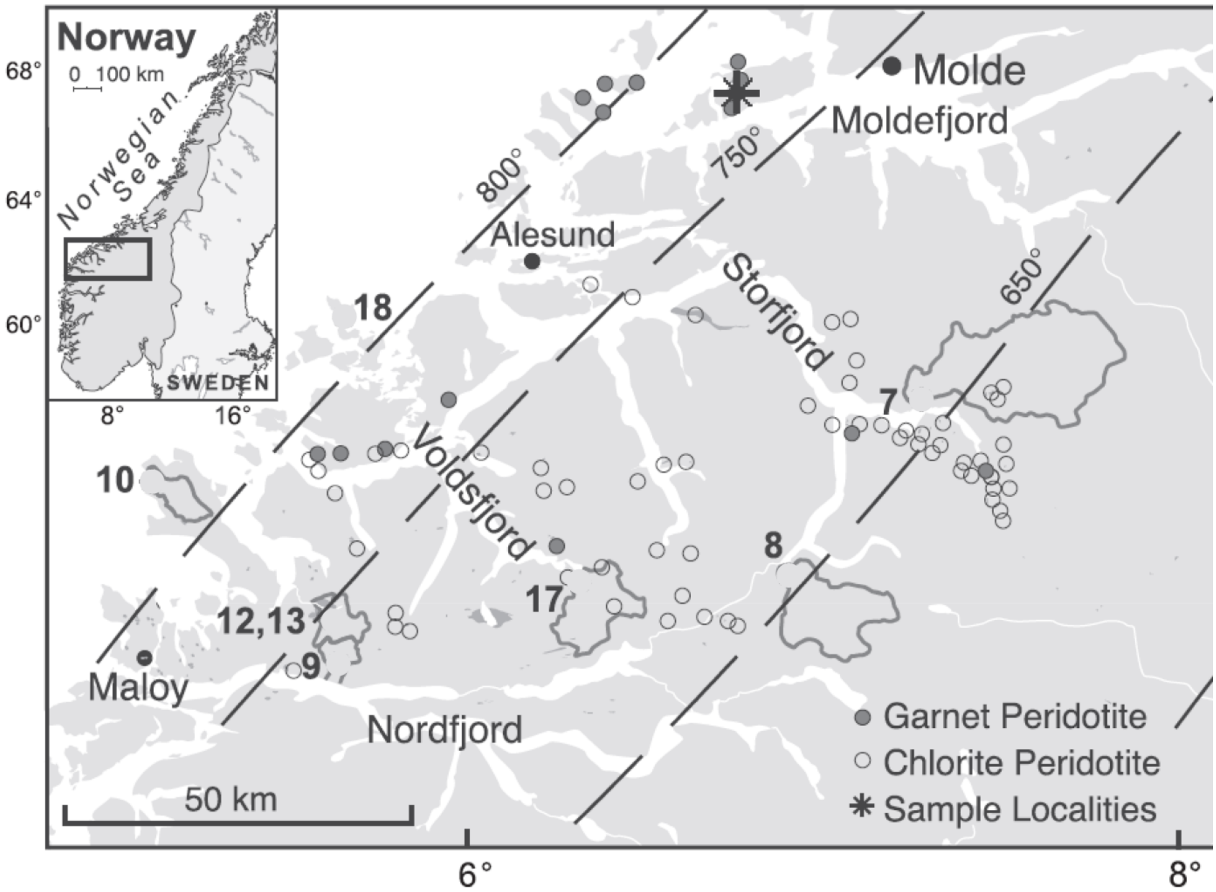

Figure 3.1-1: : Location map of the WGR showing; sample localities(*) on Otrøya, light grey shows allochtons, dashed lines show generalized isotherms for the Caledonian HP-UHP metamorphism, derived from equilibration temperatures of eclogites (after Krogh, 1977 & Beyer et al., 2012) Open circles, chlorite peridotite, filled circles, garnet-peridotite. The increasing T (and P) towards the coast should be noted (modified after Beyer et al., 2012).

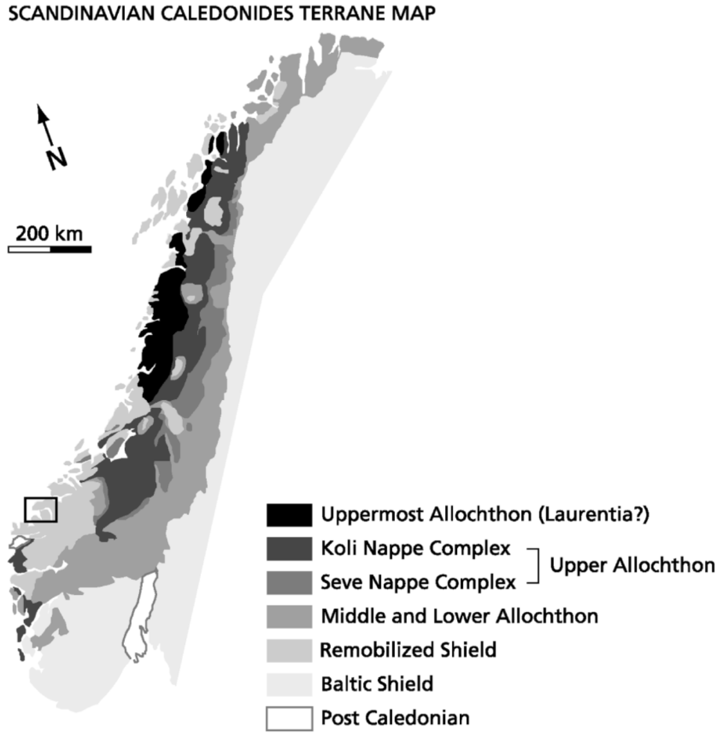

Figure 3.1-2: Map of Norway showing the Caledonian nappe complex. Black rectangle shows the location of the northwestern part of the Western Gneiss Region (After Van Roermund, 2009).

Later the Grenville-Sveconorwegian event overprinted these rocks in an early stage (1.3-1.5 Ga) with significant juvenile additions to the crust, and a later stage (1.1 to <1.0 Ga) where magmatic rocks were derived largely by remelting of the Gothian basement. However, the peridotites shows generation by extreme partial melting at least 3 Gyr ago, with at least one metasomatic refertiliation event at 2.8-2.9 Ga, and probably during later events as well. Beyer et al. (2012) concluded that the absence of any evidence of Archean crust beneath southern Baltica implies that the Archean peridotite massifs represent fragments of the subcontinental lithosphere beneath Laurentia. Based on these observations the peridotites of the WGR can be classified as *Relict subduction zone peridotites* (RSZP) (Brueckner & Medaris, 2000), as they are metamorphic products from the hanging wall, Laurentia, which contains relict assemblages formed earlier than the recrystallization recorded in the subduction eclogite-facies crustal gneisses of Baltic affinity.

The peridotites of the WGR have also been classified as Alpine type peridotite, Mg-Cr peridotite or orogenic peridotites (Spengler, 2006), as they are mantle fragments incorporated into a mountain belt during orogeny.

3.2 Regional tectonic setting: The history of the garnet peridotites of the Western Gneiss Region

As described by Van Roermund (2009), Tony Carswell drew attention to the peculiar geological setting of the WGR, with its presence of garnet peridotite (containing layers or lenses of garnet websterite, eclogite or pyroxenite) enclosed as mega-lenses within amphibolite- and high pressure granulite-facies country rock gneisses that also contained lenses of meta-gabbro and eclogite. One of Carswell's earlier works was when he mapped parts of Otrøya in the late 1960s and 1970s, and he played a leading role in the understanding of how this peculiar geological setting could be explained from a geodynamic point of view. Carswell et al. (1983 as cited in Van Roermund, 2009) was the first researcher who drew attention to the existence of two fundamentally different chemical types of garnet-bearing peridotite bodies in the WGR; The Fe-Ti type and the Mg-Cr type garnet peridotites. This discovery led to extensive mineralogical, geochronological, geochemistry and ultrahigh-pressure metamorphic petrology studies of the peridotites of the WGR. In this review of the previous studies of the peridotites of the WGR, the terminology of Scambelluri et al. (2008) is used to indicate the ages of UHP events: M1, Archean; M2, mid-Proterozoic; M3, Scandian (430-390 Ma).

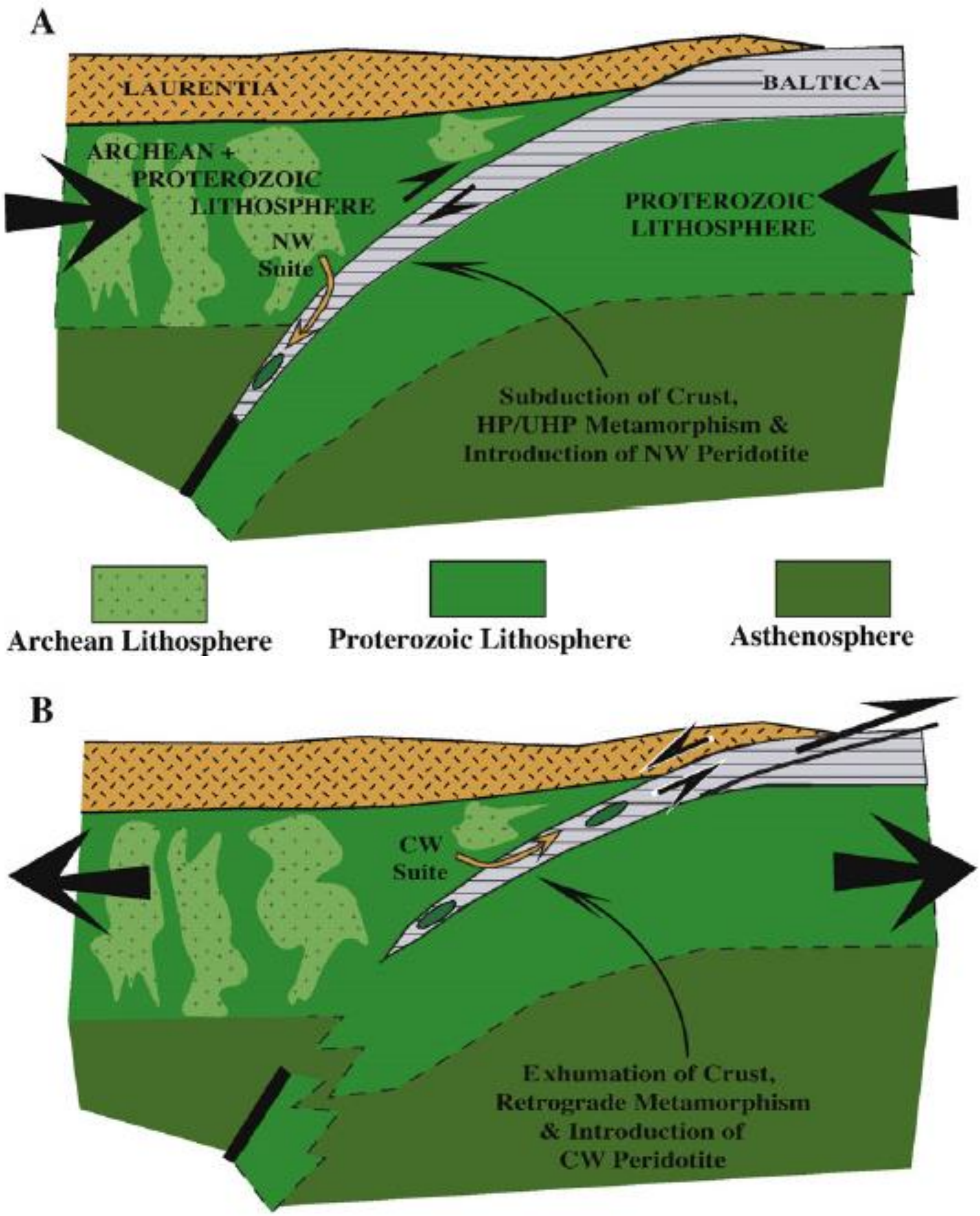

Figure 3.2-1: The Scandian orogeny showing subduction of Baltic crust underneath Laurentian lithosphere, two events of incorporation of lithosphere into the crust, and exhumation. A: introduction of peridotites from the Archean/Proterozoic sub-Laurentian mantle during subduction and further subduction to deeper levels resulting in Scandian recrystallization and metasomatism within the diamond stability field. B: introduction of peridotites into the crust from shallower and cooler levels of the mantle as the crustal slab was returning to the surface. After Brueckner et al. (2010). Present location of NW- and CW Peridotites in Figure 3.2-2, and explained in the following chapters.

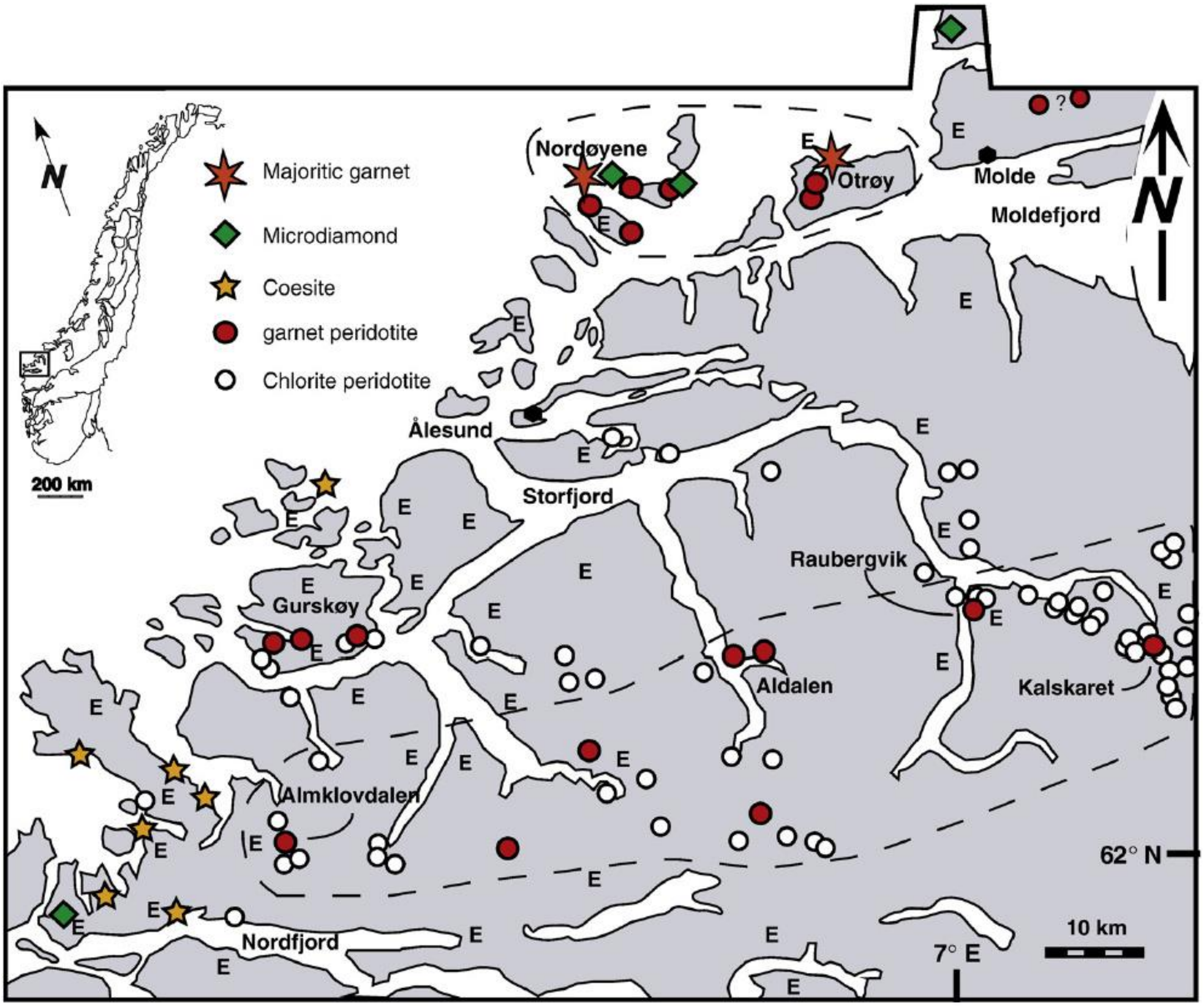

Figure 3.2-2: Generalized map of part of the Western Gneiss Region of the Norwegian Caledonides showing peridotite localities (circles) and the general distribution of eclogites (E). The garnet peridotites are divided into northwest (NW) peridotites (upper dashed field) and central-west (CW) peridotites (lower dashed field). After Brueckner et al. (2010).

3.2.1 The Mg-Cr type garnet peridotites of the Western Gneiss Region

The Fe-Ti type garnet peridotites were interpreted to have had a prograde (U)HP metamorphic history that started as the ultramafic portions of layered low pressure, Proterozoic, crustal intrusive bodies that were metamorphosed during Scandian subduction. By contrast, the Mg-Cr type garnet peridotites display characteristic upper mantle mineral and whole rock chemistries (Carswell, 1968 as cited in Van Roermund, 2008) and isotopic ratios (Brueckner, 1977 as cited in Van Roermund, 2008) consistent with derivation from very highly depleted sub-continental lithospheric mantle (SCLM).

Sm-Nd dating of garnet+clinopyroxene+whole rock in samples of the Mg-Cr garnet peridotite type and related olivine-free garnet pyroxenites, done by Bruckner et al. (2010 and studies therein), show that the earliest garnet-bearing assemblages were of mid-Proterozoic age and thus were present as stable assemblages in the SCLM long before the Scandian, subduction related, (U)HPM event experienced by the WGR. Another indication of stability of garnet-bearing assemblages before the Scandian, subduction related, (U)HPM event, is the discovery of pyroxene exsolution lamellae in megacrysts of the earliest (M1 and M2) garnet generations in samples from the Mg-Cr type peridotite bodies outcropping on Otrøya (Van Roermund et al., 2001 and references therein). The microstructure can indicate that the M1 garnets originally contained a significant majorite (i.e. high silica) component. This led to the theory of the Mg-Cr type garnet peridotites were originating within a rising mantle diapir or alternatively an uprising part of an asthenospheric convection cell from depths of at least 185km (Terry et al., 1999; Van Roermund, 2000; Drury et al., 2001, as cited in Van Roermund 2009). The pyroxene exsolution within M1 and M2 garnet have now been reported from all major rock types within the garnet peridotite bodies, including garnet websterites and garnet clinopyroxenites (Spengler et al., 2006).

Spengler et al. (2006) also looked at the pyroxene exsolution in the Mg-Cr garnets from Otrøya, and deducted that the initial majorite composition was of at least 20%, indicating an original mantle source derived from at least mantle transition zone depths (410-670km). The derivation was interpreted to be of melting during decompression at 1800°C or above and 8GPa or above. Such conditions were only present in the Archean. Further, they calculated confining pressures for stable garnet growth to be of ≥11.5 GPa corresponding to ≥350 km depth. This study of the Otrøya peridotites therefore appears to be the first reported case of orogenic peridotites produced by extensive melt depletion entirely in the garnet stability field during the Archean era (Spengler et al., 2006).

Further studies of the garnet bearing orogenic peridotites and dunites in the HP/UHP region of the WGR (Van Roermund, 2009; Brueckner et al., 2010 and references therein) showed mid-late Proterozoic Sm-Nd mineral isochron and Archean-Scandian Re-Os sulphide ages. This clearly illustrates that the WGR has experienced more than one UHPM event, a feature that may make this region unique in the World. These results suggest a common origin for all WGR peridotites, followed by different, but related, Proterozoic and Phanerozoic histories.

The peridotites of the WGR that contain garnet-bearing assemblages with evidence of a lithospheric mantle can be classified as “relict” peridotites (Brueckner & Medaris, 2000). This means that in these peridotites not only the Scandian mineral ages and crustal emplacement conditions can be reconstructed, but the Archean to mid/late Proterozoic mantle evolution of the peridotite bodies can also be reconstructed. The crustal emplacements at UHPM conditions did not completely erase the Archean to mid/late Proterozoic mantle signatures of the bodies (Van Roermund, 2008).

Due to indications of multiple histories of decompression textures in the relict Mg-Cr garnet peridotites, the multistage exhumation history theory was presented (Spengler et al., 2006; Scambelluri et al., 2008). In addition, Brueckner et al. (2010) proposed different histories for the garnet-peridotites of the northwest WGR (NW peridotites) compared to those in the central and western WGR (CW peridotites, including chlorite peridotites) (Figure 3.2-2). Figure 3.2-3 and Figure 3.2-4 are showing a summary of the Scandian tectonometamorphic evolution of garnet bearing, Mg-Cr type peridotite bodies presently exposed in the northwest WGR.

3.2.2 Three tectonometamorphic events

The three tectonometamorphic events are based on three episodes of majoritic garnet growth in the garnet peridotites of the WGR. These are the M1, M2 & M3 events, where all of them were followed by exsolution of pyroxenes (Scambelluri et al., 2008).

The earliest episode, M1, happened during the Archean during one or more episodes of mantle upwelling, melting and cooling. The first upwelling happened due to adiabatic decompression occurring at temperatures around 1700-1800°C, with a mantle melt origin from mantle transition zone depths (>350km) (Scambelluri et al., 2008). There was an extraction of HPT decompression melts, and refractory peridotite was formed containing the M1a megacrystic assemblages of majorite garnet (garnet before exsolution), containing ≥4 vol% majorite (Brueckner et al., 2010). Further upwelling of these fragments of mantle led to isobaric cooling to sites of deep cratonic roots (100-125km) while being within the garnet stability field. The M1b megacrystic majorite garnet (garnet after exsolution) was formed, whilst interstitial pyroxene exsolutions were formed from the M1a garnet (Scambelluri et al., 2008), and left the garnet with ≈ 1% majorite (Brueckner et al., 2010).

In the mid-Proterozoic (M2) another recrystallization event led to exsolution of intercrystalline pyroxene from M1b garnet. Bruckner et al. (2010) suggests continuous diffusion of M2 minerals formed ≥ 1.75 Ga ago. The M2 event was either due to further decompression and cooling at the base of the lithosphere (Spengler et al., 2006) or during a partial re-equilibration, 1.0 Ga event, either due to an upwelling thermal diapir or could be due to static diffusion (Brueckner et al., 2010). Brueckner et al. (2010) propose that the mid-Proterozoic event resulted both in $M2_{NW}$ exsolution and $M2_{CW}$ silicate melt formation, depending on position in the mantle, where the $M2_{NW}$ assemblage developed deepest down and are the assemblages currently within the NW peridotites.

During the Scandian orogeny (M3) the NW peridotites were transferred from the mantle wedge into the crust as the Western Gneiss Region was subducted into the mantle to about 200km depth (Figure 3.2-4). The subduction heterogeneously metasomatized and recrystallized the NW peridotites into M3 mineral assemblages of garnet, clinopyroxene and, where metasomatism was persistent, phlogopite, amphibole and microdiamond. The Scandian P-T conditions for the growth of the M3 assemblages are estimated to be of 850-950°C and 5.5-6.5 GPa (Van Roermund, H., 2009). The CW peridotites do not show evidence of prograde M3 re-equilibration, indicating derivation from a different part of the Laurentian mantle during exhumation.

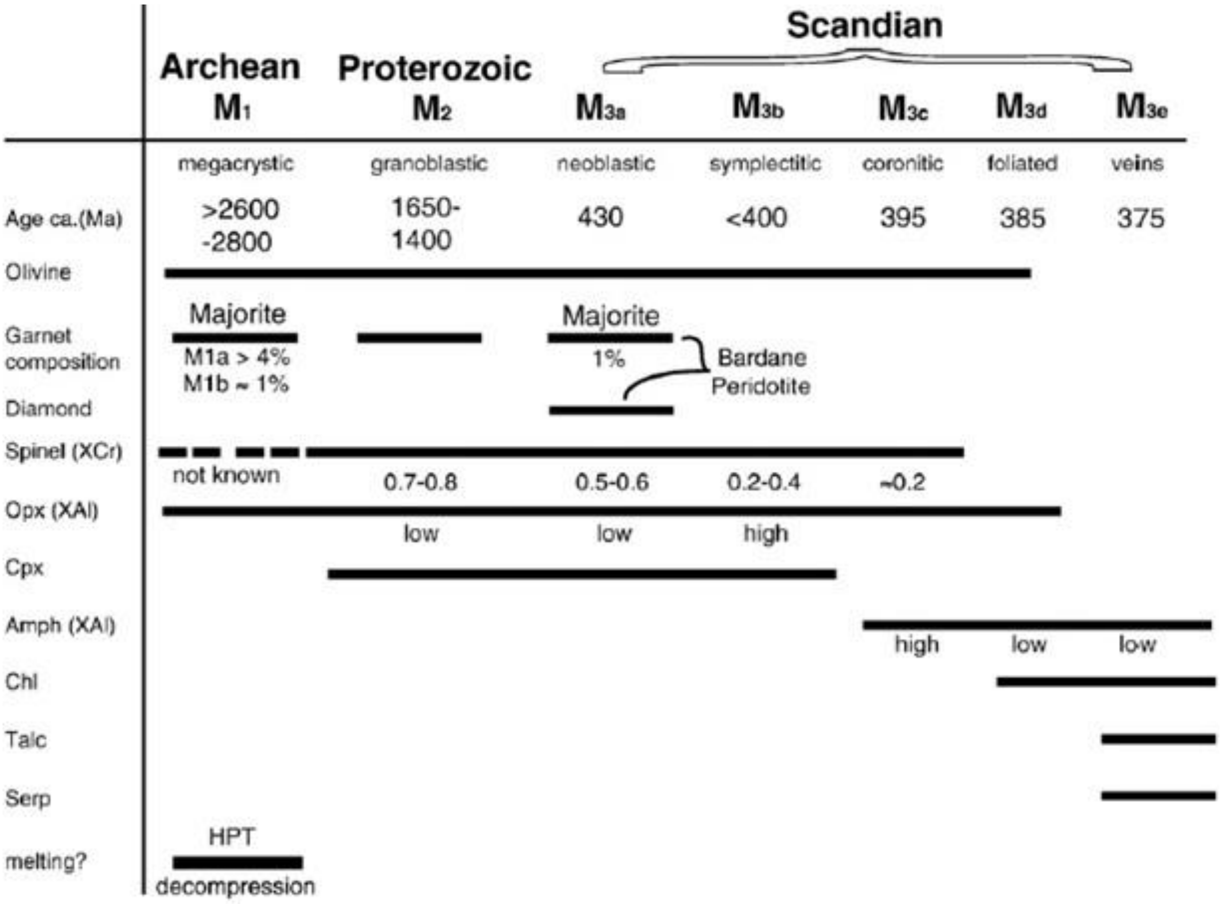

Figure 3.2-3: Tectonometamorphic evolution of garnet-bearing, Mg-Cr type peridotite bodies presently exposed in the northwest WGR After H. K. Brueckner et al. (2010).

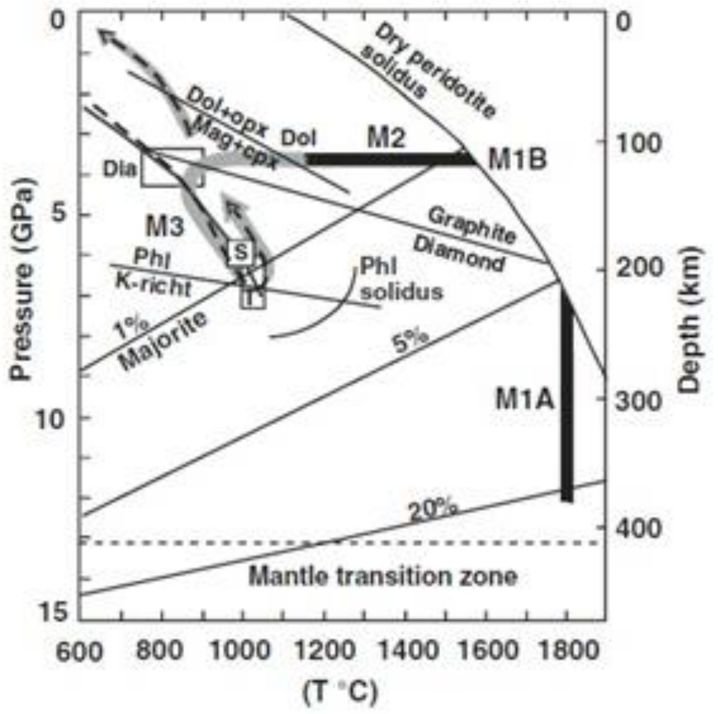

Figure 3.2-4: Pressure-temperature (P-T) path of diamond- and majorite-bearing Bardane websterite lens, within the proposed northernmost UHPM domain of the WGR. Black path: Archean M1 (A-B) to Middle Proterozoic M2 events. Light gray path – presented Scandian evolution. Dashed line – inferred P-T path of associated continental crust. White box – diamond crystallization conditions in Norway (dia). Solid black line – hot subduction geotherm (Peacock and Wang, 1999, as cited in Scambelluri et al., 2008). Thin solid lines labelled 1%, 5% , 20% - experimental isopleths for majorite component in garnet. Dol – dolomite; opx – orthopyroxene; Mag – magnesite; cpx – clinopyroxene; Phl – phlogopite; richt – richterite. After Scambelluri et al. (2008).

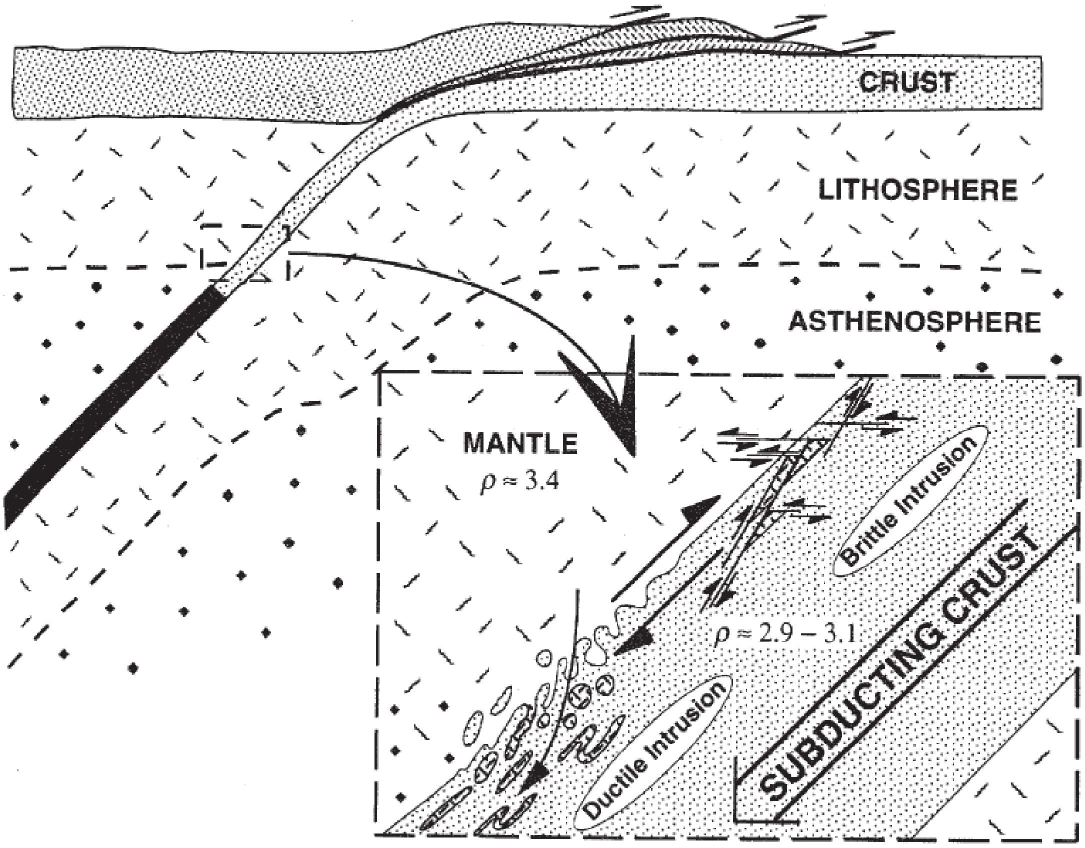

Figure 3.2-5: Schematic model for peridotite emplacement from the hanging wall into a subducted slab of continental crust through brittle and ductile mechanisms. After Brueckner (1998, as cited in Spengler, 2006).

However, the CW peridotites record a regression history, due to the presence of zoned kelyptic assemblages documenting a retrograde history through granulite and amphibolite facies conditions (Brueckner et al., 2010). This suggests that the CW peridotites were inserted into the crust as the slab returned towards the surface (Figure 3.2-5). The mechanisms for incorporating the peridotites of the WGR are proposed to be through brittle and ductile mechanisms (Brueckner & Medaris, 1998, as cited in Spengler 2006).

The Western Gneiss Region was exhumed, with a time frame from 430 Ma to 390 Ma, maybe even later (Bruckner et al., 2010). During its prograde and retrograde path the rocks of the WGR underwent eclogite, amphibolite and greenschist facies. The short time frame of exhumation has led to the preservation of many of the minerals associated with these facies (Spengler, 2006; Scambelluri et al., 2008; Spengler et al., 2009). The short time frame of exhumation can be explained by buoyancy driven return of the slab to the surface (Spengler, 2006).

3.3 Geological setting of the Investigated Area: Otrøya

The area in study, Otrøya, is in the NW, UHPM domain, of the Western Gneiss Region. The Proterozoic Baltica basement rocks exposed in this domain consists of east-west- to NNE-SSW-trending belts of interlayered augen orthogneiss, and well-layered, migmatic, dioritic-granodioritic gneiss. The interlayered augen orthogneiss often display migmatitic fabric as well as containing minor eclogitized meta-gabbro and/or eclogite. The dioritic-granodioritic gneiss encloses abundant eclogite and subordinate garnet peridotite (Van Roermund, 2009). The dominant facies is amphibolitic with subvertical foliation, commonly with a well-developed subhorizontal east-west amphibolite-facies lineation (Van Roermund, 2008).

3.3.1 Northern and southern Otrøya

The northern part of Otrøya consists of the Proterozoic Baltica basement rocks, as described above, including garnet peridotites and eclogites (Figure 3.3-1 and Figure 3.3-2). These rocks have undergone Scandian UHPM exemplified by Al_2O_3 contents in opx (orthopyroxene) as low as 0.20 and 0.15 wt% in, respectively, internal and external garnet websterites-pyroxenes (Van Roermund, 2009, and references therein).

The southern part of Otrøya was recognized by Robinson (1995, 1997 as cited in Van Roermund, 2009) to represent (infolded) allochtonous supracrustal rocks that, could be correlated with the Trollheimen nappe tectonostratigraphy in the east. The allochtonous supracrustal rocks of the southern parts of Otrøya are also recognised to very rarely contain HP minerals and/or (retro-) eclogites. This emphasises that the entire unit in the south was metamorphosed under upper amphibolite- to HP granulite-facies conditions at 700-800°C and ≤10-11 kbar (Van Roermund, 2009 and references therein).

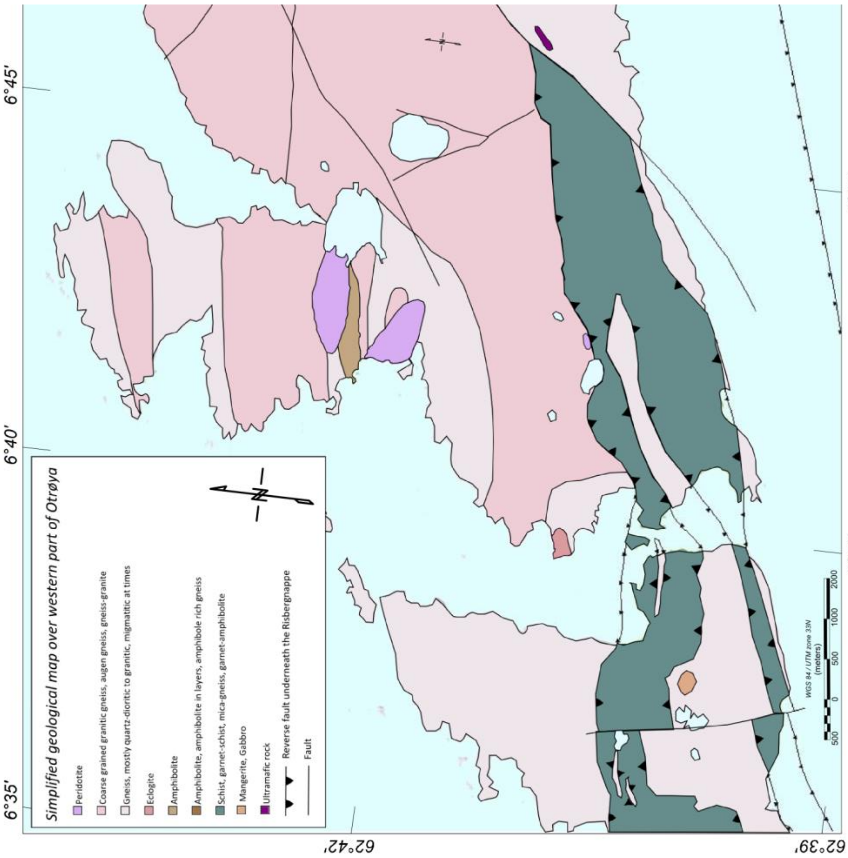

Figure 3.3-1: Geological map modified from N250 (NGU, n.d.) of the western part of Otrøya, displaying the Ugelvik and Raudhaugene peridotites within Proterozoic basement gneiss in the north, and allochtonous supracrustal rocks in the south.

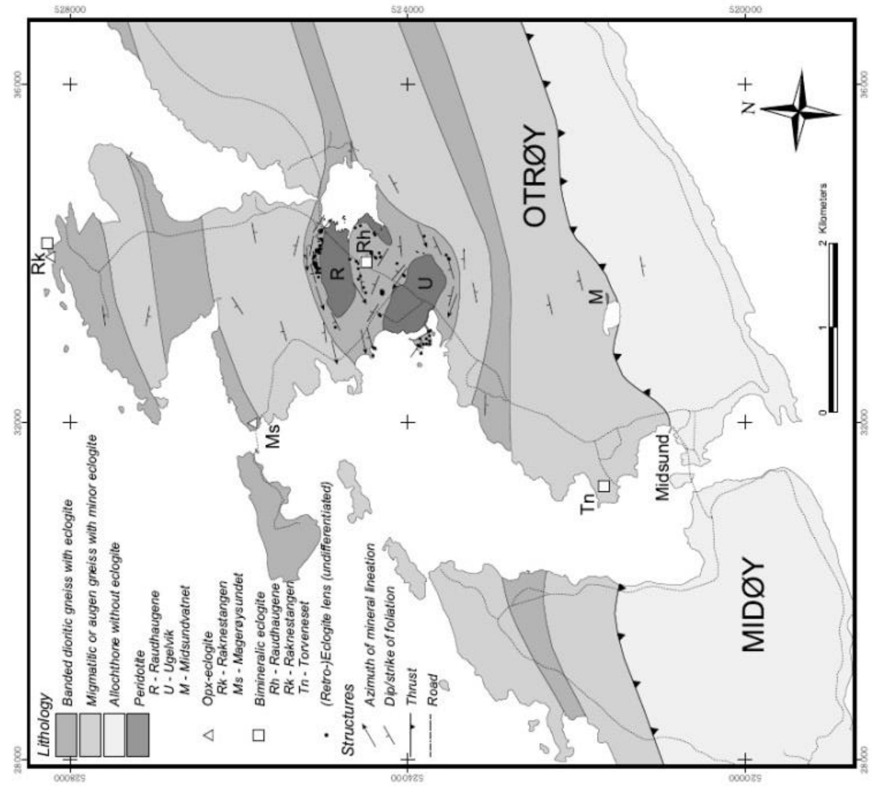

Figure 3.3-2: Simplified geological map of the western part of Otrøya, displaying three garnet peridotites and eclogite within Proterozoic basement gneiss in the north, separated from a southern allochtonous sequence lacking evidence of HP metamorphism. After Spengler (2006, and references therein).

4 The peridotites of Otrøya

Three mantle fragments, Ugelvik (U), Raudhaugene (R) and Midsundvannet (M), all garnet peridotites, occur in the western part of Otrøya (Figure 3.3-2). The bodies are of the Mg-Cr type garnet peridotite, containing evidence for the early stability of M1 (Archean) megacrystic mineral assemblages that include high P/T enstatites and majoritic garnets (presently exsolved into M2 (Proterozoic) and M3 (Scandian) assemblages). They are also considered to be among the deepest known rocks exposed on the Earth's surface, with recent estimated origin depths of at least 250-300 km depth (Zhang et al., 2011).

In this study the two largest bodies, Ugelvik and Raudhaugene, have been studied. Previous mapping (Spengler, 2006, and references therein) shows an elongated shape of the Ugelvik body with approximate dimensions of 400m width and 1000m length, with the western margin extending into the sea. The Raudhaugene body has a curved shape with a bent length of 1800m and with an increasing width from 150m in the east to 400m in the west. As shown in Figure 3.3-2, the thinnest, eastern, outcrop of the Raudhaugene peridotite body extend inland to the SW of the lake "Innafor Straumen". Based on this observation, Robinson et al. (2003), states that this almost provides a visible link in poorly exposed boggy ground with the eastern extension of the Ugelvik peridotite body. They proposed that the two peridotite bodies actually are linked at depth and that they together form a tight synformal structure with a westerly plunge.

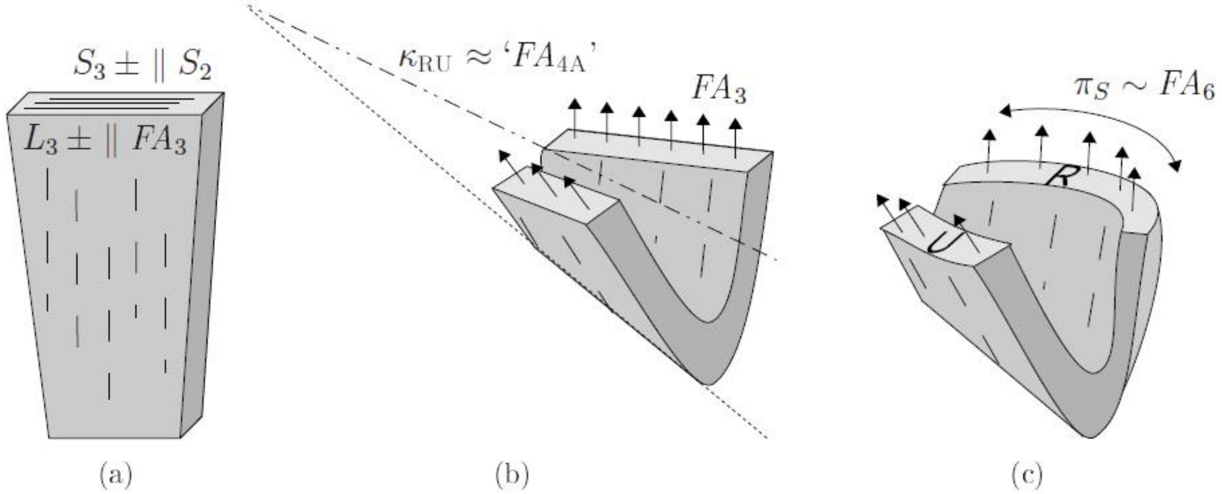

Figure 4-1: A schematic summary diagram showing three major folding phases; a, b and c, recorded in the Raudhaugene (R) and Ugelvik (U) peridotite bodies. (a) Intensive and penetrative deformation caused isoclinal folding of S_2 with FA_3 oriented sub-parallel to $L_{3.}$ (b) Km-scale non-cylindrical folding of peridotite formed an angle of 60 65° between the M_3 structues exposed at Raudhaugene and Ugelvik. (c) Late cylindrical folding around a steep FA_6 formed structural subdomains. After Spengler (2006).

4.1 Structural geology of the Ugelvik and Raudhaugene peridotites

The proposed link between the Ugelvik and Raudhaugene bodies is also supported by Spengler (2006). His interpretation shows that the peridotite bodies have experienced three major folding phases, as shown in Figure 4-1. The first, a, is an intensive and penetrative deformation causing isoclinal folding, S_2, presently shown as compositional layering. In this phase the fold axis, FA_3, is sub-parallel to the lineation, L_3. The next phase, b, is a km-scale non-cylindrical folding of the peridotite, forming an angle of 60-65° between the M_3, recrystallization assemblages of partly megacrystic M_2 assemblages exposed at Raudhaugene and Ugelvik. The latest phase, c, is a late cylindrical folding around a steep fold axis, FA_6, forming structural subdomains within the two bodies.

Spengler (2006) supports the structural indications of a link between the Raudhaugene and Ugelvik body by petrographical data. He points out that there is a common occurrence of red garnet clinopyroxenite at the northern edge of the central part of the Raudhaugene body and at the southern edge of the western part of the Ugelvik body. Spengler (2006) also proposed another possible structural interpretation of the peridotite bodies. They could represent two boudins, but, in this case, the correlation between M_3 structures and the outcrop shape is only co-incidental.

The peridotites are embedded in gneiss together with eclogite and retro-eclogite bodies, which occur more frequently in proximity to these peridotite bodies compared to other parts of western Otrøya (Figure 4.2-1). Spengler (2006) divides the gneiss into proximal gneiss, within 500m to the bodies, and distal gneiss further out. His structural interpretation of the area shows that the steeply plunging lineations, M_5, in the proximal gneiss represent statically recrystallized relicts of early eclogite-facies assemblages that became re-orientated to shallow plunging lineations, M_6, in the distal gneisses. This late amphibolite-facies deformation of early steep structures in the gneiss is the same phase that formed minor sub-domains in the peridotites by re-folding of previous structures, especially at the limbs of the Raudhaugene body.

4.2 Petrology of the Ugelvik and Raudhaugene peridotite bodies

The Ugelvik and Raudhaugene peridotite bodies contain, as mentioned before, the Mg-Cr type of garnet peridotite. They also contain spinel peridotite, garnetite and garnet pyroxenite layers in bands of varying composition, interpreted by Spengler (2006) to be S_2 layering. While orogenic peridotite typically shows a compositional layering with steep chemical gradients, dominated by lherzolitic compositions (Bodiner & Godard, 2003 as cited in Spengler 2006), the orogenic peridotites from Otrøya show a layering dominated by garnet bearing harzburgitic and dunitic compositions (Drury et al., 2001). Figure 4.2-3 and Figure 4.2-4 (Spengler, 2006) shows the composition of the exposed parts of both the Ugelvik and Raudhaugene bodies, and Figure 4.2-2 shows the mineral compositions for discussed peridotites and pyroxenites.

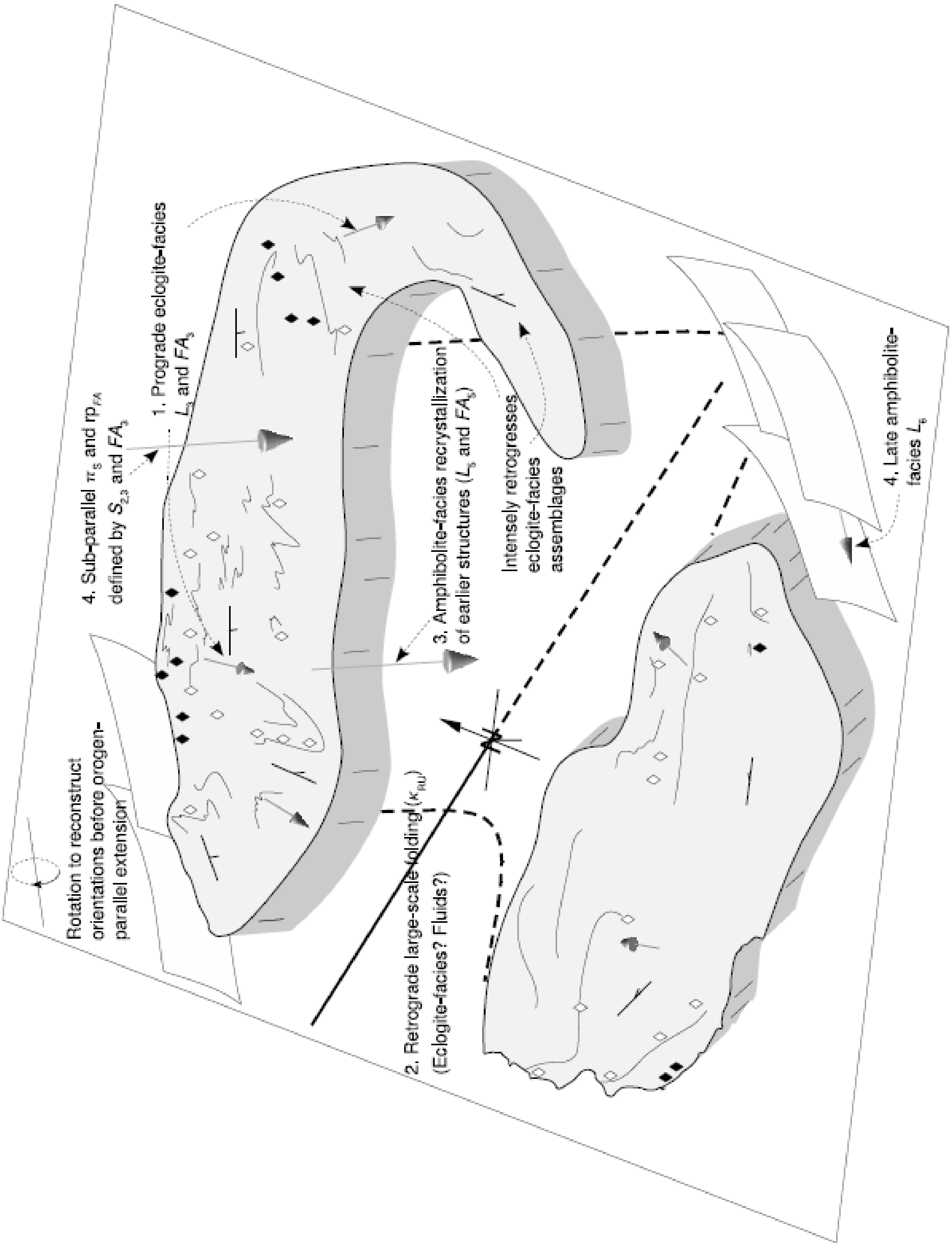

Figure 4.2-1: Cartoon of the Otrøya peridotites in surrounding gneiss that summarises the structural information to four deformation and recrystallization stages. Stage 1, 2 and 4 would be accountable for the a, b and c interpreted folding phases of the Raudhaugene and Ugelvik peridotite bodies (Spengler 2006). Filled ◊ - red grt-pyroxenute, ◊ - purple grt-pyroxenite. After Spengler (2006).

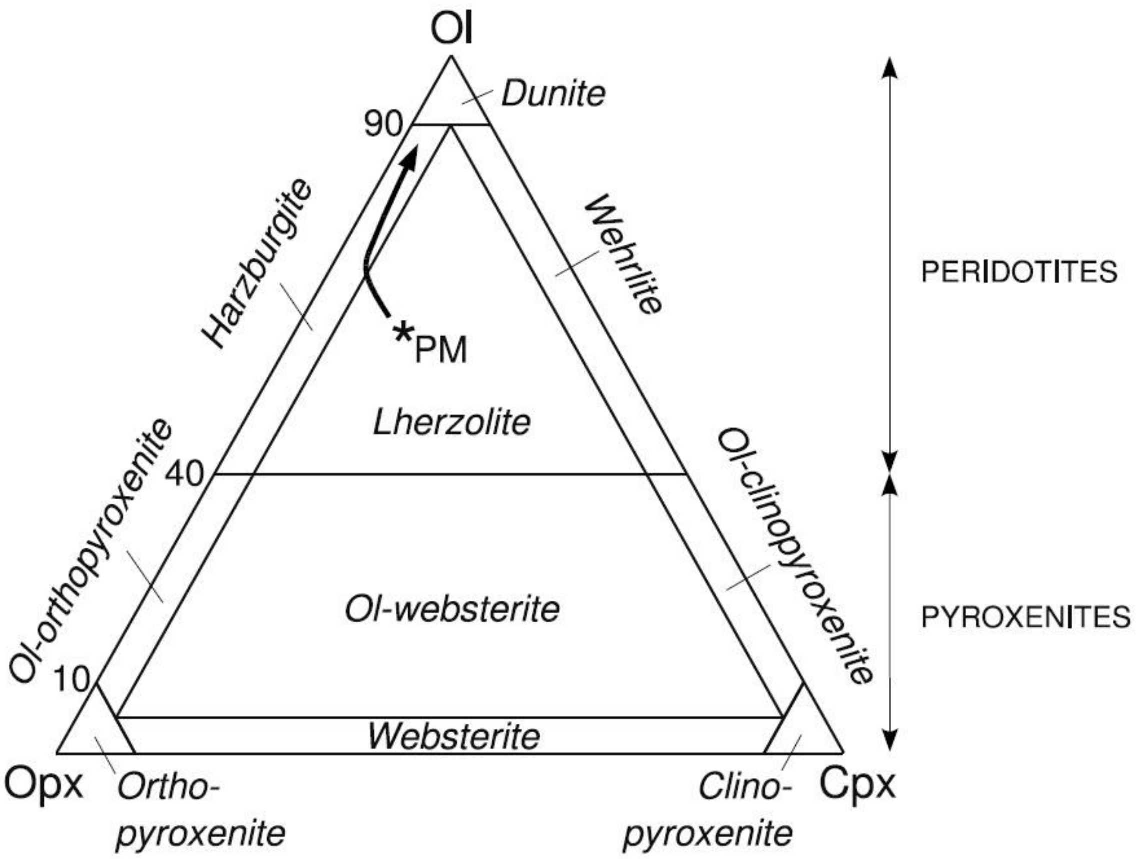

Figure 4.2-2: Classification of ultramafic rocks based on mineral modes in the ternary system Ol-Opx-Cpx. The thick arrow indicates a compositional change of residue melt with increasing melt extraction starting from primitive mantle (PM). After Spengler (2006).

Figure 3.2-3 (Brueckner et al., 2010) shows the different mineral assemblages associated with the three tectonometamorphic events of the Mg-Cr type peridotite bodies presently exposed in the north-western WGR. These minerals include olivine, garnet, Cr-spinel, orthopyroxene, clinopyroxene, amphibole, chlorite, talc and serpentine. The peridotite bodies at Otrøya have a porphyroclastic texture with porphyroclasts from the M2 mineral assemblage, and a matrix consisting of recrystallized M3 mineral assemblages. If reworked during amphibolite- and greenschist-facies conditions, the eclogite-facies assemblages were replaced including the phases amphibole, chlorite, magnetite and serpentinite (Spengler, 2006). Studies done by Brueckner et al. (2010) and studies therein, show estimates of 2% amphibolite and 39% serpentinite in a lherzolite sample from the Ugelvik body. Estimates from the Raudhaugene body shows a lherzolite sample with 35% serpentinite, and a shared pyroxenite sample with 15% serpentinite. Spengler (2006) gave an estimate for the serpentinization of the peridotite bodies to be 20-50%. A much higher estimate of serpentinization is given by Oud (2010) with estimates of 60-100% serpentinization within the peridotite, and 20-60% serpentinization within the pyroxenite lenses. Oud (2010) also identified the original rock, prior to serpentinization, to mainly consist of the magnesium-rich fosterite (Mg_2SiO_4), and the magnesium-rich enstatite ($Mg_2Si_2O_6$).

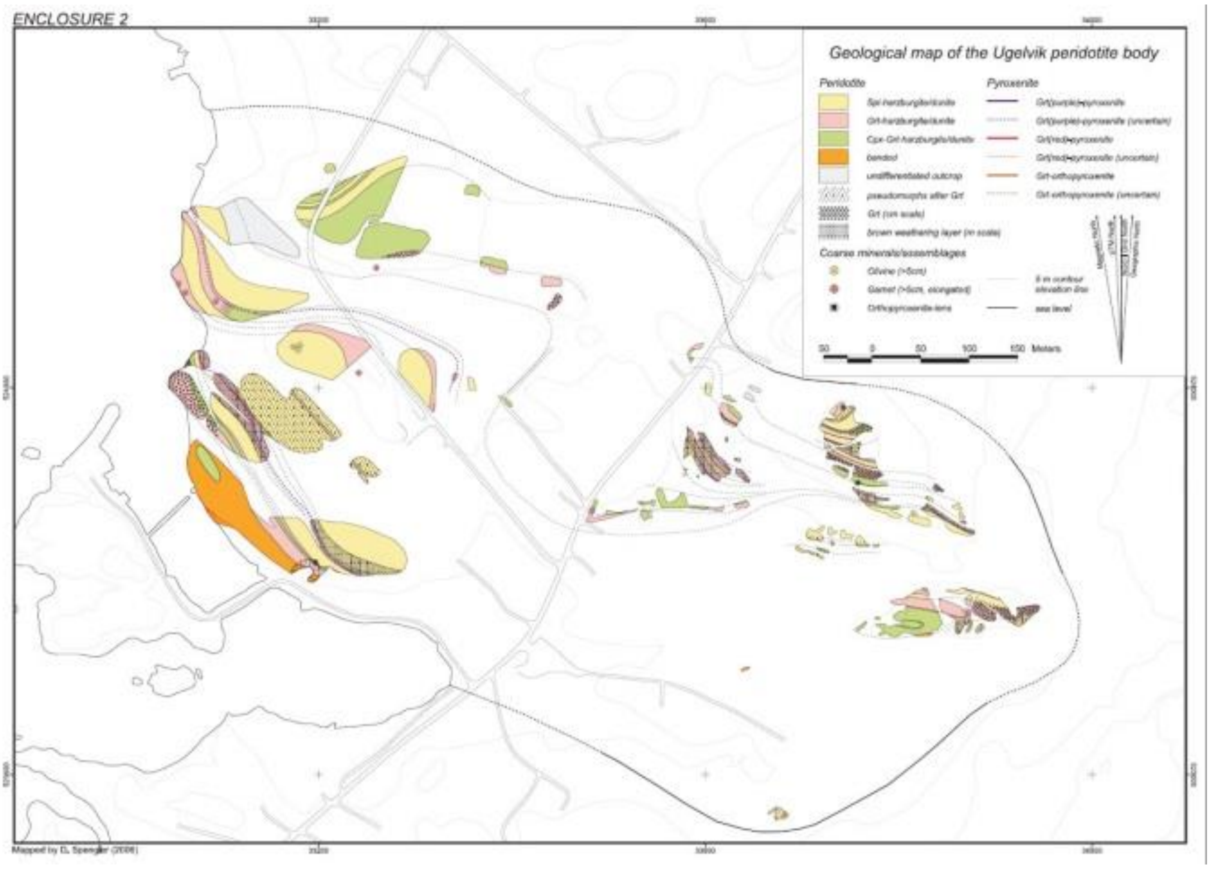

Figure 4.2-3: Geological map of the Ugelvik body. After Spengler (2006). See Figure 11.1-5 for enlarged legends.

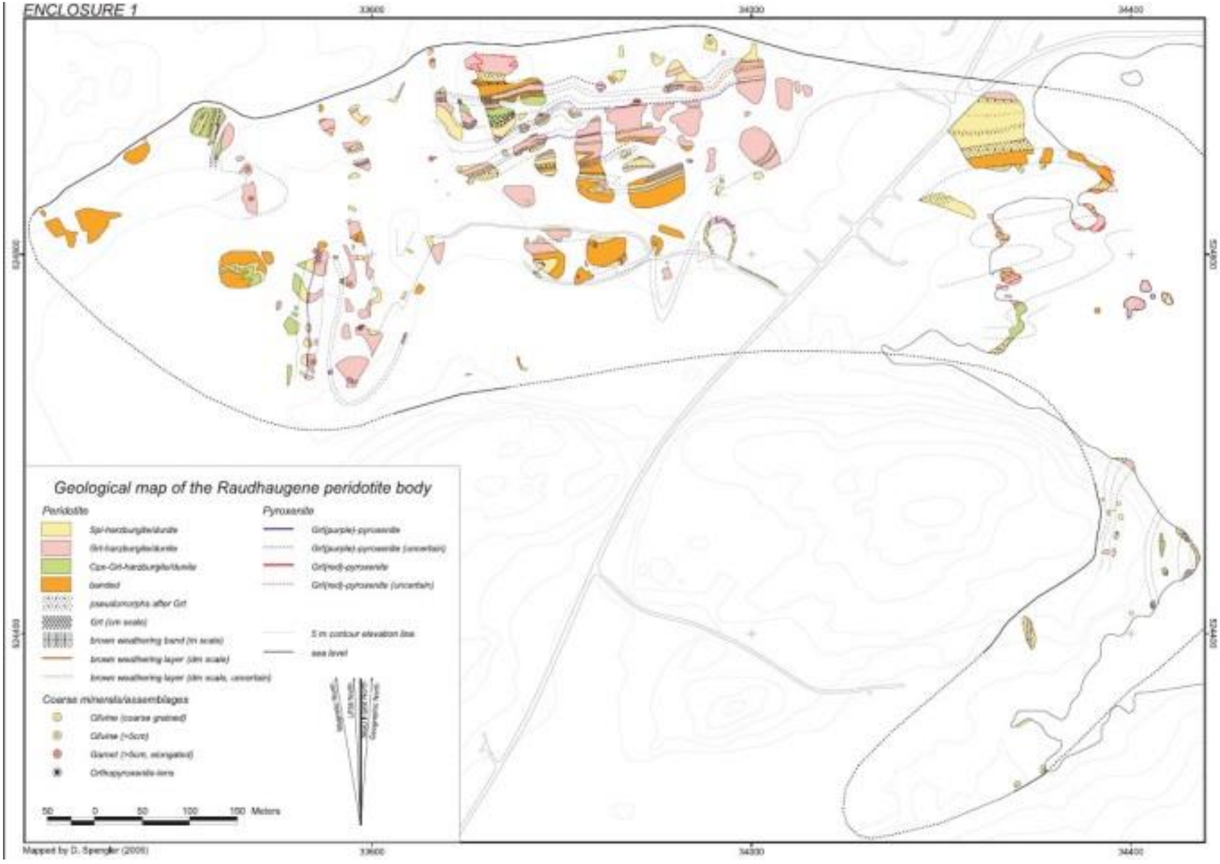

Figure 4.2-4: Geological map of the Raudhaugene body. After Spengler (2006). See Figure 11.1-4 for enlarged legends.

4.2.1 The Ugelvik body

The layers of the Ugelvik peridotite body consists of garnet-harzburgite and garnet-dunite (~65%), spinel-harzburgite and spinel-dunite (~33%) and small amounts of garnet-pyroxenite and garnet-websterite (<2%) (Drury et al., 2001; Carswell, 1968). The garnet-bearing layers contain mostly 5-10% modal garnet, but there is an increase locally up to 20% of modal garnet. Some layers of garnet-harzburgite and garnet-dunite contain isolated lenses of garnet-websterite with diameter of ≤45cm (Carswell, 1973) and garnetite with diameter of ≤25cm in diameter (Van Roermund & Drury, 1998).

4.2.2 The Raudhaugene body

The layers of the Raudhaugene body also consist of garnet-harzburgite and garnet-dunite, spinel-harzburgite and spinel-dunite as well as garnet-pyroxenite and garnet-harzburgite (Van Roermund, 2008). According to Figure 4.2-3 and Figure 4.2-4 (Spengler, 2006), it seems like the Raudhaugene body is compositionally equivalent to the Ugelvik body, regarding quantity of each layer. This is also consistent with the interpretation of the bodies being linked at depth.

4.3 Serpentinization of the Otrøya peridotites

Oud (2010) determined the mesh and fracture fill of the Otrøya peridotite bodies to be due to several generations of mineral formation, (mainly) consisting of the three main serpentine polymorphs, lizardite, chrysotile and antigorite, in various growth forms. Two generations of serpentine mesh formation were identified (M1 & M2); M1 to be of lizardite, and M2 to be of chrysotile displayed as fibrous veins and as recrystallized M1 lizardite. Oud (2010) also identified at least five generations of fracture filling growth (F1-F5). She identified F1 as chrysotile with a banded and kinked appearance in fractures, F2 as well-crystallized serpentines consisting of ribbon antigorite in fractures and of lizardite both with triangular shape in fractures and as "star-shaped" overgrowths in fibrous veins, F3 as micro-granular lizardite in fractures and as micro-granular overgrowth, and F4 as chrysotile, both in fibrous and banded/kinked growth forms, in cross-fractures. The last fracture filling growth, F5, was recognized by Oud (2010) to be of calcite in fractures. Examples of these mesh and fracture filling growth forms are displayed in Figure 4.3-1.

In addition, Oud (2010) established that pyroxene fractures also displayed growth of at least three generations of serpentine fracture filling; one as an outer rim of banded/kinked chrysotile, and one (or two) generations of lizardite. She established as well the presence of very fine-grained iron-oxides occurring as thin strings of dark red/brown (in plane polarized light (PPL)) to opaque minerals alongside mesh rims of serpentine. She did not identify whether these iron oxides were of magnetite (Fe_3O_4), hematite (Fe_2O_3) or Fe-Ni alloy.

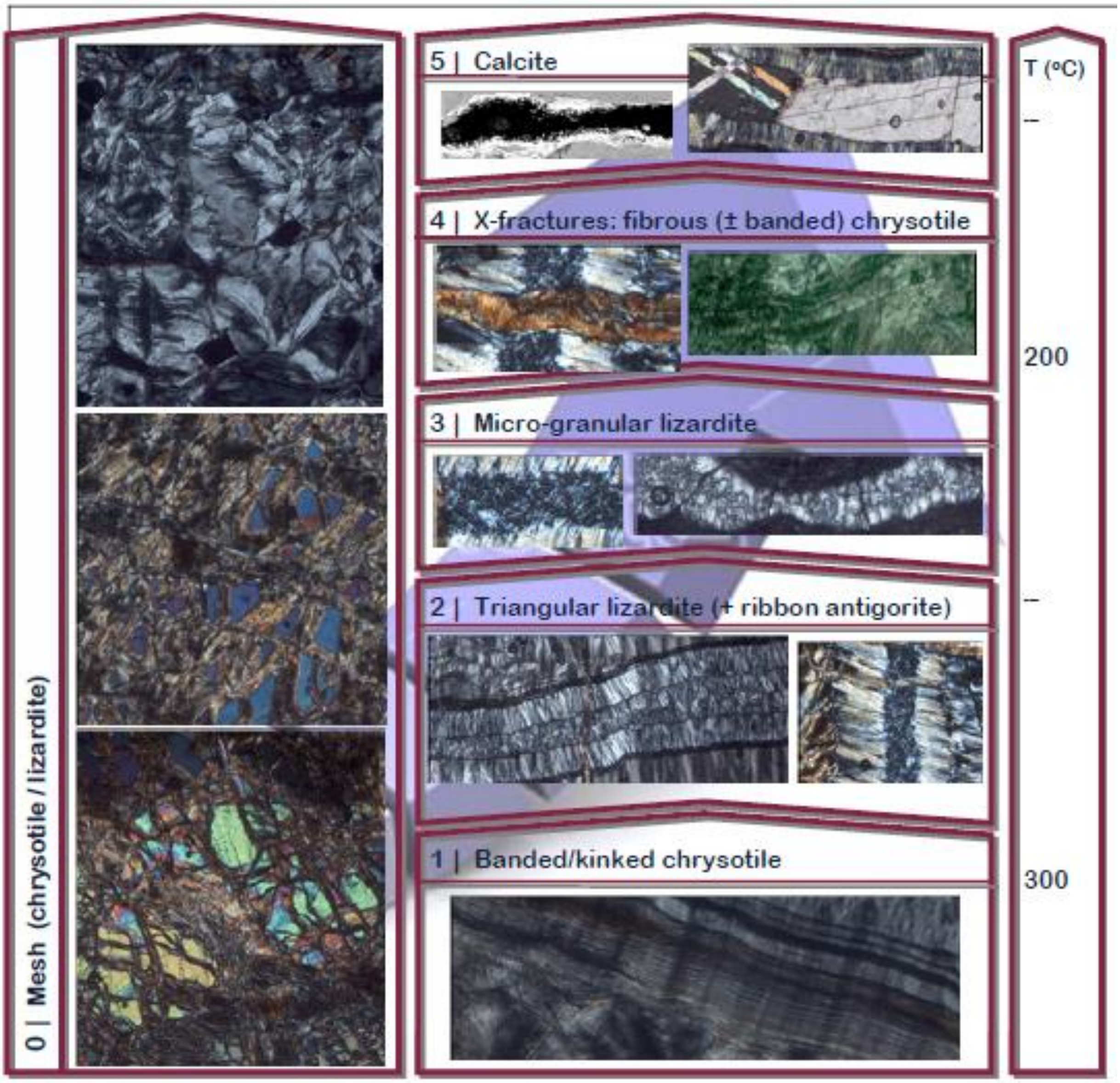

Figure 4.3-1: Scheme showing Oud's (2010) interpretation of several stages of mesh, 0 (in text referred to as M1 and M2), and fracture filling growth, 1-5, (in text referred to as F1-F5) in the Otrøya peridotites. Decreasing temperature conditions are shown in the arrow to the left. After Oud (2010).

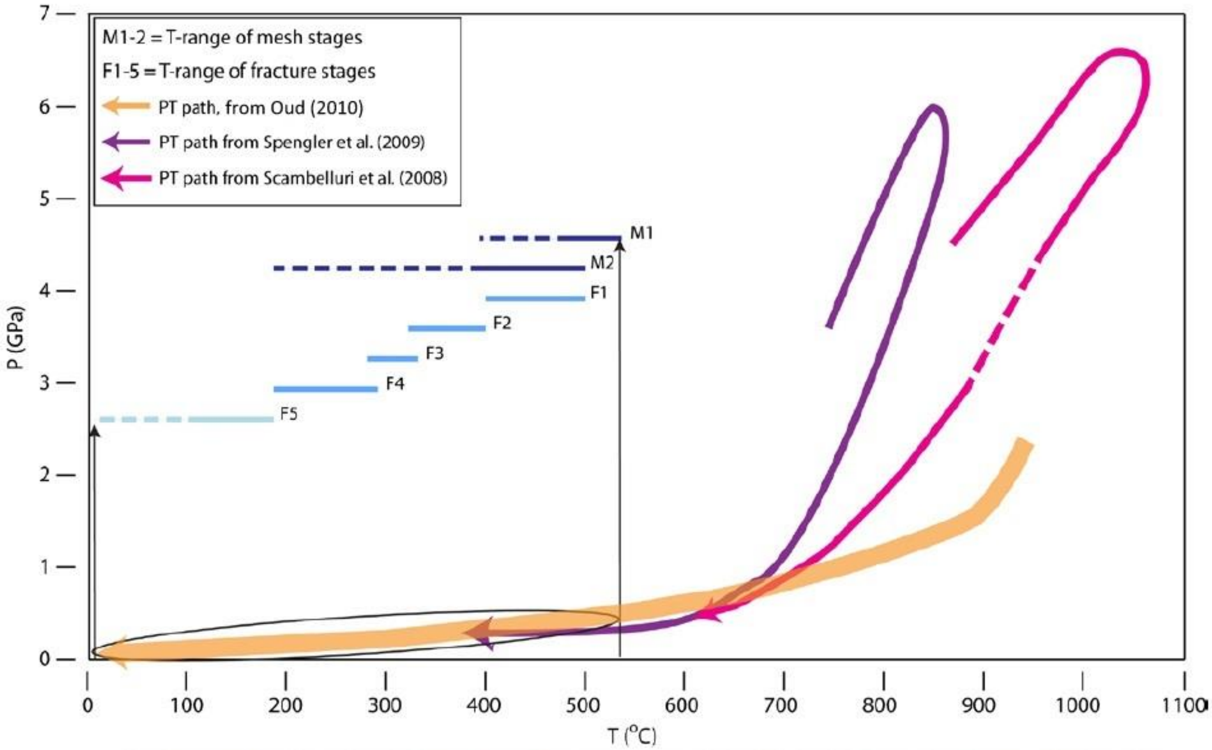

Figure 4.3-2: Proposed PT path for retrograde metamorphism of the Otrøya peridotite bodies, derived from the mineral assemblages determined in this study. PT paths for Otrøya and neighbouring Fjørtoft peridotites from Spengler et al. (2009), Scambelluri et al. (2008) and Oud (2010) are shown. The temperature range for the different stages of mesh and fracture formation are depicted by M1 to F5, seeFigure 4.3-1). After Oud (2010).

Oud (2010) based the fracture filling observations, and their mode of fracturing, to quantify the pressure and temperature conditions of serpentinization and fracturing in the latest stages of the tectonic history of the Otrøya peridotites (post-Scandian exhumation). She determined an early hydration occurring at about 530°C and 0.4-0.5 GPa through reaction of olivine (±orthopyroxene), talc (±chlorite), and H_2O to lizardite in the mesh (M1). The chrysotile growth, both in mesh (M2) and as the first fracture filling event (F1), is proposed by Oud (2010) to be forming between 400-500°C. She proposed the total phase of serpentinization to be occurring between 530-180°C and with pressures between 0.5-0.1 GPa. She also proposed the calcite filling of fractures to occur below 180°C and below 0.3 GPa.

Oud (2010) recognized the serpentinization in the mesh to be forming during most of the latest part of retrograde metamorphism of the peridotite, an interpretation based on the very high degree of serpentinization. She also recognized the later forms of serpentine to mainly be forming due to hydration of olivine and orthopyroxene. Oud (2010) also described a red-brown colour around serpentine fractures/vain and the former surface of the rock. She recognized this as weathering of serpentinite, possibly explained by oxidation of magnetite or hematite, due to presence of water and/or air.

5 Geomagnetic Theory

5.1 Earth magnetism

The Earth's magnetic field, *H,* can, for simplicity, be regarded as the dipole field of an uniformly magnetized sphere, but the geomagnetic field is in fact a direct signal from Earth's outer core (Merill et al., 1996, as cited in McEnroe et al., 2009). The Earth has a north- and a south geomagnetic pole with an axis of magnetisation inclined 11.5° to the Earth's rotational axis. The geomagnetic poles are the location of vertical field lines, better known as magnetic flux lines (Figure 5.1-2). The geomagnetic poles change its position with time. E.g. according to the webpages for the World Data Centre for Geomagnetism (WDCG, n.d.) the north magnetic pole is currently located at 80.2N, 72.2W (2014) in the Canadian Arctic Archipelago, and is moving north-westwards with a speed of around 50km/yr (Reynolds, 2011). The geomagnetic field is induced by electric currents within the liquid outer core of the Earth due to slow convective movements within it (Figure 5.1-1). The geomagnetic field can be described in terms of a total force vector, *F,* declination, *D,* and inclination, *I*. The magnetic field intensity of the Earth varies with a decrease from around 60,000nT at the poles to about 30,000nT at the geomagnetic equator (McEnroe et al., 2009b).

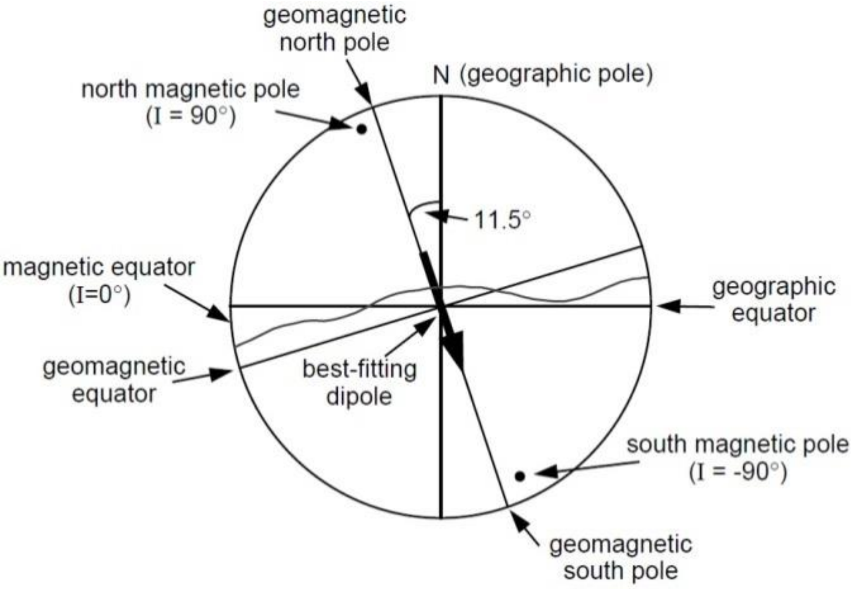

Figure 5.1-2: Inclined geocentric model. The best-fitting inclined geocentric dipole is shown in meridional cross section through the Earth in the plane of the geocentric dipole; distinctions between magnetic poles and geomagnetic poles are illustrated; a schematic comparison of geomagnetic equator is also shown. After Butler (2004).

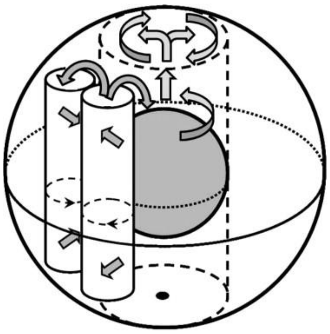

Figure 5.1-1: Anticipated structure of flow in the core. The inner core shows movement within a tangent-cylinder, shown with broken lines. Convection columns within the outer core are likely more numerous and much thinner than shown here. After Christensen (2011).

5.1.1 The International Geomagnetic Reference Field

In addition to the contribution from the geomagnetic dipole field there are contributions from eddy currents represented by around 8-12 small fictitious dipoles radically located close to the liquid core. These dipoles are linked to large-scale features with dimensions of the order of several thousand kilometres and with amplitudes up to 20,000 nT, and have been demonstrated by using the method of spherical harmonic analysis (Reynolds, 2011). The same method is used to model the spatial distribution and intensity of the total magnetic field for the whole globe. This model is called the International Geomagnetic Reference Field, and is re-calculated every five years. It needs to be recalculated regularly due to slow but progressive change in the field intensity and to correct for secular variation (Reynolds, 2011). The IGRF is of now at its eleventh generation with last revision in 2010. The computation of the IGRF makes it possible to obtain a theoretical field strength value of the Earth's magnetic field at any location on the Earth, which can be used in the data reduction process when producing a magnetic anomaly map.

5.1.2 Time variations of the Earth's magnetic field

When producing a model of the magnetic field of the Earth the variations of the Earth's magnetic field with time must be taken into account. Firstly, as noted above, corrections due to secular variations must be taken into account. According to the websites of Natural Resources Canada (2013) – most of the secular variation can be described in terms of three processes: a decrease in the strength of the dipole part of the magnetic field; a westward drift in the non-dipole part of the magnetic field; and changes in the non-drifting part of the non-dipole field. These variables are also accountable when conducting surveys covering large geographical areas, which take many months to complete, or if the surveys will be used to compare with historical data. However, there are other changes in the Earth's magnetic field that are more abrupt and sporadically. These must be corrected for when conducting a "typical" survey.

On a large scale, abrupt changes in the trend of secular variation, called geomagnetic jerks, have been observed. Although their physical origin is not understood they are thought to be due to change in the fluid flow at the surface of the Earth's core (Bloxham et al., 2002, as cited in Reynolds, 2011). There are also changes in the Earth's field on a daily period, called diurnal variations. These are caused by changes in the strength and direction of currents in the ionosphere. In addition, phenomenon of magnetically disturbance called magnetic storms can impose a great amount of noise to a survey. A magnetic storm is caused by solar activity resulting in charged particles from the sun entering the ionosphere. It is characterised by a rapid onset of fluctuations of the order of hundreds of nanoteslas (nT) followed by slower, erratic fluctuations with decreasing amplitude, and can last for several hours or even days. Due to their extreme fluctuations they are hard or even impossible to correct for.

5.2 Rock magnetism

The source of the magnetism of the Earth, a rock, or a magnet, is due to magnetic atoms. The atoms of about half of the chemical elements on Earth are magnetic, but for most of them their directions of magnetization is randomly orientated (Musset & Khan, 2000). If a magnetic substance is placed in a magnetic field, H, such as the Earth's, the magnetic atoms will align. In modern terminology, this behaviour would be referred to as magnetisation, M (Dunlop & Özdemir, 1997). Rocks can carry two types of magnetisation: induced magnetisation, M_{ind}, and remanent magnetisation, M_r

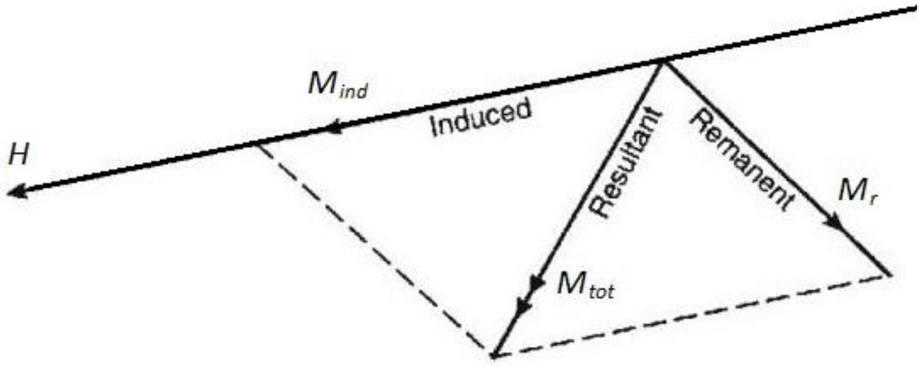

Figure 5.2-1: Vectorial summation of induced and remanent intensities of magnetisation. Modified after Reynolds (2011).

5.2.1 Induced magnetisation and Susceptibility

Induced magnetization is the magnetisation, M_{ind}, which is induced by an applied field, H, into a magnetic material, and is a vector quantity. Magnetic susceptibility, χ_m, is the physical quantity describing how magnetisable a substance can become in the presence of a field, and is defined as the ratio between magnetisation, M_{ind}, of the material in the magnetic field and the field intensity, H. The relationship between induced magnetisation, susceptibility and applied field is displayed in Formula 1 (Marcon & Ostanina, 2012):

Formula 1: $$M_{ind} = \chi_m H$$

When there is no applied field there is no measurable induced magnetisation, while there can be measurable remanent magnetisation.

5.2.2 Paleomagnetism & remanent magnetism

The magnetic atoms within a material on Earth, will, as described above, align with the Earth's field, and for most materials this alignment, or induced magnetisation, will disappear as soon as the field is removed. Paleomagnetism, on the other hand, is possible because some materials exhibit remanent magnetisation, which is the ability to retain magnetisation in the absence of a field or in the presence of a different magnetic field (Musset & Khan, 2000).

Paleomagnetism is the study of how the Earth’s field has changed through geological time. When measuring the magnetisation of a rock the resultant intensity is a vector sum made up of both the induced magnetization and the remanent magnetization (Formula 2) (Figure 5.2-1).

Formula 2: $$M_{tot} = M_{ind} + M_r = \chi_m H + M_r$$

If the remanent vector is large, the resultant vector can to a large degree differ from the geomagnetic field. The discovery of magnetisation in rocks both parallel and reversely to that of the present geomagnetic field lead to the association of normal and reverse polarities of the geomagnetic field (Dunlop & Özdemir, 1997 and references therein). What exactly happens during a polarity reversal is an ongoing field of research (e.g. Leonhardt and Fabian 2007; Aubert et al. 2008, as cited in McEnroe 2009b). However, the discovery and global acceptance of global magnetic reversals, led to the modern theory of plate tectonics, which now governs all aspects of the study of Earth history (e.g., McEnroe et al., 2009b).

The Königsberg ratio, or the Q value, is the ratio of the remanent magnetisation against the induced magnetisation (Formula 3). This ratio can indicate whether the intensity of the remanent magnetisation can overwhelm the induced magnetisation for a given locality.

Formula 3: $$Q = M_r / M_{ind}$$

As noted above, the vector directions of the remanent magnetisation and the susceptibility can differ. The resultant vector may therefore differ from the Earth field vector.

According to McEnroe et al. (2004a) would an area displaying Q values below 0.5 primarily be due to the magnetic response from the induced magnetisation of the rocks, whereas in areas displaying Q values above 1, the remanent magnetisation contributes to the anomaly. A Q value above 5, with consistent directions of NRM, would result in a magnetic response of the rock dominated by the NRM, far exceeding the induced response. Examples of vector variation of remanent and induced magnetisation, their resultant total magnetisation, and Q value can be viewed in Figure 5.2-2.

The Königsberg ratio can vary within a single rock type. However, Nagata (1961, as cited in Reynolds, 2011) defined four broad generalisations of rock types based on the Q-value, as follows: Q~1 for slowly crystallised igneous and thermally metamorphosed rocks in continental areas; Q~10 for volcanic rocks; Q~30-50 for many rapidly quenched basaltic rocks; Q<1 in sedimentary and metamorphic rocks, except when iron ore is involved.

Nagata’s generalisations of rock types based on Q-values indicate that rocks with a history of cooling from high to low temperatures inhabit large remanence. Remanent magnetisation is in fact most commonly developed when the rock is formed, due to the rock cooling from high temperatures to low temperatures while being in a magnetic field. This is called thermoremanent magnetization (TRM).

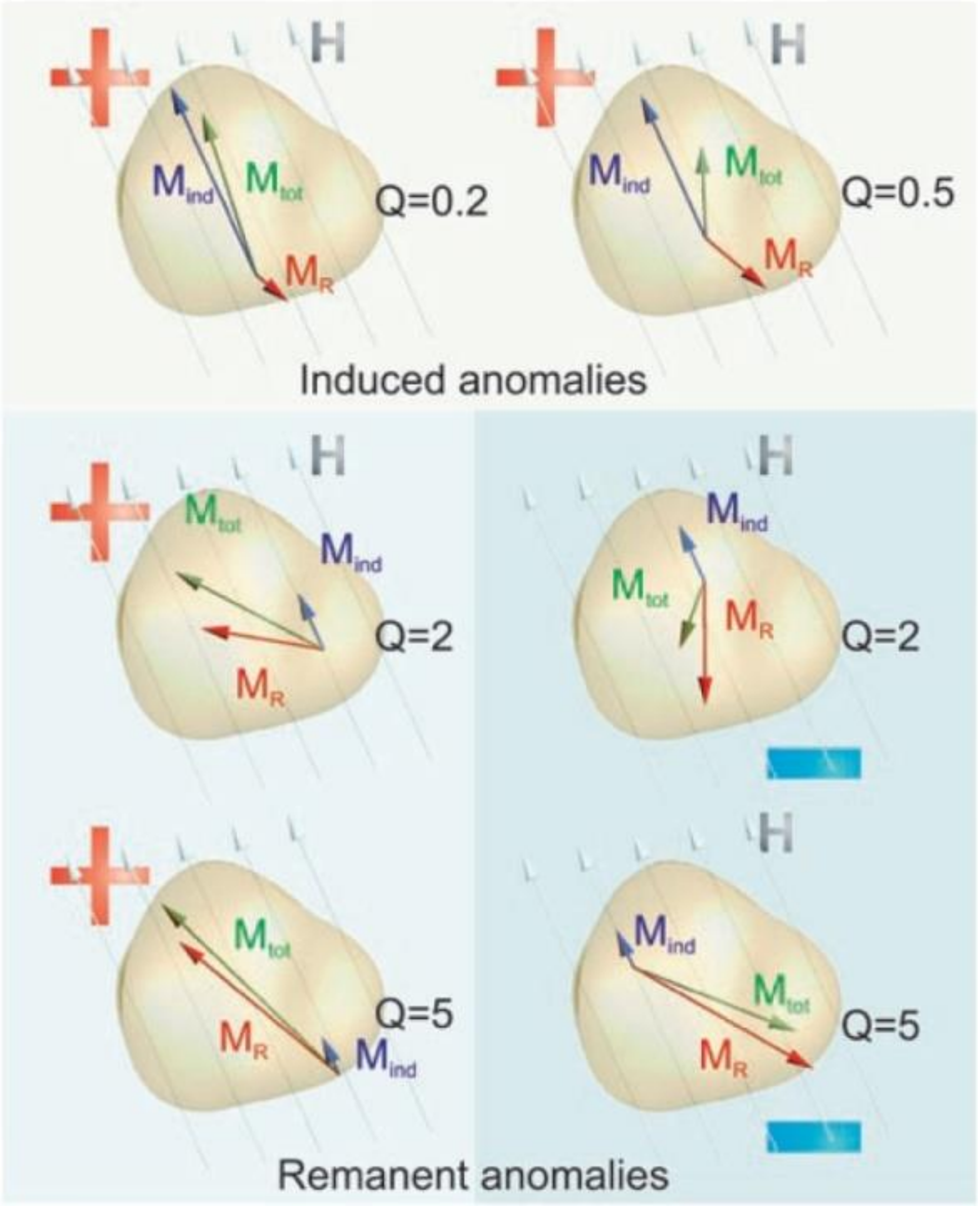

Figure 5.2-2: The total magnetization, M_{tot}, of a rock is the sum of the induced magnetisation, M_{ind}, which is a response to the external field, H, and the remanent magnetisation, Mr, carried by magnetic minerals. In general, the magnetic anomaly related to a rock is positive (+) or negative (-) according to the sign of the projection of M_{tot} onto H. Induced anomalies, where $Q = Mr/Mind << 1$, are always positive, while remanent anomalies, where $Q > 1$, can have either sign, depending on their remanence direction. After McEnroe (2009).

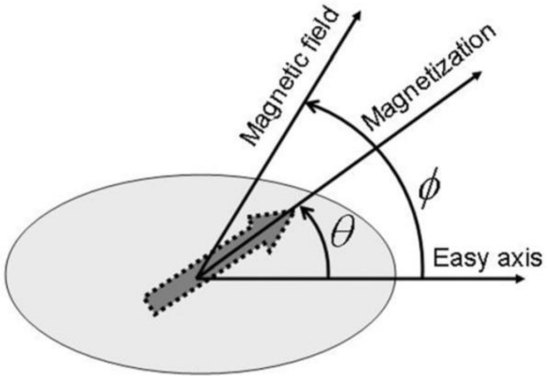

Figure 5.2-3: Schematic representation of a uniaxial single domain grain. The large arrow represents the magnetisation. After Carrey et al. (2011).

TRM is studied in paleomagnetism due to the TRM always being parallel to the field in which it was acquired and its intensity is proportional to the strength of the field. The "blocking" of the TRM required during cooling is at a single blocking temperature, T_B, determined by the size and the shape of a particular magnetic grain (Dunlop & Özdemir, 1997). In materials with remanent magnetisation, the magnetic moments of individual atoms within a grain will produce a spontaneous magnetisation, M_s. Individual magnetic moments will be constricted in regions with different directions of M_s called domains.

5.2.3 Magnetic domains

Magnetic domains are either constricted by the size of the magnetic grain, or by domain walls. Domain walls, or domain boundaries, are positioned to maximize internal flux closure and eliminate "magnetic charges" on both internal boundaries and at the crystal surface (Dunlop & Özdemir, 1997, and references therein). The domain direction is dependent on various magnetic properties, and the dependence of magnetic properties on a preferred direction is called magnetic anisotropy (Moskowitz, n.d.). There are several types of magnetic anisotropy such as the structure and shape of the grain, or applied or residual stress of the grain. Magnetic anisotropy controls the coercivity and remanence of a magnetic particle.

As stated before, magnetic domains are constructed to minimize total energy. To explain the various parameters effecting domain state the expression of total magnetic energy density, E_t, can be viewed in Formula 4 (Tauxe et al., 2002):

Formula 4:

$$E_t = E_a + E_h + E_e + E_m + E_\sigma$$

E_a is the magnetocrystalline anisotropy energy density, which is minimized along the "easy axis" of magnetisation (Figure 5.2-3), orientated along one of a number of particular crystallographic directions. E_h is the energy arising from the torque on the magnetisation vectors applied by an external field (Tauxe et al., 2002). E_e is the exchange energy, and is minimised when the average local unit cell magnetisations are parallel to each other. E_m is the magnetostatic energy produced by the magnetic particle, and when E_m becomes too large the particles will seek a more demagnetized state, e.g. divides into magnetic domains. Lastly, E_σ, is the energy produced due to stress.

The domain sizes depend on material properties. For magnetite domains are 1-100's microns in size, but even in a weak field, as the Earth's field (e.g. 50,000nT), the domains would either be rotated or some domains will be enlarged at the expense of others (Dunlop & Özdemir, 1997).

5.2.3.1 Single domain

A magnetic grain too small to accommodate a domain wall is called a single domain grain. The magnetization of a single domain grain is aligned along one of a number of easy axes. Single domain grains change their magnetisation by rotation, they have a unique TRM blocking temperature, and they exhibit a strong magnetisation for their size (Dunlop & Özdemir, 1997).

5.2.3.2 Multi domain

Larger grains containing multiple domain walls are called multidomain grains. The domain walls of a multi domain grain are mobile, and in the presence of a field the magnetic domains would either be rotated or some would be enlarged at the expense of others. Due to the mobility of the domain walls the TRM of multidomain grains does not impose one unique TRM blocking temperature.

A rock in nature containing many magnetic grains could either have a strong or weak magnetisation. This depends on the collective direction of the magnetisation of the individual grains within the rock, and if they are single domain or multi domain magnetic grains. If their direction of magnetisation are randomly oriented, the rock as a whole display little remanence. When talking of magnetic domains, this applies to just a few materials with spontaneous magnetisation, M_s. Most common natural magnetic minerals are iron oxides, sulphides or hydroxides (Dunlop & Özdemir (1997), and this natural magnetic behaviour is called ferromagnetism.

5.3 Hysteresis

For a stress free spherical magnetic mineral in zero field (H=0), the local spontaneous magnetisation, M_s, and the magnetic domains within a crystal, are related to the crystal easy axes of magnetisation. Without an applied field, the magnetisation directions of a multi domain grain could cancel each other out, resulting in zero saturated magnetisation, M_S. When a field is applied, and increased, the domain walls can move. As H is increased, the various domains reorientate themselves parallel to the applied field. The domain reorganization changes the number and location of domains and partly occurs in discrete steps called *Barkhaugsen jumps*, which are permanent (Reynolds, 2011). When there is no further increase in magnetisation, the material is magnetically saturated, H_{sat}. When the field intensity is reduced after saturation, some of the magnetic domains will stay in this new orientation, and some will return to their former orientation. The domains that stay in the "new orientation" result in remanent magnetisation, M_r. To reduce the magnetisation back to zero, after saturation, a negative field, the coercive force, $-H_c$, has to be applied (Figure 5.3-1). The coercivity is an indication of the "hardness", or remanence, of the magnetisation of the material (Reynolds, 2011). Due to this, larger magnetic grains, containing multiple magnetic domains, are easier to magnetise than fine grained single domain grains, which are magnetically hard. This is reflected in the high susceptibility and low remanence of the multi domain grains and the high coercivity and low susceptibility of single domain grains. By applying, and increasing, a negative field, the material will reach the same magnetic saturation, but with a negative value. The various hysteresis parameters are dependent on grain size, domain state, stresses, and temperature – and the various types of magnetic domains will therefore result in different shapes of the hysteresis loop.

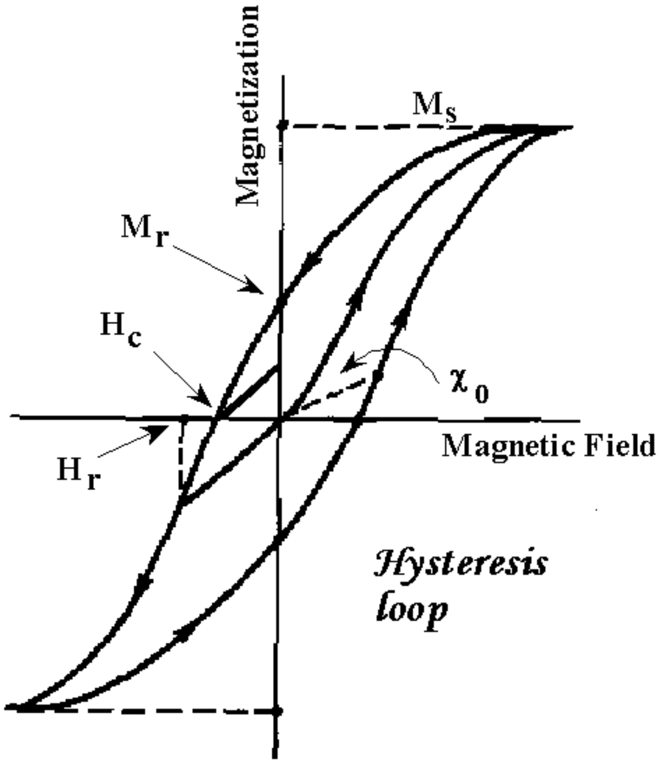

Figure 5.3-1: Hysteresis loop showing saturation magnetisation (Ms), saturation remanence (Mr), coercivity (Hc), coercivity of remanence (Hc) and initial susceptibility (X0) which is the magnetisation observed in low fields, on the order of the Earth's field. X-axis represents magnetic field strength applied, y-axis represent magnetisation of material. After Moskowitz (n.d.).

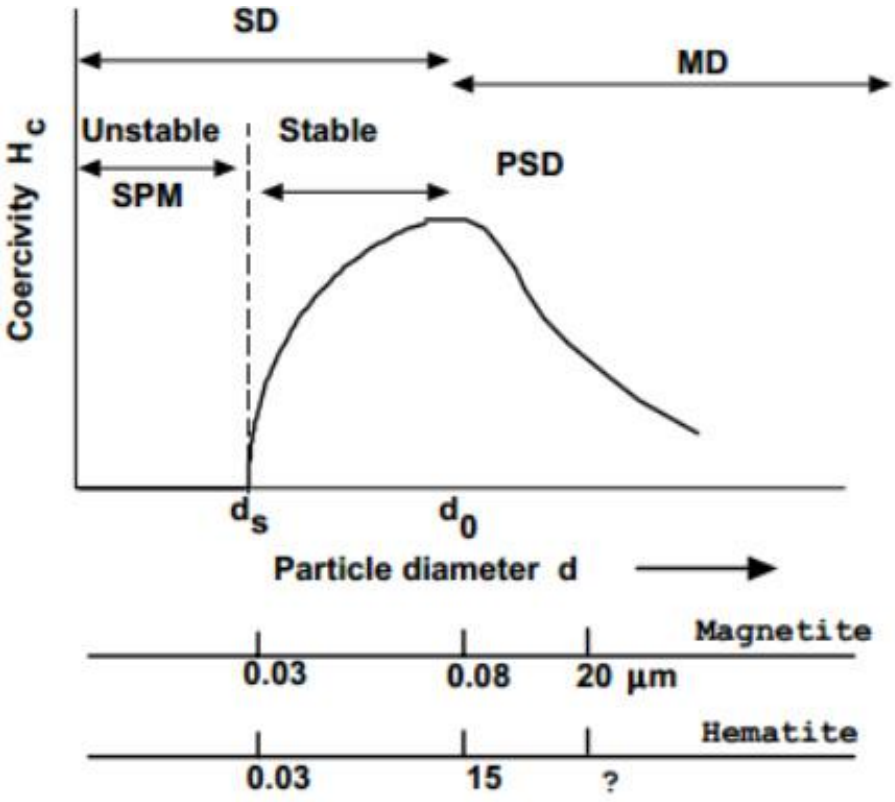

Figure 5.3-2: The different particle diameters associated with different types of magnetic domains in magnetite and hematite. Increasing coercivity, *H_c*, at y-axis, and increasing particle diameter, d, at x-axis of the diagram.

5.3.1 Size dependence of domain states

The existence of domains is hinted by the observation that some magnetic properties, in particular coercivity and remanence, vary greatly with grain size. On basis of this, the magnetic behaviour can be subdivided into; superparamagnetic (SPM), single domain (SD), pseudo-single domain (PSD), and multidomain (MD) behaviour (Moskowitz, n. d.). The different particle diameters associated with these magnetic domains within magnetite and hematite are shown in Figure 5.3-2.

The critical sizes for different magnetic domains depend on several factors including magnetic anisotropy. The reason for different grain sizes for the same domain states in magnetite and hematite is mainly due to parameters such as saturation magnetisation, temperature dependence, as well as composition (Moskowitz, n.d.).

The change between SD and MD magnetite can be observed at around 0.08µm. Previously, in section 5.2.3, SD and MD state have been explained, and their distinction of being either only of one domain or several is resolute. However, small MD grains exhibit a mixture of low coercivity (MD-like), and high remanence (SD-like) behaviour, called pseudosingle domain (PSD) behaviour. For magnetite this behaviour occurs in the size range between 1-15 µm (Tauxe et al., 2002), which covers the range in sizes that most commonly occur in natural samples (Moskowitz, n.d.).

SPM behaviour is, on the other hand, observed for decreasing SD sizes. It is defined by a critical point where remanence and coercivity goes to zero. For SPM grains, in an applied field, there will be a net statistical alignment of magnetic moments, but the net magnetic moment in zero field (at $T>0K$) will average to zero. Though this is the same behaviour as for paramagnetic behaviour it differs by the SPM domains not being of a single atom, but of about the same number of atoms as Fe spins in the SPM grain. This depends on the volume of the grain, but is by Moskowitz (n.d.) indicated to be of about 10^5 atoms. SPM grains will therefore indicate much higher susceptibility values than for paramagnetic materials. Earlier, blocking temperature, $T_{B,}$ has been explained as the temperature where a magnetic mineral acquire stable remanence. Due to the existence of SPM grains, a blocking volume, V_B, can also be defined. For spherical shaped magnetite at room-temperature, the change from SPM to SD behaviour is observed in the size increase from 22 to 33 nm (Moskowitz, n.d.).

5.3.2 Physical interpretation of hysteresis loops

Hysteresis measurements are methods for characterising magnetic behaviour of rocks in magnetic studies. Hysteresis is sensitive to grain size, domain state, mineralogy, and state of stress. For diamagnetic and paramagnetic materials, a hysteresis measurement will not display a loop, but a steep line, respectively with negative and positive slope (Figure 5.3-3). Due to the diamagnetic and paramagnetic behaviour, in technically available laboratory fields at room temperature, the materials will never reach a saturated magnetisation state. Their hysteresis measurements will display straight lines with slope value equal to the measured material’s susceptibility.

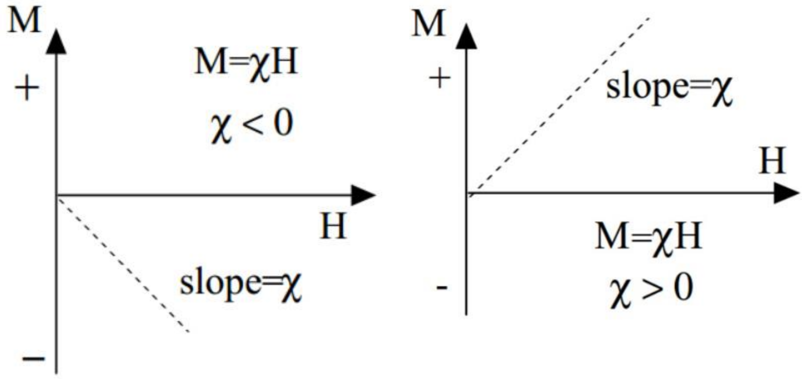

Figure 5.3-3: Hysteresis measurement showing increasing field, H, with (right) increasing negative susceptibility, χ , of a diamagnetic material, and (left) increasing positive susceptibbility of a paramagnetic material. After Moskowitz (n.d.).

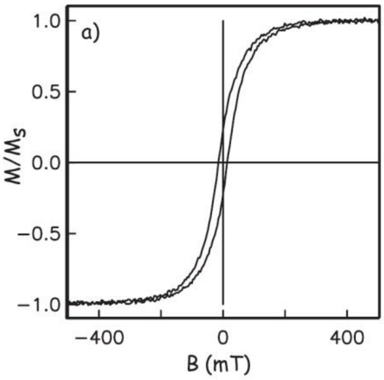

Figure 5.3-4: A typical "pseudosingle domain" hysteresis loop. Magnetisation (M/M_s) shown on y-axis, and field applied (B) shown on x-axis. After Tauxe et al. (2002).

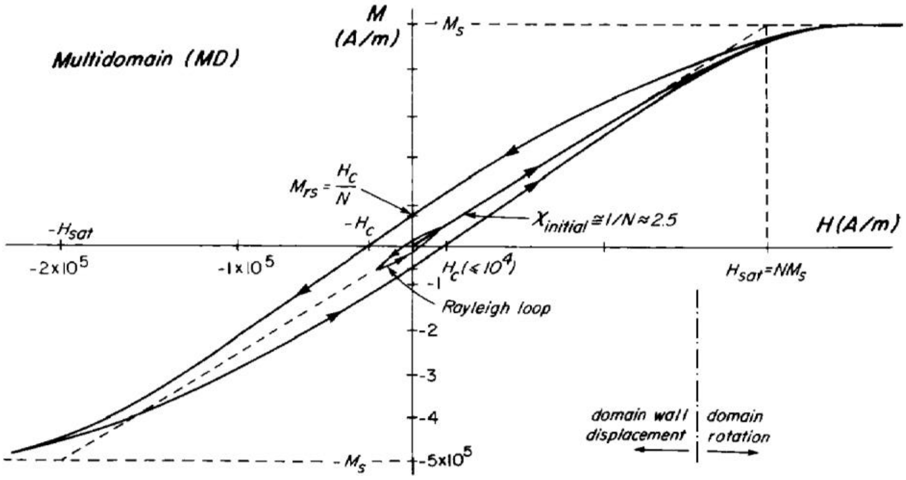

Figure 5.3-5: Idealized hysteresis loop for a large multidomain grain of magnetite. After Dunlop & Özdemir, 1997.

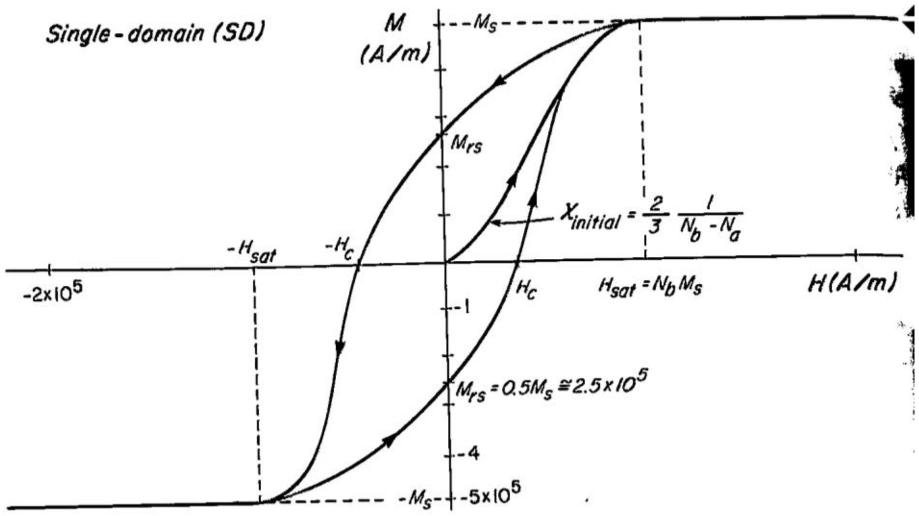

Figure 5.3-6: Idealized hysteresis loop for randomly orientated uniaxial single-domain grains. Numerical value for magnetite. After Dunlop & Özdemir, 1997.

For ferromagnetic and ferrimagnetic (explained in chapter 5.4) materials, the shape of a hysteresis loop is partly determined by the domain state of the magnetic material. E.g. SD materials display wider loops than MD materials due to the higher coercivity and remanence in SD materials. Idealised hysteresis loops for magnetite with large multidomain grains and randomly orientated uniaxial single-domain grains are shown in Figure 5.3-5 and Figure 5.3-6. A typical pseudosingle domain hysteresis loop is shown in Figure 5.3-4.

5.3.3 Day plot

The hysteresis loop parameters have proven very useful in distinguishing the domain states of SD, PSD and MD particles. A graph of the saturation remanence to saturation magnetisation, M_r/M_s, against the ratio of remanent coercive force to coercive force, H_{cr}/H_c, is one method for distinguishing these domain states, and, by implication, grain size, proposed by Day et al. (1977), and further developed by Dunlop (2002, and references therein). A theoretical Day plot curve for magnetite is shown in Figure 5.3-7. It shows theoretical model curves for SD + MD mixtures, with a boundary between PSD and MD regions defined by M_r/M_s=0.02 and H_{cr}/H_c=5, and a SD region above M_r/M_s = 0.5. It also shows a region with $0.1 \leq M_r/M_s \leq 0.5$ and H_{cr}/H_c values ≤ 100 associated with mixtures of SP and stable SD grains, and a theoretical SP saturation threshold or “envelope” above M_r/M_s of 0.3.

Though most of natural grain sizes display hysteresis parameters within the PSD area of the day plot, they may not be of grain size or domain state associated with the PSD. Tauxe et al. (2002) commentated on several behaviours that control hysteresis in the PSD. E.g. Many loops may be distorted by mixing of SD and SP grains, by mixing of uniaxial SD and SP behaviours, by stress in MD particles, or mixing of two phases such as magnetite and hematite.

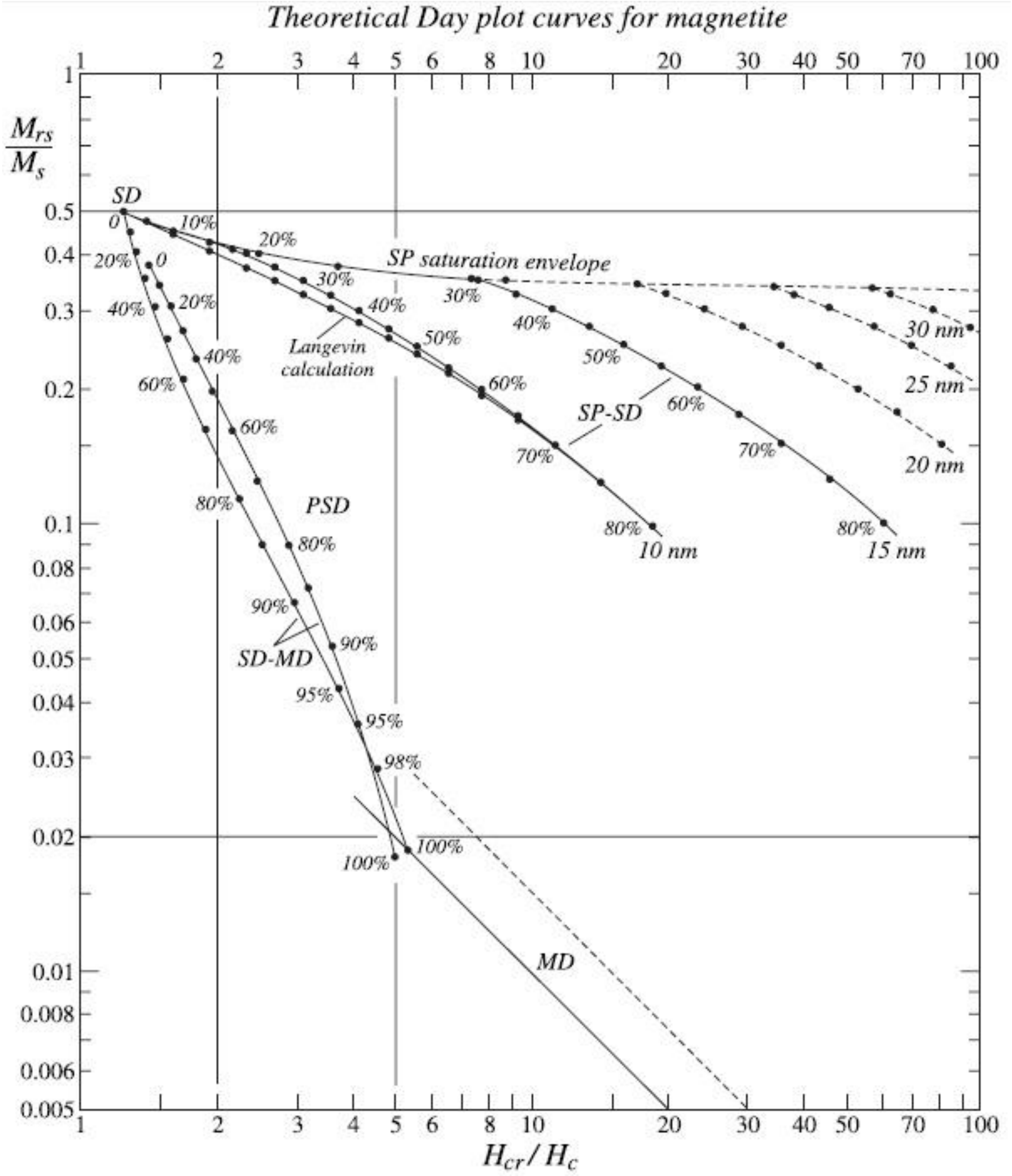

Figure 5.3-7: Theoretical Day plot curves calculated for magnetite. Numbers along curves are volume fractions of the soft component (SP or MD) in mixtures with SD grains. After Dunlop (2002).

5.4 Types of magnetism: Diamagnetism, paramagnetism, ferromagnetism, ferrimagnetism and antiferromagnetism

The origin of magnetism lies in the orbital and spin motions of electrons and how the electrons interact with each other. All matter is magnetic, but some materials are significantly more magnetic than others. The main distinction between magnetic materials is that in some materials there is no collective interaction of atomic magnetic moments, whereas in other materials there are very strong interactions between atomic moments (Moskowitz, n.d.).

The behaviour of magnetic materials can be classified into five major groups; Diamagnetism, paramagnetism, ferromagnetism, ferrimagnetism and antiferromagnetism. Diamagnetic and paramagnetic behaviour exhibit no collective magnetic interaction and are not magnetically ordered. Ferromagnetic, ferrimagnetic and antiferromagnetic behaviour exhibit long-range magnetic ordering below a certain critical temperature (Néel or Curie temperature). The behaviours commonly known as magnetic, or “behaving as iron”, are ferromagnetism and ferrimagnetism. Diamagnetism and paramagnetism are so weak that they commonly are thought of as “non-magnetic” (Moskowitz, n.d.).

Magnetic materials can also be classified by value of magnetic susceptibility, χ_m. Here they are classified into diamagnetic materials, paramagnetic materials and ferromagnetic materials, based on 100% pure samples, as follows (Marcon & Ostanina, 2012):

- diamagnetic materials: $-1 < \chi_m < 0$,
- paramagnetic materials: $0 < \chi_m << 1$,
- ferromagnetic materials: $\chi_m >> 1$.

5.4.1 Diamagnetism and Paramagnetism

Diamagnetism is a property of all materials, and is usually very weak. In diamagnetic materials all the orbital shells of the atoms are filled so there are no unpaired electrons. Diamagnetic materials have therefore atoms which have no net magnetic moment. However, when exposed to an applied magnetic field a negative magnetisation is produced, and the susceptibility becomes negative. This is due to non-cooperative behaviour of the orbiting electrons (Moskowitz, n.d.). Characteristic diamagnetic behaviours are; the field being zero if the magnetisation is zero and the susceptibility being temperature independent. Examples of diamagnetic minerals are quartz, calcite and feldspars (Dunlop & Özdemir, 1997).

In paramagnetic materials some of the atoms or ions have individual net magnetic moment due to unpaired electrons in partially filled orbitals. The individual magnetic moments of the atoms are assumed to be non-interacting (this is not strictly true in a crystal lattice, where atoms interact both magnetically and electrostatically (Dunlop & Özdemir, 1997)), and result in zero magnetisation when there is no applied field. When a magnetic field is applied to paramagnetic materials there is a partial alignment of the atomic magnetic moments in the same direction as the applied field. Only thermal perturbations prevent perfect alignment of the moment with the applied field (Dunlop & Özdemir, 1997). This results in temperature dependant susceptibility, known as the Curie Law (Moskowitz, n.d.). At normal temperatures the partial alignment of magnetic moments results in a positive net magnetisation and a positive susceptibility. Although the degree of alignment is small at ordinary temperatures, it is sufficient to outweigh diamagnetism. Most iron-bearing sulphides, carbonates and silicates are paramagnetic with susceptibilities usually 10-100 times greater than those of diamagnetic minerals (Dunlop & Özdemir, 1997).

Paramagnetic susceptibility is independent of the applied field, unless the temperature is very low (<<100 K) or the field is very high. Therefore, in normal conditions, the paramagnetic susceptibility will be proportional to the total iron content. In natural samples with low concentration of iron oxides the paramagnetism of the matrix minerals can be significant and a paramagnetic correction may be needed (Moskowitz, n.d.).

The magnetisation of both paramagnetic and diamagnetic materials is induced or temporary. The magnetisation will disappear when the external field is removed. To align the permanent moments of paramagnetic atoms or ions and yield saturation at ordinary temperatures, extremely large fields (10^6 Gauss or 100 Tesla) are needed (Dunlop & Özdemir, 1997).

5.4.2 Ferromagnetism

Unlike paramagnetic materials, ferromagnetic materials only need weak fields to saturate their magnetisation. Typical elements that are ferromagnetic include iron, nickel and cobalt, and many of their alloys. A soft iron ring would only need approximately 0.01 Tesla to reach saturation, and a measurable remanent magnetisation, $M_{r,}$ remains (Dunlop & Özdemir, 1997). This is due to the strong interactions of the atomic moments in these materials. The interactions are produced by electronic exchange forces which results in an antiparallel, or parallel alignment of atomic moments. These exchange forces are so large that they would be equivalent to a field up to 1000 Tesla. This is approximately 100 million times the strength of the earth's field (Moskowitz, n.d.).

Ferromagnetic materials have two distinct characteristics; they have a spontaneous magnetisation, and they have a magnetic ordering temperature.

In the absence of a field, the spontaneous magnetisation is the net magnetisation existing inside a uniformly magnetised microscopic volume. At 0 Kelvin, the magnitude of the magnetisation is dependent on the spin magnetic moments of electrons. Another, related term is the saturation magnetisation, M_s, which is the maximum induced magnetic moment that can be obtained in a magnetic field (Moskowitz, n.d.). Saturation magnetisation is independent of particle size, but is dependent on temperature.

Magnetic ordering temperature, or Curie Temperature (T_C), is a temperature threshold indicating where the thermal energy overcomes the electronic exchange forces of ferromagnets and produces a randomising effect. The result of this effect makes the magnetic moments, above Curie temperature, non-interacting. A ferromagnet above Curie temperature is therefore paramagnetic, and the saturation magnetisation goes to zero.

5.4.3 Ferrimagnetism and antiferromagnetism

In terrestrial rocks, we are concerned with iron oxides, hydroxides and sulphides. In these compounds, iron atoms are not close enough for direct exchange interactions. Instead, there is interaction of 3d electrons through overlap of their orbitals with 2p orbitals of intervening oxygen ions, or 3p orbitals of sulphur ions (Dunlop & Özdemir, 1997). These interactions are called indirect exchange or superexchange interactions, and describes the mechanism where dominant negative interactions establishes two magnetic sublattices, A and B, of opposite spin directions and magnetic moments. The strongest superexchange interactions occurs if the Fe-O bonds make an angle close to 180° and the weakest occur if the angle is close to 90° (Dunlop & Özdemir, 1997), that is, respectively, parallel or antiparallel alignment of spins.

5.4.3.1 Ferrimagnetism

In ferrimagnets, the magnetic moments of sublattice A and B are un-equal. Below the Curie temperature, a spontaneous magnetisation occurs. Ferri- and ferromagnets are similar in that they both have spontaneous magnetisation, Curie temperatures, hysteresis, and remanence, but differ in magnetic ordering (Moskowitz, n.d.).

5.4.3.2 Antiferromagnetism

An antiferromagnet is a ferromagnet where the magnetic moment of sublattice A and B is the same in magnitude, but are opposite in direction, at all temperatures. Thus there is no observable spontaneous magnetisation. Many natural magnetic minerals are perfect, or imperfect (slightly ferromagnetic) antiferromagnets, among them hematite (αFe_2O_3), ilmenite ($FeTiO_3$) and goethite ($\alpha FeOOH$). Although the sum of the sublattice magnetisations is zero in the absence of an applied field, antiferromagnetic materials do have an induced magnetisation in the presence of an applied field (Dunlop & Özdemir, 1997).

Antiferromagnets have zero remanence and no hysteresis, but they do exhibit a small positive susceptibility that varies with temperature. At temperatures above 0 Kelvin local thermal rotations of the magnetic moments of sublattice A and B result in some torque and a small susceptibility, which increases as temperature increases (Dunlop & Özdemir, 1997), until the ordering temperature for antiferromagnets is reached. This temperature is called the Néel temperature (T_N), and above this temperature the susceptibility obeys the Curie Weiss law for paramagnets, but with a negative intercept indicating negative exchange interactions (Moskowitz, n.d.).

Imperfect antiferromagnetism can occur if the anti-parallelism is not exact. Above the Morin transition temperature, hematite is such an antiferromagnet with a weak “parasitic” ferromagnetism. The sublattice magnetisations are permanently tilted, or canted, at an angle of about 0.2° (Dunlop & Özdemir, 1997). In the absence of an external field, the canting will produce a small net magnetisation perpendicular to the A and B sublattice moments. Although the ferromagnetism of hematite is weak, it is extremely important due to recording of ancient geomagnetic fields (Dunlop & Özdemir, 1997).

5.5 Types of remanence

Remanence can be described as retained magnetisation in the absence of a field or in the presence of a different magnetic field. TRM, or thermal remanent magnetisation, is the most common reason for acquired primary remanence within a rock, though a rock can acquire remanence in multiple ways and at several times. The remanence carried by a rock is called natural remanent magnetisation (NRM), and is the vector sum of all the different possible components of magnetisation acquired over its history (Moskowitz, n.d.). The main types of NRM include: Thermoremanent magnetisation (TRM), Chemical Remanent Magnetisation (CRM), Viscous Remanent Magnetisation (VRM), Isothermal Remanent Magnetisation (IRM), Depositional Remanent Magnetisation (DRM), and Post Depositional Remanent Magnetisation (PDRM).

Primary magnetisation is typically acquired by TRM or DRM. The primary magnetisation acquired can later be remagnetised and the rock acquires secondary remanence such as chemical, viscous or post-depositional remanent magnetisation. Secondary magnetism can either overprint or completely overwrite the previous remanence acquired by the rock. Secondary remanence is common in igneous rocks which often has undergone one or more periods of metamorphism (Reynolds, 2011). Two important contributors to secondary NRM in igneous rocks, with respect to LWMA, are chemical remanent magnetisation and viscous remanent magnetisation.

5.5.1 Chemical remanent magnetisation

Chemical remanent magnetisation is any chemical alteration that leads to remanence in a rock. This can be due to low-temperature oxidation exsolution, diagnesis or dehydration (Moskowitz, n.d.), well below the Curie temperature in presence of a magnetic field. There are two main types of CRM, either growth of new magnetic minerals, or recrystallization or alteration of pre-existing parent mineral into a new daughter mineral. The first type acquires remanence when the grains grow past a blocking volume, V_B, while being exposed to a field, H. In this case the remanence is acquired when the grains grow from SPM to SD state. The process of attaining remanence is more complex for the second type of CRM. The growing daughter phase is influenced not only by an external field, H, but also by its magnetic parent phase, to which it may be magnetostatically or exchange coupled with, with varying degrees of efficiency (Dunlop & Özdemir, 1997). There is also another type of chemical remanent magnetisation called thermal-chemical remanent magnetisation (TCRM) which is acquired during chemical alteration and cooling (Reynolds, 2011).

5.5.2 Viscous Remanent Magnetisation

Viscous remanent magnetisation (VRM) is a remanent magnetisation that is gradually acquired during exposure to weak magnetic fields. VRM can be obtained for SD-, PSD- and

MD particles. For SD particles, the acquisition of VRM is basically the inverse of magnetic relaxation. It is also shown that with increased temperature the intensity of VRM increases, due to decrease in coercive force allowing rotation of the magnetic moments (Butler, 2004 an references therein). The same principle holds for PSD- and MD particles where thermal energy leads to domain wall motion, resulting in increased magnetisation in the direction of the applied field. For MD particles, a general inverse relationship exists between coercive force and the viscosity coefficient. This explains the observation of VRM most commonly being carried by magnetite MD grains which display low coercive force.

For substantially elevated temperatures, such as in the deep crust, the resulting VRM is referred to as thermoviscous remanent magnetisation (TVRM). It is commonly observed that temperatures required to erase TVRM or VRM components are higher than those predicted by theory for SD particles (Butler, 2004).

5.6 Terrestrial magnetic minerals and rocks

The most important terrestrial magnetic minerals are oxides of iron and titanium. Their compositions can be viewed in the Ti^{4+}-Fe^{2+}-Fe^{3+} ternary diagram in Figure 5.6-1. The ternary diagram is divided into titanomagnetites (TM), titanomaghemites and titanohematites. The titanomagnetites are cubic minerals with spinel structure. The mole per cent of Ti^{4+} is measured by the composition parameter x, so a composition of x=0 (TM0) would be magnetite and TM100 is ulvöspinel. Titanomaghemites are cation-deficient oxidation products of titanomagnetites with spinel structure, whereas titanohematites are rhombohedral (Dunlop & Özdemir, 1997). On earth magnetite is viewed as the dominant contributor to magnetic anomalies, but other oxides, such as Cr-spinel and hemo-ilmenite, are also present and can provide stable remanent magnetisation.

5.6.1 Magnetite

Magnetite ($Fe^{2+}Fe_2^{3+}O_4$), or an exsolved phase close to TM0 in composition, is the single most important magnetic mineral on earth (Dunlop & Özdemir, 1997). Magnetite is one of the most abundant oxide minerals in igneous and metamorphic rocks, and occurs typically as an accessory mineral (Deer, 2009). It is a ferrimagnetic mineral where two magnetic sublattices, A and B, are defined respectively by tetrahedral Fe (Fe^{3+}) sites, and octahedral Fe (Fe^{2+}, Fe^{3+}) sites. The net magnetic moment of magnetite is due to the B-site (Moskowitz, n.d.). Magnetite is a high temperature mineral generally associated with igneous or metamorphic rocks. It is typically present in minor amounts, and may be difficult to identify.

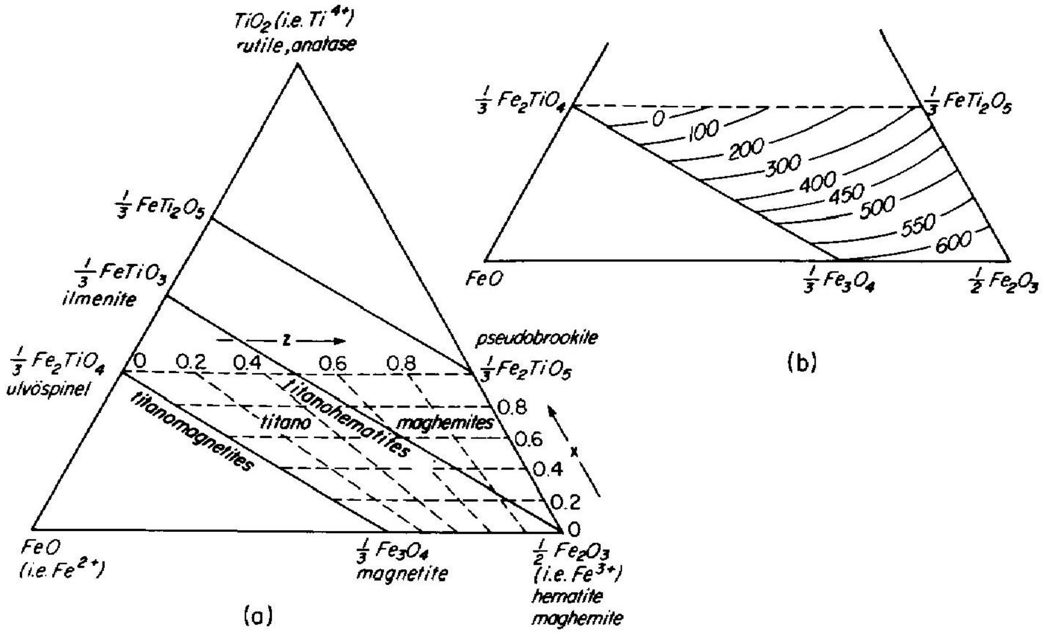

Figure 5.6-1: (a) TiO_2-FeO-Fe_2O_3 ternary diagram, showing the titanomagnetite and titanohematite solid-solution lines and the titanomaghemite field. (b) Curie temperature contours for syntetic titanomaghemites. After Dunlop & Özdemir, 1997, and referances therein.

For identification in thin section magnetites will appear isotropic, opaque in transmitted light and can appear black-greyish in plane polarized light. It is cleavage less, has a metallic luster, and displays greater reflectivity than ilmenite and less than hematite (Philpotts, 2003). Magnetite is identified in electron backscatter microscopes by its bright white appearance (Figure 5.6-2A).

MD magnetite dominates the magnetic response of many rock types, especially in high-grade metamorphic rocks. MD magnetite contributes to the induced magnetisation of a rock. If the magnetite is of SD size, they are capable of carrying extremely stable remanence due to their shape anisotropy (Dunlop & Özdemir, 1997). The magnetic signal of magnetite is commonly limited to depths in the crust corresponding to its Curie isotherm of 580°C.

5.6.2 Cr-spinel and chromites

Fe-Cr spinels or chromites ($FeCr_2O_4$-Fe_3O_4) are common in submarine gabbros and peridotites in marine sediments derived from these rocks, and in lunar igneous rocks. Depending on composition they may be ferromagnetic, antiferromagnetic or paramagnetic at ordinary temperatures. The Currie temperature for $FeCr_2O_4$ is -185°C, and rises with decreasing Cr content. Some naturally occurring chromites can carry remanence, but they are seldom major contributors to the total NRM (Dunlop & Özdemir, 1997, and references therein). The remanence carried by chromites is typically TRM.

For identification in thin section Cr-spinels will appear isotropic, dark brown to opaque in transmitted light and dark grey to brownish in plane polarized light. They reflect less light than magnetite and ilmenite in reflected light (Philpotts, 2003). In backscatter electron microscopy chromites will appear darker than magnetites.

5.6.3 Hemo-ilmenite

Minerals of the hematite-ilmenite solid solution series can be found in sedimentary, igneous and metamorphic rocks. Depending on magnetic structure, and/or degree of exsolution, the remanent response can dominate the induced component (McEnroe et al., 2004b). Granulate-facies rocks, continental igneous rocks, and anorthosites, with high average NRMs (4-6 A/m) and/or low susceptibility (0.001 SI) were reported by McEnroe and Brown (2000) & McEnroe et al., 2001, 2004a, 2008, 2009a). These observations of strong and stable NRMs, in rocks dominated by exsolved hematite or ilmenite, with or without magnetite, lead to the discovery of lamellar magnetism. The magnetism carried by hemo-ilmenites is typically TCRM.

Lamellar magnetism relates to interfaces of fine exsolution lamellae of near end-member hematite and ilmenite. Here fine-scale intergrowths of canted antiferromagnetic hematite and paramagnetic ilmenite leads to phase interface ferrimagnetism of individual lamella which are magnetically aligned. The intensity of lamellar magnetism is proportional to the density of lamellae at the surface of contact layers, and retains properties of high coercivity and thermal stability (McEnroe et al., 2009b). Experiments on natural hemo-ilmenite grains at temperatures and pressures indicative of lower crustal conditions (10 kbar, 580°C) show that this type of magnetic structures is highly stable (McEnroe et al., 2004b).

Ilmenites appear opaque in thin section in transmitted light. In plane polarized light it appears greyish brown with a pinkish or violet tint. It reflects less light than both magnetite and hematite. Internal exsolved hematite lamella would therefore appear brighter. Hematite is also opaque in transmitted light, and in plane polarized light it appears bright greyish white. Both ilmenite and hematite are strongly anisotropic (Philpotts, 2003). In electron backscatter microscopes hematite lamella appear light grey, and ilmenite as dark grey (Figure 5.6-2.)

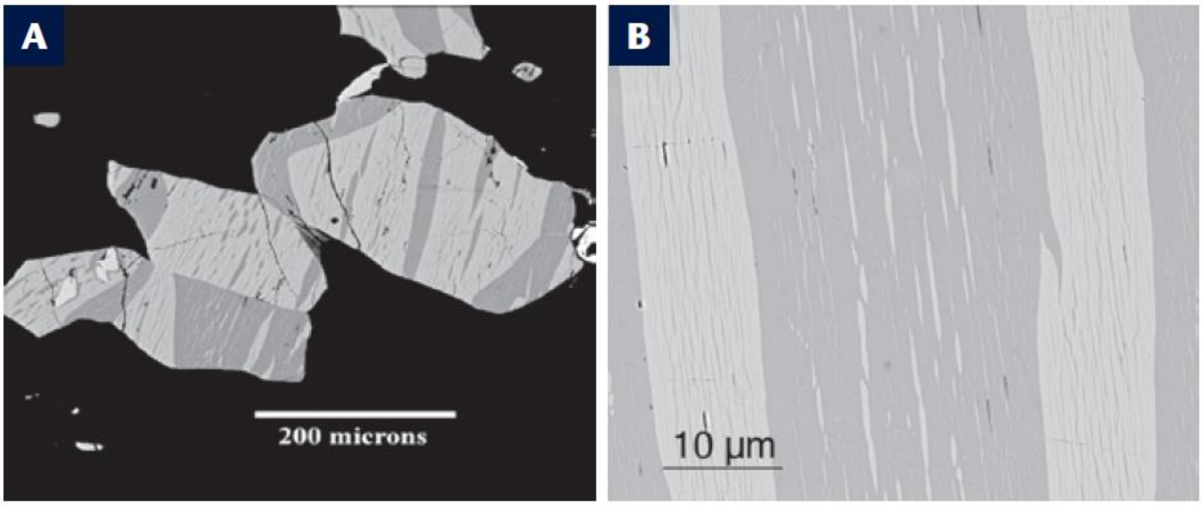

Figure 5.6-2: (A) Electron backscatter image of an intergrowth of exsolved hematite and ilmenite, and minor magnetite. (B) Electron backscatter image of hemo-ilmenite. Hematite lamellae displays as light-grey and ilmenite dark-grey, whilst the minor magnetite in A appears white. After McEnroe et al. (2009b).

5.6.4 Magnetic minerals in deep crustal- and upper mantle rocks

The knowledge of magnetic mineralogy and magnetic petrology is largely based on studies on rocks at the Earth’s surface. The magnetic mineralogy and magnetic petrology of deep crustal rocks and in the upper mantle is therefore limited. Measurements are largely confined to tectonically emplaced ophiolite suites, altered dredghaul or manned submersible samples from mid-ocean rift valleys and fractures zones, and few are from fresh, young, tectonically unaffected oceanic intrusives (Dunlop & Özdemir, 1997). Results from deep drilling and constraints from seismic (Prodehl and Mooney, 2012, as cited in Purucker and Whaler, 2013) suggest a generally mafic composition. According to Jackson (1998 as cited in Ferré et al., 2014) the upper mantle is mainly consisting of lherzolites, hazburgites and dunites, and accessorily pyroxenites, wehrlites and eclogites. These rocks are abundant in silicate minerals, such as olivine, pyroxene, amphibole and garnet. While these silicate minerals often contain iron, they generally behave paramagnetically (Dunlop & Özdemir, 1997). A ferromagnetic component can be recorded, and are due to iron being incorporated in magnetite. While most non-iron bearing minerals such as quartz, calcite and feldspars are purely diamagnetic, their susceptibilities are small, but temperature independent. Thus at high temperatures, if the amount of paramagnetic and ferromagnetic minerals are small, the negative moment of silicate matrix of a rock may become significant (Dunlop & Özdemir, 1997).

Table 5.6-1: summary of the magnetic susceptibility at 300 K (~26.85°C) and saturation magnetisation (MS) of common minerals in mantle peridotite (Ferré et al., 2014).

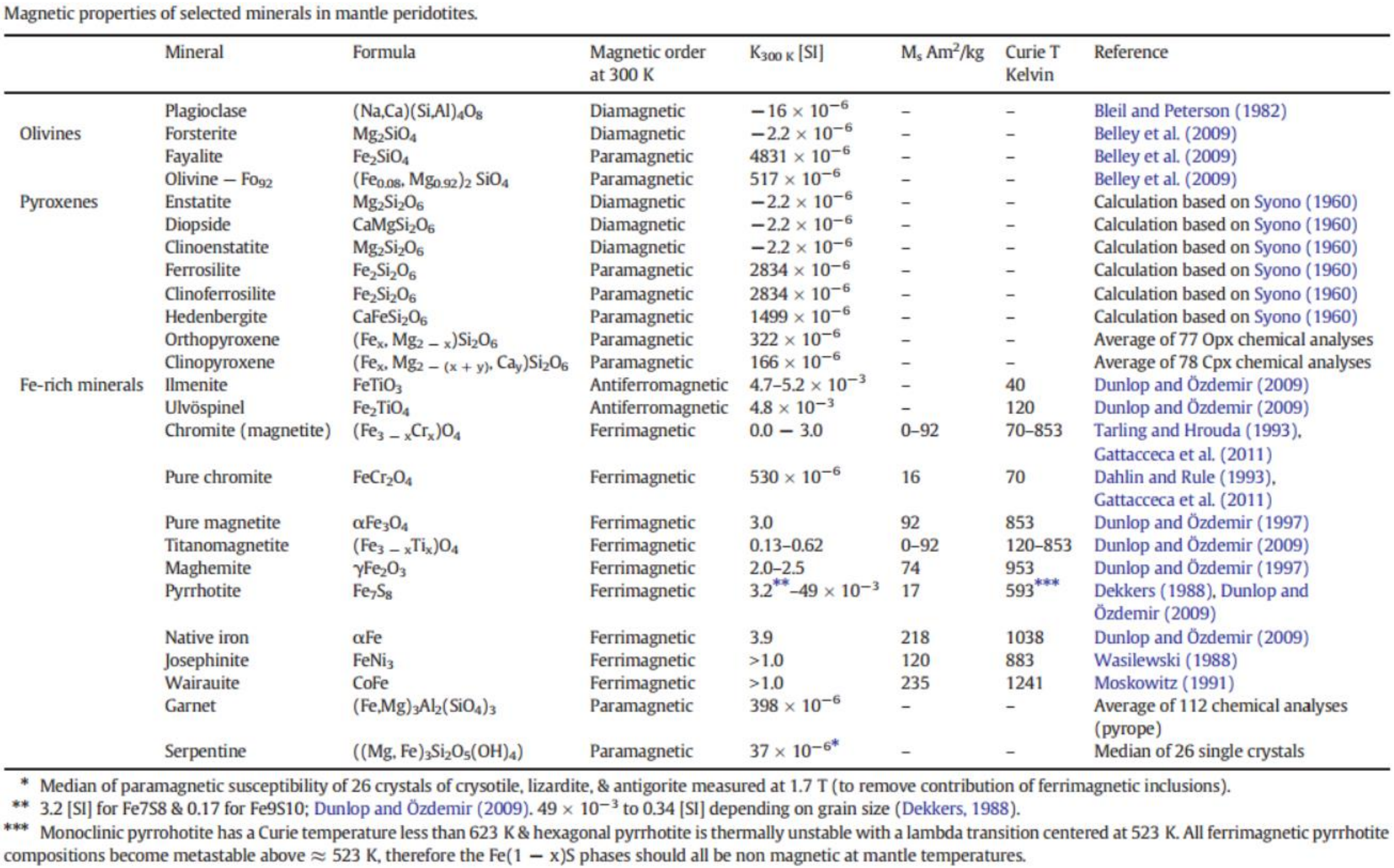

Magnetic properties of selected minerals in mantle peridotites.

	Mineral	Formula	Magnetic order at 300 K	$K_{300\ K}$ [SI]	M_s Am^2/kg	Curie T Kelvin	Reference
	Plagioclase	$(Na,Ca)(Si,Al)_4O_8$	Diamagnetic	-16×10^{-6}	–	–	Bleil and Peterson (1982)
Olivines	Forsterite	Mg_2SiO_4	Diamagnetic	-2.2×10^{-6}	–	–	Belley et al. (2009)
	Fayalite	Fe_2SiO_4	Paramagnetic	4831×10^{-6}	–	–	Belley et al. (2009)
	Olivine – Fo_{92}	$(Fe_{0.08}, Mg_{0.92})_2\ SiO_4$	Paramagnetic	517×10^{-6}	–	–	Belley et al. (2009)
Pyroxenes	Enstatite	$Mg_2Si_2O_6$	Diamagnetic	-2.2×10^{-6}	–	–	Calculation based on Syono (1960)
	Diopside	$CaMgSi_2O_6$	Diamagnetic	-2.2×10^{-6}	–	–	Calculation based on Syono (1960)
	Clinoenstatite	$Mg_2Si_2O_6$	Diamagnetic	-2.2×10^{-6}	–	–	Calculation based on Syono (1960)
	Ferrosilite	$Fe_2Si_2O_6$	Paramagnetic	2834×10^{-6}	–	–	Calculation based on Syono (1960)
	Clinoferrosilite	$Fe_2Si_2O_6$	Paramagnetic	2834×10^{-6}	–	–	Calculation based on Syono (1960)
	Hedenbergite	$CaFeSi_2O_6$	Paramagnetic	1499×10^{-6}	–	–	Calculation based on Syono (1960)
	Orthopyroxene	$(Fe_x, Mg_{2-x})Si_2O_6$	Paramagnetic	322×10^{-6}	–	–	Average of 77 Opx chemical analyses
	Clinopyroxene	$(Fe_x, Mg_{2-(x+y)}, Ca_y)Si_2O_6$	Paramagnetic	166×10^{-6}	–	–	Average of 78 Cpx chemical analyses
Fe-rich minerals	Ilmenite	$FeTiO_3$	Antiferromagnetic	$4.7–5.2 \times 10^{-3}$	–	40	Dunlop and Özdemir (2009)
	Ulvöspinel	Fe_2TiO_4	Antiferromagnetic	4.8×10^{-3}	–	120	Dunlop and Özdemir (2009)
	Chromite (magnetite)	$(Fe_{3-x}Cr_x)O_4$	Ferrimagnetic	$0.0 - 3.0$	0–92	70–853	Tarling and Hrouda (1993), Gattacceca et al. (2011)
	Pure chromite	$FeCr_2O_4$	Ferrimagnetic	530×10^{-6}	16	70	Dahlin and Rule (1993), Gattacceca et al. (2011)
	Pure magnetite	αFe_3O_4	Ferrimagnetic	3.0	92	853	Dunlop and Özdemir (1997)
	Titanomagnetite	$(Fe_{3-x}Ti_x)O_4$	Ferrimagnetic	0.13–0.62	0–92	120–853	Dunlop and Özdemir (2009)
	Maghemite	γFe_2O_3	Ferrimagnetic	2.0–2.5	74	953	Dunlop and Özdemir (1997)
	Pyrrhotite	Fe_7S_8	Ferrimagnetic	$3.2^{**}–49 \times 10^{-3}$	17	593^{***}	Dekkers (1988), Dunlop and Özdemir (2009)
	Native iron	αFe	Ferrimagnetic	3.9	218	1038	Dunlop and Özdemir (2009)
	Josephinite	$FeNi_3$	Ferrimagnetic	>1.0	120	883	Wasilewski (1988)
	Wairauite	CoFe	Ferrimagnetic	>1.0	235	1241	Moskowitz (1991)
	Garnet	$(Fe,Mg)_3Al_2(SiO_4)_3$	Paramagnetic	398×10^{-6}	–	–	Average of 112 chemical analyses (pyrope)
	Serpentine	$((Mg, Fe)_3Si_2O_5(OH)_4)$	Paramagnetic	$37 \times 10^{-6*}$	–	–	Median of 26 single crystals

* Median of paramagnetic susceptibility of 26 crystals of crysotile, lizardite, & antigorite measured at 1.7 T (to remove contribution of ferrimagnetic inclusions).

** 3.2 [SI] for Fe7S8 & 0.17 for Fe9S10; Dunlop and Özdemir (2009). 49 × 10^{-3} to 0.34 [SI] depending on grain size (Dekkers, 1988).

*** Monoclinic pyrrohotite has a Curie temperature less than 623 K & hexagonal pyrrhotite is thermally unstable with a lambda transition centered at 523 K. All ferrimagnetic pyrrhotite compositions become metastable above ≈ 523 K, therefore the $Fe(1 - x)S$ phases should all be non magnetic at mantle temperatures.

5.6.5 Peridotites

Lherzolites, harzburgites, dunites, and wehrlites are all peridotite rocks, which are the most abundant rocks in the mantle. The remanent magnetisation recorded by peridotites arises from minor phases such as Fe-oxides, FeNi-alloys and some Fe-sulphides that show ferromagnetic behaviour (Ferré et al., 2014).

Table 5.6-1 provides a summary of the magnetic properties of selected minerals which are common in mantle peridotites.

In the upper lithospheric mantle peridotites mainly consist of the plagioclase- and spinel-type, whilst garnet-lherzolites are present at greater depths (Ferré et al., 2014). According to Ferré et al. (2014), some of the upper mantle is below the Curie temperature and could potentially contribute to magnetic anomalies, whilst deeper peridotite above the Curie temperature, is too hot to carry magnetic remanence.

Magnetic minerals occurring as a primary phase in mantle peridotites are e.g. Cr-rich spinels. As noted above, these will stabilize at increased depths as the Cr content increases, and in peridotite – they will coexist with garnet. While Cr-spinels are common in upper mantle peridotites, they are only ferromagnetic if $Al + Mg < 0.2$ and $Fe > 0.3$, which are uncommon in mantle peridotites (Ferré et al., 2014 and references therein). Magnetite is the magnetic mineral that most commonly provides magnetism within peridotite, and generally forms as a secondary phase resulting from interaction with fluids or melts, causing serpentinization.

5.6.5.1 Exhumed peridotites

Mantle peridotites found at the Earth's surface are ophiolites, Alpine-type peridotites, or xenoliths (Ferré et al., 2014, and references therein). In these exhumed peridotites subsolidus recrystallization of titanomagnetites or serpentinization may occur during exhumation during initial cooling below the Curie temperature (Dunlop & Özdemir, 1997, and references therein).

Weathering and alteration by meteoritic fluids, of exposed peridotites, is known to form Ti-poor magnetite commonly occurring with maghemite, hematite and goethite, giving peridotites an olive green to ochre colour depending on the degree of weathering (Ferré et al., 2014, and references therein). Magnetic remanent phases formed after exhumation often record different magnetisation directions than former primary or secondary remanence.

5.6.5.2 Magnetism of serpentinized peridotites

Exposed peridotites usually have reversible thermomagnetic curves, with Curie points of 520-580°C (Dunlop & Özdemir, 1997 and references therein). As noted alter mantle rocks through serpentinization, a process which forms a by-product of abundant magnetite. NRM varies enormously depending on the grade of serpentinization and the domain state of the exsolved magnetite. If the magnetite is of SD or pseudo-SD size the NRM they carry is hard and stable. Further growth of the inclusions could lead to MD size, imparting an inducing magnetisation on the rock. A serpentinized peridotite with inclusions of SD size could display NRM values close to those of fresh basalts (Dunlop & Özdemir, 1997 and references therein).

Ferré et al., (2014, and references therein) reports formation of magnetite through serpentinization at mantle depths and at intermediate depths. While Evans et al. (2013), as previously discussed, state that it is a relatively low-temperature hydration occurring at shallow depths in the crust, or even at Earth surface conditions.

5.7 Serpentinization and serpentinites

Serpentinites are rocks consisting mostly of the serpentine-group minerals chrysotile, lizardite and antigorite (Figure 5.7-1). They are formed by serpentinization, a relatively low-temperature hydration of MgFe-rich ultramafic rocks. During serpentinization, MgFe-rich minerals, such as olivine, orthopyroxene and clinopyroxene, are altered and replaced by serpentine minerals (approximate formula $Mg_3Si_2O_5(OH)_4$), magnetite and in some cases brucite ($Mg(OH)_2$) (Evans et al., 2013). Serpentinite contain over ~13 wt% H_2O, and are moderately to strongly enriched in fluid-mobile elements, independent of their place of origin and ultimate geological setting (Guillot & Hattori 2013 and references therein). A typical serpentinized rock have a fine-grained, dark green to black appearance, due to the mineral product, and are commonly crossed by veins of chrysotile or calcite. Their densities are significantly lower than that of their primary rock, and their magnetic susceptibility is up to nearly two orders of magnitude greater (Evans et al., 2013). Serpentinites have a low-temperature stability range, and at high pressures (30-100 km depth) and/or temperatures, the internal H_2O is released during dehydration (Guillot & Hattori, 2013).

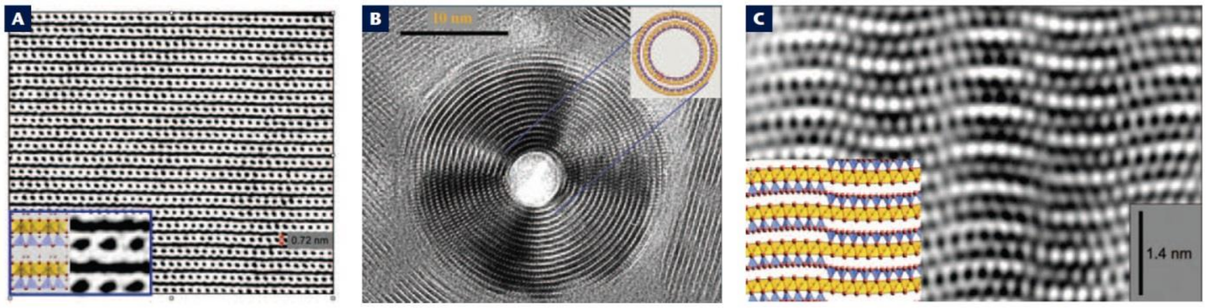

Figure 5.7-1: High-resolution transmission electron microscopy (TEM) micrograph of; (A) the flat lizardite microstructure in which the basic structural unit is 0.72 nm thick, (B) the cross section of a chrysotile nanotube with a hollow core, and (C) the wave structure of antigorite along its b-axis. The microscope images shows only Mg and Si atoms without O atoms. Inserts shows polyhedral models of; (A) the lizardite microstructure, (B) of the tube-in-tube cylindrical structure of chrysotile, and (C) approximate structure of antigorite. After Evans et al. (2013).

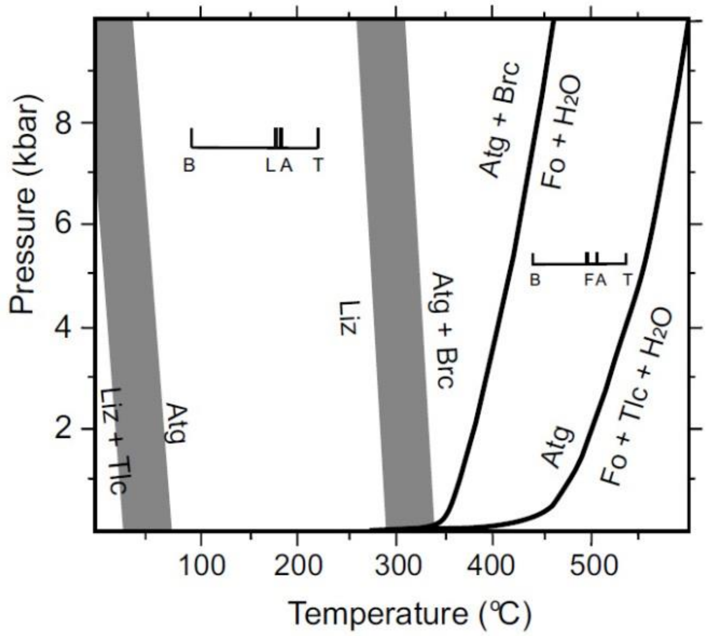

Figure 5.7-2: Possible phase diagram for the MgO-SiO$_2$-H$_2$O system. Two steep H$_2$O-conserved reactions are shown. Their wide grey bands illustrate uncertainty. A transition from lizordite and chrysotile to antigorite is shown with a steep negative dP/dT slope at approximately 300°C. Abbreviations: A, Atg = antigorite; B, Brc = brucite; F, Fo = forsterite; L, Liz = lizardite; T, Tlc = talc. After Evans et al. (2013).

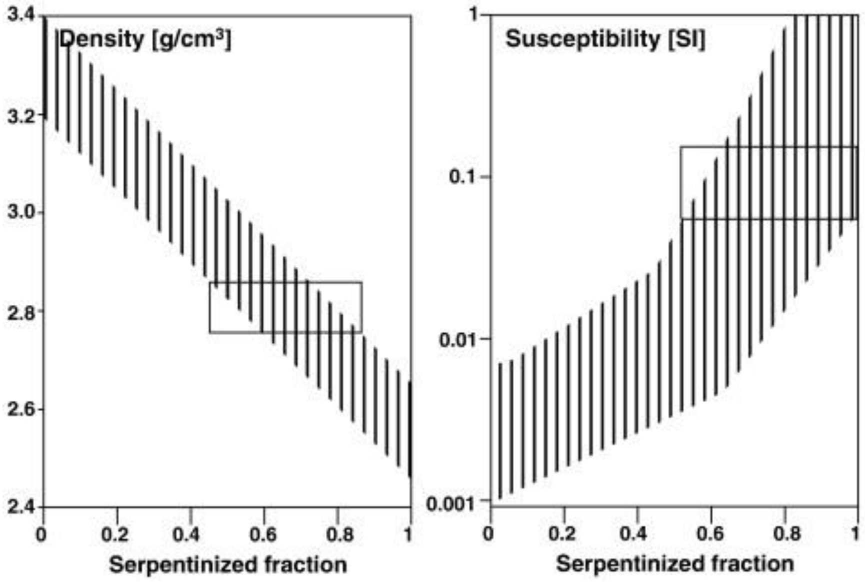

Figure 5.7-3: Densities and magnetic susceptibilities for serpentinites. After Fichler et al. (2011).

5.7.1 The serpentine minerals

The serpentine minerals form under a wide range of temperatures, including Earth surface conditions and hot hydrothermal temperatures (Evans et al., 2013). The three most common serpentine minerals are lizardite, chrysotile, and antigorite. Lizardite has a flat structure (Figure 5.7-1A), and commonly pseudomorphs olivine. It is optically recognised in microscope by its hourglass and mesh structures. Chrysotile forms multiwall nanotubes or nanoscrolls (Figure 5.7-1B). It occurs mainly as a filling of fractures that crosscut serpentinite. It is recognised in microscope by its parallel fibre orientation, which commonly is determined by repeated opening of fractures. Antigorite is recognised by its curved, wavy layers (Figure 5.7-1C), and is considered to be a high-temperature phase of serpentine. Antigorite grows from lizardite and chrysotile with increasing grade of metamorphism at temperatures above 320°C (Figure 5.7-2; Evans et al., 2013). It is therefore common in partially recrystallized and metamorphosed serpentinite, where it usually forms interlocking, elongated, blade-shaped crystals that overprint earlier formed serpentinite. The serpentine minerals display very low birefringence colours which result in anomalous interference colours (Perkins, 2011). In addition to lizardite, chrysotile and antigorite, some serpentine mineral microstructures have been recognized (Evans et al., 2013).

5.7.2 Serpentinization of MgFe-rich ultramafic rocks

Serpentinization of MgFe-rich ultramafic rocks involves internal buffering of pore fluid, reduction of oxygen fugacity, and partial oxidation of Fe^{2+} to Fe^{3+}. When the MgFe-rich mineral olivine is being serpentinized the residual olivine retains its primary composition of magnesium until it is completely consumed. The resulting serpentine mineral is similar restricted in its content of ferrous iron. This is due to a very slow rate of MgFe diffusion in olivine at low temperatures (Evans, 2010 as cited in Evans, 2013). The resulting mass balance problem is resolved by precipitation of magnetite and release of H_2 gas (Evans et al., 2013):

Formula 5: $MgFe\ olivine + H_2O \rightarrow MgFe\ serpentine + magnetite + MgFe\ brucite + H_2$

As stated before, the serpentinization leads to significantly lower densities in the serpentinitized rock compared to that of their primary rock, and their magnetic susceptibility becomes up to nearly two orders of magnitude greater (Figure 5.7-3). Magnetite is the primary source accountable for the increase in susceptibility. The greatest modal amount of magnetite (and hydrogen gas) is obtained when brucite does not form, such as in the peridotite rock harzburgite, a rock rich in orthopyroxene (Figure 4.2-2). Greater amount of magnetite can also be obtained when the primary rock becomes heavily serpentinized. The initial growth of brucite will then be reversed, and low-Fe lizardite and magnetite are formed (Evans et al., 2013). This observation finds support in the increasing slope of data points on the graph of magnetic susceptibility relative to density (Figure 5.7-3). In addition will a transition from lizardite to antigorite result in magnetite growth, due to the antigorite being less Fe^{3+} rich than lizardite (Evans et al., 2012). The degree of serpentinization is primarily limited by supply of H_2O at the grain scale (Evans et al., 2013).

5.7.3 Location of serpentinites

The serpentine minerals form principally after retrograde hydrothermal alteration of ultrabasic rocks, e.g. dunites, peridotites or pyroxenites, or by prograde metamorphism of pre-existing serpentinite (Deer, 2009). Consequently, serpentinites are primarily produced by seawater hydration under a variety of conditions. They can be produced under low-temperature seafloor serpentinization e.g. at both slow and fast spreading ridges, and along faults at outer rises near trenches. They can be produced under moderately high temperatures (e.g. 350°C) by ocean-ridge hydrothermal activity, and mantle peridotites at the forearc can be serpentinized due to water expelled from a the subducting slab (Evans et al., 2013).

Serpentinites contribute to the geochemical cycle of subduction zones. They act as lubricant along plates during aseismic creep. They are buoyant compared to their precursor rock (2.6 g/cm^3 relative to 3.2 g/cm^3 (Evans et al., 2013)), and weakens the physical strength of a subduction channel. They also occur near the base of the mantle wedge at depths greater than 10km. Due to their buoyancy they are able to rise from the base of the mantle wedge to the surface (Saumur et al., 2010 as cited in Evans et al., 2013). In the mantle, they are a reservoir of water and fluid-mobile elements (Guillot & Hattori 2013).

Serpentinites occur in all ancient orogenic belts as minor bodies and lenses. In these orogenic belts they are within a suit of rocks mostly containing ultramafic, gabbroic, and basaltic rocks, with minor chert. This type of suite is referred to as an ophiolite. Ancient serpentinites on continents are commonly well exposed in suture zones associated with the closure of paleo-oceans (Guillot & Hattori 2013), e.g. the Iapetus Ocean (Figure 5.7-4). The protholits of ancient serpentinites can have various origins, and can present cumulate from a variety of mafic melts or depleted residual-mantle peridotites, including abyssal and mantle-wedge peridotites (Evans et al., 2013).

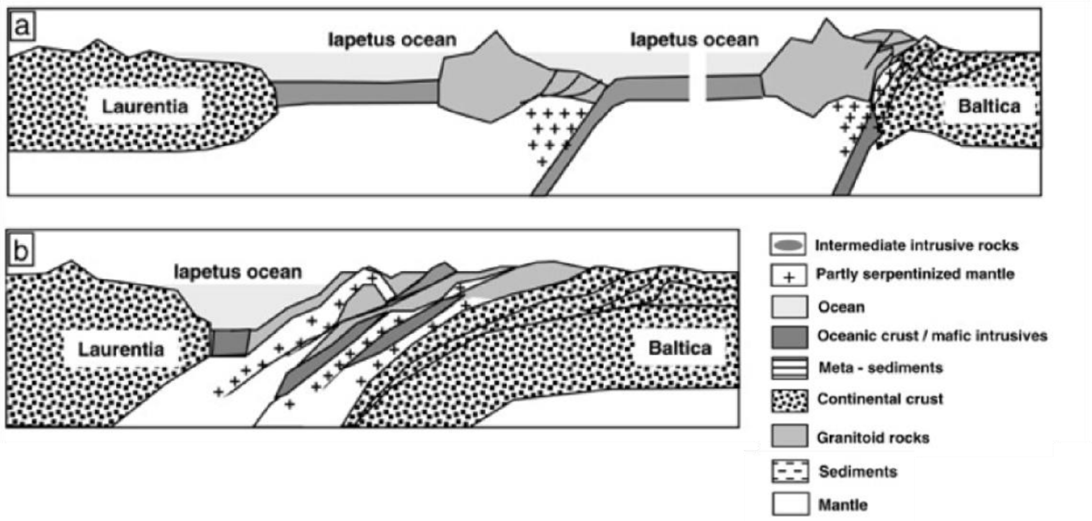

Figure 5.7-4: Formation of inherited structures in the North Sea Crust with focus on serpentinites and meta-serpentinites; (a) late Ordovician, (b) Middle Silurian. After Fichler et al. (2011).

6 Field work

6.1 Ground magnetic surveying

The field area was selected based on geological maps from the geological map data base of NGU (the Norwegian Geological Survey) and from geological maps within Spengler (2006).

When conducting a ground magnetic survey, which measures the total magnetic field intensity (TMI), over a selected field area, cultural noise such as power lines, cars, houses or other objects could create a magnetic field other than the field created by the bedrocks. To check for possible sources for cultural noise at the field area a topographical overlay map, taken from NGU's database, showing power lines and houses was investigated. The topographic map was superimposed the Raudhaugene and Ugelvik peridotite borders, taken from the structural geological map of Spengler and Haker (2006), thus indicating areas which possibly could be effected by cultural noise.

The investigation showed a power line crossing the mapped Ugelvik body, and a power line going parallel with the mapped western border of the Raudhaugene body. Therefore, these areas could be affected by cultural noise. An indication of problems regarding cultural noise associated with houses was predominantly indicated for the Ugelvik body, whilst magnetic response from the Raudhaugene body could acquire some noise due to houses located on the eastern side of the body.

The G-859AP Mineral Mag portable cesium vapour magnetometer used in the ground magnetic survey was a magnetometer for conducting total field magnetic (TMI) surveys. The standard settings of the magnetometer were used in the survey in question. They provided a low noise to high sensitivity ratio of 0.008nT/√Hz RMS, and a sample speed of three data points per second. Geometrics (n.d.) states that the magnetometer is the best in the industry for rejecting AC power line grid noise (50/60 Hz), which possibly reduces the indicated cultural noise from the power lines in the given study area. The integrated Novatel Smart V1^{TM} GPS saved the mapping positions automatically. After a day in the field the data could easily be transferred to the graphical editing program MagMap2000 where a simple gridded map automatically was drawn to get an indication of the progress made. Any unexpected anomalies could then be followed up on, and changes to the planned survey could be done.

The survey lines were run as parallel as possible to each other, however, the field area consisted of marsh, a lake, rivers, dense forest, some steep rocky areas, and private property including farmland, hindering the acquisition to be conducted in parallel lines. The line spacing for the survey was planned with 200m line spacing, but due to the obstructions described above, the lines became much wider than planned. Based on the previous mapping of the Ugelvik and Raudhaugene peridotite bodies, additional lines were conducted in the locations of these bodies.

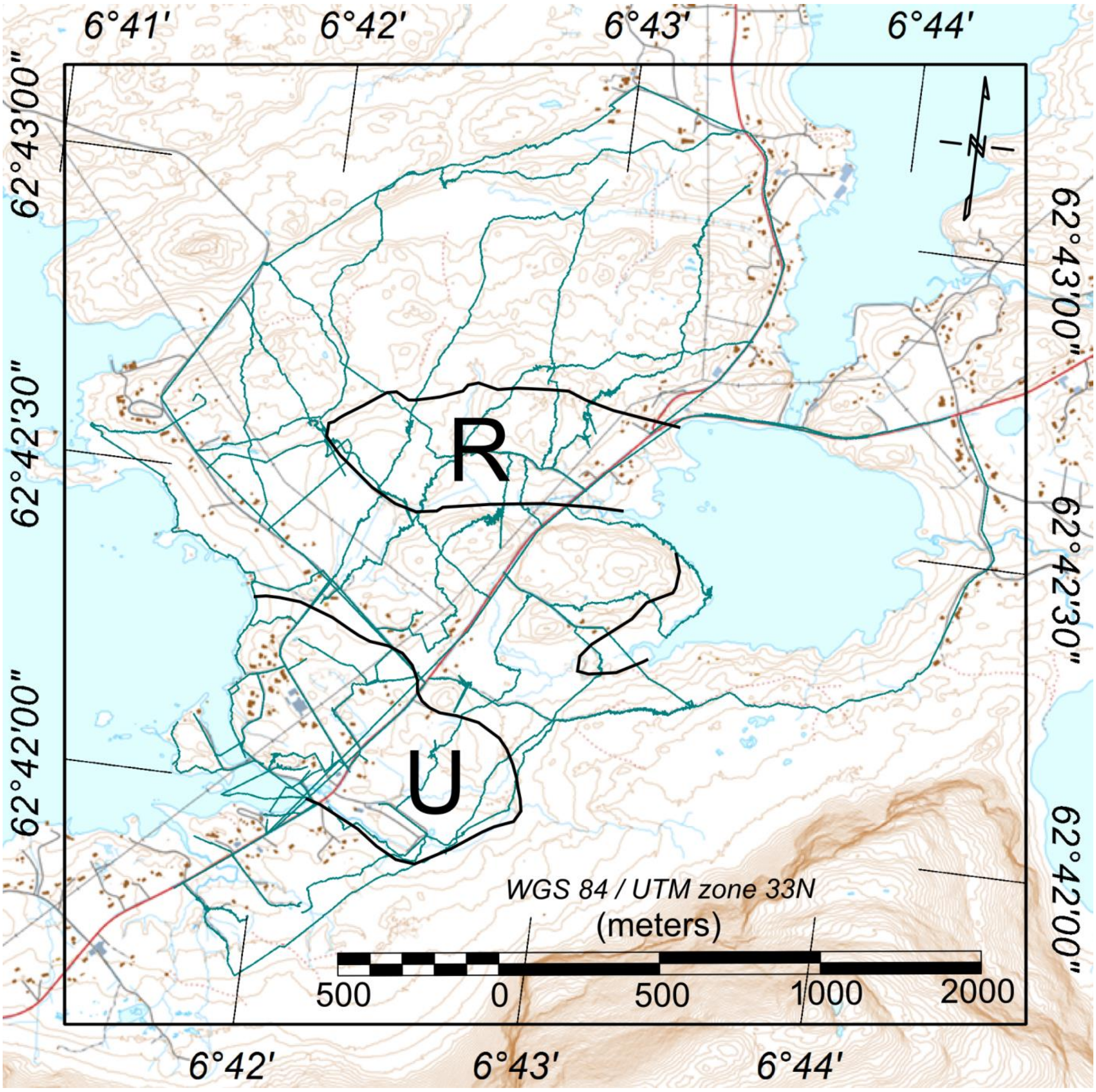

Figure 6.1-1: Topographic overlay map from NGU's database (n.d.) with the borders of the Ugelvik and Raudhaugene peridotite bodies indicated based on the structural geological map by Spengler (2006). The topographic map indicates potential sources for cultural noise; such as houses and power lines. Conducted ground magnetic lines are displayed as green solid lines.

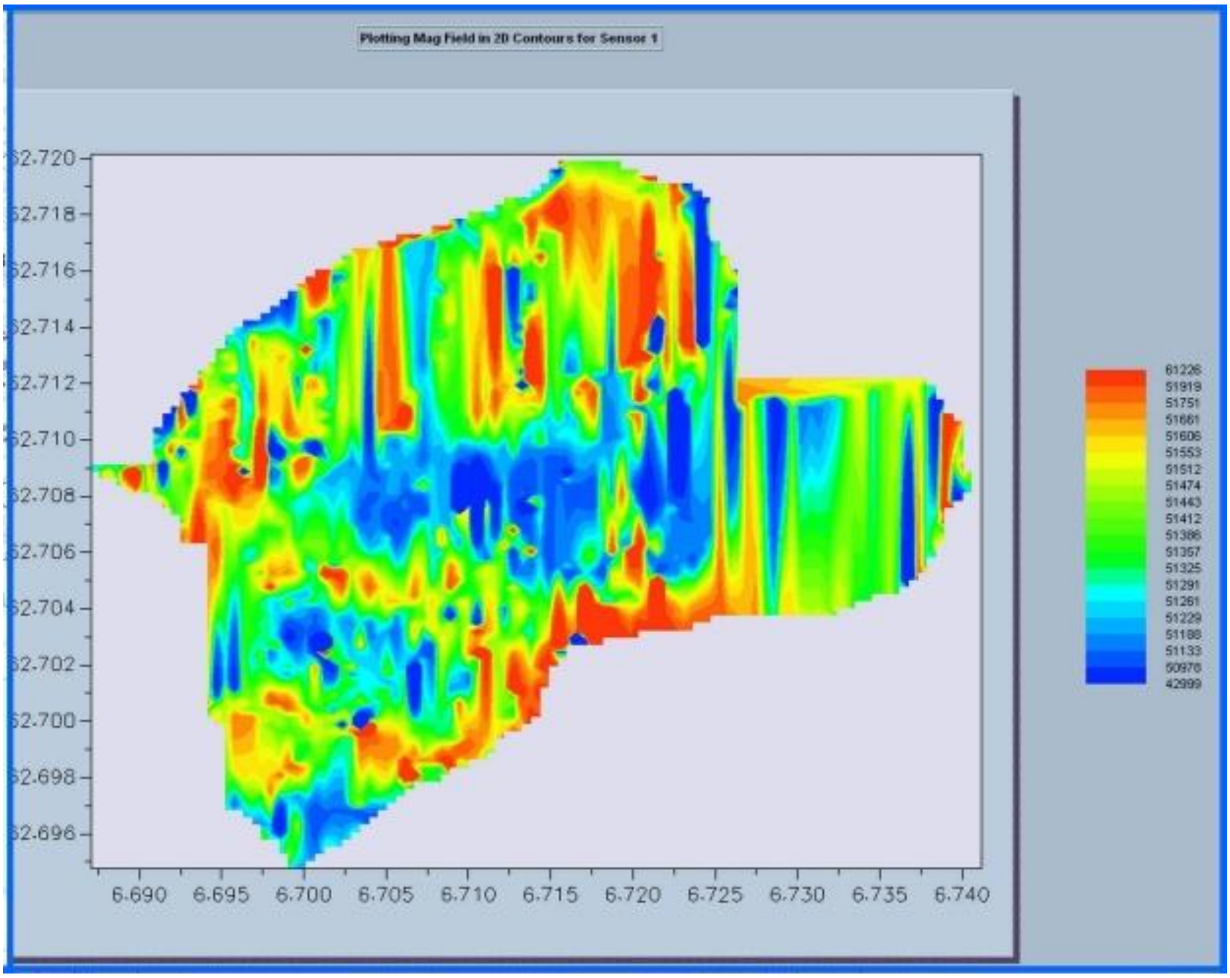

Figure 6.1-2: Gridded map was made using the MagMap2000 software and the TMI measured after conducting the ground magnetic survey at Otrøya.

Conducted lines are shown in Figure 6.1-1, showing lines predominantly going NE-SW, following the main road, and lines going normal to those, in a NW-SE direction.

After six days of magnetic surveying the resulting TMI map created by the MagMap2000 software indicated two wide anomaly lows, possibly created by the two garnetiferous peridotite bodies Ugelvik and Raudhaugene (Figure 6.1-2).

6.1.1 Susceptibility measurements conducted in the field area

The susceptibility of outcropping rocks were measured using a KT-6 Kappameter. The sensitivity of the instrument is of $1x10^{-5}$ SI units, with measuring ranges from -999 to $9999x10^{-3}$ SI units, and with operating frequency of 10 kHz (SatisGeo, s.r.o., n.d.). Susceptibility measurements were done both in areas where orientated block samples were taken, and in areas not represented by orientated block samples. Most of the measurements were done on the bedrocks, mostly consisting of gneisses, enclosing the Ugelvik and Raudhaugene peridotite bodies. The localities are indicated in Figure 6.1-3.

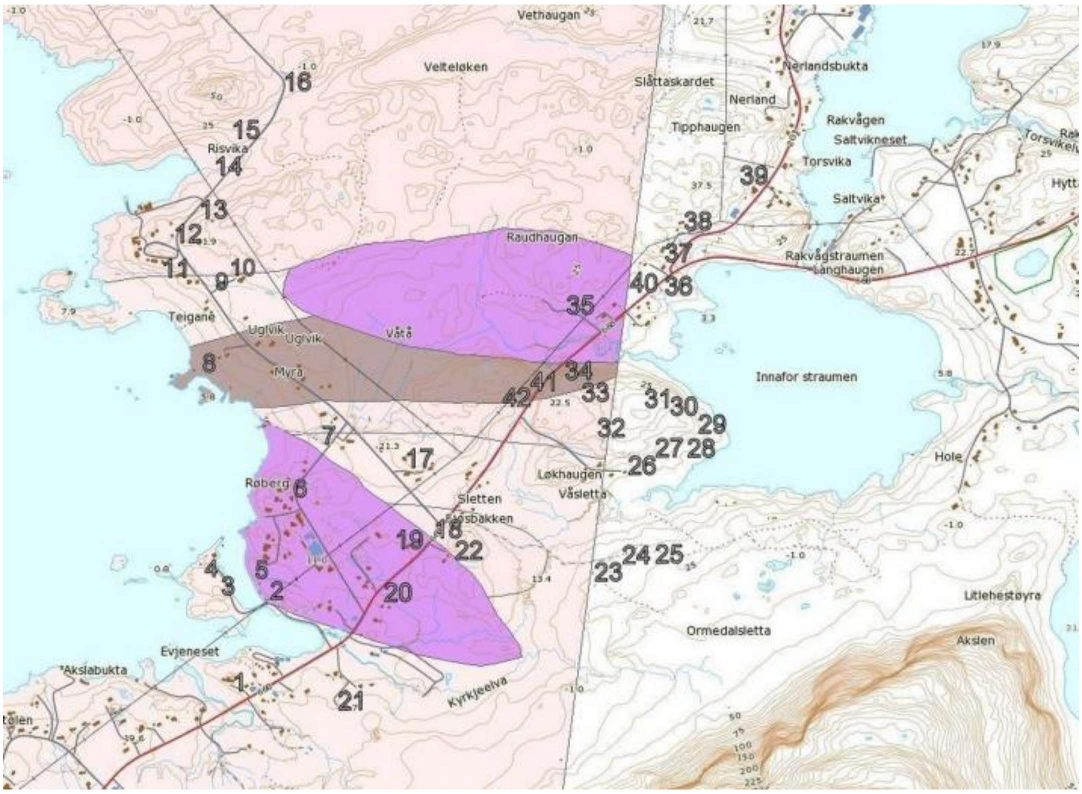

Figure 6.1-3: Susceptibilities measured in field. Locations are indicated by number. The map displayed consists of both the topographical map from NGU and N50 geological map collected from NGU's database.

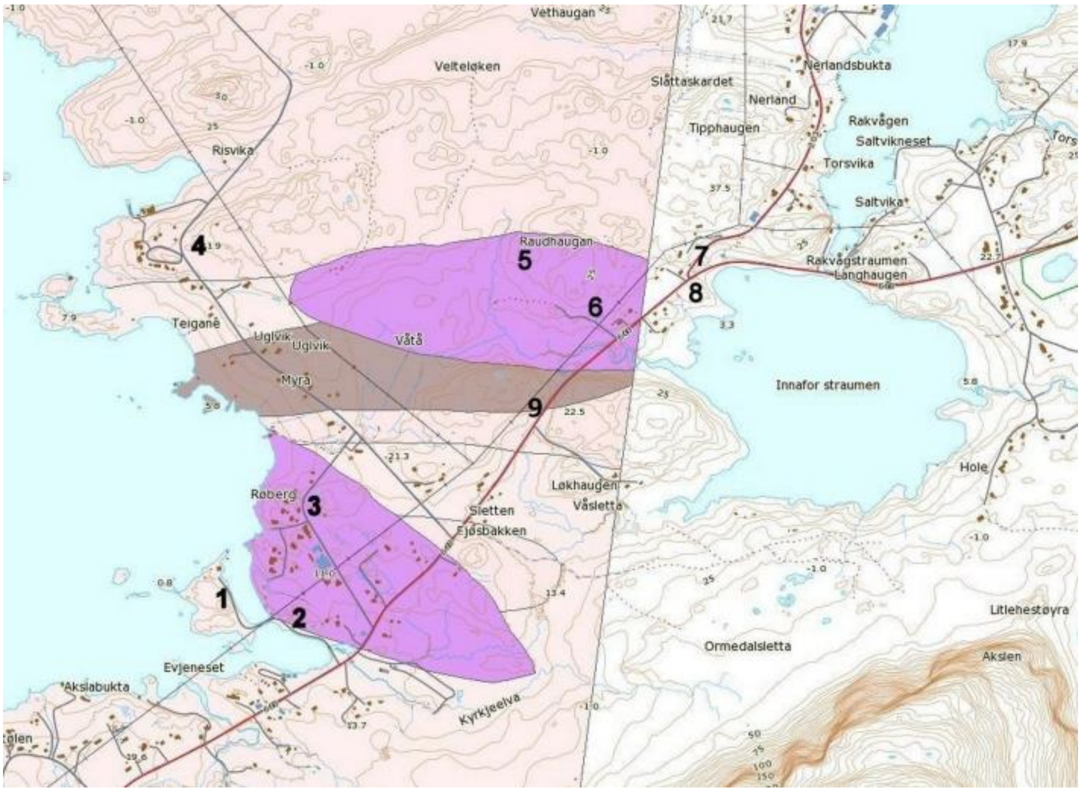

Figure 6.1-4: Locations where samples were collected. Locations are indicated by number. The map displayed consists of both the topographical map from NGU and N50 geological map collected from NGU's database.

6.1.2 Sampling procedures

The main objective of the sampling was to sample the two peridotite bodies; Ugelvik and Raudhaugene, located at Otrøya. Samples were also taken from the bedrocks, mostly consisting of gneisses. The annotation of localities and samples of the constricting bedrocks were for simplicity called “gneiss locations” and “gneiss samples”. Eleven samples, from four localities, were sampled from the gneisses, and twenty four samples, at five localities, were sampled from the two peridotite bodies. The samples collected in this study were oriented joint block samples. They were oriented by marking and determining the dip and dip direction of a surface, and then removed from the outcrop. For each site multiple samples were taken to allow within-site homogeneity of the magnetic properties to be evaluated.

The susceptibility of the samples was measured using the KT-6 Kappameter. If many samples within one locality displayed approximately the same values and were similar in mineralogy and weight, they were excluded from the study. Samples which were too small for further studies were also excluded. In all, seven of the gneiss samples and nineteen of the peridotite samples were chosen for further studies.

7 Laboratory work

7.1 Preparing of specimens

From each sample cores were drilled using a diamond drill bit with an inner diameter of one inch (25.4mm). Where possible, at least three cores were drilled from each sample. Every core was marked for orientation by the right hand rule. The specimens were prepared by cutting the cores into pieces with lengths between 19 and 21 mm. As many specimens as possible were obtained from each core. The specimens were marked with the same orientation as the origin sample. In all, 25 samples were drilled, each with at least 3 cores, except for one sample (4.2) where only one core was drilled due to little material. 251 specimens were cut from the cores. By cutting multiple specimens from a sample additional checks of homogeneity of the magnetic properties of the rock as well as check of experimental procedures can be obtained.

When the specimens were obtained the designation of name was based on [locality. sample-core.specimen]. E.g. specimen 2.1-3a is from locality 2, the first sample sampled at that locality, the third core drilled out from the sample, and “a” is the first specimen collected from that core. If a specimen was made including the top part of the core, the last letter assigned was T (top), e.g. 3.1-6T. If a specimen was made including the bottom part of the core, the last letter assigned was B (bottom), e.g. 2.5-3B.

Figure 7.1-1: core drilling of samples.

Figure 7.1-2: cutting of cores with brass blades.

Figure 7.1-3: cutting and re-cutting of cores into specimens.

7.2 Density measurements of specimens

Density was measured using two different scales. For the first measurements a weight (Figure 7.2-1), with two decimal places accuracy, was used, in addition to a measuring cylinder. The dry mass of the sample specimen was measured, and the weight of the specimen in water, “wet weight”, with a given volume, 30ml, was measured. The densities of 119 of 251 specimens were calculated using Formula 6. The volumes of the specimens were calculated using Formula 7.

Formula 6: $$\text{Density (g/cm3)} = \left(\frac{\text{Dry mass (g)}}{\text{Volume cylinder} - \text{Wet weight (g)} - \text{Dry mass (g)}}\right)$$

Formula 7: $$\text{Volume } (\text{cm}^3) = \left(\frac{\text{dry mass (g)}}{\text{density } \frac{(\text{g})}{\text{cm}^3}}\right)$$

The second measurements, using a weight and density scale, were done by Church, N. For these samples both dry mass, dry density, wet mass and wet density was obtained. Wet mass and wet density was measured by soaking the specimens for 24hours before measuring. By soaking the specimens any error on the volume calculation due to possible porosity, was limited.

For calculation of sample volumes of these specimens, formula 2 was used with wet mass and wet density as input. The measured dry density was assigned these samples. The additional measurements were primarily done to obtain density and volumes for specimens measured with the cryogenic magnetometer. At least one specimen within each sample group was, in addition, measured to check repeatability of specimen values. In total 153 of the 251 were measured densities for.

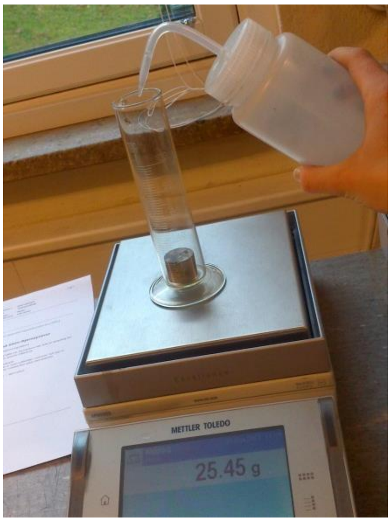

Figure 7.2-1: Density measurements.

Figure 7.2-2: Susceptibility bridge.

Figure 7.2-3: NRM JR-6 spinner magnetometer.

7.2.1 SI Susceptibility measurements of specimens

For measuring susceptibility a Sapphire Instruments susceptibility bridge (Figure 7.2-2) at the Norwegian University of Science (NTNU) was used. A known susceptibility value of a magnesium specimen with a known volume of 8 cm^3 was used to calibrate the machine. The drilled and cut sample specimens were measured, and the measured susceptibilities were corrected for volume. The machine registered the background value before and after each specimen was measured. In that way any drift would be recognised and could be corrected for.

7.3 Natural Remanent Magnetization (NRM) measurements of specimens

For measuring natural remanent magnetization (NRM) the rock specimens were measured using the JR-6A Spinner Magnetometer (Figure 7.2-3) at NGU. The specimens were placed in a shaft, which by rotation produced an oscillating magnetic field due to the rotating magnetic moment of the specimen (Butler, 2004).

An AC voltage was induced in the coils whose amplitude and phase was dependent on the magnitude and direction of the remanent vector of the specimen. The voltage was amplified, filtered and digitized. By Fourier analysis the computer calculated two rectangular components of the projection of the remanent vector into the plane perpendicular to the axis of rotation (Agico, 2004). Intensity, a best-fit direction of NRM in sample coordinates and in geographic coordinates, and error percentage was obtained.

Additional measurements of thirty one specimens were done using a 2 G cryogenic magnetometer at the University of Massachusetts (UMASS). These measurements were done due to: gluing of two fractured samples (4.1-1a & 4.1-1b) making them too big to measure on the Spinner Magnetometer at NGU, due to the need for more measurements on samples where few specimens were obtained, and to check for repeatability of NRM intensities and directions.

All samples both obtained by the Spinner Magnetometer at NGU and by the cryogenic magnetometer at UMASS, were normalised by volume obtained by Formula 7. For samples not measured for density, the average volume value within given sample group was assigned. Specimens with varying size, such as top or bottom pieces of the cores, were excluded from these calculations.

7.4 Display of NRM directions

Vector directions in geomagnetism are described in terms of inclination, *I*, (with respect to horizontal at the collecting location) and declination, *D*, (with respect to geographic north). To display the three-dimensional information on a two-dimensional page the equal-area projection plot was used with the software Stereonet 8 (Cardozo & Allmendinger, 2013). The equal-area projection was chosen because of its ability to show the amount of directional scatter in distributions of the NRM directions. Mean vector estimates based on the Fisher distribution were calculated for each locality, and for the Ugelvik body, the Raudhaugene body, and the surrounding gneisses, respectively, using Stereonet 8 (Allmendinger et al., 2012).

7.5 Optical microscopy of thin sections

25 polished thin sections, representing all of the sample locations within the area of study, were studied on oxide mineral content, e.g. study of magnetic mineral content. To a lesser extent, the overall mineral content and the degree of serpentinization were studied.

An optical microscope was used to look at thin sections and to identify the minerals in the samples. Transmitted and cross polarized light was used to identify the minerals depending on relief, colour, interference colour, cleavage and other unique properties. For additional identification of oxides their reflectivity and their colour in reflected light was studied.

Estimation of degree of serpentinization was done based mainly on identification of serpentine minerals by optical microscopy. Serpentinization leads to growth of mainly three types of serpentine minerals; lizardite, chrysotile, and antigorite. To distinguish between these three types of minerals their microstructures were studied.

Published books (MacKenzie, 1982; Marshall, 2004; Sørensen, 2013; Philpotts, 1989) and unpublished directions for microscopy classes were used to identify the different minerals in the thin sections.

7.6 SEM of thin sections

To further investigate the oxide mineralogy within the samples, a Scanning Electron Microscope (SEM) was used to perform backscatter electron microscopy. The thin sections studied were carbon coated before imaged. In backscatter electron imaging the electrons gets reflected or “backscattered” when interacting with the mineral atoms. Heavy elements will reflect more electrons than light elements. Heavy elements will therefore appear brighter than light elements.

For back scatter electron microscopy, nine thin sections, two from the Ugelvik body, four from the Raudhaugene body, and three from the enclosing gneisses were chosen. They were chosen based on observed oxide mineralogy in thin section and due to observed magnetic properties, mainly because they displayed NRM values above 1 or susceptibility values above 0.003, or both. A high NRM value could be diagnostic of SD sized magnetite, while a high susceptibility value could be diagnostic of MD sized magnetite. The investigation by SEM therefore gave additional information on whether these magnetite grain sizes were present in the samples, in addition to giving information on possible mineral phases other than magnetite contributing magnetically.

7.7 Vibrating Sample Magnetometer (VSM) measurements

To further investigate the magnetic properties obtained a Vibrating Sample Magnetometer (VSM) was used. Thirty seven specimens displaying high Q-values, and either high or low remanence and susceptibility values were prepared by breaking tiny leftover pieces (chips) from the cores. These chips were weighted prior to the measurements to make it possible to normalise the magnetic properties based on weight. The samples were fixed on a sample holder with silicone gel. A chiller was turned on to prevent overheating of the field coils. A computer with a VSM program was used to record the results. The sample holder was fastened in the apparatus and adjusted between two sets of coils so the machine records the best possible signal. The measurements of hysteresis loops were done to obtain the hysteresis properties of the samples: the saturation magnetization (M_s), the remanent magnetization (M_{rs}) and the coercivity (H_c). In addition was the remanent coercivity, H_{cr}, obtained.

After the measurements were finished some corrections for weight and paramagnetic features were made to make the M_s estimations more accurate. Further, the M_s, M_r and H_c values were normalised by weight for further comparison of values obtained from other samples.

Based on the shape of the hysteresis loops the samples were classified into magnetic properties displaying mostly paramagnetic, ferromagnetic, or a mixture of both properties. The hysteresis loops were also used to assign whether the samples displayed single domain or multi domain behaviour.

By plotting the obtained values for M_s, M_r, H_c and H_{cr} in a Day Plot the previous assignation of single domain or multi domain behaviour was investigated. The Day Plot made it, in addition, possible to assign pseudo-single domain behaviour to the samples, and comment on possible contribution from other magnetic minerals.

8 Processing, presentation of data, and modelling

This chapter gives an overview of the workflow and describes constraints and reasons as an introduction to the following chapters where all details are presented.

8.1 Processing of ground magnetic data

The Total Magnetic Intensity (TMI) measured while conducting the ground magnetic survey was exported into a Geosoft compatible xyz file using MagMap2000, and loaded into the modelling program Oasis montaj. The drop-outs (zero readings) were removed, and the lines were plotted based on their GPS coordinates. A grid, with a cell size of 1m, was gridded to get an initial impression of the quality of the data (Figure 8.1-1). Geological maps from NGU were integrated with the magnetic data by comparing the magnetic lines with roads and shorelines in the geological maps. Orthophotos with and without topographic contour lines from "Norge i bilder" (n.d.) were also integrated as described above.

8.1.1 Gridding of TMI data

The magnetic lines conducted in the ground magnetic survey was gridded to image possible anomalies created by the rocks within the mapped region. The data obtained in the survey did not have a dominant trend direction, but was mostly run normal or parallel to each other (see Figure 8.1-1). The survey was continues and provided data which were smooth between sample points, it was conducted with tie lines, and the lines conducted were recorded for height above sea level due to the GPS recordings.

Due to the lines being run normal to each other, and the data being smooth between sample points, the survey data were classified as non-parallel line data (geosoft, 2012b), and were therefore gridded with RANGRID by using minimum curvature. The RANGRID fits a minimum curvature surface to the data using a method similar to the methods described by Swain (1976) and Briggs (1974). The grid quality was controlled by using the default settings with tolerance of 1% of the data range, a percentage of 99% and the maximum iteration value set at 100.

The strengths of using RANGRID are many; it works with any number of data points in any location, the minimum curvature gridding does not impose a directional bias in the data, and tie line information will be included in the gridding process, properly levelling the survey lines (geosoft, 2012b). However, the weaknesses of minimum curvature gridding could be a "pimpling effect" in filtered products that enhance the high-frequency parts of data. The minimum curvature gridding can also introduce "bulls-eye" or "string-of-beads" effects for features that have a narrow width with respect to the survey line direction, due to the gridding not being able to strengthen trends perpendicular to the survey lines (geosoft, 2012b).

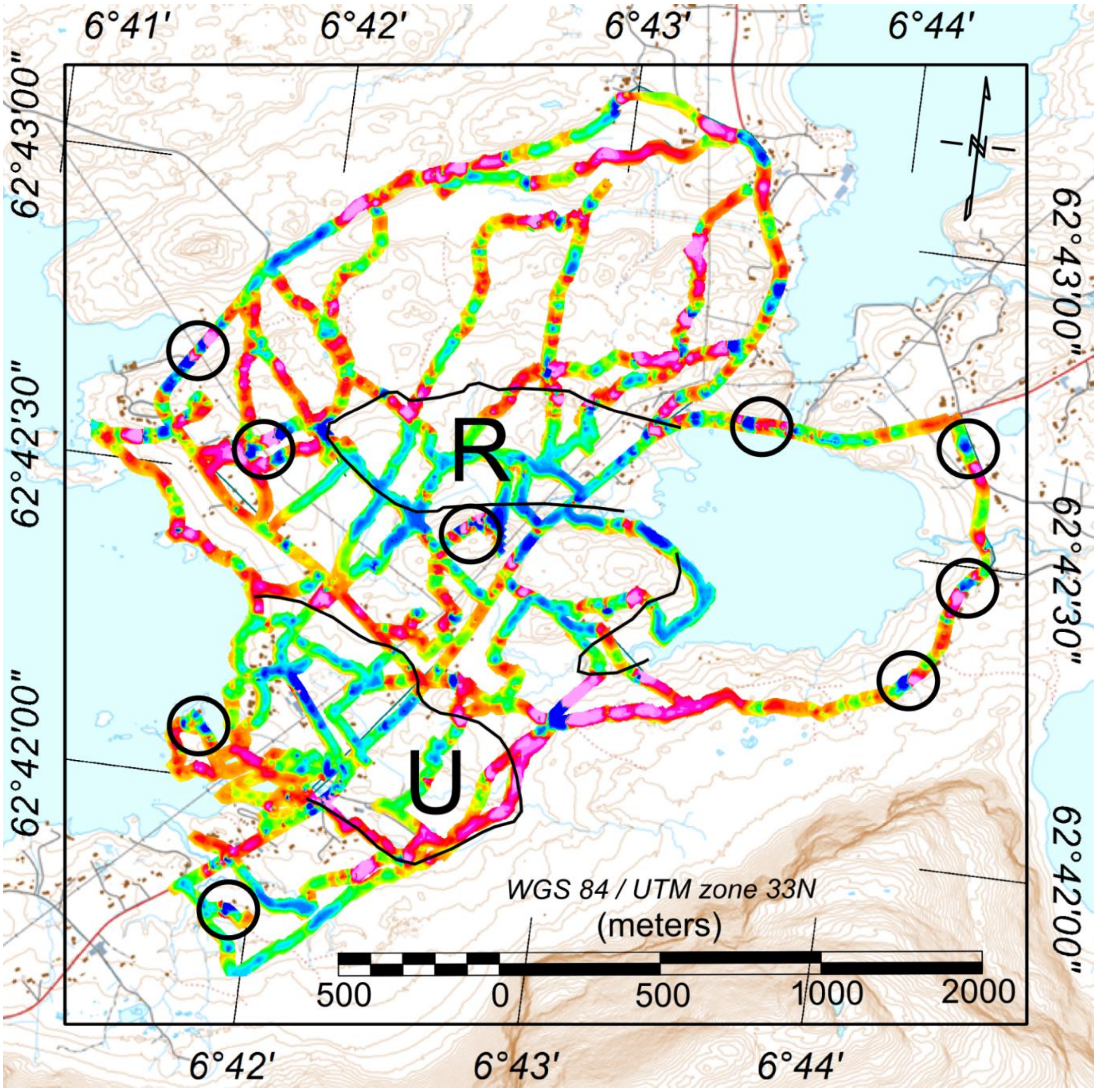

Figure 8.1-1: Topographic map from NGU's database showing contour lines, the study area at Otrøya, magnetic lines conducted with gridded data using gridding cell size of 1m and Minimum curvature gridding with RANGRID. U=Ugelvik body and R=Raudhaugene body. Circles indicates anoamlies possibly arrising from cultural noise or/and high frequency data creating the "pimpeling effect" – also indicated in Figure 8.1-3.

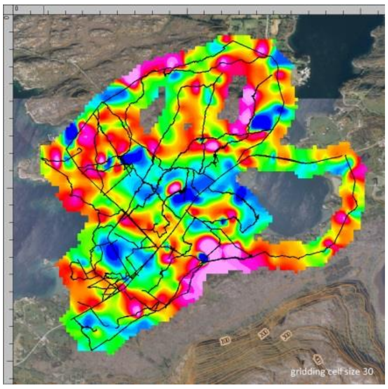

Figure 8.1-2: Grid cell size of 30m

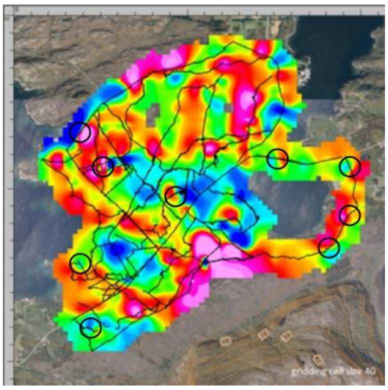

Figure 8.1-3: Grid cell size of 40m. Circles indicating possible cultural noise or/and the pimpeling effect.

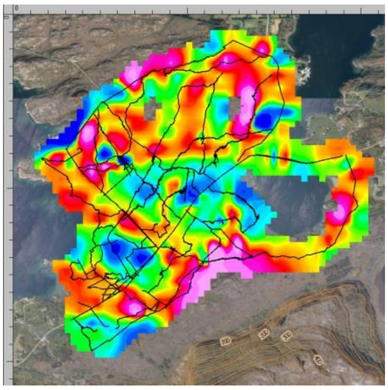

Figure 8.1-4: Grid cell size of 50m

Cell size was selected based on the minimum curvature gridding requiring a cell size not much less than half the nominal data point interval found in the areas of interest. The magnetic lines conducted had a spacing mostly ranging from 100m to 300m, with the narrowest being closest to the previously mapped outcrops of the Ugelvik and Raudhaugene peridotite bodies. There were, in addition, a few very close lines with line spacing as close as 10m, and some lines with wide line spacing, due to lakes or areas of very wet marsh. Based on line spacing of 100m or less in the areas of the previously mapped outcrops of the Ugelvik and Raudhaugene bodies, a grid cell size of 50m (Figure 8.1-4), 40m (Figure 8.1-3) and 30m (Figure 8.1-2) was applied.

By comparing the outcrops on the N250 geological map from NGU with the anomalies on the gridded anomaly maps, the cell size of 40m was selected for further work.

8.1.2 Filtering of TMI data

The resulting anomaly maps gridded with cell size of 1m (Figure 8.1-1) and 40m (Figure 8.1-3) both displayed some sharp anomalies, possibly arising from cultural noise or/and artefacts such as the “pimpling effect”. Based on these observations the data was low-pass filtered using the LOWPASS GX filter.

The LOWPASS GX filter smooth’s the input data by applying a convolution filter to the data (Fraser, 1966 as cited in geosoft, 2012a). The filter is called “low-pass” due to it allowing low frequency waves to pass to an assigned output channel. Wavelengths displaying shorter wavelengths than the cutoff wavelength are removed.

As shown in Figure 8.1-5, the data from a line conducted during the ground magnetic survey (in white), was applied several low-pass filters; A cutoff of 200m (grey) created a profile which followed the original data quite closely, a cutoff of 500m (green) was less affected by the small variations in the data compared with the previous, while a cutoff of 1000m (turquoise) created a profile with long wavelengths and less detail. By looking at gridded low-pass filtered data and their profiles, a cutoff wavelength of 500m was chosen. The resulting data was gridded with a cell size of 1m and 40m.

8.1.3 Cultural noise

The resulting anomaly maps provided after filtering and gridding with both 1m and 40m cell sizes were compared with previous observed possible sources of cultural noise. Based on these observations some lines were edited or removed due to anomalies coinciding with sources such as containers, parked cars or massive car fences. In Figure 8.1-6 examples of cultural noise removed from the dataset are shown, illustrated by; pictures of the objects creating the anomalies, the anomalies in profile view, and the anomalies as displayed on an anomaly map, gridded with 1m cell size, superimposed over a topographic map (NGU).

The resulting anomaly map created after filtering, editing and gridding with 40m cell size can be viewed in Figure 8.1-8.

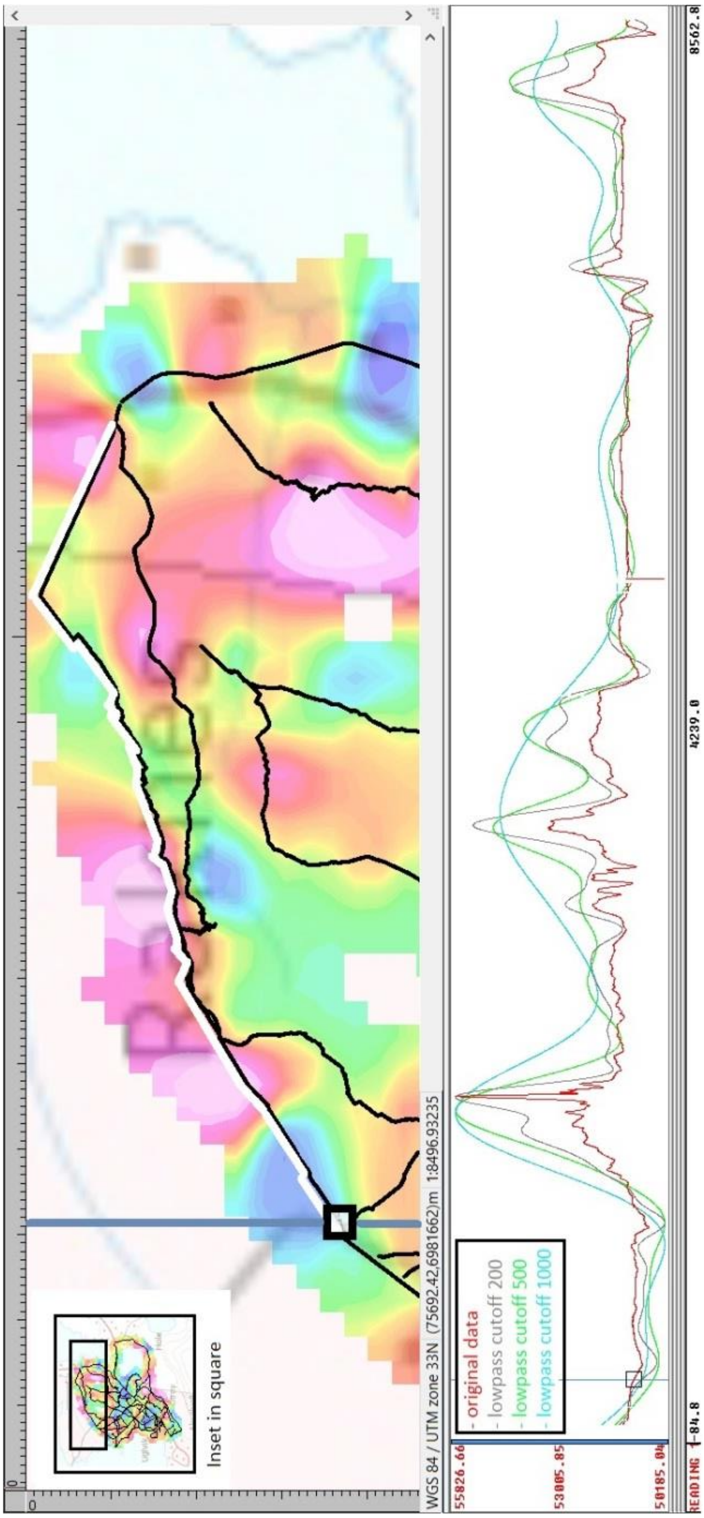

Figure 8.1-5: Left part display the line in question in white transposed onto a grid made by data low-pass filtered with a cutoff of 500m and a cell size of 40m. Right part display the original line data together with three lines created by applying a low-pass filter; grey: 200m cutoff, green: 500m cutoff, turquoise: 1000m cutoff.

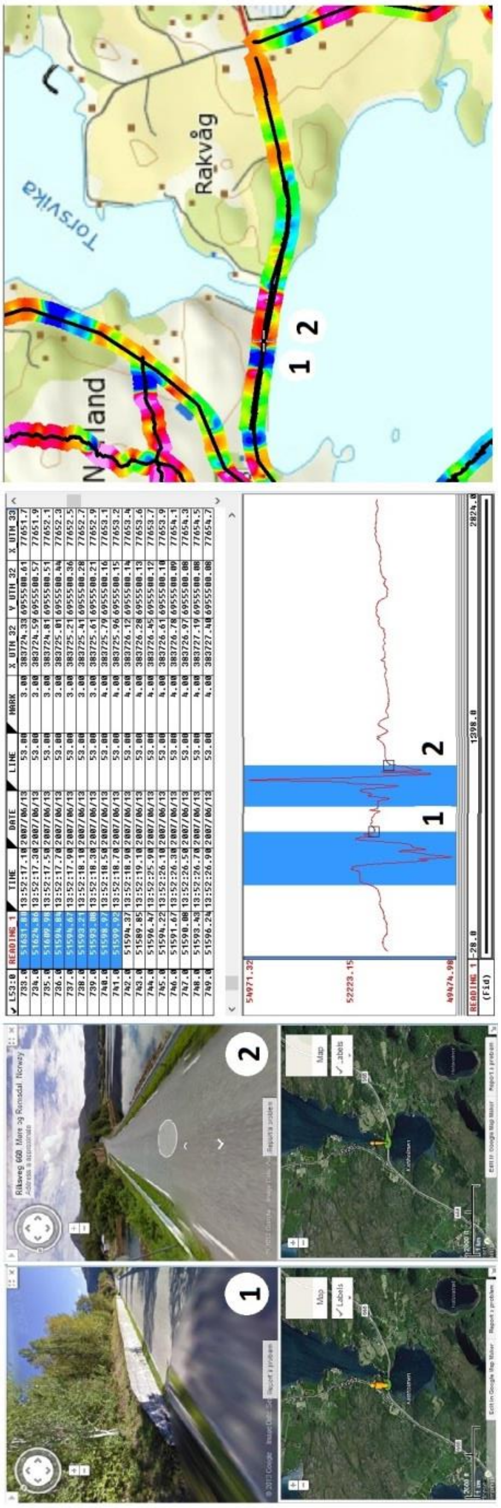

Figure 8.1-6: From bottom up; pictures and positions of two anomalies created by cultural noise, pictures taken from google earth, profile with the two anomalies highlighted in blue, and the positions of the two anomalies on the raw data line gridded with a cell size of 1m.

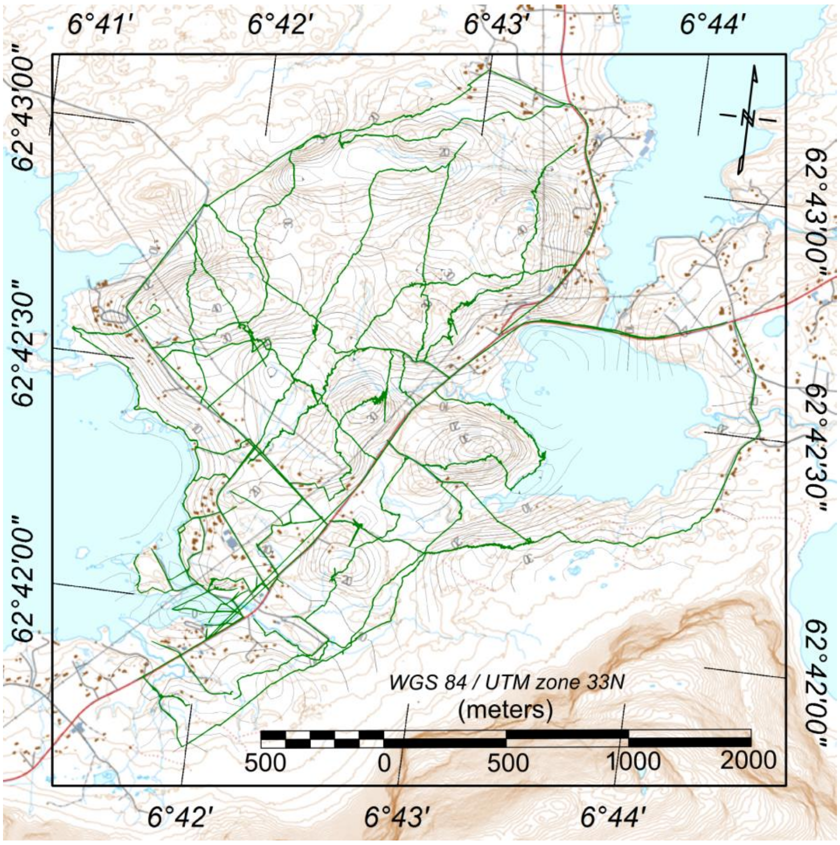

Figure 8.1-7: Topographic contour lines made from gridded GPS height recorded data (gray lines)transposed over a topographic map over the field area (taken from NGU's database). Green lines=magnetic lines.

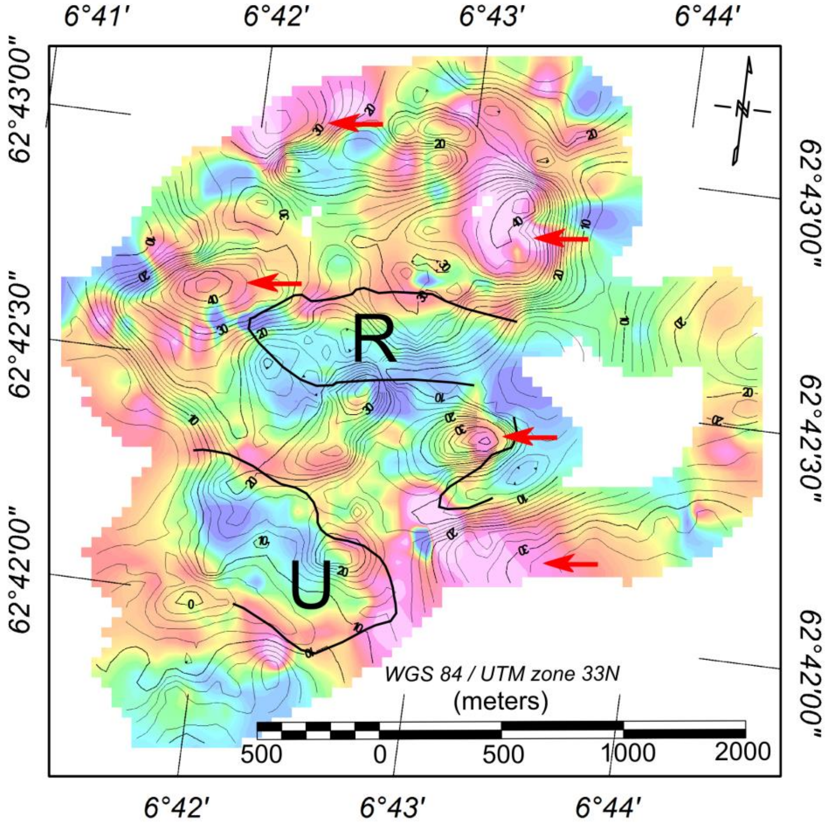

Figure 8.1-8: Topographic contour lines made from gridded GPS height recorded data transposed over gridded TMI data with 60% transparancy. R=Raudhaugene body and U=Ugelvik body. Red arrows indicate corrolation with topographically higher areas and gneiss lithology.

8.1.4 Quality control - topography

The validity of the resulting anomaly map is naturally subject to how well the actual observed field conforms to the assumptions and corrections described above. One assumption was that the topography from the GPS recordings was correct. To control whether the GPS recorded a height similar to the topography within the topographic map from NGU's database, a grid of the GPS recorded height data was gridded using geosoft's minimum curvature gridding and a grid cell size of 40m. Topographic contour lines made from the gridded map were superimposed the topographic map (Figure 8.1-7). The resulting topographic contour lines were not exactly equal to the topography map, but coincided mostly. The difference was the largest at areas with large line spacing, where the GPS contour lines differed up to 200m from the topographic contour lines. However, due to the peridotites being the focal point of the study, and these bodies being in areas with narrow line spacing, the topographic data from the survey was considered as well enough for the study in question.

By comparing the topography with the gridded TMI data a check of topographic influence indicated some apparent correlation (Figure 8.1-8). However, the survey was done over two types of rock with expected differences in magnetic properties. Where the gneisses are expected to display high susceptibility values, the peridotites are expected to display low susceptibility values. Additionally, due to the rocks' difference in mineralogy, these rocks weather quite differently. Since the peridotites easily weather, while the enclosing gneisses are competent rocks, the topography will reflect the position of these rock types, as well as magnetic response. Therefore, some correlation between rock type and topography was expected. This is indicated in Figure 8.1-8 by red arrows indicating anomaly highs coinciding with gneiss lithology and anomaly lows within the borders of the two outcropping peridotite bodies.

8.2 Display of susceptibility-, NRM intensity- and density data

Susceptibility data were collected both in the field, and by measuring the specimens made from the collected samples from the field area. The susceptibility field data were assigned UTM zone 33N coordinates by comparing coordinates from pictures of measuring localities and field notes, with orthophotos from the internet map database “Norge i bilder” (n.d.). An average of all the susceptibility field measurements for each locality was calculated. The susceptibility field values and their respective coordinates were loaded into Oasis montaj as a text (txt) file through the import database, Ascii, option.

The susceptibility, NRM and density data obtained from the specimens were all given an average value for each sample and sample locality they originated from. The sample positions and sample localities were assigned UTM zone 33N coordinates based on field notes and field map notations, and loaded into Oasis Montaj by the same method as described for the susceptibility field data.

Displayed data can be shown in e.g. Figure 11.1-1, Figure 11.1-2 and Figure 11.1-3.

8.3 2D modelling

Based on the structural interpretations done by Spengler (2006), the structural geology map of Spengler and Haker (2006) and the N250 map (NGU, n.d.), several geological models were made and compared with the magnetic response from the TMI survey. The position of the bodies at the surface was based on the geological map modified from N250 (NGU, n.d.), and the structural data collected by Spengler (2006) was used as basis for their position at depth. The rock types modelled were gneiss and peridotite. Their magnetic properties were assigned based on susceptibility field measurements and the susceptibility data obtained from rock specimens.

Mainly one structural model of how the Ugelvik and Raudhaugene peridotite bodies extend at depth was investigated. This model was proposed by Spengler (2006) and was of the two bodies linking at depth forming a tight synformal structure. However, another model proposed by Spengler was of the bodies representing two boudins. This model has to a lesser extent been investigated. The difference in lithologies within the constricting bedrocks has not been investigated in this 2D modelling. The constricting bedrocks have to a large degree been treated as an isotropic rock body named “gneiss”.

8.3.1 Structural constraints

The profile was chosen based on the structural constraints given by Spengler (2006). The first constrain was the inferred fold axis of the interpreted synfold, plunging 115 degrees south, with a plunge of 38 degrees. A profile investigating a synformal shape should be run normal to this strike, thus 25 degrees north.

Secondly, the structural interpretations of Spengler (2006), showed that the two peridotite bodies could be divided into several sub-domains. The Ugelvik body can be divided into a western and eastern side, while the Raudhaugene body can be divided into an upper western, lower western, central, upper eastern and lower eastern side. For a model based on a simple cylindrical synformal structure, the flanks would show similar strike. Based on the structural data within Spengler (2006), the Ugelvik eastern and Raudhaugene central part appears to approximately coincide regarding strike of internal layering.

Spengler (2006) also interpreted the angle of the interpreted synformal fold to be of 60-65 degrees. Additionally, his structural data indicated that the layers of the eastern sub-domain of Ugelvik were dipping approximately 40 degrees NE. The structural data of the central Raudhaugene body was more complex, but most of the layers seemed to dip approximately 80 degrees. Though, Spengler (2006) interpreted the synformal structure to be of a non-cylindrical synform – simple 2D modelling needs a simple model. Thus, based on the structural interpretations of Spengler (2006), a model of a simple synformal fold forming an angle of 60 degrees, with the southern flank (Ugelvik body) dipping 40 degrees north and the northern flank (Raudhaugene body) dipping 80 degrees south, was investigated.

Based on the inferred axial plunge direction of the interpreted simple cylindrical synform, and the divisions of the bodies into several sub-domains, a profile for 2D modelling (A-A’ in Figure 8.3-1) was chosen to run through the Eastern sub-domain of the Ugelvik body and central sub-domain of the Raudhaugene body, approximately 5 degrees north. The 20 degree difference, from the normal of the strike of the interpreted simple synform (25 degrees), was due to constraints from structural sub-domains.

For the investigation of the model of Ugelvik and Raudhaugene bodies forming two boudins, the inferred axial plunge direction was of no importance. Though, the structural data and the position of the outcropping bodies were still holding as constraints on how the boudins would extend at depth. Due to this, and due to comparison of the two main models, the modelling of two boudins was conducted using the same profile as for the synformal model.

8.3.2 Constraints on position of bodies

The position of the two bodies was constrained by using the geological maps N250 (NGU, n.d.) and maps within Spengler (2006). Both the TMI data and the N250 geological map (NGU, n.d.) was imaged using WGS 84 UTM 33N zonation. Due to this, the N250 map was used as base for positioning for both the Ugelvik and Raudhaugene bodies within the profile (Figure 8.3-1). The structural geological map of Spengler and Haker (2006) was used for comparison.

8.3.3 Constraints for magnetic properties

Due to the peridotites being the focal point in this study, the main models were divided into two rock types: gneiss and peridotite. The two rock types were initially assigned magnetic properties based on the average of the calculated average field and specimen susceptibility of gneiss (approximately 0.02 SI) and the average of the average susceptibility value of the Ugelvik and Raudhaugene peridotite bodies (approximately 0.0015 SI). For simplicity, and for the objective of the modelling, in addition to literature stating that peridotites inhabit small or negligible amounts of remanence, remanence was not taken into account when modelling was proceeded. Furthermore, the anomaly response from changing the susceptibility values of the peridotite and gneiss was investigated.

Information about the Earth’s magnetic field at location was assigned based on the IGRF WMM2010 model for the Molde region (Declination: 0.65, inclination: 74.30 and Total Field: 51536 nT).

The modelling was done in Oasis Montaj, using the GM-SYS Profile Modelling extension. The profile data were imported into GM-SYS by defining the profile line in the gridded TMI survey map. Elevation for data points and topography was given by gridded GPS heights recorded during the TMI survey.

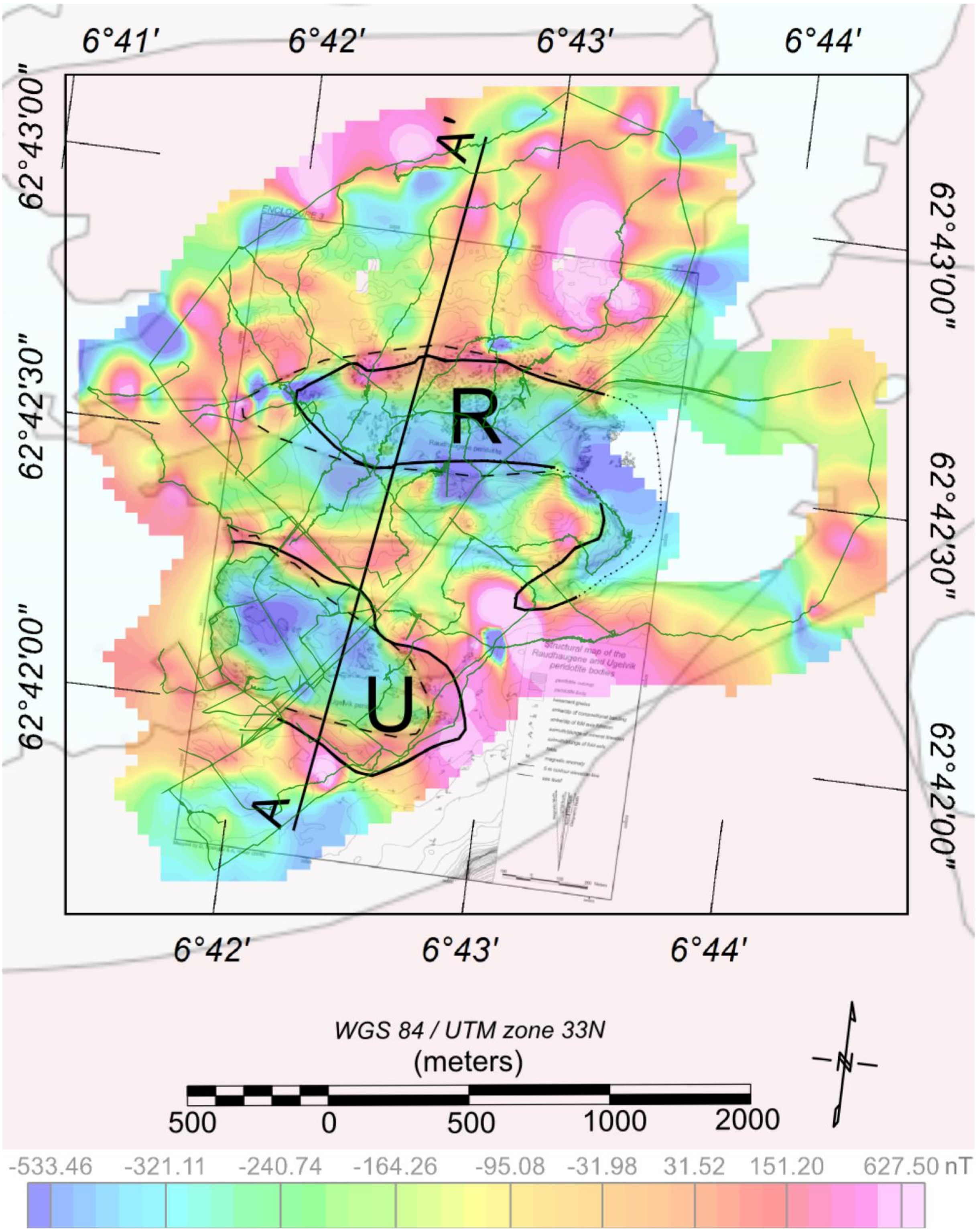

Figure 8.3-1: Position of the Ugelvik and Raudhaugene bodies given by the N250 map of NGU (n.d) in stipled black line, and by Spengler and Haker (2006) in solid black line. The model profile, A-A', is displayed as a solid black line running approximately 5 degrees north. Green lines=magnetic lines.

9 Restrictions and sources for errors

9.1 Ground magnetic surveying

Due to instrumental restrictions there was no possible way to control the quality of the GPS readings saved to the data points while conducting the ground magnetic survey. It was not possible to see how many satellites provided signals, or if the GPS data were saved. Sources for cultural noise were observed, and written down in the field notes. Due to the survey being conducted by only one person in addition of being continuous, this was difficult. Due to safety issues regarding only one person conducting the survey, a phone was carried at all times. This could impose some systematic error. To control for systematic error the magnetometer was used to read the magnetic field with and without equipment in the beginning of every survey day, approximately at the same spot. The difference from readings with and without equipment was at its most 10nT, but was commonly only differing with 2nT above the “measured without equipment” value. This is only a minor amplitude compared with the total magnetic field range.

9.2 Susceptibility measurements conducted in the field area

When using a KT-6 Kappameter to measure the susceptibility of a rock surface, an ideal surface for measuring is completely flat. Most of the sampled surfaces had some irregularities. The smoothest surfaces were of the gneisses, whilst the peridotites were more irregular, especially those with well-developed garnets or pyroxene layers. This could impose a possible source for error making the measured susceptibility value lower than the real susceptibility value of the measured rock. However, by comparing the average field value with the average sample specimen value for the same location, no apparent difference was observed (see chapter 11.1.1 and 11.1.2).

9.3 Sampling procedures and preparation of specimens

When sampling orientated joint block samples, limited accuracy of orientation is commonly common due to rough surfaces. The joint blocks sampled in this study were probably more weathered than the massive portions of the outcrops, limiting accuracy of orientations and possibly impose a source of error. Error due to sampling of joint block samples was evaluated to probably occur for the peridotites, and to a less extent occur for the gneisses. When the samples were drilled there was no ideal way of levelling the orientated surface of the samples. For each sample the surface was approximately levelled by using wood pieces, fastened by four metal staffs, and screwed into position. Due to the approximate way of levelling the samples an additional source for error on orientation is possible. When the cores were cut, sixty four specimens were cut using a cutter with bras blades. When heated these blades expanded and the surfaces became antiparallel. The specimens were therefore re-cut with a diamond saw, together with the rest of the cores not previously cut into specimens. The blade of the diamond saw could, but not likely, introduce some error by contaminating the samples with magnetic particles.

9.4 Density and volumes of specimens

When measuring density for the specimens, the method for measuring using a weight and a cylinder were conducted using a measuring cylinder which was slightly too large. This could reduce the accuracy of the filled volume, imposing an error of accuracy on the measured values. The specimens could in addition contain porosity. To account for the possible source of error of porosity the samples could have been soaked for 24 hours before measuring “wet weight”. In addition, only 153 of the 251 specimens were measured for density. Specimens that were not measured were assigned the average density from its respective sample. If the specimens with assigned density in reality differed much from the assigned density, this could be a possible error. Based on these possible errors, the volume estimation could be somewhat inaccurate, hence the volume corrected NRM and susceptibility values could be slightly wrong. A volume calculation with either too small or too big volume would give a volume corrected NRM or susceptibility value, respectively too big or too small compared with real value.

9.5 Optical microscopy of thin sections

The author’s lack of experience when identifying minerals by optical microscopy could impose a source of error regarding misinterpretation of minerals. In addition, estimation of degree of serpentinization through optical microscopy is highly biased, and the thin sections could be non-representative of its respective sample.

9.6 NRM and VSM measurements

The specimen holder for the JR-6A Spinner Magnetometer at NGU, used for measuring the NRM of the specimens, was too small diameter wise, resulting in the specimens not fitting in the holder. The holder was therefore widened by polishing. This treatment could possibly make the holder somewhat unstable, imposing a possible source for error.

The tiny chips used for hysteresis property measurements could be non-representative of its respective sample, hence possibly displaying misleading values. To correct for this, measurements of several chips from each specimen could be conducted to look for variability.

9.7 Processing and modelling

Due to the author’s lack of experience and knowledge regarding processing and modelling of magnetic data the methods described and used are chosen based on the recommendations from the geosoft guides (geosoft 2012a & b). Other methods for processing the data, resulting in better anomaly maps, could exist, creating an anomaly map more representative of the rocks within the field area.

The GM-SYS Profile Modelling extension was, in the author’s opinion, difficult to work in. The author could not find an application for controlling dips on the structures drawn. In addition, the freedom of modelling was restricted due to rock body construction through linking to the surface. This made the freedom of moving bodies around quite constricted.

With the possibility of “unconnected” bodies more models would have been made. A lot of time was, in addition, used on changing the rock properties for each and every drawn rock body. If there had been a possibility to define standard rock types a lot of time would have been saved. All in all, the author’s opinion of the program was that it was inflexible and tedious to work in.

Due to the restrictions mentioned the geometries of the modelled rock bodies were constructed using as few data points as possible, with the aim of having better control on dip and shape on models. The aim of the modelling was to investigate how differences in geometries and susceptibilities control the shape of the magnetic anomalies. More points would have provided more geological geometries of the models. However, more points could weaken the geometry- and dip control of the models, thus, the shape of the magnetic anomalies created by the various models could be due to uncontrolled geometry changes. The resulting geometries of the models are therefore constructed with few data points, and are of simple geometries containing sharp angles and flat bottoms, which are uncommon geologically (see chapter 15).

10 Magnetic minerals

The N250 geological map (NGU, n.d.) was used as main framework for lithological description of rock samples. This map displayed peridotite, and surrounding bedrock consisting of amphibolite (Amph) and two divisions of gneiss rocks. The first gneiss was defined as a coarse grained granitic gneiss, augen gneiss and gneiss-granite (GA-G), and the other was defined with a more general gneiss classification mostly consisting of quartz-dioritic to granitic gneiss, and to a less extent migmatitic gneiss (QDGM-G). The rocks sampled from the peridotites were subdivided by composition based on the detailed mapping by Spengler (2006). These subdivisions were spinel-harzburgite/dunite (Spl-P), Garnet-harzburgite/dunite (Grt-P), Cpx-Grt-harzburgite/dunite (Cpx-Grt-P), and banded peridotite (B-P). The identified mineral composition for both the peridotites and the surrounding bedrocks can be viewed in

Table 10.1-1. For further nomenclature they are, for simplicity, often referred to as gneisses even though one location is defined as amphibolite in the N250 geological map.

10.1 Optical microscopy of thin sections from the Ugelvik and Raudhaugene peridotite bodies

The peridotite samples from Otrøya displayed considerable variation in mineral content, and variation in estimated degree of serpentinization. Within the Ugelvik body the estimated degree of serpentinization showed an average of 15% for sample locality 2 and above 40% for locality 3. Within the Raudhaugene body, the estimated average degree of serpentinization was, for sample locality 5 of 40%, above 65% for sample locality 6, and above 90% serpentinization for sample locality 8. The samples with estimated high degree of serpentinization showed only small remnants of primary minerals. Samples with estimated low degree of serpentinization displayed most of their primary minerals with surrounding serpentine minerals which had altered some of the original mineralogy.

10.1.1 Major porphyroclasts

The major porphyroclasts identified in thin sections were, as reported by Spengler (2006), of olivine, garnet and Cr-spinel. Porphyroclasts of orthopyroxene and clinopyroxene were also reported by Spengler, but not identified in this study. Of these minerals Cr-spinel was the only mineral known to possibly give a slight contribution to remanence, and was therefore the only magnetic mineral amongst the reported major porphyroclasts.

In this study, olivine displayed high relief, pale pastel colours, and interference colours up to third order. Its crystals looked subhedral and appeared altered around the edge. The olivine varied in abundance according to variation in serpentinization. Garnet displayed high relief, pale pink colours and interference colours in dark grey or dark brownish grey to black. It appeared isotropic and subhedral. In some thin sections a fibrous reaction rim was observed as a fibrous circle around the garnet (Figure 10.1-5). Reaction rims have previously been described by Spengler (2006) as kelyphtic reaction rims occurring where garnets are in contact with olivine matrix.

Table 10.1-1: Identification of minerals in thin section. Mapped definitions for the peridotites are based on the mapped petrology by Spengler (2006); spinel-harzburgite/dunite (Spl-P), Garnet-hazburgite/dunite (Grt-P), Cpx-Grt-hazburgite/dunite (Cpx-Grt-P), and banded peridotite (B-P). Mapped definitions for the surrounding bedrocks are based on the geological map N250 (NGU, n.d.); Amphibolite (Amph), coarse grained granitic gneiss, augen gneiss and gneiss-granite (GA-G), and quartz-dioritic to granitic gneiss, and to a minor extent migmatitic gneiss (QDGM-G). The minerals found in the bedrocks were; Garnet (Grt), Plagioclase (Pl), Orthoclase (Or), Quartz (Qtz), Biotite (Bt), Hornblende (Hbl), Pyrite (Py), Magnetite (Mag), Ilmenite (Ilm), and hematite (Hem). The minerals found in the Peridotites were; Garnet (Grt), Olivine (Ol), Chromium Spinel (Cr-Spl), Rutile (Rt), Chl (Chlorite), Pyrite (Py), Magnetite (Mag), and Serpentinite (Serp). An estimation of serpentinization (% serp) is indicated. Sample 6.9 was sampled by McEnroe, S. A. and mapped definition for this sample was therefore unknown (unkn.).

Thin section data											
Surrounding bedrocks		**Mineral content**									
Thin section	Mapped def.	Grt	Pl/Or	Qtz	Rt	Bt	Py	Mag	Ilm	Hem	Hbl
1.1	QDGM-G	x	x	x		x	x	x	x		x
4.2	GA-G		x	x	x			x	x		
7.1	GA-G	x		x		x		x	x	x	x
7.4	GA-G			x		x		x	x	x	x
9.1	Amph	x	x	x		x		x	x	x	
Peridotite		**Mineral content**									
Thin section	Mapped def.	Grt	Ol	Cr-Spl	Rt	Chl	Py	Mag	Serp	% serp.	% serp. avg.
2.1	B-P	x	x		x	x	x	x	x	20	
2.2-1c	B-P		x					x	x	20	
2.2-3a	B-P		x	x	x	x	x	x	x	20	
2.4	Grt-P	x	x	x				x	x	10	
2.5	Grt-P	x		x		x		x	x	<10	15
3.1	Spl-P		x	x		x		x	x	50	
3.2	Spl-P	x	x	x	x	x		x	x	40	
3.3	Cpx-Grt-P		x		x			x	x	60	
3.4	Cpx-Grt-P	x	x					x	x	20	>40
5.1	Grt-P	x	x		x			x	x	50	
5.2	Cpx-Grt-P	x	x	x	x			x	x	50	
5.3	Grt-P	x	x		x	x		x	x	20	40
6.1	Spl-P	x	x	x				x	x	80	
6.2	Spl-P	altered		x	x	x		x	x	>90	
6.3	Spl-P		x	x		x		x		60	
6.6	Spl-P	x	x	x	x	x		x	x	50	
6.9	unkn.	x	x		x			x	x	50	>65
8.1	Grt-P	altered	x	x	x	x		x	x	90	
8.2	Spl-P	altered		x	x	x		x	x	>90	
8.3	Spl-P	altered		x				x	x	>90	>90

Spengler (2006) identified the kelyptic reaction rim to contain garnet, spinel and clinopyroxene. The major porphyroclast of Cr-spinel, in this study, appeared opaque to dark brownish with a bright metallic slightly grey-bluish lustre in reflected light. Additionally, it appeared massive with no internal structures. As observed by Oud (2010) the Cr-spinels were often observed close to garnets or within it, indicating being a reaction product due to breakdown of garnet.

10.1.2 Minor porphyroclasts and matrix minerals

Most of the matrix within the thin sections from the Ugelvik and Raudhaugene peridotite bodies was identified as serpentine, or altered (serpentinized) earlier minerals. The minor porphyroclasts recognised in the thin sections were chlorite, rutile and magnetite. Of these minor porphyroclasts magnetite was the only known magnetic mineral.

Serpentine displayed low relief, was colourless, and displayed interference colours in first order bluish-grey. It occurred as a mesh within the rock and as fibrous crystals in veins and fractures where it seemed to have intruded into the other minerals and pushed them apart. Chlorite displayed medium relief, pale yellow colours and first order interference colours. The crystals appeared flake-like. Rutile displayed high relief, dark red/brown colours, and seemed black in plane cross-polarized light, though with some red-brownish hint. In reflected light it displayed medium grey with red brown internal reflection. It looked anhedral, and displayed some exsolution. Magnetite was opaque and displayed a bright white metallic lustre in reflected light. It appeared massive with no internal structures. The magnetite was mainly observed as small veins, or as rims around Cr-spinel, but also as rounded, or irregular grains often with a dendritic shape. Small magnetite grains appeared in reflected light as a “starry sky” appearance within the light-grey mesh of serpentine.

10.1.3 Magnetic minerals and serpentines at each peridotite location

The thin sections from location 2 (Ugelvik) inhabited a lot of unaltered olivine. This was reflected in the low degree of serpentinization (15%). The serpentine present were fibrous and displayed an hourglass structure. The observed magnetite appeared as small pieces of pseudomorphed olivine grains, with sizes of approximately 40µm in diameter (D). Some, but few, were observed in the mesh as small grains (D<1 µm) (Figure 10.1-1). Cr-spinel was observed with a diameter above 30 µm. Some Cr-Spinels displayed reaction rims of magnetite (Figure 10.1-2).

Location 3 (Ugelvik north-west) appeared more serpentinized (>40%). The serpentinite was observed as through going seams in the primary minerals, as large veins going through the whole length of the thin section, and as the mesh making up the majority of the matrix (Figure 10.1-3). The little, but observed magnetite were mostly of small grains (D<1 µm) within, or as seams running next to altered primary minerals. A few grains were as big as 60 µm in diameter. These were all in the mesh, or appeared as small pieces of possibly pseudomorphed olivine. No magnetite was observed within the large veins.

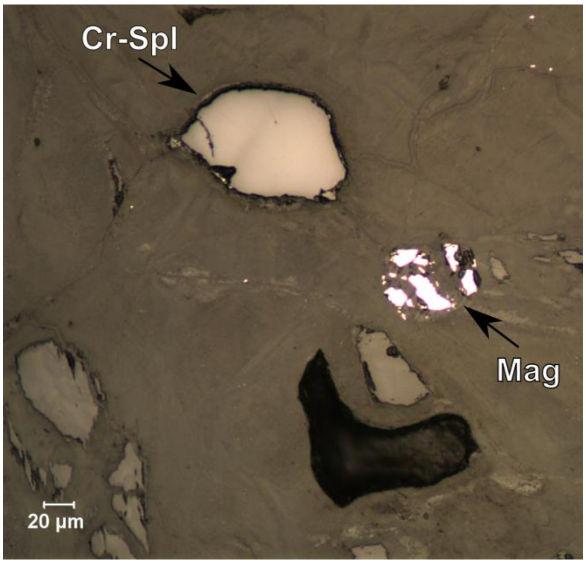

Figure 10.1-1: Cr-Spinel and a large magnetite grain. The matrix consists of serpentinite with small magnetite grains appearing as a "starry sky". Picture taken from sample 2.1.

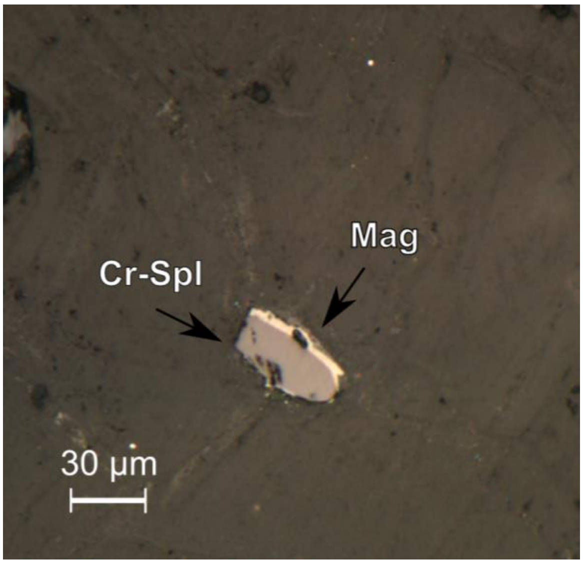

Figure 10.1-2: Cr-spinel with a rim of magnetite. The matrix consists of serpentinite with small magnetite grains appearing as a “starry sky”. Picture taken from sample 2.5.

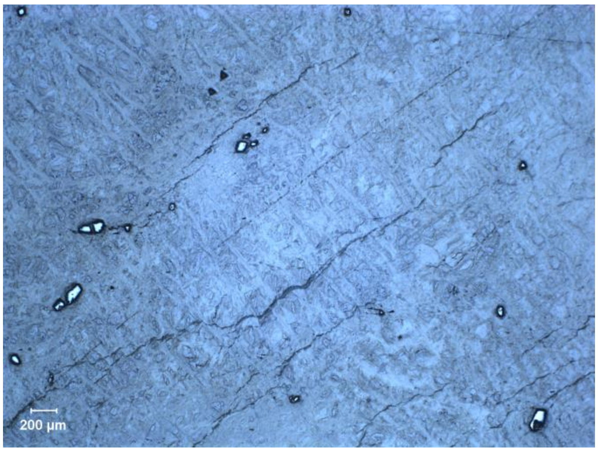

Figure 10.1-3: Cr-Spinels in mesh of serpentinite. The serpentine also appearce as seams going vertical accros the picture. Picture taken from sample 6.1.

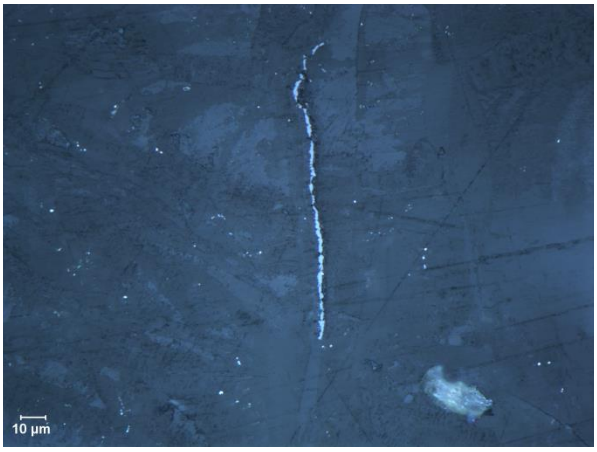

Figure 10.1-4: Magnetite, both as a long seam parallel with the mesh rim, and as small grains within the mesh. Picture taken from sample 6.2.

Location 5 (central Raudhaugene) looked similar in degree of serpentinization (40%) compared to location 3. Magnetite grains with diameter of 20-30 µm in diameter was observed within the mesh with an irregular dendritic appearance. Some magnetite was observed as small magnetite grains (D<1 µm) in the mesh, primarily in the mesh rims. Cr-spinel and rutile were present, and some grains were hard to distinguish from each other.

Location 6 (Central Raudhaugene) was estimated to be of a higher degree of serpentinization (>65%) compared to the previous locations. The thin sections displayed large Cr-Spinels (D~100µm) (Figure 10.1-3). The observed magnetite was mostly small (D<3 µm), but seams of magnetite were observed parallel with the mesh rims with a width of approximately 1 µm and length of approximately 100 µm (Figure 10.1-4).

Location 8 (Raudhaugene central east) appeared more, if not completely, serpentinized (>90), compared to the other peridotite samples. Large Cr-Spinels (50-150 µm) were identified, commonly displaying rims of magnetite. Magnetite was observed as both long (~100 µm), thick (~15 µm) as well as thin (~1 µm) seams, and with dendritic shapes. Two of the four thin sections (8.2 & 8.3) were weathered, making the mineral identification difficult. The weathering could in addition indicate possible porosity within the samples.

10.1.3.1 Serpentine and magnetite

The serpentine associated with veins, and the serpentine in the mesh, displayed different microstructures. Based on Oud's (2010) work, and literature, the serpentinites were identified as lizardite, chrysotile and antigorite. According to Oud, the chrysotile was the first mineral to form in fracture filling events. In this study, possible chrysotile was displayed in thin section as wavy and yellowish bands at the border of fractures. The second minerals to form were, according to Oud, antigorite and lizardite. Possible antigorite was identified in thin section as ribbons going normal to the earlier (possible) chrysotile. Possible lizardite was identified as micro-granular grains in the centre of fractures. Observations can be viewed in Figure 10.1-6.

Most of the thin sections did not display large serpentine veins. They mostly displayed mesh comprising, based on Oud's (2010) observations, Chrysotile and Lizardite serpentine polymorphs. This mesh commonly inhabited small magnetite grains (D<1 µm).

Magnetite was also commonly observed in serpentine seams going through primary minerals, while the larger veins did not display any visible magnetite (Figure 10.1-5).

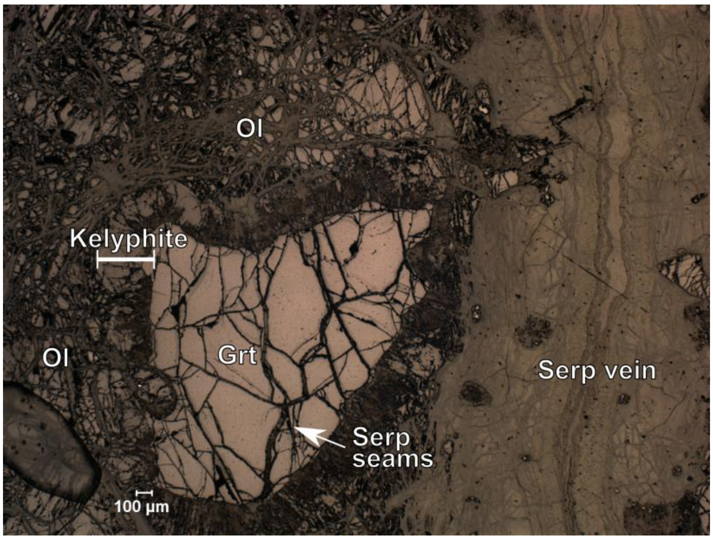

Figure 10.1-5: Garnet with a kelyphite alteration rim and through going serpentine seams. The minerals comprising the garnet are mostly of Olivine and serpentine. A large serpentine vein is cutting through at the right. Small magnetite grains (<1 µm in diameter) was observed in the matrix between the garnet and the serpentine vein, and within the serpentine seams. Picture taken from sample 3.2.

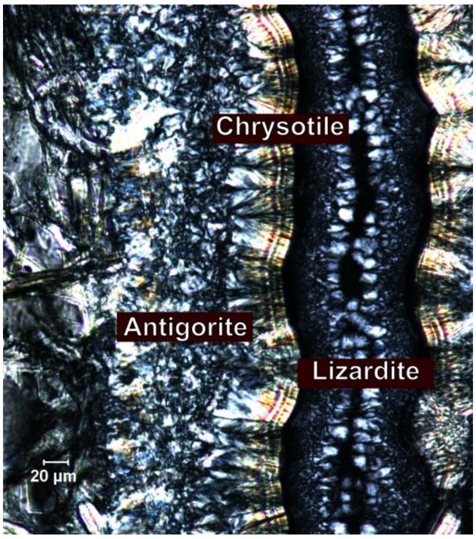

Figure 10.1-6: Three possible types of serpentine. The banded, wavy, yellowish could be Chrysotile. The inner triangular grey/blue could be Lizardite. The fibrous/ribbonish, observed outside the banded, wavy Chrysotile, could be Antigorite. Picture is from sample 3.2.

10.2 Optical microscopy of thin sections from the surrounding bedrocks

The surrounding bedrocks differed somewhat in mineral composition, but both the two gneiss types and sample 9.1, which were sampled from an area previously mapped as amphibolite, contained similar mineralogy. The magnetic minerals identified in thin section were magnetite and hemo-ilmenite.

Garnet displayed high relief, pale pink colour and was black under crossed polarized light. It was isotropic and subhedral. Plagioclase displayed low relief, was colourless, and had white interference colour. It showed distinct twinning when turned, appeared as anhedral crystals, and some displayed exsolutions. Quartz displayed low relief, was colourless, and had white interference colour (Figure 10.2-1). It displayed a wavy extinction and appeared anhedral. Biotite displayed medium relief, strong brown or green colour and interference colours in second order red. It appeared anisotropic or flaky like. Its extinction angle was parallel to cleavage. Hornblende displayed high relief with anhedral appearance, yellow to green colour, and interference colour in brown. Ilmenite displayed grey colour and interference colours which seemed to be a bit brown. Where it was observed within biotite it appeared as thin needle-like crystals. Some crystals showed exsolution, and some of these were identified as hematite lamellae. Hematite displayed light grey colours with higher reflectance than ilmenite, and was observed as thin long lines within the ilmenite. Pyrite was observed within the biotite with a pale yellow colour. It was isotropic and displayed high reflectance and exsolution. Magnetite was opaque and displayed a bright white metallic lustre in transmitted light. It appeared massive with no internal structures. The magnetite was observed as big grains (D>100 µm) (Figure 10.2-2), as rims around other minerals, but also as smaller grains ~15 µm.

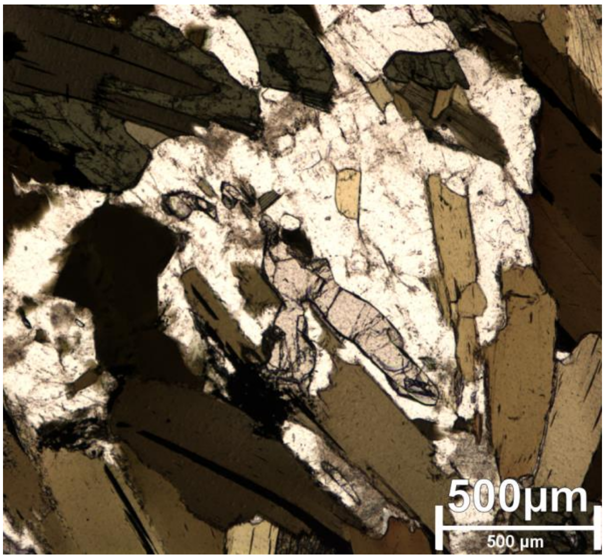

Figure 10.2-1: Thin section 1.1 displaying large and well-developed mineral grains discussed in text.

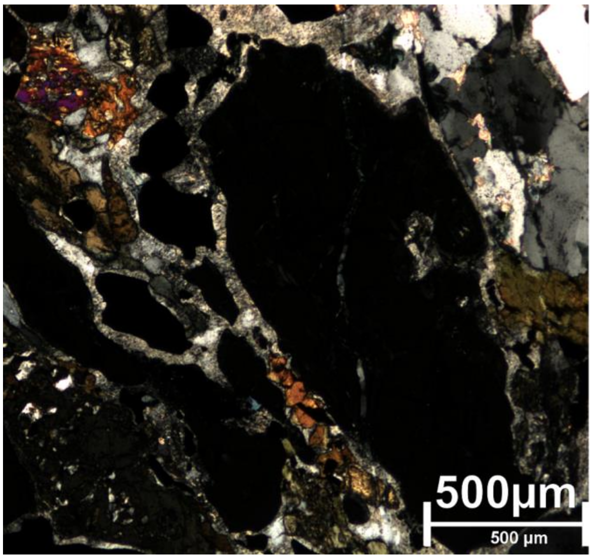

Figure 10.2-2: Thin section 9.1 displaying large well-developed grains of magnetite.

10.3 Back scatter electron microscopy of thin sections

To confirm the observations of magnetite, Cr-spinel and hemo-ilmenite in thin section, as well as investigating the relative composition of the Cr-spinels, back scatter electron microscopy and point estimations were conducted.

In back scatter electron microscopy heavy elements will appear brighter than light elements. Oxide minerals, such as magnetite, Cr-spinel and hemo-ilmenite consist of heavy elements, and will reflect more electrons than light elements. The magnetic minerals investigated therefore appeared bright in the obtained images. In the peridotite thin sections, the less dense serpentines, olivines and pyroxenes were dark appearing in the back scatter electron microscopy. The oxides, consisting mainly of magnetite and Cr-spinels were therefore easy to recognise. In the gneiss thin sections several oxides were present and made the recognition of magnetite somewhat more difficult, however the lamellas of the hemo-ilmenite were easy to recognize due to the hematite being denser than the ilmenite.

10.3.1 Investigation of the oxide minerals of the peridotite locations

The investigation of thin section 2.2-3a from location 2 (Ugelvik body) confirmed the presence of relatively large magnetite grains (~15 µm in D), while the small oxides in the mesh, previously defined as magnetite, were too small for analysis. The previously identified magnetite with sizes above 40 µm was not recognised in the thin section, but chromites, with aluminium (Al) and magnesium (Mg) impurities, were observed within this size region. Chromite with relatively high Al composition, hence possibly Alumo-chrompicotite, were additionally recognized in what appeared as kelyphite rims (Figure 10.3-3). Possible previous recognition of magnetite in seams displayed high copper (Cu) content in spot analysis. This Cu-rich mineral was not identified.

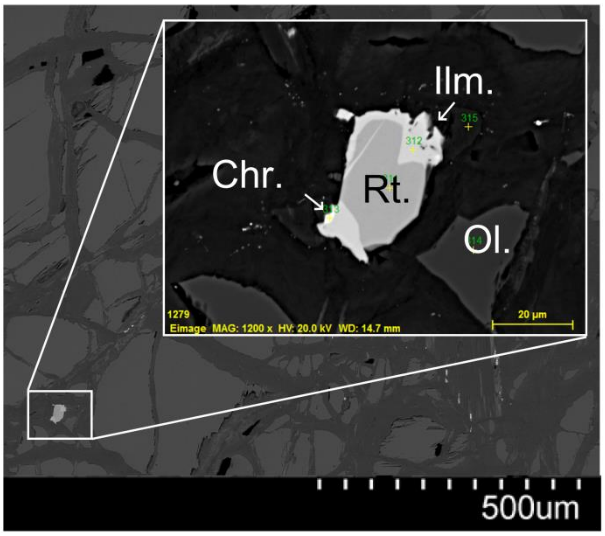

Figure 10.3-1: Thin section 3.2 displaying rutile with ilmenite and chromite rims. The grain is surrounded by olivine grains and serpentine mesh.

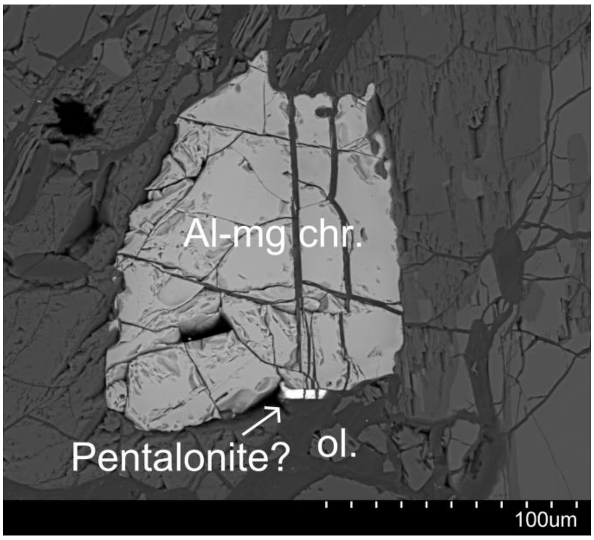

Figure 10.3-2: Thin section 2.2-3a displaying aluminium rich chromite, possibly alumbocrezovite, possible pentalonite and surrounding olivine grains.

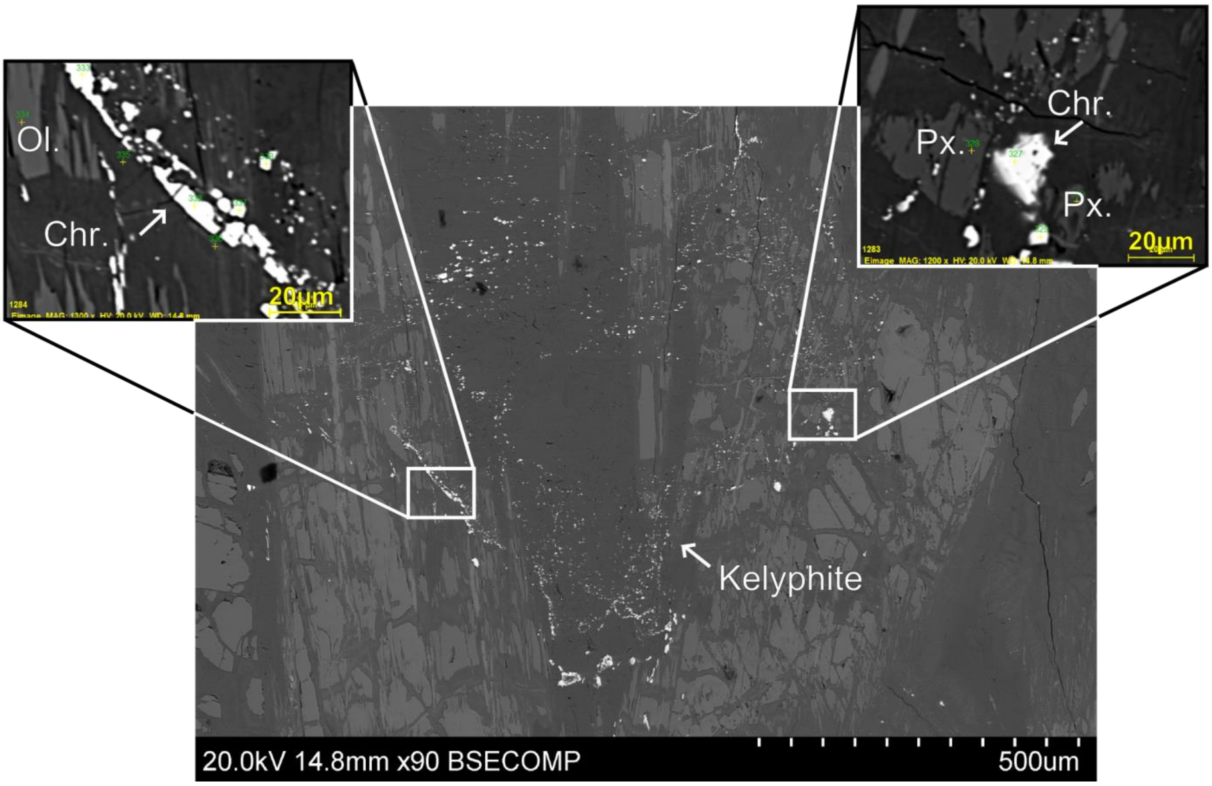

Figure 10.3-3: Thin section 2.2-3a displaying a possible kelyphite rim. Minerals within are chromite of high Al composition, hence possibly Alumo-chrompicotite, in addition to high Al pyroxene and olivine.

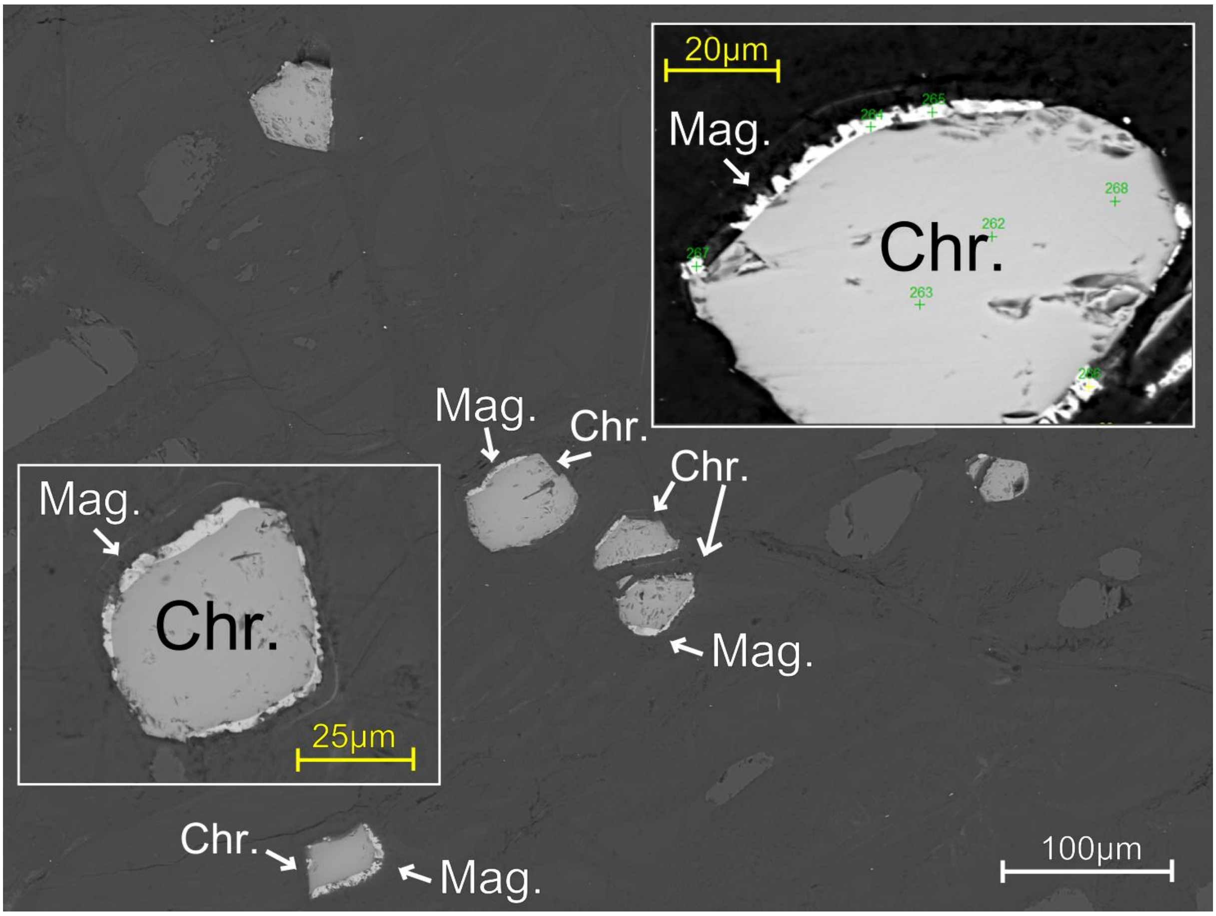

Figure 10.3-4: Thin section 5.2 displaying chromite with Al and Mg impurities and well-defined rims of magnetite.

Thin section 3.2 from location 3 (Ugelvik body) did not display any large magnetite grains, but displayed Al-Mg rich chromites within the size range of (60-100 µm in D), possibly previously described as magnetite grains. These Al-Mg rich chromites could be alumbocrezovite based on relative composition from spot analysis. Of minerals with rims, rutile was the only mineral recognized, though not of magnetite as previously described, but of both ilmenite and chromite (Figure 10.3-1).

Thin section 5.2 from location 5 (Raudhaugene body) displayed possible magnetite in seams with sizes below 1 µm, but these were not identified due to their small size. However, magnetite was observed as well-defined rims around chromites, with rim diameters below 3µm. In addition, Al-Mg rich chromites were identified and could be of alumobocrezovite composition based on spot analysis.

Thin section 6.1 from location 6 (Raudhaugene body) displayed the same morphologies of magnetite as observed in optical microscopy, including magnetite in seams (Figure 10.3-5). Additionally, some magnetite grains with dendritic appearance (~15 µm in D) were recognized. The previously described Cr-Spinels were also recognized, as well as Al-rich chromium. Chromite, with some Al and Mg impurities was recognized in what appeared to be kelyphtic rims.

Thin sections 8.1 and 8.2, both from location 8 (Raudhaugene body), displayed large Cr-spinels, previously described from optical microscopy. However, the spot analysis indicated chromites instead of Cr-spinels. Some of these displayed Al and Mg impurities, others with high Al content. Well-developed magnetite seams previously described from optical microscopy were also identified. In addition, several magnetite morphologies were observed. Fire-like structures of magnetite were observed at the rims of the chromites as well as through going seams within chromite grains (Figure 10.3-6). In seams swirly magnetites, with approximate with of 20 µm, were observed (Figure 10.3-7) as well as magnetite with bud-like structures (Figure 10.3-9). In addition, large magnetite grains of ~30 µm length and ~ 10 µm widths were observed in the serpentine mesh (Figure 10.3-8).

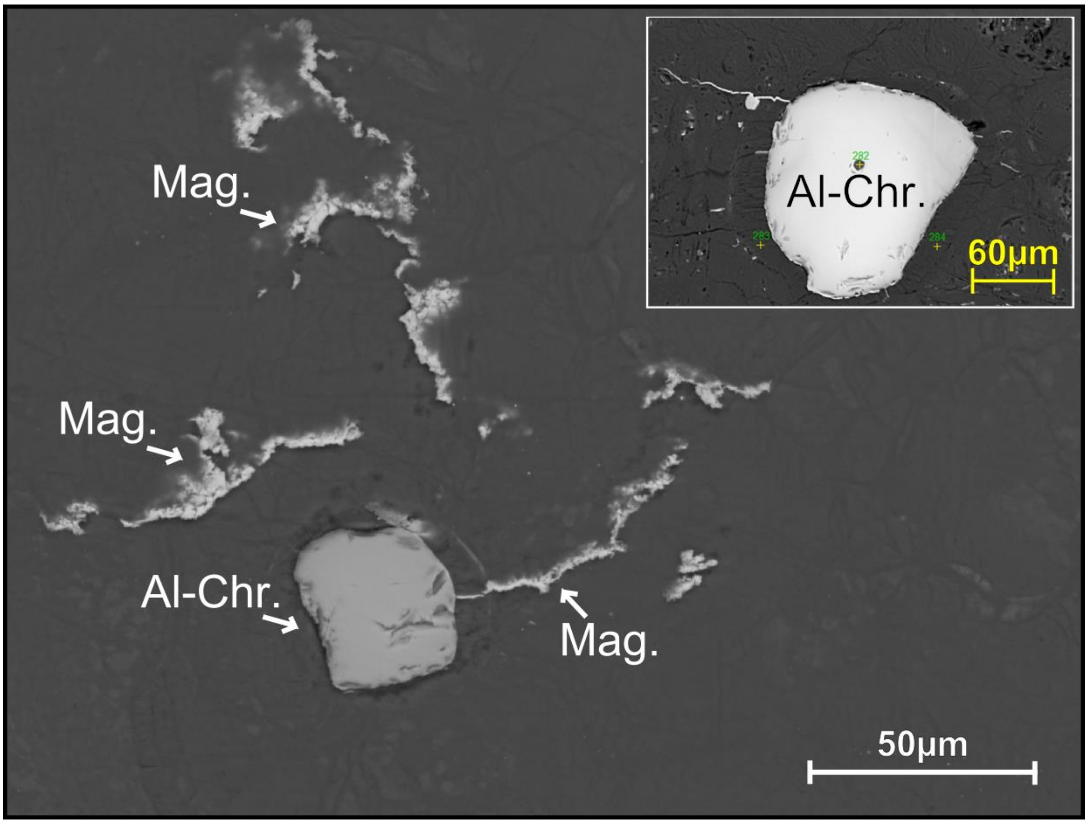

Figure 10.3-5: Thin section 6.1 displaying Al. rich chromite without alteration rims, and magnetite in small seams.

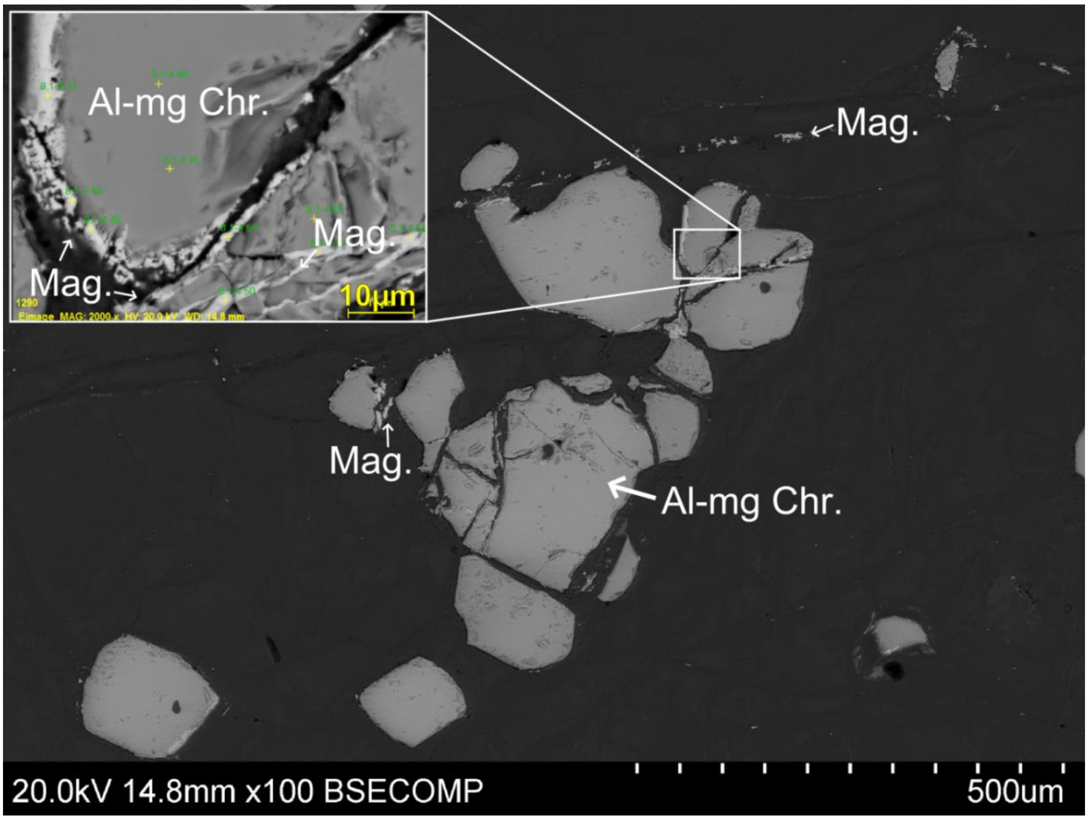

Figure 10.3-6: Thin section 8.1 displaying large chromites with high Al and Mg content. Rimming these were tiny magnetite fire-like structures, as well as magnetite alteration seams running through the chromite grains.

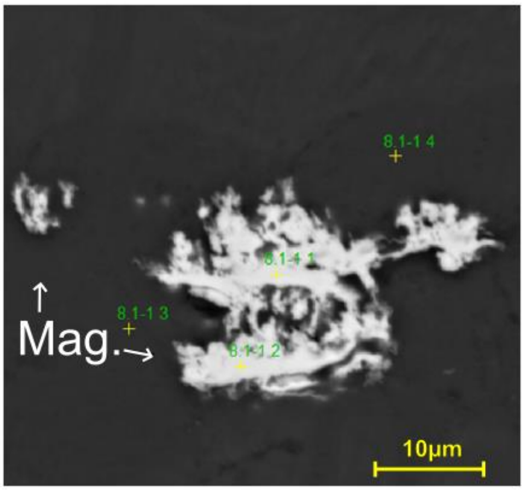

Figure 10.3-7: Thin section 8.1 displaying swirliy magnetite in seam.

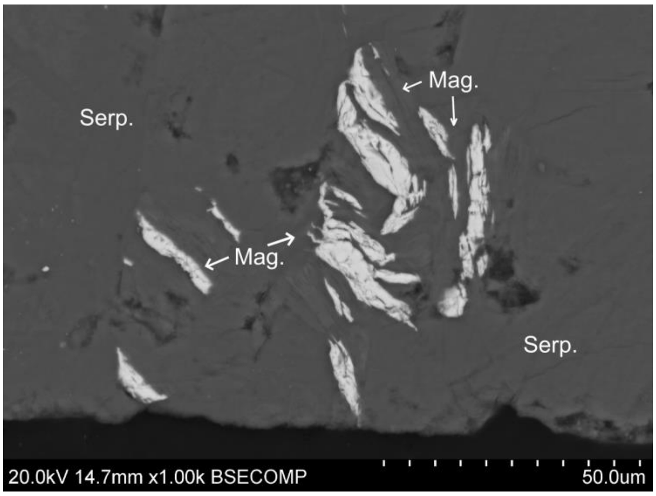

Figure 10.3-8: Thin section 8.2 displaying big magnetite grains in serpentine mesh.

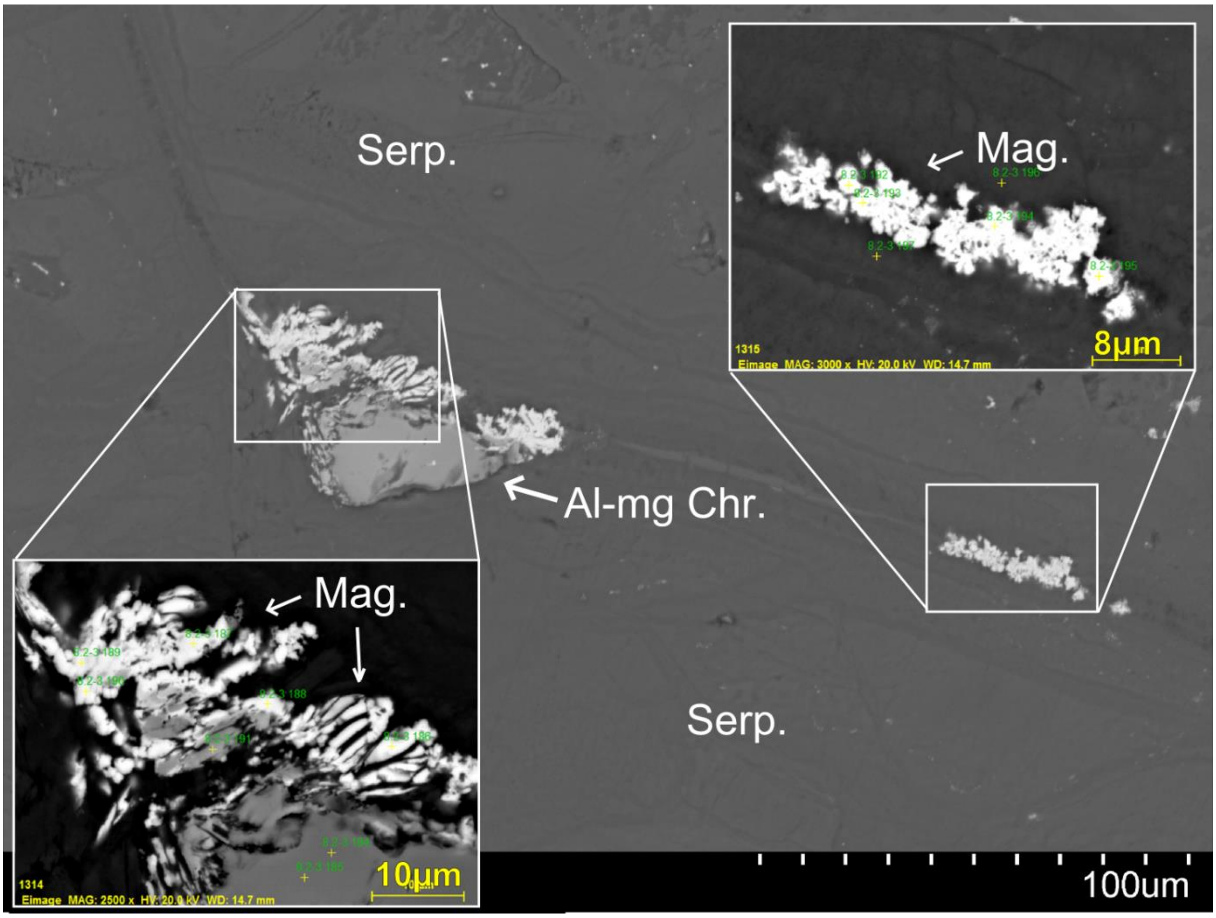

Figure 10.3-9: Thin section 8.2 displaying well-developed magnetite in seam with a bud-like apparence, and as fire-like and massive appearance around aluminium rich chromite possibly of alumoberezovite composition.

10.3.2 Investigation of the oxide minerals within the surrounding bedrock locations

Thin section 4.2 from location 4 displayed hemo-ilmenite (Figure 10.3-11) as well as big magnetite grains with D>50 µm (Figure 10.3-12). It also displayed altered rutile (possibly of Anderbergite composition) with fire-like structure of magnetite, at the rim of the grain (Figure 10.3-13). These magnetite structures were of less than 1 µm of width.

Thin section 7.4, from location 7, displayed hemo-ilmenite (Figure 10.3-14) as well as small seams of magnetite (Figure 10.3-13). In addition was large magnetite grains with D>100 µm observed next to ilmenite grains (Figure 10.3-15).

The lithology of both location 4 and 7 has previously been described as coarse grained granitic gneiss, and to a less extent migmatitic gneiss. Thin section 9.1, from location 9, however, has previously been described as Amphibolite. This thin section displayed many morphologies of magnetite. Magnetite was observed as large grains of D>50 µm next to hemo-ilmenite (Figure 10.3-10), as coarse magnetite seams within pyroxene displaying grains smaller than <1 µm (Figure 10.3-16) small grains approximately of 1-5 µm in D with some trace V, and as seams of approximate length of 150 µm and width of 3 µm.

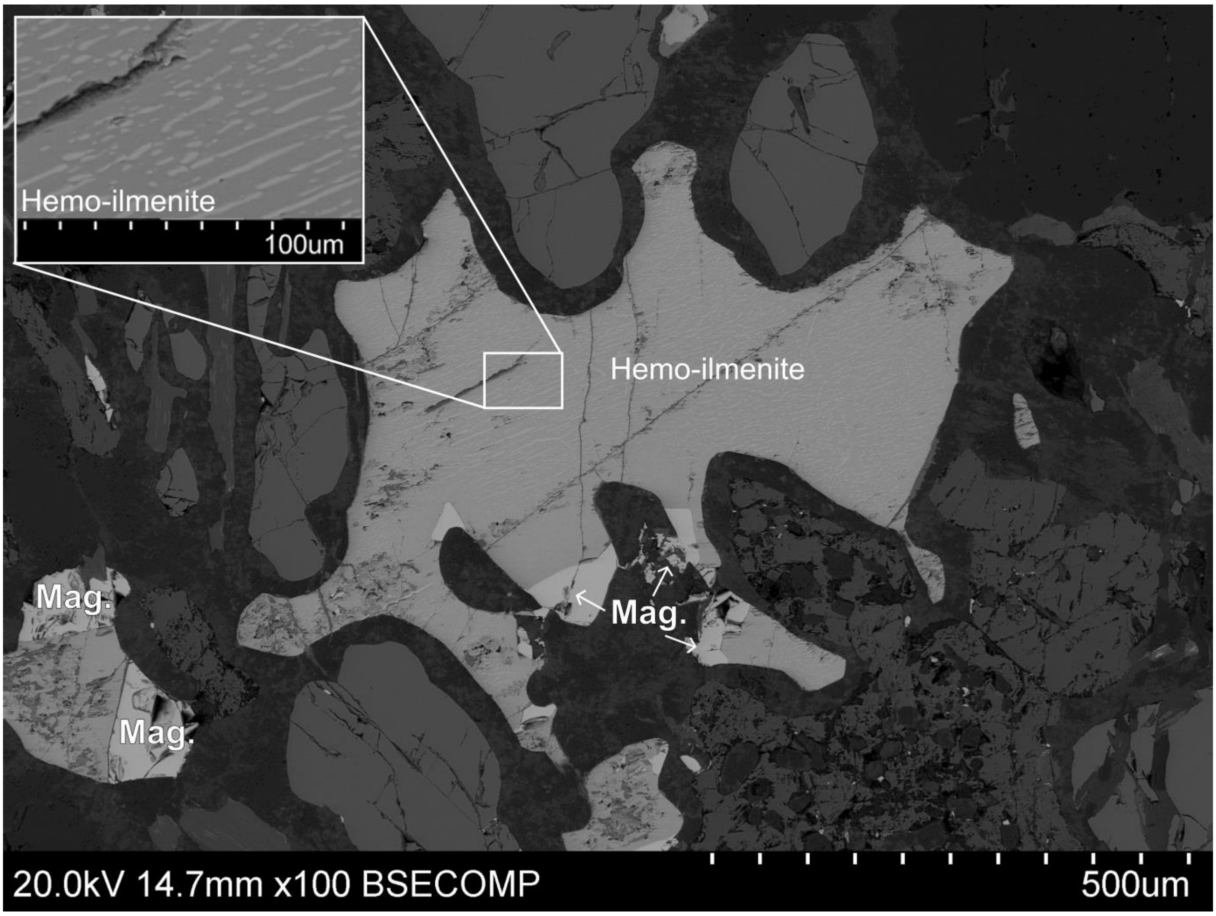

Figure 10.3-10: Thin section 9.1 displaying hemo-ilmenite and large magnetite grains.

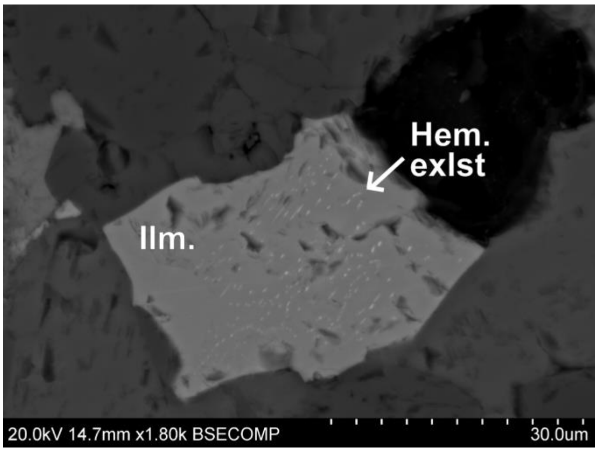

Figure 10.3-11: Thin section 4.2 displaying hemo-ilmenite.

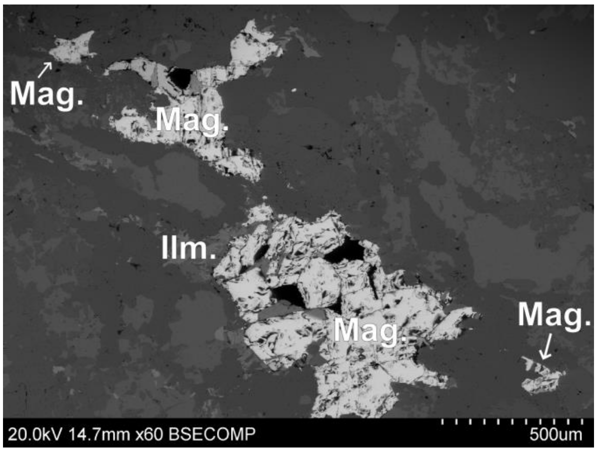

Figure 10.3-12: Thin section 4.2 displaying big magnetite grains.

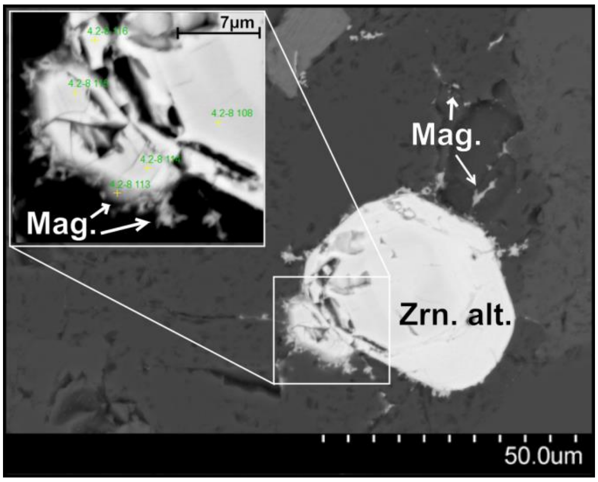

Figure 10.3-13: Thin section 4.2 displaying altered zircon of possibly Anderbergite composition, with small magnetites with flame like structures at the rim of the grain.

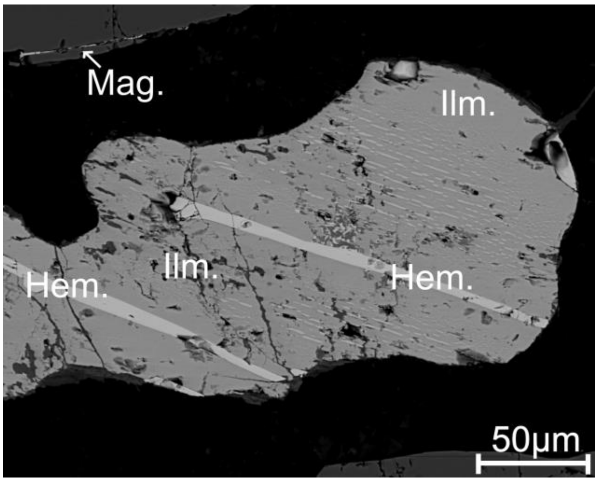

Figure 10.3-14: Thin section 7.4 displaying hemo-ilmenite and a tiny magnetite seem.

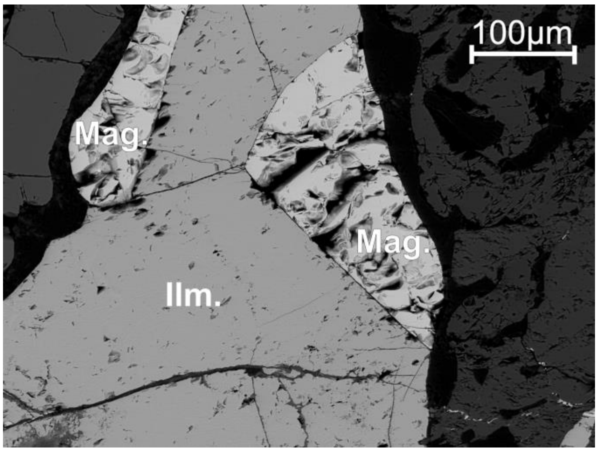

Figure 10.3-15: Thin section 7.4 displaying large magnetite grains next to ilmenite.

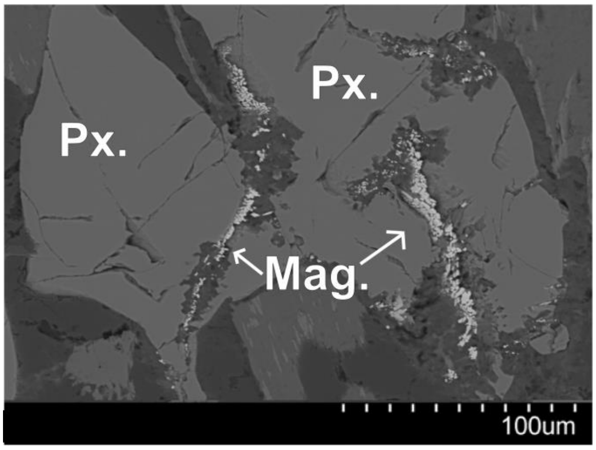

Figure 10.3-16: Thin section 9.1 displaying coarse magnetite in within pyroxene grains.

10.4 Indications of domain size of magnetite based on microscopy

Based on both optical and back scatter electron microscopy the size ranges of magnetite varied from SD, PSD to MD sizes based on size classification of Tauxe et al. (2002) and Moskowitz (n.d.).

Within the peridotite thin sections, many large grains were observed in optical microscopy as magnetite, which probably were varieties of chromite based on identifications in back scatter electron microscopy. Especially for location 2 and 3, the optical microscopy observations of possible magnetite of pseudomorphed olivine were in back scatter electron microscopy identified as chromites. For location 2 the identified magnetite was therefore of ~15 µm in diameter (D) and as small magnetite grains in mesh corresponding to PSD to SD magnetite. For location 3 the observed magnetite was D<1 µm within mesh or as tiny seams corresponding to SD magnetite. For location 5 possible magnetite in seams with D<1 µm was observed, corresponding to SD magnetite. In addition, magnetite rims with diameters below 3µm were identified around chromites, corresponding to PSD magnetite. For location 6 the identified magnetite was mostly small (D<3 µm). It was also observed as seams with a width of approximately 1 µm and length of approximately 100 µm. Both morphologies could correspond to SD or PSD magnetite. In addition, dendritic appearing magnetite of ~15 µm in D was also identified, corresponding to PSD magnetite. Location 8 displayed a large variety of identified magnetite morphologies ranging from SD, PSD to MD magnetites.

Within the surrounding bedrocks the identified magnetite was as large as D>50 µm, corresponding to MD magnetite. Additionally, magnetite with fire-like structures was identified at location 4, and small seams of magnetite were observed at location 7, corresponding to SD size. At location 9 many morphologies of magnetite was identified, ranging from SD, PSD to MD magnetites.

11 Magnetic properties

11.1 Magnetic properties and densities obtained from specimens and field measurements

The magnetic properties and densities obtained at Otrøya showed variations between lithology, within lithology and, in addition, variation between the Ugelvik and Raudhaugene bodies. All of the magnetic properties and density values discussed can be viewed in Table 11.1-1, Figure 11.1-1, Figure 11.1-2 and Figure 11.1-3

11.1.1 Susceptibility values obtained from specimens

The median and average susceptibility value of the Ugelvik body was respectively 0.0010 and 0.0014 SI, which is much lower than indicated for the susceptibility range [0.0955, 0.196 SI] given for peridotites by Reynolds (2011). The body's susceptibility values had standard deviation of 0.001, indicating little variation in susceptibility values. Though, the maximum value (0.0045 SI) indicated some high extreme values.

The Raudhaugene body displayed similar values, though slightly more varying, with a median and average susceptibility value of respectively 0.0008 and 0.0016. Compared to the Ugelvik body, the Raudhaugene body displayed an increased standard deviation indicating higher variation in the data. In addition, the maximum value (0.009 SI) was higher, though the minimum value (0.0004 SI) was approximately the same, indicating a greater amount of high extreme values within the Raudhaugene body.

The median and average values of the constricting gneisses were respectively 0.0203 and 0.0244 SI. These values were within the indicated susceptibility range [0.000125, 0.025 SI] given for gneiss by Reynolds (2011), though close to the upper value. The slightly varying average and median values indicated some variability in the data, also indicated by the standard deviation of 0.02 SI.

11.1.2 Susceptibility values obtained from field measurements

The susceptibility values collected in field showed similar average and median values compared to the susceptibility specimen values for the Ugelvik body, while displayed higher susceptibility values for the Raudhaugene body. For the Raudhaugene body the minimum value of the field measurement was significantly higher compared with the specimen minimum susceptibility value, while the maximum value was somewhat lower, resulting in a smaller standard deviation for the field measurements.

The gneisses showed substantially lower variance for the obtained field values compared to the specimen values, though, same minimum and maximum value. The lower variants could be due to the larger area covered by measurements in field compared to the values obtained for the sample localities, providing a greater amount of normal values compared to extreme values.

Difference in average values for specimen susceptibility and field susceptibility at specimen locations can be viewed in the susceptibility map (Figure 11.1-1). Upward triangles indicate values obtained from specimens, hence the sample localities. By viewing the susceptibility map it became evident that most of the gneiss localities displayed similar values for field and specimen values, except for locality 1, west of the Ugelvik body. This gneiss locality showed a difference of approximately 0.015 SI between field and specimen susceptibility value. Within the peridotite bodies only small or no variation was observed between specimen and field value. The biggest difference was for locality 8, at the boarder of the central-eastern part of the Raudhaugene body, which displayed a difference of 0.002 SI.

Due to the similar values of field and specimen susceptibility, for each locality, it is possible to compare the susceptibility values measured in field with values obtained from specimens. The Ugelvik body displayed consistently low susceptibility values at all measurement localities. So does the Raudhaugene body, only with some minor variation in the central-eastern part, with an increased susceptibility value of approximately 0.002-0.003 SI. The map made it in addition easy to recognise the substantially lower susceptibility values provided by the peridotite bodies compared with the constricting gneisses. Though, the gneisses showed a larger variability in susceptibility values, with locations displaying average extreme values above 0.03 SI, while other localities displayed values as low as 0.005 SI.

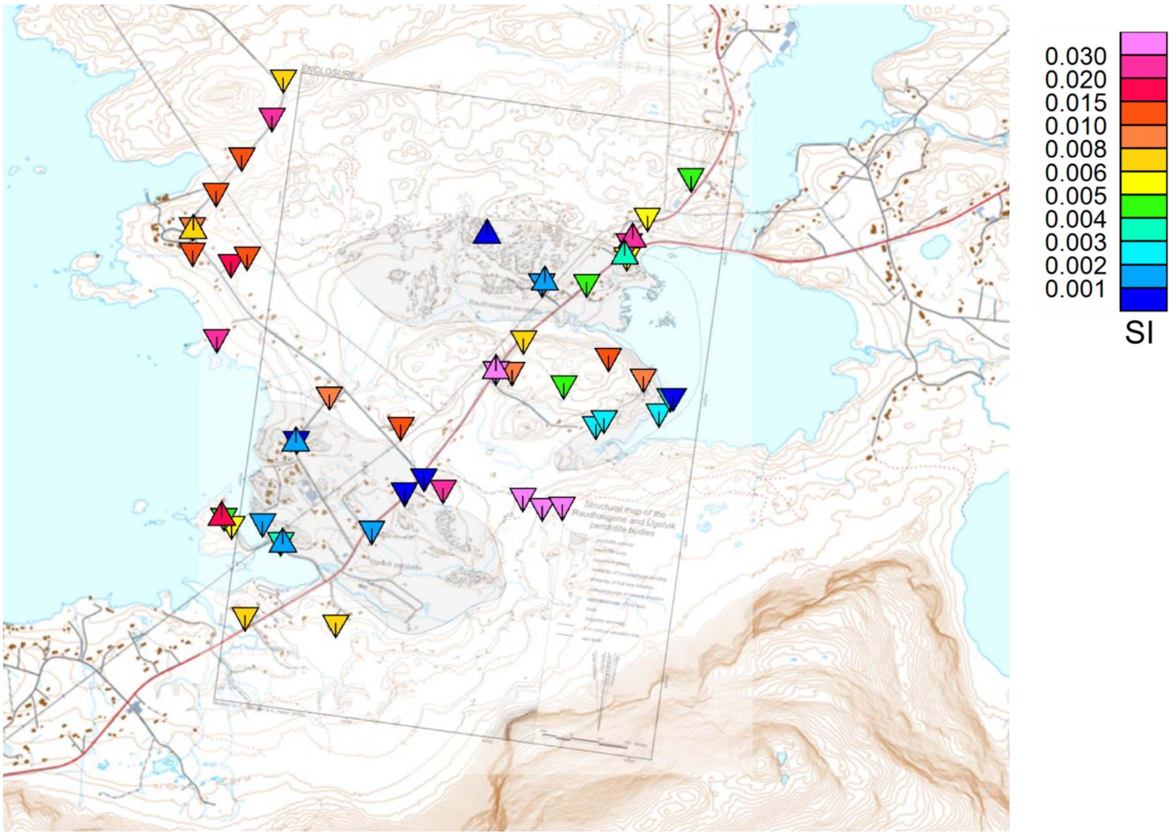

Figure 11.1-1: Susceptibility map. Both the susceptibility values obtained from specimens (△) and field measurements (▽) are averaged by location, and superimposed over both a structural geological map over the Ugelvik and Raudhaugene bodies (Spengler and Haker, 2006) and a topographical map (NGU,n.d.). Colour bar is of an approximate equal area distribution.

Table 11.1-1: Magnetic properties and density values for the Ugelvik (A) and Raudhaugene (B) peridotite bodies, and for the gneisses (C) surrounding the two peridotite bodies. N indicates the number of specimen measured.

A) Ugelvik

N=76	Density (g/cm3)	vol. corr. NRM (A/m)	Field Susc. (SI)	Volume corr. Susc. (SI)	Induced magn. (A/m)	Q-value
median	2.67	0.0538	0.0012	0.0010	0.0420	1.27
average	2.66	0.1270	0.0015	0.0014	0.0589	2.02
max	2.96	0.9049	0.0032	0.0045	0.1846	11.11
min	2.45	0.0101	0.0006	0.0004	0.0184	0.55
StDev	0.11	0.1626	0.0009	0.0010	0.0424	1.94

B) Raudhaugene

N=120	Density (g/cm3)	vol. corr. NRM (A/m)	Field Susc. (SI)	Volume corr. Susc. (SI)	Induced magn. (A/m)	Q-value
median	2.45	0.1513	0.0027	0.0008	0.0325	2.41
average	2.46	0.3879	0.0032	0.0016	0.0670	6.45
max	2.73	5.7202	0.0058	0.0091	0.3724	38.64
min	2.25	0.0064	0.0013	0.0004	0.0179	0.23
StDev	0.11	0.7086	0.0014	0.0017	0.0685	8.35

C) Constricting bedrocks (referred to as gneiss)

N=55	Density (g/cm3)	vol. corr. NRM (A/m)	Field Susc. (SI)	Volume corr. Susc. (SI)	Induced magn. (A/m)	Q-value
median	2.75	1.6379	0.0089	0.0203	0.8346	1.24
average	2.82	2.6882	0.0143	0.0245	1.0045	3.01
max	3.31	48.6836	0.0676	0.0669	2.7455	26.98
min	2.44	0.0006	0.0002	0.0002	0.0090	0.05
StDev	0.27	6.6304	0.0134	0.0215	0.8813	5.24

11.1.3 Density values obtained from specimens

The two peridotite bodies displayed quite similar density values. Within the two bodies, the average and median values were approximately the same, though the values for the Ugelvik body where slightly higher (average=2.66 g/cm^3) compared to the Raudhaugene values (average=2.46 g/cm^3). They display the same standard deviation, which strengthens validity of the comparison of the averages values. The gneisses displayed a larger variability reflected by the deviating median and average values (respectively 2.75 and 2.82 g/cm^3), and in the greater standard deviation (0.28 g/cm^3).

By looking at the density map (Figure 11.1-2) it becomes evident that there was some variation in average densities for each locality as well as variation between the two bodies. The Ugelvik body displayed the highest densities of the two, with 2.71 g/cm^3 and 2.61 g/cm^3 for location 2 and 3 respectively. The Raudhaugene body displayed lowest densities, with a maximum difference from the Ugelvik body of 0.31 g/cm^3. Location 6 and 8 at the east displayed low density values of 2.46 and 2.40 g/cm^3, while location 5 displayed a density value of 2.54g/cm^3. This was approximately 0.10g/cm^3 lighter than for the two other locations. Most of the gneisses displayed large density values above 2.76g/cm^3, with location 4 as an exception. This locality displayed a density (2.50g/cm^3) more similar to the densities of the peridotites.

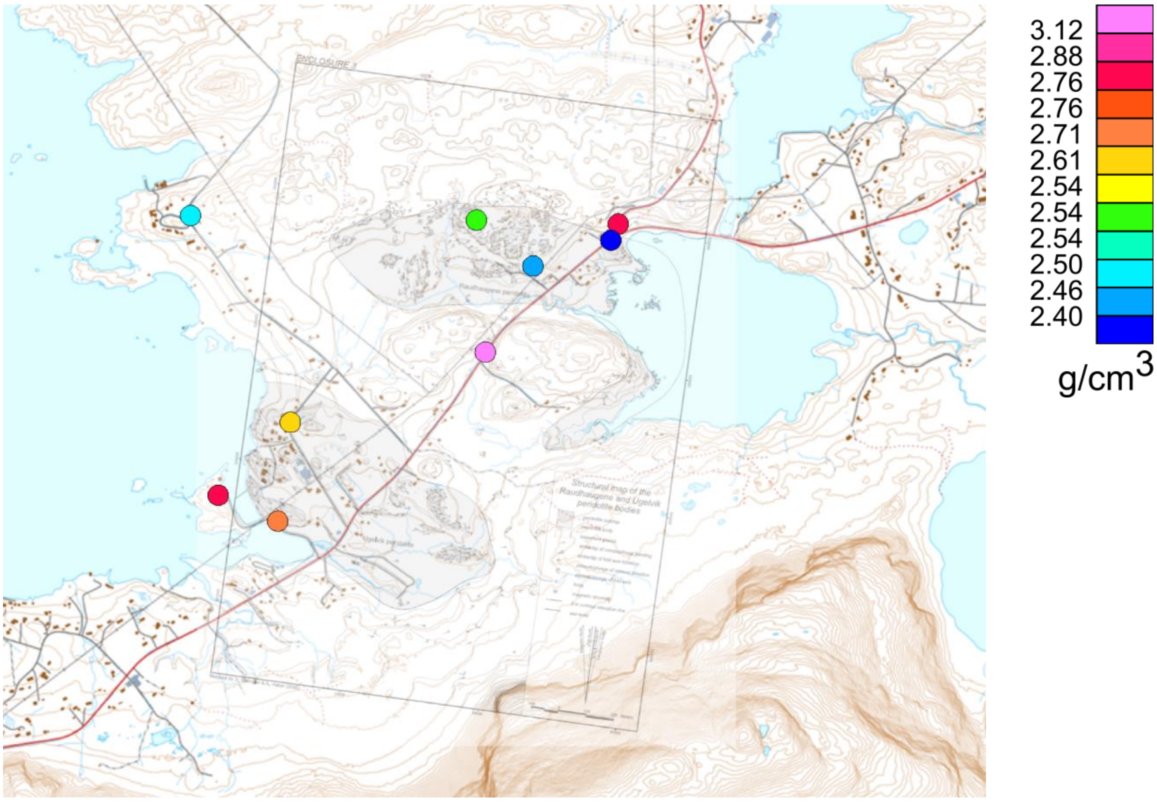

Figure 11.1-2: Density map. Density values (○) obtained from specimens are averaged by location and superimposed a structural geological map over the Ugelvik and Raudhaugene bodies (Spengler and Haker, 2006) and a topographical map (NGU,n.d.). Colour bar indicates accurate average values for locations.

11.1.4 NRM intensities obtained from specimens

The NRM values obtained from specimens showed substantially larger variation compared to the obtained susceptibility specimen value variations. Of the peridotite bodies, the Ugelvik body displayed the lowest NRM values with average value of 0.1270 (A/m) and a standard deviation of 0.1626 (A/m), whilst the Raudhaugene body displayed much more variability (StDev=0.7086 A/m) and an average value (0.3879 A/m) three times as large as for the Ugelvik body. This was indicated by both the minimum and maximum NRM value, of the Raudhaugene body, being much more extreme than for the Ugelvik body (Table 11.1-1 A&B). The gneisses displayed much more extreme variability with average value of 2.6882 A/m and a standard deviation of 6.6304 A/m).

Within the NRM map (Figure 11.1-3) the Ugelvik body displayed the least variability with both of its locations carrying average NRM intensities below 0.159 A/m. Within the NRM map, larger NRM variability can be viewed within the Raudhaugene peridotite body and the constricting gneisses. The Raudhaugene body displayed higher NRM intensities compared with the Ugelvik body. At location 8, eastern part of the body, the average NRM intensity was of 0.757 A/m, and at location 5 the average NRM intensity was of 0.593 A/m. At location 6 the average NRM intensity was of 0.104 A/m – more similar to the NRMs of the Ugelvik body. Overall were the gneiss locations displaying high average NRM values (>1.539) A/m). The highest average NRM intensity (9.663 A/m) was observed at location 9. This location inhabited a specimen carrying the highest NRM intensity observed in the dataset (48.68 A/m). By excluding this value the average NRM intensity of location 9 became 1.859 A/m. With this abnormal value excluded from the dataset the highest average NRM intensity was observed at location 4 with an intensity of 2.711 A/m.

11.1.5 NRM directions obtained from specimens

Equal area plots of the obtained NRM directions can be viewed in Figure 11.1-4, Figure 11.1-5 and Figure 11.1-6. The NRM directions can be viewed for their respective sample locations. The average Fisher mean vector for the NRM values are shown as solid large circles, whilst the average Fisher mean vector for the whole body (Ugelvik or Raudhaugene) or for the Gneiss can be viewed as dotted large circles. The field vector is plotted as a yellow square in all equal-area plots. For the Ugelvik and Raudhaugene body the different samples, and specimens measured in the cryogenic magnetometer, are colour coded. Fisher mean vector calculations for all locations can be viewed in Table 11.3-1.

The NRM directions (N=75) within the Ugelvik body (location 2 and 3) carried mostly positive directions (77%). The Fisher mean vector for the positive NRM directions displayed a steep gradient with inclination (I) =72.0° and declination (D) =128.3°, a mean length of 0.67502, and a 13.2° circle of confidence at the 95% level (α_{95}). This total positive mean vector displayed quite equal plotting direction compared to the respective positive mean vectors for location 2 and 3, reflected by the narrow circle of confidence. Mean vectors for the negative NRM directions were not significant, due to vast scatter of intensities carrying negative directions.

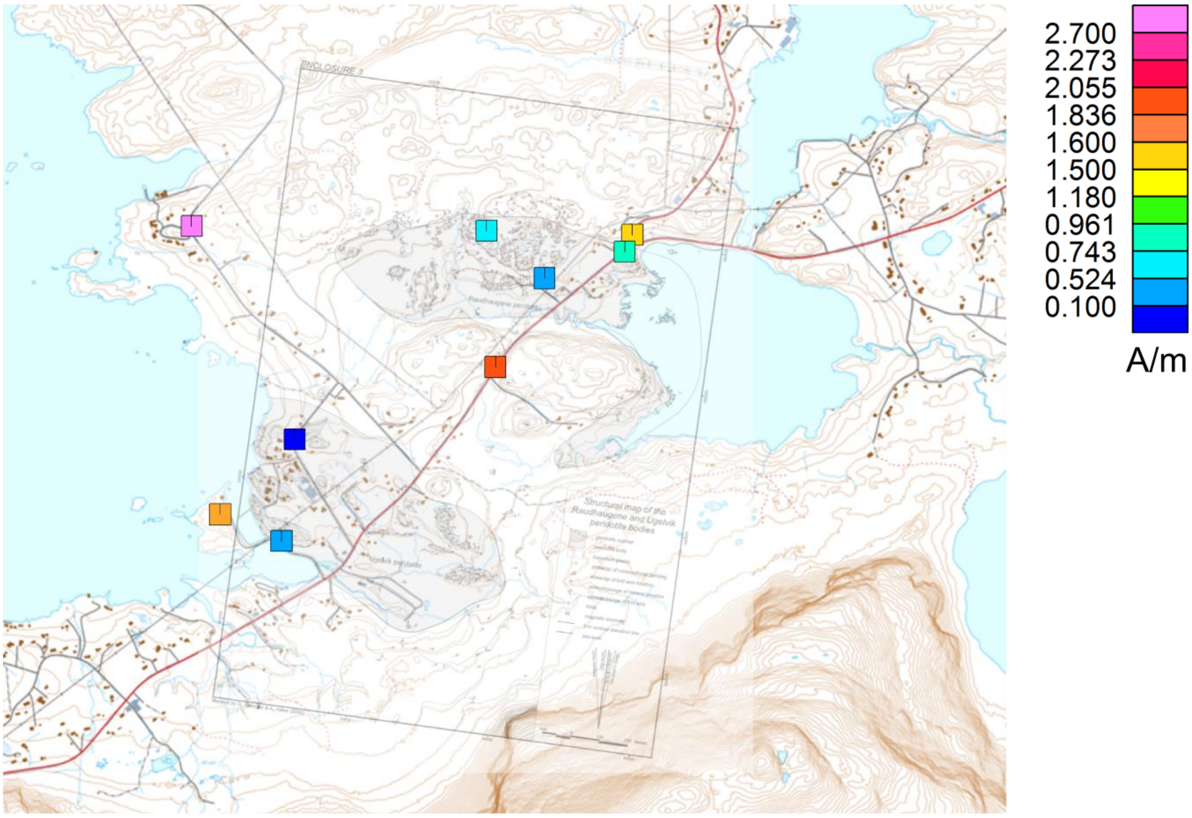

Figure 11.1-3: NRM map. The NRM values obtained from specimens (□) are averaged by location, superimposed over both a structural geological map over the Ugelvik and Raudhuagene bodies (Spengler and Haker, 2006) and a topographical map (NGU, n.d.). Colour bar is of an approximate linear fit.

The NRM directions (N=120) within the Raudhaugene body (location 5, 6 and 8) consisted mostly of positive values (83%), though most of the negative directions were within location 5. Approximately half (45%) of the directions (N=31) within location 5 were negative. Both the mean vectors for the negative and positive NRM directions, within this location, were of significance. They displayed relatively shallow inclinations, plotting close to each other. This indicated that the positive and negative NRM vectors could possibly cancel each other out. The negative mean vector of location 5 plotted at the same place as the negative mean vector for the whole body.

The negative mean vector for location 5 displayed I=-33.6°, D=247.4°, a mean length of 0.7172, and a 20.6° circle of confidence at the 95% level (α_{95}). The wide circle of confidence was reflected by some scatter of the negative NRM directions within the Raudhaugene body, though 67% of the negative directions plotted in the third quadrant of the equal area plot. The positive mean vector of location 5, did, on the other hand, plot quite far from the steep positive total mean vector of the whole Raudhaugene body. This steep vector displayed I=81.1°, D=237.9°, a mean length of 0.7005, and a 9.3° circle of confidence at the 95% level (α_{95}). The positive directions (N=89) of location 6 and 8 plotted closely to the steep, positive total mean vector for the whole body, explaining the small circle of confidence.

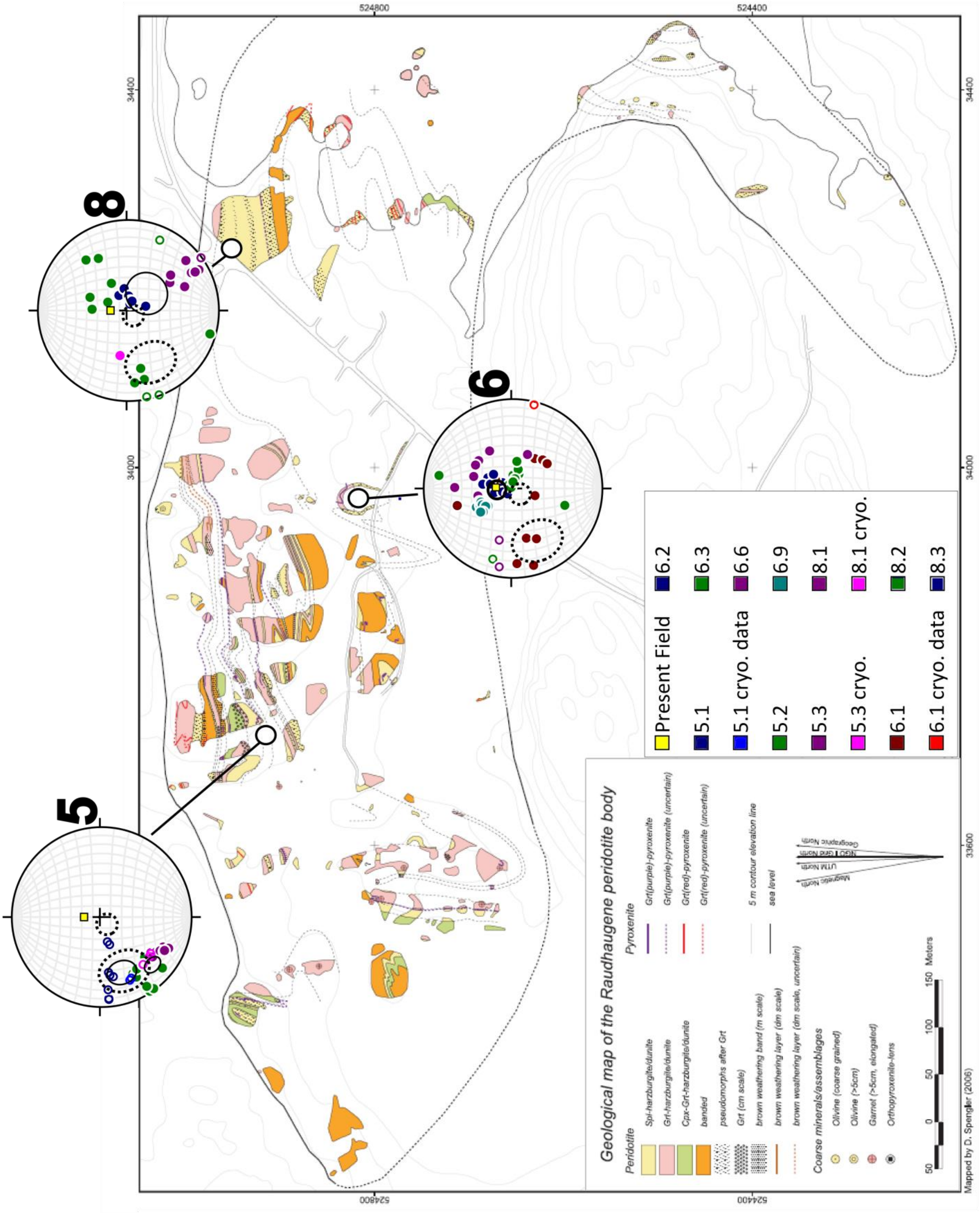

Figure 11.1-4: NRM direction map of the Raudhaugene body. Geological map is after Spengler (2006). NRM directions for sample area 5, 6 and 8 are plotted on their respective equal-area projection plots. Open symbols indicate upward (negative) inclinations; solid symbols represent downward (positive) inclinations. Yellow square indicates the present day field vector. Dashed big circles indicate mean vectors for the whole body. Big solid circles indicate mean vectors for location.

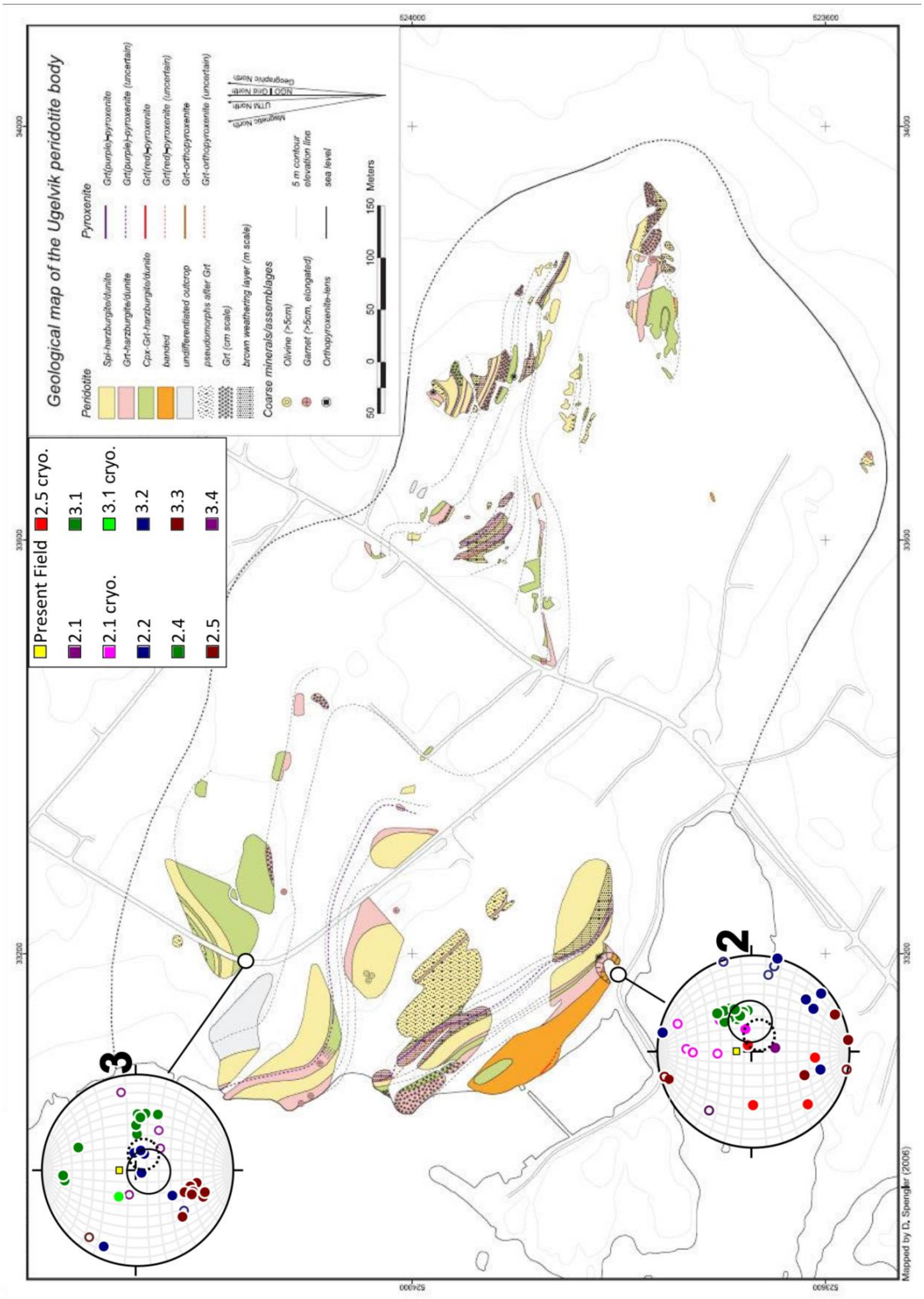

Figure 11.1-5 NRM direction map of the Ugelvik body. NRM directions for sample area 5, 6 and 8 are plotted on their respective equal-area projection plots. See Figure 11.1-4 for further explanation.

The gneisses showed large variation in NRM directions, reflected in the calculated total mean vectors, for gneiss as a whole, not being of significance. First of all did all of the locations display almost equal amount of negative and positive directions, in addition to the respective directions showing quite some scatter. For location 1 (N=6) only the positive mean vector was of significance, but it was calculated by only two measurements (33% of total), making the validity of the calculated vector questionable. Location 7 (N=31) carried mostly positive directions (61%), while only the negative mean vector was of significance. Location 9 (N=4) did also carry mostly positive directions (75%), with a positive mean vector of slight significance displaying I=57.0°, D=231.5°, a mean length of 0.9097, and a 49.6° circle of confidence at the 95% level (α_{95}). Location 4 (N=12) was the only location, within the gneiss population, that exhibited a significant total mean vector. This was calculated to be of I=5.4°, D=055.9°, a mean length of 0.8790, and a 16.9° circle of confidence at the 95% level (α_{95}).

By looking at the Raudhaugene NRM direction map (Figure 11.1-4) it became evident that the positive total mean vector for the Raudhaugene body plotted quite closely to the present day field vector. For location 6 the correlation between the present field vector and the positive mean vector for the locality was strikingly similar in direction. The negative total mean vector for the body as a whole plotted shallowly and almost normal to the present field vector. Though, within each location, the negative mean vector was only of significance for location 5.

By looking at the Ugelvik NRM direction map (Figure 11.1-5) it became evident that the total positive mean vector for the body also plotted quite closely to the present day field direction. Both the mean vectors for location 2 and 3 coincided with this total positive mean vector of the body. It also became apparent that both the positive total mean vector for the Raudhaugene and Ugelvik body was quite similar in direction.

The gneiss NRM map showed that there was no correlation between the mean vectors between each location. In addition did the mean vectors vary in direction, with location 1 and 2 being positive, location 7 being negative, and location 4 showing a total vector with both positive and negative directions.

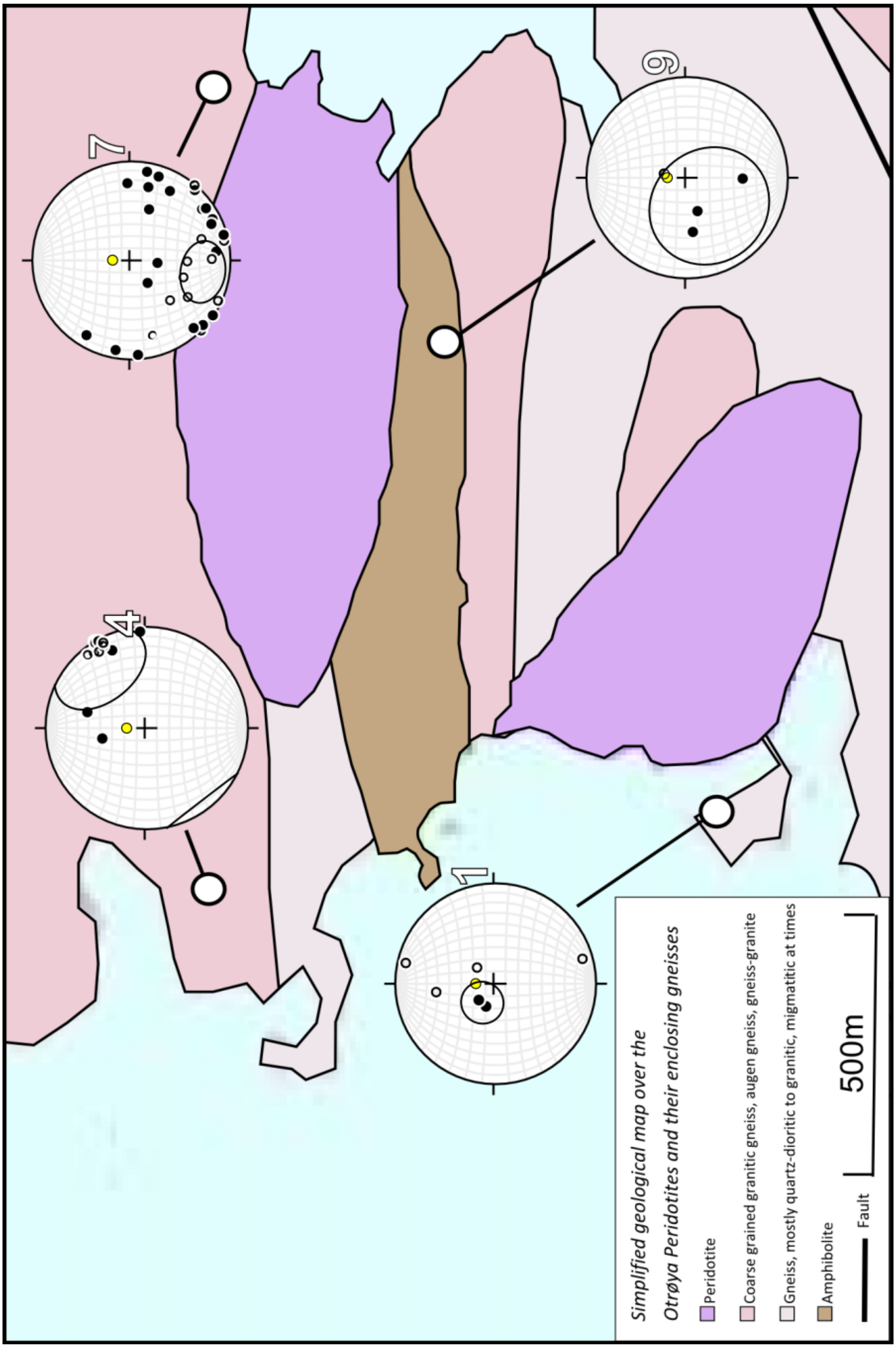

Figure 11.1-6: NRM direction map for the enclosing gneisses. The simplified geological map over the area is modified after N250 (NGU, n.d.)). NRM directions for sample area 1, 4, 7 and 9 are plotted on their respective equal-area projection plots. Open symbols indicate upward (negative) inclinations, and solid symbols represent downward (positive) inclinations. Yellow circle indicates the direction of the present day field vector. Big circle indicates the mean vector for location.

11.2 The Q-value – a method for evaluating the susceptibility versus the remanent magnetisation

The Q-value (Königsberger ratio) is a parameter to evaluate the two most important magnetic parameters – the NRM and susceptibility values. The Q-value was calculated by dividing the NRM by the induced magnetisation (susceptibility*ambient field). The ambient field used was taken from the IGRF (WMM 2010) for the Molde region (51536nT), and was converted into 41.01 A/m.

After calculation, both the Ugelvik and gneiss specimens displayed a quite similar median Q-value (~1.25), while the Raudhaugene body displayed a median which was almost twice as big (Q~2.41) compared to the two others. For all of the rocks the average Q-value was higher than the median Q-value. The Ugelvik body displayed the least difference between these values (0.75) and Raudhaugene the largest difference (4.04), indicating a non-normal distribution. The Ugelvik body displayed a relatively low standard deviation (1.94) of the values, indicating somewhat consistent values, while the gneiss rocks displayed a much higher standard deviation (5.24) and a large maximum value (26.98) indicating high extreme values. The Raudhaugene body displayed the largest standard deviation and the highest extreme values of all of them.

11.2.1 Q-value range evaluation

To evaluate the range of Q-values within each peridotite body and within the gneiss rocks, as well as its magnetic parameters, a plot of the induced magnetisation versus the NRM, with Q-value diagonals, was plotted (Figure 11.2-1). The specimens who displayed a Q-value above 1 indicated that remanence potentially could be a major contributor to the magnetic response of the rock, whilst the specimens which displayed a Q-value above 10 indicated remanence certainly dominating the magnetic response. Based on the distribution of specimens within the plot, the Raudhaugene body displayed the largest extreme values, resulting in (22%) of its Q-values being above 10 and 85% being above 1. This indicated that remanence could be a large contributor to the magnetic response for this body. For the Ugelvik and gneiss rocks, respectively 46% and 56% of the Q-values were above 1 and only 1% and 7% were above 10. These values indicated that susceptibility could be the main contributor to the magnetic response of these rocks.

In addition, the plots made it evident that the gneiss rocks predominantly consisted of two populations, where the lower population, which showed induced magnetisation of approximately 0.01 (A/m), consisted of all of the twelve specimens obtained from sample 7.2. The other population displayed considerable higher induced magnetisation values, ranging from 0.6-3 A/m. The deviation between these two populations may explain the large standard deviation for both the susceptibility and NRM values of the gneiss rocks. The plot also displayed the small range of susceptibility values within the peridotite bodies, indicated by the narrow range of induced magnetisation values.

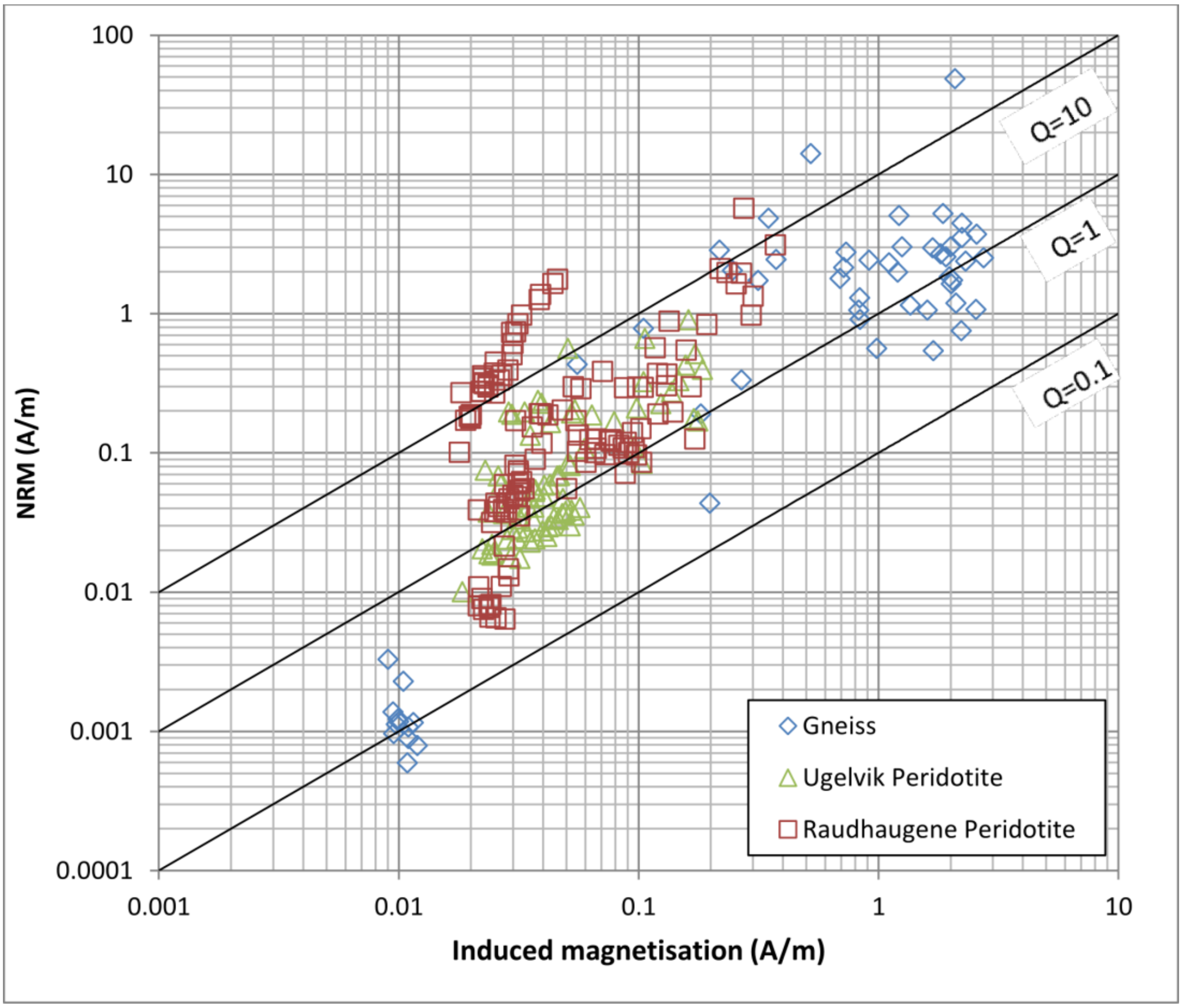

Figure 11.2-1: Log-log plot of NRM versus Induced magnetisation of 251 specimens from Otrøya. Q-value diagonals indicate the distribution of Q-values for each specimen.

11.2.2 What is controlling the Q-value?

Based on the obtained Q-values, the specimens from the Raudhaugene body showed quite some variation in contribution from remanence onto the total field vector, while the gneiss and Ugelvik specimens showed predominantly contribution from susceptibility. In Figure 11.3-1 a & b, NRM, induced magnetisation and Q-values are plotted to evaluate the relative contributions of susceptibility and remanence onto the varying Q-values.

As previously indicated by the small standard deviation of the peridotite susceptibilities, the range of susceptibilities, on the induced magnetisation versus Q-value plot (Figure 11.3-1a), was small. The plot showed, in addition, very little change in susceptibility with increasing Q-value. Figure 11.3-1b, on the other hand, indicated a much larger range and an almost linear trend between increasing NRM and increasing Q-value for the peridotite rocks. Based on this the remanence would be the controlling factor of the Q-value for the peridotite rocks.

Concerning the gneiss rocks, both of the populations showed little variation in susceptibility values compared to Q-values. The first population plotted very consistently with an average induced magnetisation of 0.01 A/m, while the other plotted with somewhat more variation with an average induced magnetisation of approximately 1.5 A/m. Though both of the gneiss populations displayed little variation they might show a minor trend indicating decreasing susceptibility with increasing Q-value. Figure 11.3-1b, on the other hand, showed an opposite trend of increasing NRM values with increasing Q-values. Based on this, remanence would be the controlling factor of the Q-value for the gneiss rocks, though susceptibility variation would be of some influence.

11.3 Real impact of remanence on total field vector

The log-log plot, of NRM versus induced magnetisation with Q-value diagonals, indicated that a large portion of the specimens could inhabit remanence that possibly could be of large contribution to the total field vector. This Q-value is a reflection of the contribution from remanence if all of the NRM vectors were in the same direction, had the same intensities, and were in exactly the same direction as the induced magnetisation vector. This infers that the Q-value only gives an estimate of maximum contribution from remanence onto the total field vector. The real contribution from remanence will always be smaller than indicated by the Q-value. To further investigate the contribution of remanence onto the total field vector, the specimens carrying negative NRM directions were compared with the specimens carrying positive NRM directions. Discussed values can be viewed in Table 11.3-1.

a

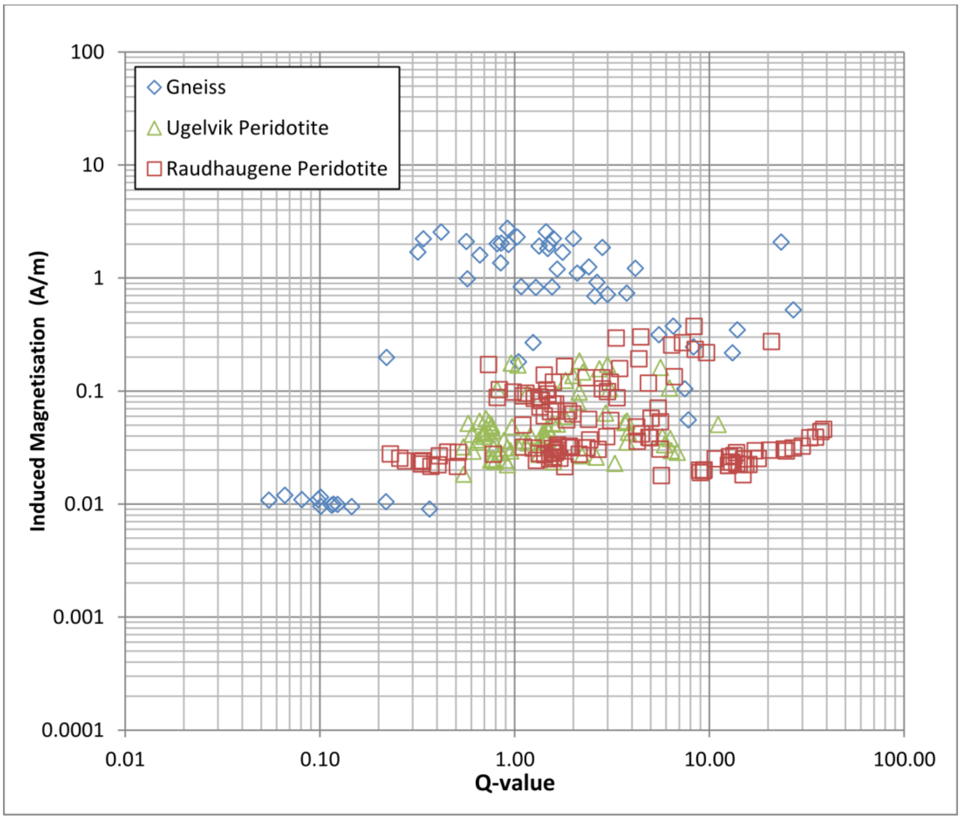

b

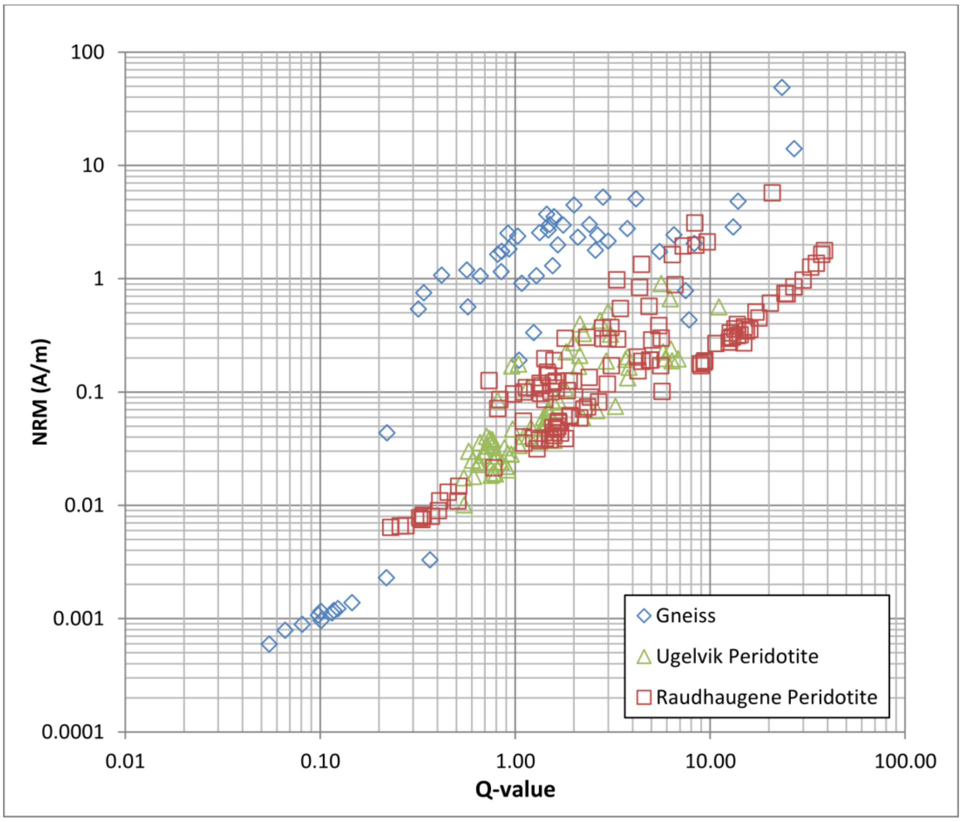

Figure 11.3-1: Log-log plots of magnetic properties of 251 specimens from Otrøya. (a) Plot of induced magnetisation versus Q-value. (b) Natural remanent magnetisation versus Q-value.

11.3.1 Investigation of variation in NRM intensity based on direction of remanence

The difference in intensities was evaluated by taking the average value of the magnetic properties of respectively the specimens displaying negative NRM directions and positive directions, of respectively the Ugelvik body, the Raudhaugene body and the gneisses. For both of the peridotite bodies the specimens carrying negative directions displayed NRM intensities with an average increase of about 50% compared with the specimens carrying positive directions. This average increase was of 0.0594 A/m and 0.1828 A/m, respectively for the Ugelvik and Raudhaugene body. However, the susceptibility of the Ugelvik body was almost the same for specimens showing positive and negative directions, with just a slight susceptibility increase of 7% for the specimens carrying negative direction. Contrary, for the Raudhaugene body, the susceptibility slightly decreased 17% (0.000294 SI) for the NRMs carrying negative directions. The gneisses displayed greatly varying values by a median value indicating 48% increase of NRM values for specimens carrying negative directions, while the average value indicated a 47% decrease of NRM intensities for the specimens carrying negative directions. Due to the little variance of values, the Ugelvik body's negative and positive directions were investigated collectively. While the Raudhaugene body, and especially the gneiss rocks displayed more varying values, and their intensities of specimens carrying opposite directions were investigated for each location.

1.1.1.1 The Ugelvik peridotite body

The two locations (2 and 3) within the Ugelvik body showed similar distribution of positive and negative directions. They also displayed similar intensities of remanence within respectively positive and negative populations. The positive mean vectors, for both locations at the Ugelvik body, were the only ones of significance and plotted quite closely, resulting in a significant total positive mean vector. When multiplying this total positive mean vector length (0.6702) with the average NRM value (0.1142 A/m) for all of the specimens carrying positive directions within the Ugelvik body, the resultant positive NRM intensity became 0.0765 A/m, which is a decrease of 33%. Even though the specimens carrying negative directions did not result in a significant total negative mean vector, they would still make an impact on the total positive mean vector, lowering the resultant positive NRM contribution of the Ugelvik body.

Table 11.3-1: Fisher mean vector calculations for positive, negative, and all values at each location, and for each peridotite body (U. all and R. all) and the constricting bedrocks (G. all). Values in bold are displaying mean values of significance used in calculations. For location 9 an odd value of 48.684A/m is excluded from the dataset. The resultant calculated NRM intensity for each location and each direction is calculated, as well as the resultant Q-value based on these resultant NRM intensities and the average induced magnetisation for each peridotite body and for the gneiss rocks.

Data set:	V.	N	D	I	a95	mean length	+ dir.	average NRM (A/m)	resultant NRM (A/m)	difr. NRM	result. Q	difr. Q
U. 2	all	42	78.6	51.3	--	0.4578		0.1597	0.0731	-54%	1.24	-39 %
	(+)	31	99.6	63.5	17.7	0.6882	74%	0.1377	0.0948	-31%	1.61	-20 %
	(-)	11	31.2	-41.4	--	0.5614		0.2279	0.1280	-44%	2.17	8 %
U. 3	all	33	178.2	66.2	--	0.4663		0.0865	0.0403	-53%	0.68	-66 %
	(+)	27	179.3	71.9	18.8	0.6963	82%	0.0872	0.0607	-30%	1.03	-49 %
	(-)	6	160.2	-84.4	--	0.6336		0.0831	0.0527	-37%	0.89	-56 %
U. all	all	75	107.8	66.6	--	0.4226		0.1270	0.0537	-58%	0.91	-55 %
	(+)	**58**	**128.3**	**72**	**13.2**	**0.6702**	**77%**	**0.1142**	**0.0765**	**-33%**	**1.30**	**-36 %**
	(-)	17	34.9	-60.7	--	0.5305		0.1736	0.0921	-47%	1.56	-23 %
R. 5	**all**	**31**	**234.2**	**0.2**	**12.3**	**0.82**		**0.5292**	**0.3926**	**-26%**	**5.86**	**-9%**
	(+)	18	224.1	22.9	7	0.9632	58%	0.7020	0.6762	-4%	10.10	57 %
	(-)	13	250.3	-33.5	11.8	0.9307		0.2899	0.2698	-7%	4.03	-38 %
R. 6	all	57	341.6	73.9	10.2	0.777		0.1036	0.0805	-22%	1.20	-81 %
	(+)	**53**	**348.7**	**75.3**	**8.1**	**0.8546**	**93%**	**0.0990**	**0.0846**	**-15%**	**1.26**	**-80 %**
	(-)	4	283.8	-37	--	0.5255		0.1638	0.0861	-47%	1.29	-80 %
R. 8	all	32	152.3	64.9	--	0.6055		0.7573	0.4586	-39%	6.85	6 %
	(+)	**28**	**142.2**	**68.8**	**18.8**	**0.6879**	**88%**	**0.6195**	**0.4261**	**-31%**	**6.36**	**-1 %**
	(-)	4	194.9	-12.5	--	0.4663		1.7223	0.8031	-53%	11.99	86 %
R. All	all	120	243.2	68.9	--	0.5374		0.3879	0.2084	-46%	3.11	-52 %
	(+)	99	237.9	81.1	9.3	0.7005	83%	0.3559	0.2493	-30%	3.72	-42 %
	(-)	21	247.7	-33.6	20.6	0.7172		0.5387	0.3864	-28%	5.77	-11 %
G. 1	all	6	3	-2.5	--	0.2321		1.6041	0.3723	-77%	0.37	-88 %
	(+)	**2**	**304.3**	**71.1**	**17.1**	**0.9977**	**33%**	**1.1807**	**1.1780**	**0%**	**1.17**	**-61 %**
	(-)	4	30.6	-58.5	--	0.5708		1.8158	1.0365	-43%	1.03	-66 %
G. 4	**all**	**12**	**55.9**	**5.4**	**16.9**	**0.879**		**2.7107**	**2.3827**	**-12%**	**2.37**	**-21 %**
	(+)	6	52.3	22	33.9	0.828	50%	3.3073	2.7384	-17%	2.73	-9 %
	(-)	6	58.8	-8.4	4.7	0.996		2.1141	2.1057	0%	2.10	-30 %
G. 7	all	31	173.7	4.4	--	0.5824		1.5395	0.8966	-42%	0.89	-70 %
	(+)	19	159.8	29.7	--	0.5963	61%	1.5720	0.9374	-40%	0.93	-69 %
	(-)	**12**	**189.4**	**-25.7**	**22**	**0.8119**		**1.4881**	**1.2082**	**-19%**	**1.20**	**-60 %**
G. 9	all	4	241	46.7	--	0.4603		1.8586	0.8555	-54%	0.85	-72 %
	(+)	**3**	**231.5**	**57**	**49.1**	**0.9097**	**75%**	**1.3777**	**1.2533**	**-9%**	**1.25**	**-59 %**
	(-)	1	10.8	-71.4	--	1		2.5799	2.5799	0%	2.57	-15 %
G. all	all	53	139.4	13.9	--	0.2876		2.6882	0.7731	-71%	0.77	-74 %
	(+)	30	142.5	53	--	0.4866	57%	3.3835	1.6464	-51%	1.64	-46 %
	(-)	23	134.8	-52.9	--	0.4357		1.7902	0.7800	-56%	0.78	-74 %

1.1.1.2 The Raudhaugene peridotite body

Within the peridotite bodies, location 5 within the Raudhaugene body was the only location which displayed both a negative and positive mean vector of significance. The location was also the only location of the peridotites which displayed intensities of positive directions higher than the intensities of the negative directions. When multiplying the length of the positive mean vector (0.963), and the negative mean vector (0.931), with their respective calculated NRM intensities their resultant intensities were of 0.702 A/m and 0.290 A/m, respectively. This was only a decrease of 7% for the negative directions, and 4% for the positive directions. Within location 5, an average total vector of I=0.2°, D=234.2° and mean length of 0.82 were, in addition, of significance based on the Fisher mean value calculation. Though this mean length does not take intensity into account, it did indicate that the negative and positive NRM directions plotted close to each other. By multiplying the percentages of each direction with its respective resultant intensity, and subtracting positive contribution with negative contribution, a possible resultant vector would be positive with intensity of 0.3926 A/m and would possibly be in the same direction as the calculated average total vector.

The two other localities (6 and 8) within the Raudhaugene body displayed significant positive mean vectors with approximately 90% positive directions, which plotted close to each other. However, they varied in intensities. The resultant positive intensity of locality 6 was calculated to be of 0.0846 A/m, while the positive resultant intensity for location 8 was substantially higher with a calculated intensity of 0.4261 A/m. For both of the locations the negative resultant vector was of no significance. Even so, it would contribute some to lower the intensity of the resultant positive intensity.

1.1.1.3 The constricting gneisses

Amongst the gneiss locations there was a large variability in mean vector orientations, displaying a negative-, positive- or total vector of significance. Their NRM and susceptibility values did also vary from location to location (Figure 11.1-1 and Figure 11.1-3). For location 1 there was only 6 measurements, were the only significant mean vector was consisting of two positive NRM directions. Both the positive and negative NRM vectors displayed similar average intensities of approximately 1.8 A/m. The calculated resultant positive intensity was of 1.178A/m, but is probably substantially lower due to the contribution from the negative NRM intensities.

For location 4 there was an equal amount of positive and negative NRM directions, with resultant intensities of respectively, 2.738 A/m and 2.106 A/m. Both vectors plotted extremely shallow at the same place within the equal area plot, resulting in a significant total vector. Based on their intensities they could cancel each other out, only giving a small positive contribution. Another explanation, favoured by the author, is that a slight error was imposed on the obtained directions due to sampling or measuring in the spinner- or cryogenic magnetometer. A slight error can easily swap the direction of the obtained NRM intensity due to the extreme shallow inclination of the vector. Based on this, the intensity of the total resultant vector could either give a strong positive or strong negative contribution with a resultant calculated intensity of 2.383 A/m.

Location 7 displayed a large scatter in distribution of NRM directions, while the negative and positive intensities displayed quite similar values (1.488 A/m and 1.572 A/m, respectively). However, as previously indicated, specimens from sample 7.2 carried much weaker susceptibility and remanence intensities than the other gneiss samples, though it carried both negative (N=8) and positive (N=6) directions. For further calculations, these values were included. The location displayed mostly positive directions (61%) but the resultant negative vector was the only one of significance. The resultant negative intensity was of 1.208 A/m, but due to the impact from the positive directions, this value is probably much lower.

Location 9 displayed the largest NRM intensities of all the gneisses. This average intensity was largely controlled by one extreme value of 48.7 A/m, and was excluded from calculations. The resultant positive vector consisted of 75% of the measured specimens (N=4) and was the only one of significance. Its resultant positive intensity was of 0.975 A/m. The only specimen displaying a negative value displayed a much higher intensity of 2.580 A/m, and would lower the resultant positive intensity.

11.3.2 Real intensity of remanence and its effect on the Q-value

Due to little change in susceptibility for both the specimens carrying negative and positive directions, and due to the trend plots (Figure 11.3-1) indicating that remanence largely explains the variety in Q-values, the average induced magnetisation for respectively the Ugelvik and Raudhaugene bodies and the gneisses were used for calculating the resultant Q-value at each location. For the purpose of showing the effect of vector direction onto the resulting Q-value, using the average induced value is good enough for the calculation, even though it did vary from location to location and between intensity directions. In addition, the resultant Q-value for each location is compared with the average Q-value from the whole peridotite body, or the average Q-value for all the gneiss rocks. This comparison is probably also incorrect due to the variation described above, but is also evaluated as good enough for this demonstration of effect of vector direction onto the resulting Q-value.

For the Raudhaugene body, location 5 had a calculated total remanent intensity of 0.393 A/m. By dividing this total intensity with the average induced magnetisation of the Raudhaugene body (0.0669 A/m) the Q-value became 5.86, displaying a decrease of 9% from the initial average Q-value (6.45) of the whole body. For location 6 and 8, the positive remanent intensity was evaluated, and for location 6 this resultant intensity was 0.085 A/m, with a resultant Q-value of 1.26, displaying a decrease of 80% from the initial Q-value (6.45). For location 8, the positive resultant intensity was 0.426 A/m, and the resultant Q-value was 6.36, displaying a decrease of 1%.

For the gneiss rocks the average induced magnetisation was of 1.0045 A/m and the average Q-value was 3.01. At locality 1 and 9 the positive remanent intensity was evaluated. At location 1 this was 1.1780 A/m resulting in a Q-value of 1.17, displaying a decrease of 61%. At location 9 the intensity was 1.2533 A/m resulting in a Q-value of 1.25, displaying a decrease of 59%. For location 4 a total remanent intensity, was 2.3827 A/m resulting in a Q-value of 2.37, displaying a decrease of 21%. Lastly, at location 7 a negative remanent intensity of 1.2082 A/m was evaluated, resulting in a Q-value of 1.20, displaying a decrease of 60%.

11.3.3 The real contribution of remanence to the total magnetic field intensity

Based on the real intensity of remanence, the Q-value would be substantially lowered for all locations when taking vector directions and intensity differences into account. In addition would the calculated resultant intensity for each location be an approximate maximum contribution, due to the resultant vector intensity being calculated just for the vector of significance, which in most cases was either negative or positive. This was an exception for location 5 and 4, which displayed significant total vectors. For location 5 the calculated total vector would probably be closer to the real intensity, due to the opposing intensities being taken into account during the calculation. For location 4 the calculated total intensity is the maximum intensity either in a positive or negative direction. However, as discussed, another possibility would be that they cancel each other out.

Plots and calculations demonstrated that, regarding the peridotite bodies, the controlling factor of the Q-value was the remanent intensity, due to the very low and stable susceptibility values of the specimens. For the Ugelvik body the remanent intensities were also low, reflected in the low resultant Q-value of 1.3. The total positive remanent intensities within the Ugelvik body had a direction close to the earth’s magnetic field at Otrøya, and due to the low remanent intensities a contribution to the total field would possibly, in this case, only create a minor positive anomaly.

The Raudhaugene body displayed high remanent intensities at location 5 and 8, with corresponding high resultant Q-values (5.86 and 6.36). For location 5 the resultant NRM direction was plotting positive and shallowly almost normal to the field intensity, and would therefore probably only result in a slight positive anomaly, even though its specimens carried remanence of relatively strong intensities. On the other hand, at location 8 the positive mean vector was plotting almost at the same place as the field vector. Based on this it would make a greater positive contribution to the total magnetic field at location, possibly creating a positive anomaly. Location 6 displayed similar remanent intensities and Q-values as the Ugelvik body. Its remanent contribution was positive in the same direction as the magnetic field at location. Based on this dataset, location 6 could create a slight positive anomaly.

Compared to the peridotites, the constricting gneisses displayed Q-values similar to the Ugelvik body, while the plots of remanent and induced magnetisation demonstrated that the constricting gneisses carried higher intensities, except for one odd core (7.2) at location 7. The overall higher intensities of remanent magnetisation displayed by specimens collected from the constricting gneisses, indicates that the gneisses probably would give a greater contribution to the total magnetic field intensity, compared with the peridotites. For location 1 the remanent vector plots close to the ambient field vector, possibly resulting in a positive contribution to the total magnetic intensity, thus a positive anomaly. For location 4 the remanent vector plots shallowly to the field vector, and could either make a positive or negative contribution to the total magnetic field, creating a positive or negative anomaly. Another possible scenario is that these “opposite intensities” could cancel each other out possibly resulting in no contribution onto the total magnetic field. For location 7 the remanent vector is negative plotting shallowly almost normal to the field vector, making a slight negative contribution onto the total magnetic intensity, possibly creating a negative anomaly. Location 9 displayed a positive remanent vector with an approximate angle of 45° onto the steep field vector giving a positive contribution to the total magnetic intensity at location, thus possibly creating a positive anomaly.

11.4 Magnetic properties obtained from hysteresis measurements

Information on saturation and coercivity properties of the rocks were provided by room-temperature hysteresis measurements made on fourteen chips from the Ugelvik body, sixteen chips from the Raudhaugene body, and seven chips from the constricting gneisses. All values were obtained after paramagnetic corrections, and values discussed can be viewed in Table 11.4-1. Based on the shape of the hysteresis loops obtained from the chips, their respective specimens were classified into magnetic properties displaying mostly paramagnetic, ferromagnetic, or a mixture of both properties. Based on the assumption of magnetite being present in the samples, the width of the loops indicated presence of both SD and MD magnetite. A Day-Plot gave further information on domain state of magnetite, possibly being of either the SD or MD state, or a possible mixture of these domains, as well as possible PSD magnetite. Some samples plotted outside the plot due to low *Hcr/Hc* and M_{rs}/M_s ratios, probably due to too small amounts of magnetic minerals present in the chip. Some plotted outside the plot due to high *Hcr* values indicating possible contribution from other magnetic minerals.

11.4.1 Saturation and coercivity properties

The Ugelvik body displayed a range of saturation magnetisation (M_s) from 2.745 to 165,300 µA m^2/kg, and a far lower saturation remanence (M_{rs}) ranging from 0.2313 to 32,670 µA m^2/kg. The M_{rs}/M_s ratios were all less than 0.14. Based on Dunlop (2002) nonequidimensional grains consisting of magnetite indicate a M_{rs}/M_s value of maximum 0.5. This Ugelvik M_{rs}/M_s ratios with maximum value of less than 0.14 indicates a dominant induced component, possibly explained by presence of MD magnetite.

Table 11.4-1: Table over obtained hysteresis parameters, coercivity (Hc), remanent coercivity *(Hcr)*, saturation remanence (M_{rs}), saturation magnetisation (M_s), M_{rs}/M_s ratios and *Hcr/Hc* ratios. Cells in green are from the Ugelvik body, cells in red are from the Raudhaugene body, and cells in blue are from the constricting bedrocks. Red text indicates chips that were not plotted in the Day plot (Figure 11.6-1).

Chip	Hc (mT)	Mrs (µAm^2/kg)	Ms (µAm^2/kg)	Hcr (mT)	Mrs/Ms	Hcr/Hc	Magnetism	Mag. Domain
1.1-2T	2.467	67.98	918.2	5.617	0.05786	2.27685	Ferro	PSD
2.1-3	19.05	18.59	116.9	24.61	0.06066	1.29186	Ferro/Para	PSD
2.2-1	8.949	21700	165300	19.34	0.07980	2.16114	Ferro	85% MD
2.2-2T	16.08	32670	154300	27.4	0.12505	1.70398	Ferro	70% MD
2.2-3T	9.691	77.16	400.6	17.77	0.13299	1.83366	Ferro	70% MD
2.4-4	15.25	4093	42620	24.93	0.02284	1.63475	Para/Ferro	PSD
2.5-2	15.08	3.163	27.37	32.52	0.01676	2.15650	Para/Ferro	PSD
2.5-4	13.25	6168	26830	24.92	0.04818	1.88075	Ferro/Para	PSD
3.1-3	13.94	5077	36780	28.32	0.04287	2.03156	Para/Ferro	PSD
3.1-4	14.42	6519	43910	32.58	0.04528	2.25936	Para/Ferro	PSD
3.1-5	13.65	7.191	60.1	30.26	0.03699	2.21685	Para/Ferro	PSD
3.2-3T	-1.321	0.2313	2.745	22.46	0.00142	-17.00227	Para	
3.2-4B	19.05	20480	72790	27.69	0.09931	1.45354	Ferro/Para	PSD
3.3-4	9.991	8214	57740	18.75	0.05684	1.87669	Ferro/Para	PSD
3.4-1	14.04	1874	21490	31.9	0.01470	2.27208	Para/Ferro	PSD
4.2-1B	1.709	1429	181000	21.82	0.00747	12.76770	Ferro	
4.4-2T	0.259	0.3015	323.2	23.51	0.00087	90.77220	Ferro	
5.1-3	7.069	8.306	10.74	13.4	0.02873	1.89560	Para	PSD
5.2-1B	10.89	-2.138	35.16	35.67	-0.00812	3.27548	Para/Ferro	
5.2-3B	6.134	1048	40520	22.16	0.00800	3.61265	Para/Ferro	
5.3-3	13.19	2.714	33.78	49.65	0.01418	3.76422	Para/Ferro	PSD
6.1-2B	25.78	35190	111900	33.77	0.16050	1.30993	Ferro	60% MD
6.1-3B	29.93	52930	127100	37.41	0.23505	1.24992	Ferro	40% MD
6.2-2B	18.21	44.01	219.1	29.86	0.11089	1.63976	Ferro	75% MD
6.3-1B	9.941	2159	50040	44.41	0.01535	4.46736	Para/Ferro	PSD
6.3-3B	16.37	2919	35670	45.78	0.02331	2.79658	Para/Ferro	PSD
6.6-1B	33.07	17060	68670	54.55	0.09977	1.64953	Ferro	75% MD
6.6-5	32.88	25.28	95	50.22	0.10193	1.52737	Ferro	75% MD
7.1-2	2.238	49.02	2495	11.28	0.01697	5.04021	Ferro	MD
7.2-5	25.28	178.3	1318	54.74	0.00479	2.16535	Para	
7.4-3	5.519	252.4	4291	20.27	0.05414	3.67277	Ferro	90% MD
8.1-1	18.85	48800	156700	25.81	0.20045	1.36923	Ferro	50% MD
8.1-5	12.88	80.63	410.6	26.55	0.15241	2.06134	Ferro	75% MD
8.2-1	20.32	63970	215300	31.06	0.20908	1.52854	Ferro	55% MD
8.2-2	21.32	150.8	493.1	30.76	0.22578	1.44278	Ferro	50% MD
8.3-3B	19.1	28.88	97.98	32.88	0.13140	1.72147	Ferro/Para	70% MD
9.1-2	3.627	39.57	903.6	19.69	0.02726	5.42873	Ferro/Para	MD

One chip, from location 5 (5.2-1B) within the Raudhaugene body, displayed paramagnetic features due to negative M_{rs} value, indicating the value probably was zero. The rest of the chips displayed M_s values ranging from 10.74 to 215,300 µA m^2/kg, and a far lower M_{rs} range from 2.714 to 63,970 µA m^2/kg. All M_{rs}/M_s ratios were less than 0.28, indicating presence of minerals contributing both to the induced and remanent component, possibly explained by presence of both MD and SD magnetite.

The M_s values within the Raudhaugene body, were substantially larger compared to the M_s values of the Ugelvik body. This is indicative of presence of more magnetic material. Additionally, the higher M_{rs}/M_s value of the Raudhaugene body indicating that the Raudhaugene body probably contains more SD magnetite than the Ugelvik body.

The gneisses displayed a significantly larger range in hysteresis properties than the peridotites. A chip from location 7 (7.2-5) displayed paramagnetic features due to a very low M_{rs}/M_s ratio. On the other hand, a chip (4.2-1B) from location 4 showed considerably higher hysteresis parameters than the rest of the gneisses, with a M_s value of 181000 µA m^2/kg and a M_{rs} value of 1429 µA m^2/kg. Though, another chip (4.4-2T) from the same location, but from another core, showed the lowest hysteresis values within the gneisses, with a M_s value of 323.2 µA m^2/kg, and a M_{rs} value of 0.3015 µA m^2/kg. The M_{rs}/M_s ratios did also display quite some range, from 0.87 10^{-3} to 0.058, though all of them were extremely low compared to the peridotite ratios. The gneiss M_{rs}/M_s ratio showed that the induced component by far was the dominant magnetic contributor. If only explained by magnetite, this could indicate presence of MD magnetite.

Due to the different mineral composition of the gneisses compared to the peridotites, the normalised values of M_{rs} and M_s, based on mass, could not be compared from one rock type to the other. The comparison of the magnetic properties obtained from the two peridotite bodies was based on the assumption that they inhabit approximately the same mineral content.

11.5 Hysteresis loop interpretation

The Ugelvik body displayed mostly a mixture of a paramagnetic and ferromagnetic behaviour, with the paramagnetic behaviour being the prominent (Figure 11.5-1). Though, chips from core 2.2 displayed ferromagnetic behaviour. In addition, in chips within sample 3, paramagnetic behaviour (chip 3.2-3T) and a mixture with prominent ferromagnetic behaviour (Figure 11.5-2) were observed.

Within the Raudhaugene body all of the chips from location 6 and 8 displayed prominent ferromagnetic behaviour (Figure 11.5-3 and Figure 11.5-4), with exception from chips from core 6.3, which displayed a prominent paramagnetic behaviour with a small ferromagnetic contributor (Figure 11.5-5). At location, 5 chip 5.1-3 displayed prominent paramagnetic behaviour (Figure 11.5-6). The other chips from location 5 displayed a mix of paramagnetic and ferromagnetic behaviour, with paramagnetic being the prominent one.

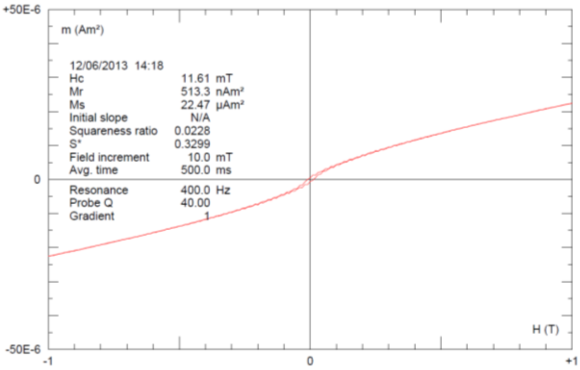

Figure 11.5-1: Chip from specimen 2.4-4 displaying a paramagnetic and ferromagnetic behaviour, with paramagnetic being the prominent one.

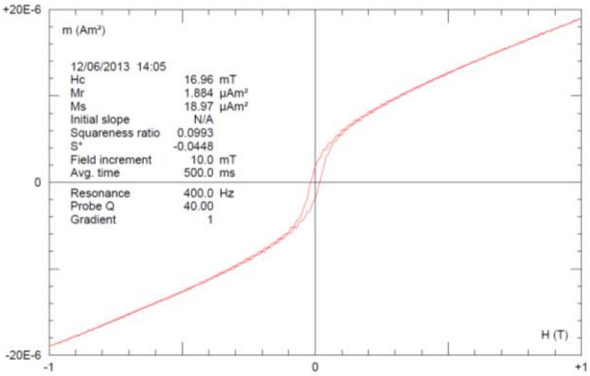

Figure 11.5-2: Chip from specimen 3.2-4B displaying a mix of ferromagnetic and paramagnetic behaviour, with ferromagnetic being the prominent one.

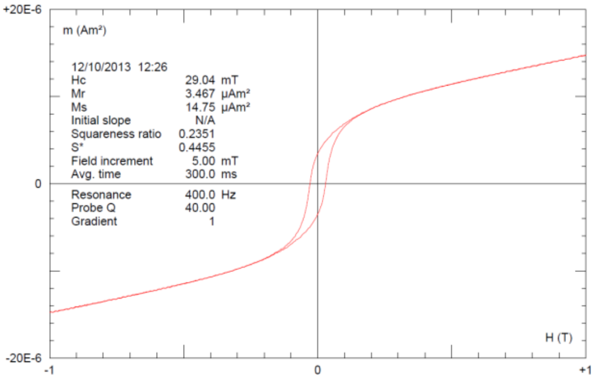

Figure 11.5-3: Chip from specimen 6.1-3B displaying a prominent ferromagnetic behaviour, with a large H_c value.

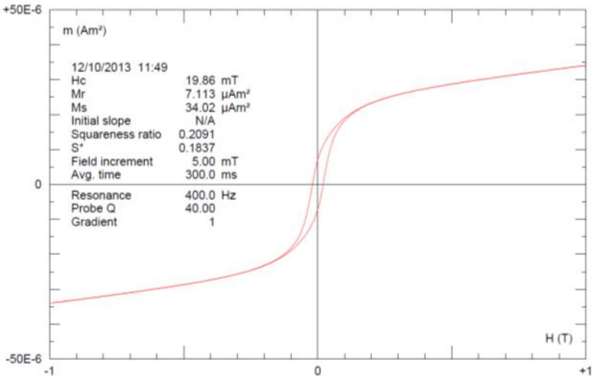

Figure 11.5-4: Chip from specimen 8.2-1 displaying a prominent ferromagnetic behaviour, with a large M_s value.

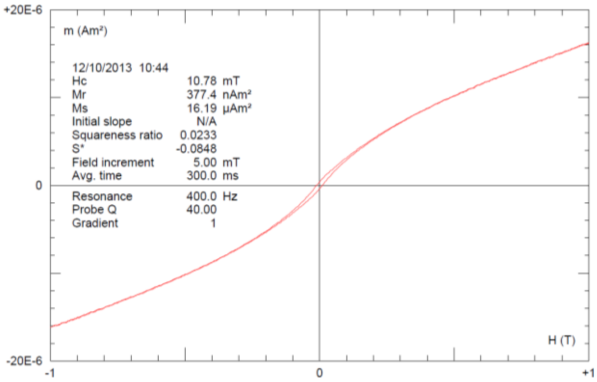

Figure 11.5-5: Chip from specimen 6.3-3B displaying a mix of paramagnetic and ferromagnetic behaviour, with paramagnetic being the prominent one.

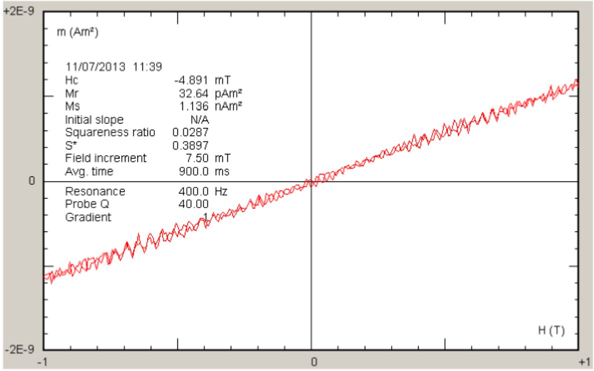

Figure 11.5-6: Chip from specimen 5.1-3 displaying prominently paramagnetic behaviour and a lot of noise possibly giving errors in data.

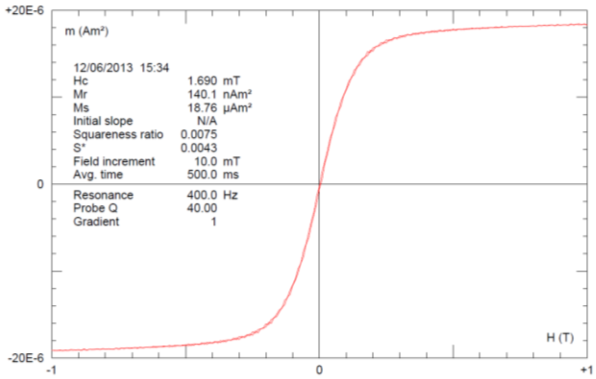

Figure 11.5-7: Chip from specimen 4.2-1B displaying ferromagnetic behaviour with approximately no paramagnetic contribution.

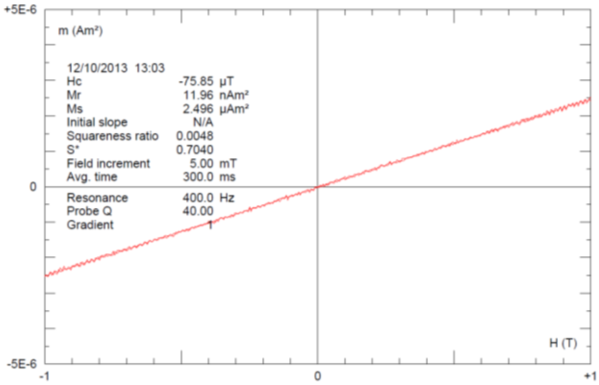

Figure 11.5-8: Chip from specimen 7.2-5 displaying a distinct paramagnetic behaviour.

The gneisses displayed prominent ferromagnetic behaviour with little or close to no paramagnetic contribution (Figure 11.5-7). The only exception was from chip 7.2-5, which showed a distinct paramagnetic hysteresis curve (Figure 11.5-8).

The width of the hysteresis loops were interpreted based on presence of magnetite, indicating its possible domain state. The chips from the Ugelvik body mostly displayed slim loops indicating multi domain behaviour, with exception from the three chips obtained from core 2.2. They displayed somewhat wider loops indicating single domain behaviour. Apart from the chips displaying dominating paramagnetic behaviour, the chips originating from the Raudhaugene body mostly displayed relatively wide loops. Especially the loops from sample 6.1 and location 8 displayed wide loops, indicating single domain behaviour. The hysteresis loops obtained from the gneisses were all very slim. The chip from specimen 7.4-3 was the only chip displaying a hysteresis loop with some width. Inferred from this, all of the gneisses displayed hysteresis loops indicating MD magnetite behaviour.

11.6 Day plot interpretation

Due to the Day-plot being constructed on theoretical and experimental data of pure, end-member, TM0 magnetite, any contribution from other minerals would make a contribution on the plotting results. This implies that the plot gives an indication on the domain state of the magnetite present in the samples, but errors such as the chips not being representative of the magnetite content within the whole sample, or other minerals interfering with the magnetic signal of magnetite could obstruct the plotted values. However, assuming only end-member magnetite present in the samples, the Day plot gives information on the domain state of magnetite present in the samples, and is presented in the section below. Further evaluations on the effect of other magnetic minerals were also done. To obtain more information on the domain state of the magnetite present in the samples, magnetic separates could be studied.

11.6.1 Domain state of magnetite present in chips

By plotting the obtained values for M_s, M_{rs}, H_c and H_{cr} in a Day Plot (Figure 11.6-1), further investigation of domain state of possible magnetite was investigated. The plot made it obvious that all of the peridotite chips displayed PSD behaviour for magnetite. However, four chips, previously indicated with prominent paramagnetic behaviour or mixed behaviour with paramagnetic being the prominent one (3.2-3T, 5.2-1B, 5.2-3B and 7.2-5), plotted outside the Day plot, due to their M_{rs}/M_s ratios being below 0.01, or due to negative Hcr/Hc ratios. All of these chips displayed, in addition, hysteresis loops with a lot of noise. This noise indicates little magnetic content within the sample, and noise can explain the presence of negative values. In addition plotted two chips (5.3-3 and 6.3-1B), from the Raudhaugene body, close to the multi domain area of the Day Plot. These were previously indicated as behaving mixed with paramagnetic being the prominent one. The high *Hcr* value of these chips could be explained by noise.

Based on Dunlop's (2002) theory, about the PSD behaviour being explained by a mix of both SD and MD magnetite grains, his two theoretical mixing lines, based on experimental data of pure TM0 magnetite, were drawn into the plot. The rest of the Raudhaugene chips, not discussed, plotted as two populations close to the far left single domain-multi domain (SD-MD) mixing line at the SD side. Based on this mixing line, the population closes to the SD side, consisting of chips from sample 8.2, 6.1 and chip 8.1-1, indicated 40% to 60% SD magnetite behaviour of the grains. The other population consisted of chips from sample 6.2 and 6.6, and chips 8.1-5 and 8.3-3B, indicating a 20 to 40% SD magnetite behaviour of the grains. The majority of the Ugelvik samples plotted relatively far from the SD-MD magnetite mixing lines. A paramagnetic-ferromagnetic (P-F) border was drawn into the Day plot based on previous observed hysteresis behaviours of the chips. The Ugelvik chips plotting closely above the line showed a mix with prominently ferromagnetic behaviour, while the ones plotting below it displayed a prominently paramagnetic behaviour. Except from the chips displaying mixed behaviours, three chips, all from sample 2.2 plotted closely to the SD-MD magnetite mixing line, indicating 25-30% SD behaviour.

Only four of the seven chips from the gneisses plotted within the Day plot. Of the ones plotting outside were both of the samples from location 4, which displayed M_{rs}/M_s ratios below 0.01, and Hcr/Hc ratios of 12.9 and 92.6. These values possibly indicated magnetic contribution from another magnetic mineral. The other chip was 7.2-5, which previously was indicated with dominating paramagnetic behaviour and displayed a negative Hcr/Hc ratio, as previously explained, due to noise. Within the day plot, chip 1.1-2T plotted within the PSD, 7.4-3 plotted at the SD-MD mixing line indicating 90% MD magnetite behaviour, 7.1-2 plotted within the MD area, and 9.1-2 plotted above the MD area.

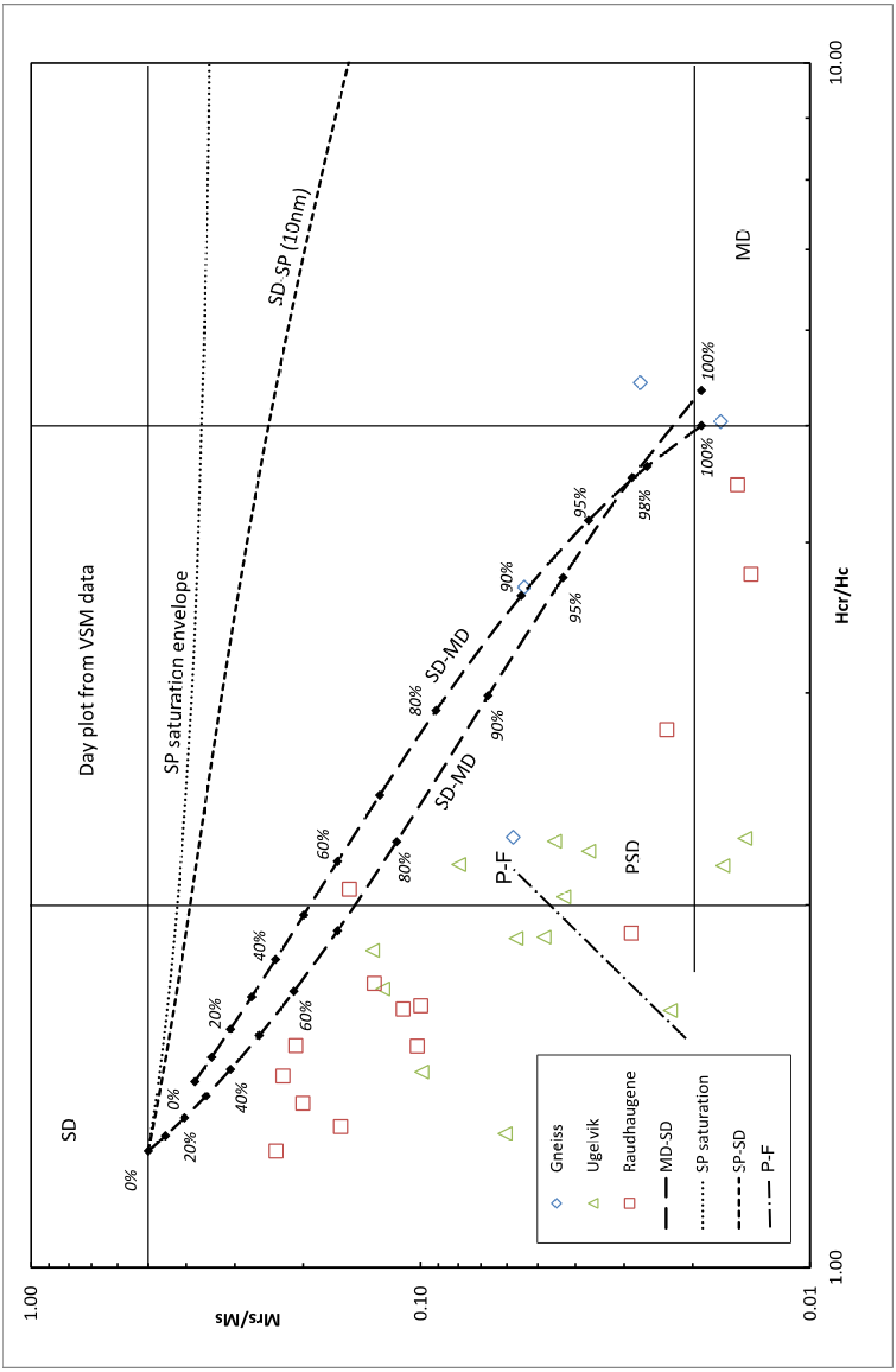

Figure 11.6-1: Day plot of the obtained *Ms, Mr, Hc* and *Hcr* values. The P-F line indicates an observed boarder between loops indicating mixed paramagnetic and ferromagnetic behaviour, with prominent paramagnetic contribution plotting below, and with prominent ferromagnetic contribution plotting closely above. See text for further explanation. The plot is based on the theoretical day plot curves for magnetite, by Dunlop (2002).

11.6.2 The effect of several magnetic minerals in the Day plot

The assumption of magnetite being the only magnetically contributing mineral was not correct. This became evident after investigations of magnetic minerals both in optical microscopy and backscatter electron microscopy. Within the thin sections of peridotite, both magnetite and varieties of Cr-spinel and chromites were present. Within the constricting bedrocks, referred to as gneiss, thin sections contained both magnetite and hemo-ilmenite lamellae. Cr-spinels, chromites and hemo-ilmenite lamellae are known to contribute magnetically, while they contribute differently. The hemo-ilmenite creates strong remanent magnetisation, while Cr-spinels and Chromites are seldom a major contributor to remanence, and based on their composition they can either be ferromagnetic, antiferromagnetic or paramagnetic at ordinary temperatures.

11.6.2.1 The peridotites

The Day-plot displayed mostly peridotite plotting closely, but under, the SD-MD mixing lines. The magnetic contribution of Cr-spinels and chromites could be the reason for these chips plotting slightly of the mixing line. When these minerals are under conditions that are close to their T_c they could carry a remanent intensity which is lower than normal, but its susceptibility would be approximately the same for these conditions. This effect could contribute to lower the Mrs/Ms ratio, explaining the chips in the Day plot in this study plotting slightly lower than the theoretical mixing line. However, if the composition of these Cr-spinels and chromites indicates possibility of magnetic contribution – has not been investigated. However, if the Cr-spinels and the chromites contribute in such a way that the chips are plotting slightly shifted away from the mixing lines, the chips plotting close to the mixing line could possibly be consisting of a mix of SD and MD magnetite grains creating PSD behaviour.

11.6.2.2 The gneisses

All of the samples from the constricting gneiss rocks displayed ilmenite with hematite exsolutions. A magnetic contribution from hemo-ilmenite lamellae would possibly make the chips plotting differently than if they were only containing magnetite. However, the effect of hemo-ilmenite on the Day plot has not been studied.

The chips of location 4 displayed high *Hcr/Hc* ratios, and therefore plotted outside the Day-plot diagram. In addition, they displayed fairly low M_{rs}/M_s ratios. These observations could be due to magnetic contribution from hemo-ilmenite. Of the constricting bedrocks, thin section from sample 9.1 displayed the largest concentration of oxides, being especially abundant in hemo-ilmenite and large magnetite grains. This sample plotted above the MD area of the Day Plot indicating both high M_{rs}/M_s and *Hcr/Hc* ratios. This high M_{rs}/M_s ratio could possibly be due to magnetic contribution from lamellar magnetism. Contrastingly, chip 1.1-2T plotted in the PSD area displaying fairly low *Hcr/Hc* ratios. A thin section from this area did display hemo-ilmenite and magnetite. In addition did NRM intensities of specimens from this location display high NRM intensities. An explanation for this PSD position of the chip in the day plot could be due to the chip not being representative of the magnetic minerals of the whole sample (1.1). The chips from sample 7 plotted within the MD area and on the uppermost mixing line, not displaying interference from another magnetic mineral than magnetite. Though, they both inhabited hemo-ilmenite. Due to the small chip size the chip could also not be representative for its origin sample, and hemo-ilmenite could be lacking from these chips. Thus, the chips could possibly only be responding to the magnetite present in the chips, and can therefore be observed nicely plotting on the mixing line.

12 Investigation of magnetic response of magnetic minerals based on density and magnetic properties

The magnetic properties and densities were compared with each other, as well as the mineralogy of the locations, and finally its magnetic response. The investigation is based on the intensity of NRM before vector directions was taken into account; hence also Q-values reflect this uncorrected NRM intensity.

12.1 Density variation within the peridotites

Based on Evans et al. (2013) and Fichler et al. (2011) a serpentinized rock displays decreasing densities with increasing degree of serpentinization, while their magnetic susceptibility is increasing with increasing degree of serpentinization. The peridotite rocks of Otrøya are known to have undergone serpentinization, hence should be lighter than un-serpentinized peridotite rocks. Based on Fichler et al. (2011) an un-serpentinized rock displays a density range of 3.2 to 3.4g/cm^3. All of the peridotite specimens from the Ugelvik and Raudhaugene body displayed densities lower than this density range.

Based on the density observations of the peridotite rocks the Ugelvik body displayed specimens which were substantially denser than the Raudhaugene specimens, as shown by plotting the densities for each sample with its corresponding susceptibility value (Figure 12.1-1). In addition, change in density versus susceptibility appeared with a possible trend for the Raudhaugene specimens. A trendline with the same slope was plotted for the Ugelvik body. For the Ugelvik specimens this correlation between decreasing density versus increasing susceptibility was less apparent.

By optical microscopy the estimated degree of serpentinization (Table 12.2-1) indicated that the Ugelvik body was less serpentinized than the Raudhaugene body. This fits well with the observations in Figure 12.1-1. In addition, the Raudhaugene specimens display higher susceptibility values than the Ugelvik specimens, which fits with the statement of decreasing density with increasing susceptibility. However, specimens with low densities were plotting both for low and high susceptibilities. This could indicate alteration or weathering processes possibly creating porosity in the rock, making it less dense as a result other than serpentinization. Another explanation, favoured by the author, is that the varying peridotite lithology within the peridotite bodies could impose a controlling factor on creation of magnetite through serpentinization.

A plot of density versus NRM (Figure 12.1-2) for the Ugelvik and Raudhaugene bodies displays that the Raudhaugene specimens also carry the highest NRM values, though a correlation between decreasing density and increasing NRM is not apparent in this plot. However, the Ugelvik specimens could possibly display increasing NRM with decreasing density. Some of the Raudhaugene specimens seem to follow this trend.

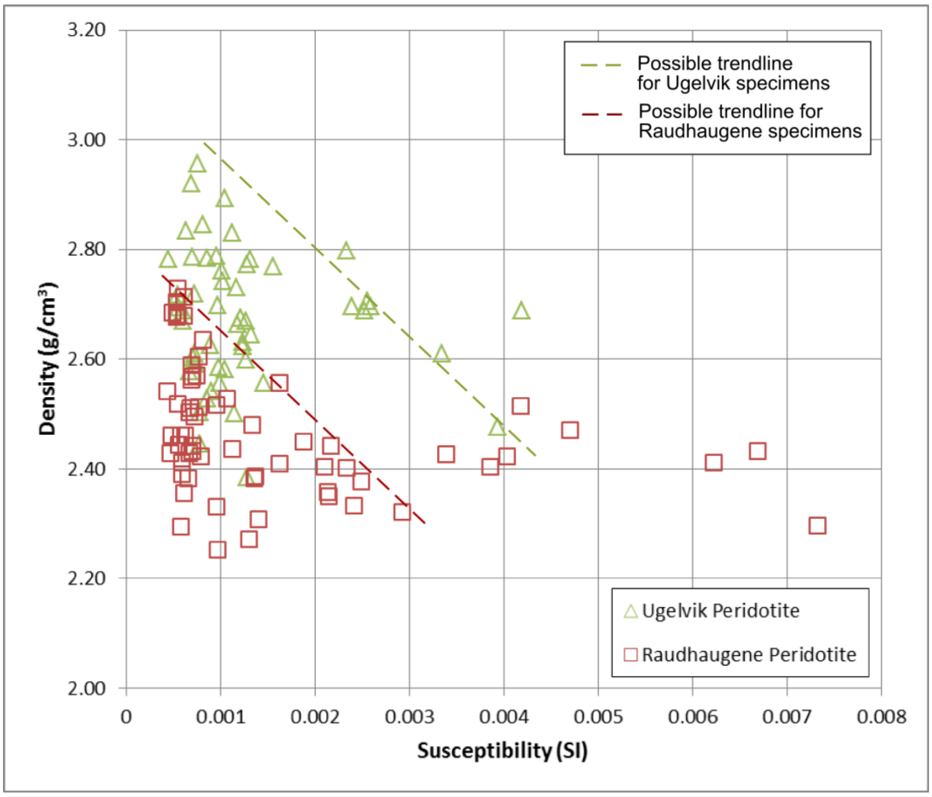

Figure 12.1-1: Density versus susceptibility for the Ugelvik and Raudhaugene peridotite specimens. A slight possible trendline is plotted for the Raudhaugene body, and a even less apparent trendline, with the same slope, is plotted for the Ugelvik specimens.

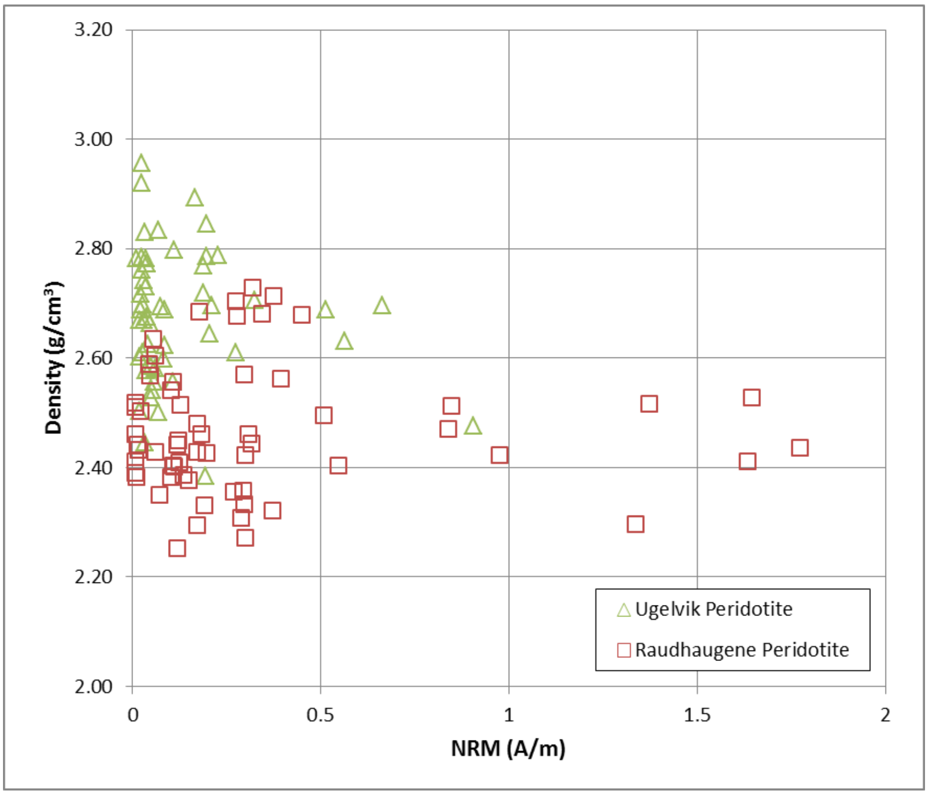

Figure 12.1-2: Density versus NRM for the Ugelvik and Raudhaugene peridotite specimens. A slight possible trend for decreasing density with increasing NRM for the Ugelvik specimens is somewhat apparent. Specimen 8.2-2a is excluded from the plot due to high value (5.7292 A/m).

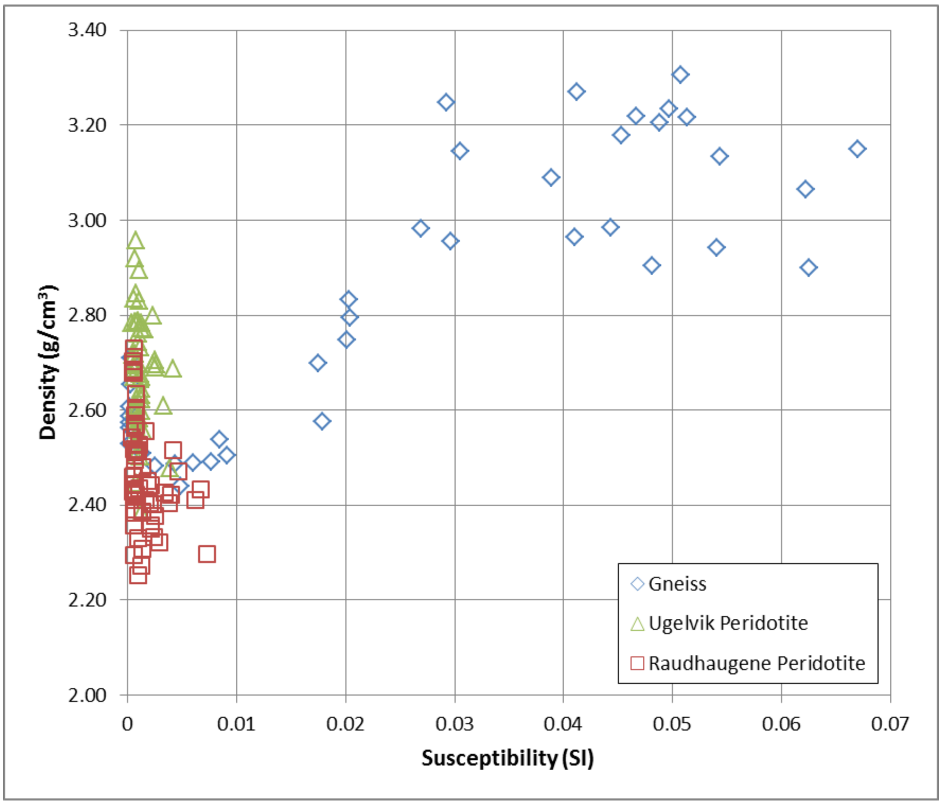

Figure 12.1-3: Density versus susceptibility for all specimens. A possible trend for increasing density with increasing NRM for the gneiss specimens is apparent.

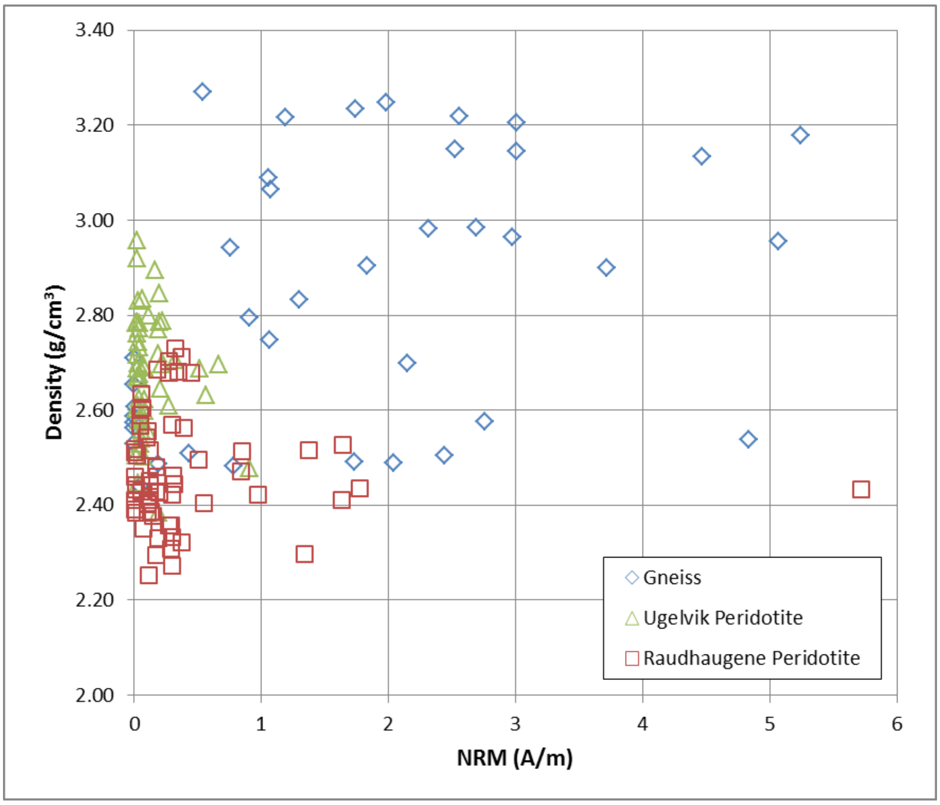

Figure 12.1-4: Density versus NRM for all specimens. No correlation between density and NRM is apparent for the gneiss specimens.

12.2 Density variation within the gneisses

By adding the susceptibility and NRM intensities of the gneiss specimens in the density versus susceptibility and density versus NRM plots, respectively, Figure 12.1-3 and Figure 12.1-4, the gneiss specimens were evaluated. It became apparent that the gneiss specimens display a possible trend of increasing susceptibility with increasing density. This correlates well with the observations of higher magnetite content in the thin sections sampled from areas with high susceptibility values. An example is for thin section 9.1 and 7.4 which both displayed large magnetite grains of MD size.

In the density versus NRM plot (Figure 12.1-4) the gneisses displays no correlation between the two properties. Based on microscopy, hemo-ilmenite and magnetite were the magnetic minerals that could be the main contributors to remanence for the gneisses. This scatter could be explained by differences in content of these. For a specimen with magnetite carrying the remanence, its density could be fairly low compared to a specimen with presence of hemo-ilmenite contributing to remanence. Magnetite of SD size would make up a tiny part of the total volume percent in the specimen, compared to hemo-ilmenite which would make up a bigger part of the total volume, while making the same contribution to remanence in respect to intensity.

Locality	assigned density (g/cm3)	est. Degree of serp. (%)	vol. corr. NRM (A/m)	Q-value	volume corr. Susc. (SI)	calc.vol % mag.
Ugelvik 2	2.71	15	0.1597	2.33	0.0017	0.05
Ugelvik 3	2.61	>40	0.0865	1.64	0.0010	0.03
Ugelvik all	2.66	>25	0.1270	2.02	0.0014	0.04
Raudh. 5	2.54	40	0.5292	17.53	0.0007	0.02
Raudh. 6	2.46	67	0.1036	1.63	0.0013	0.04
Raudh. 8	2.40	>90	0.7573	4.29	0.0032	0.09
Raudh. All	2.46	>65	0.3879	6.45	0.0016	0.05
Gneiss 1	2.76		1.6041	2.03	0.0196	0.56
Gneiss 4	2.50		2.7107	7.99	0.0072	0.21
Gneiss 7	2.88		1.5395	0.97	0.0264	0.76
Gneiss 9	3.12		1.8586	0.81	0.0548	1.58
Gneiss all	2.82		2.6882	3.01	0.0245	0.71

Table 12.2-1: Localities with their respective average properties. Average for both peridotite rocks and for the constricting rocks referred to as gneiss. For average densities the assigned densities for specimens not measured density on is included in calculations. The presented NRM values have not been corrected for their directions, hence Q-values are a reflection of intensity of NRM, not vector intensities of NRM. Estimation of degree of serpentinization is based on optical microscopy.

Susceptibility and remanence variation

An estimate for the magnetite (volume %) present in the different samples was done using the relationship presented by Clark (1997) where volume percent of magnetite=susceptibility in SI/0.0347. The calculated magnetite percentages can be viewed in Table 12.2-1, together with average properties for each location, peridotite body, and gneisses.

Based on the assumption that magnetite is the only magnetic mineral contributing to the susceptibility value, the Ugelvik body displays an average magnetite volume percentage of 0.04%, whilst the Raudhaugene body displays a slightly higher average volume percentage of 0.05%. Based on these estimates the peridotite bodies display very little magnetite content. Of the locations within the bodies, location 8 displays the highest of 0.09%, almost twice as big as the second highest from location 2 (0.05%). The gneisses display the overall highest estimate of volume percentages of magnetite with an average of 0.71%.

12.2.1 The Ugelvik and Raudhaugene peridotites

Based on the identification of magnetic minerals in optical microscopy and backscatter electron microscopy the peridotite samples displayed both magnetites in several morphologies and sizes as well as varieties of chromites and Cr-spinels. Also, as previously described, an estimate of degree of serpentinization was done. Based on the process of serpentinization leading to creation of magnetite as a by-product, a high degree of serpentinization would lead to an expected high susceptibility value, due to more magnetite being created as well as growing from SD to MD size.

Of the peridotites the lowest estimated degree of serpentinization was observed for location 2 (15%). However, the location displayed a susceptibility value which was the second highest for all of the peridotite locations, hence also displaying the second largest estimated volume percentage (0.05%) of magnetite present of all the samples. However, these values are very low, and are reflected by the very little magnetite content identified in thin section. Of what was there it displayed sizes corresponding to MD to PSD behaviour, mostly of dendritic shapes. These could be the source for the higher susceptibility value compared with the other locations. In addition, in optical microscopy, some, but very few rims of magnetite were observed in the few chromites which were visible in the thin sections. The observed rims were of PSD size and could also contribute to the susceptibility value or to the fairly low NRM value. However, these observed rims were not verified in backscatter electron microscopy.

However, location 5 displayed well defined rims of magnetite on chromite grains, similar to location 2. On the other hand, location 5 displayed the lowest susceptibility and the second highest NRM value of all the peridotite locations. Due to the low susceptibility value it also displays the lowest estimated volume percentage of magnetite (0.02%). In addition was the estimated degree of serpentinization fairly low (40%). This could indicate that the magnetites created by serpentinization stayed within SD or small PSD sizes, contributing to NRM. Size wise, the same observation was done for the rims of magnetite on the chromite grains, which displayed narrow rims below 3µm in diameter.

Location 3 showed a similar estimated degree of serpentinization compared with location 5, and displayed the lowest NRM value and the second lowest susceptibility value of the peridotite locations. The resulting estimated magnetite volume percentage was of 0.03% and reflects the observation of little magnetite content in the thin sections. Some magnetites of MD size were observed, which probably are contributing to the susceptibility. Cr-spinel and chromites were observed, but without rims of magnetite.

Location 6 showed an approximate degree of serpentinization above 65%, and its susceptibility and NRM values were slightly higher than for location 3. Correspondingly, it shows an estimated magnetite volume percentage of 0.04%, which is 0.01% more than for location 3. Compared to location 3, location 6 displays more magnetite in seams, often with a dendritic appearance, and in mesh, though it was still little magnetite present. The grains and seams were both of SD, PSD to MD sizes, explaining the increased NRM and susceptibility values. It did also contain Cr-spinel and aluminium rich chromite, but no rims of magnetite.

Location 8 was the location with the highest estimate of serpentinization (>90%), and displayed correspondingly both the highest susceptibility values and highest estimated volume percent of magnetite (0.09%) amongst the peridotites. This fits with the observations during microscopy where location 8 was the location displaying the highest amount of magnetite amongst the peridotite locations. The morphologies of the observed magnetites were many, indicating SD, PSD and MD sizes. The observations of SD sized magnetite are reflected by location 8 displaying the highest remanent intensity amongst the peridotite locations. In comparison with location 2 and 5, the observed chromites in the thin sections also displayed magnetite at the rim, though not as defined rims, but as “fire-like” structures growing out from the borders of the chromite grains. These structures displayed narrow sizes close or at SD size, and could possibly contribute to the NRM and not to susceptibility.

12.2.2 The gneisses

Based on the identification of magnetic minerals in optical microscopy and electron back scatter microscopy the gneiss samples displayed both magnetite and hemo-ilmenite. The magnetite grains were substantially larger than for the peridotites resulting in significantly higher susceptibility values compared with the peridotites. Correspondingly, their estimated volume percentages of magnetite were larger than for the peridotites, with a range of 0.21 to 1.58%. Their remanence was in addition markedly higher, probably due to the hemo-ilmenite present in the samples, as well as SD magnetite. Estimates of volume percentage were based on magnetite being the only contributor to susceptibility.

Location 4 displayed the lowest estimate of magnetite with a calculated volume percentage of 0.21%. However, in back scatter electron microscopy large magnetite grains were identified. An explanation for this incoherence could be due to the thin section not being representative for the samples collected at location. In addition, the location displayed the highest NRM value of all the gneisses, and only some hemo-ilmenite was identified in thin section. Again, this incoherence could be due to a non-representative thin section. However, the NRM could also be due to SD magnetite displayed as “flame-structures” around other minerals, such as altered zircon, and within small seams.

Location 1 also displayed a relatively low estimate of 0.56 volume percent of magnetite, and displayed similar abundance of MD magnetite compared with location 4. However, it displayed somewhat lower content of hemo-ilmenite possibly reflected by the lower NRM value. Location 1 was not investigated by back scatter microscopy and the presence of SD size magnetite is therefore unknown.

Location 7 displayed an estimated volume percentage of magnetite of 0.76%. This location displayed both large magnetites of MD sizes, as well as magnetite in seams displaying mostly PSD to MD sizes. This is reflected in the high susceptibility of the location. In microscopy well developed hemo-ilmenite lamellas were identified, however the NRM value of the location was the lowest of all the gneiss locations.

Location 9 displayed the highest susceptibility value and the highest magnetite volume percentage estimate (1.58%). Correspondingly this was the location with thin section showing the largest amount of magnetite with well-developed MD grains. In addition were some PSD size magnetite present, as well as long seams of magnetite which had morphologies indicating SD, PSD as well as MD magnetite sizes. The NRM of the location was fairly high and could be explained by the SD magnetite, as well as presence of hemo-ilmenite.

12.3 Variation with hysteresis parameters

The results from the hysteresis measurements gave an indication on the domain size of the magnetite present in the samples. Based on the hysteresis loops, most of the gneisses displayed MD behaviour, corresponding to the big magnetite grains observed in thin section. In addition, chips plotting within the MD region and close to the MD line did also confirm these observations. The gneiss chips plotting outside the Day plot has previously been discussed based on magnetic contribution from hemo-ilmenite. The chip plotting within the PSD area has previously been discussed based on the chip not being representative of its location’s magnetic content. For the peridotite chips, the hysteresis measurements indicated PSD for all peridotite locations, which agrees with observed magnetite sizes of PSD observed in microscopy. In addition, some chips plotted close to the theoretical mixing line of MD and SD magnetite, and could therefore indicate a mix of SD and MD magnetite sizes.

For location 8 the mixing line indicated a possible mix of SD and MD magnetite with a range of 50-70% MD magnetite. This correlates well with the observed magnetite sizes in microscopy of SD, PSD and MD. In addition, its loops displayed SD behaviour, which corresponds well with the large abundance of magnetite present, also reflected by the relatively high NRM intensity and susceptibility at location.

For location 6, specimens from core 6.1 also displayed a possible mix consisting of 40-70% MD magnetite. These chips also displayed hysteresis loops indicating SD contribution. In thin section, no MD size of magnetite was observed, while some seams of magnetite could be the reason for the SD signature. Apart from these observations, location 6 displayed little magnetite content, and of what was there was of PSD.

For location 2, specimens from core 2.2 did also display mixed behaviour in the Day plot, indicating 70-85% MD contribution, also reflected by its loops being narrower than the previous. In microscopy some possible SD magnetite was observed in the mesh which could agree with the SD signal, however no MD magnetite was observed. A possibility for this contribution could be the rims observed in optical microscopy. However, these were not confirmed as magnetite in backscatter electron microscopy. As for location 6, little magnetite content was observed, and of what was there was predominantly of PSD, probably contributing to the PSD signal.

Location 3 plotted within the PSD of the Day-plot, and displayed loops of paramagnetic to SD ferromagnetic behaviour. The thin sections displayed very little magnetic material, which agrees with the paramagnetic signal. The magnetite observed was of SD or PSD, verifying the SD signature of the hysteresis loops.

Location 5 plotted mostly outside the Day-plot and displayed hysteresis loops of predominantly paramagnetic behaviour. This agrees with the very little magnetite observed in thin section. However, it displays the second highest NRM value of the peridotites. Additionally, it is the only location carrying positive NRM intensities which are greater than the negative ones. Morphologically, it is the only location which in backscatter electron microscopy has confirmed well-defined magnetite rims on chromites. If these rims are responsible for the relatively high NRM value, it could be that the measured chips are not representative for the magnetic response of the location, due to the chromites with magnetite rims not being present in the chips.

13 Discussion of magnetic minerals, their properties and their intensity directions

Based on the density variation, the susceptibility variation, remanence variation and direction, the hysteresis properties, and the morphological variations of magnetite, their sizes and their abundance, the peridotite locations show some distinct differences and similarities.

All of the peridotite locations display low abundance of magnetite, except for location 8. This is reflected by location 8 displaying the highest NRM and susceptibility values, the highest estimated degree of serpentinization and the lowest densities of specimens. In addition shows location 8 a large variety in morphologies and domain sizes of magnetite.

Compared with location 2, 3, 5 and 6, all of these displayed lower magnetic intensities than location 8, and specimens with higher densities, corresponding to lower estimated degrees of serpentinization and low observed magnetite content. Of these, location 2 and 6 displayed the highest susceptibility values, which could be due to the dendritic magnetites of PSD sizes observed in veins. These were not observed for location 3 and 5 which displayed lower susceptibilities. Of all of the locations location 3 was displaying the least abundance of magnetite, hence also low susceptibility and the lowest NRM intensities of all of the locations. Location 5 did also display little content of magnetite, hence the lowest susceptibility value, while this location displayed significantly higher NRM intensities.

Based on Oud (2010) and Spengler (2006) the Cr-spinels present in the Ugelvik and Raudhaugene bodies have been reported as present prior to exhumation as well as being exsolved during subduction and exhumation of the peridotite bodies. In addition, the reported growth of magnetite due to serpentinization is reported for the last stage of exhumation. If this is the case, the magnetite rimming the chromites in locality 5 could be of an earlier stage than the other magnetites. This is supported by the rest of the magnetites being observed in cracks and seams in the mesh and along serpentinized grains of primary minerals, which all indicates late stages of creation. In addition, locality 5 is displaying the lowest amount of positive NRM directions carried by its specimens (58%), compared with the other peridotite locations. It is also the only location with positive NRM intensities displaying a higher average intensity than the negative ones. Whether the negative or positive directions, or both, are due to the magnetite rims has not been investigated. However, based on this interpretation, these magnetite rims could be earlier forms of magnetites compared with the magnetites at the other localities, displaying different morphologies. Based on the directions and intensities of the remanence at each location, location 5 is the only peridotite location displaying vectors plotting shallowly, in addition to be significant both for the positive and negative directions. The other locations displayed vectors plotting steeply, located closely to the present field vector, with the same (positive) direction as the present day field vector. This indicates creation of magnetite at a time with approximately the same magnetic field direction as today's field vector, thus also indicating that these locations inhabit late stage magnetite. In comparison, the intensity of remanence at location 5 plots differently than today's field vector, an observation in favour of the magnetite rims being created earlier than the rest of the magnetite at the other locations.

Concerning the constricting bedrocks (often referred to as the gneisses) their intensities of remanence and susceptibility were significantly higher than the peridotites. Their magnetic signature was mostly of MD magnetite and they inhabited in addition hemo-ilmenite possibly contributing to the remanence. Their remanent directions were both positive and negative plotting both steeply and shallowly. Additionally, they showed variety in abundance in positive directions versus negative directions. Whether the positive or the negative values are due to either magnetite or hemo-ilmenite, or both, has not been investigated in this study.

14 The magnetic anomaly map

From the TMI map, created from the magnetic data collected during the ground magnetic survey over the two peridotite bodies at Otrøya and their constricting rocks, an anomaly map was created by subtracting the IGRF of 51536nT (model WMM2010) for the Molde region at acquisition time (03.07-11.07.2013). The resulting anomaly map displayed an anomaly range from -2275nT to 3947nT (statistics in Figure 14-1). Two wide areas of magnetic lows can be viewed within the map located in the same area as previously mapped peridotite. Around these two wide lows, both highs and lows can be observed within the constricting bedrocks previously mapped as mostly consisting of gneisses. Anomaly peaks within the two wide anomaly lows, and anomaly peaks in the bedrocks surrounding these two, are indicated within the magnetic anomaly map below (Figure 14-2).

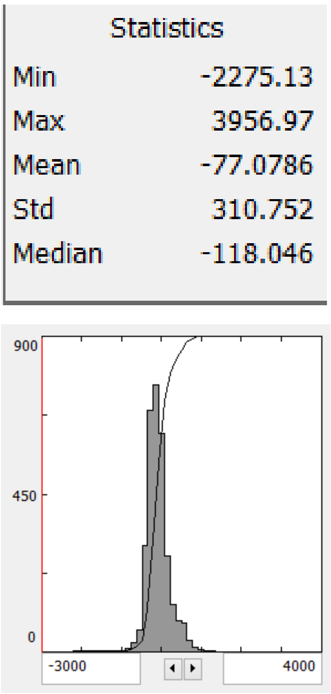

Statistics

Min	-2275.13
Max	3956.97
Mean	-77.0786
Std	310.752
Median	-118.046

Figure 14-1: Above: anomaly map statistics. Below: the distribution of anomaly values presented in a histogram. Y-axis indicates number of values, x-axis displays anomaly values.

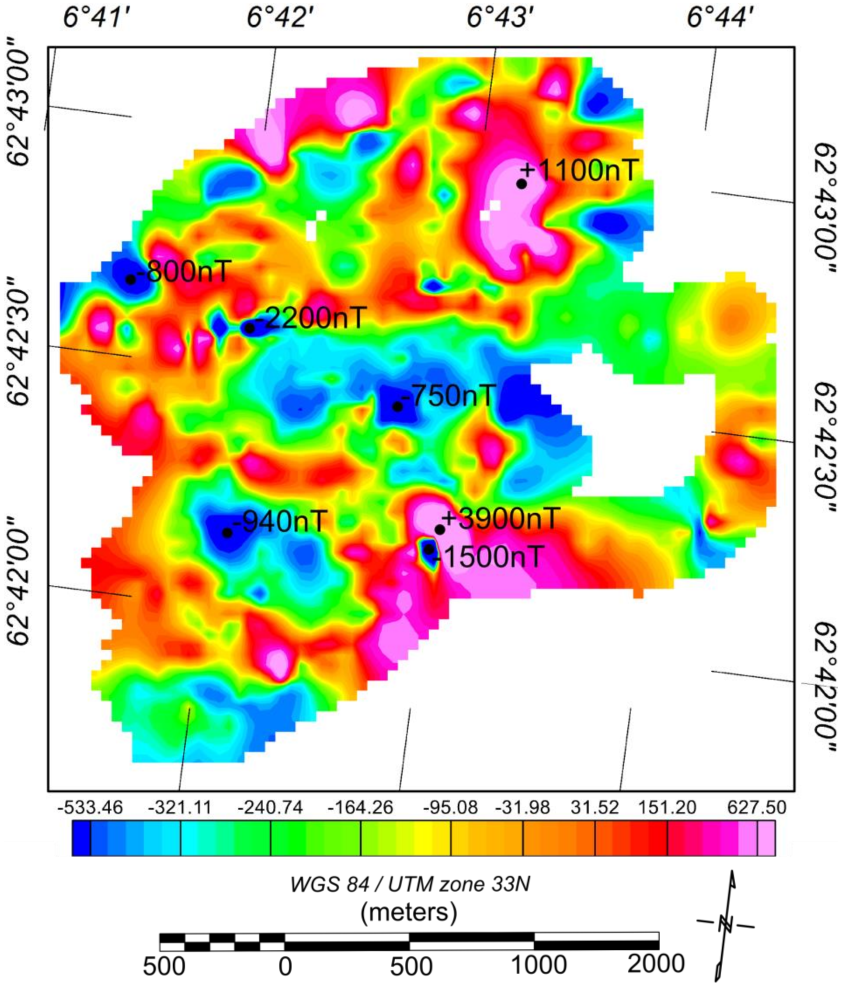

Figure 14-2: Ground magnetic anomaly map. Colour shades: light pink=values above 627nT, dark blue=values below -533.46nT, orange=intermediate. Some negative and positive extreme values are indicated in the anomaly map by black dots and their respective value.

14.1 Correlation between anomalies and previously mapped geology

Previous geological mapping (simplified geological map (Spengler et al., 2006), and N250 (NGU, n.d)) of western Otrøya, with its peridotite bodies and surrounding gneisses differ somewhat in bedrock borders and lithology (Figure 14.1-1). The simplified geological map displays two peridotite bodies with constricting migmatitic or augen gneiss with minor eclogite, while the N250 geological map displays lithological division between these constricting gneisses, as well as including an amphibolite body at the southern border of the Raudhaugene body. Both of the maps display the Ugelvik and the Raudhaugene body, but the simplified geological map additionally displays peridotite south east of the "main" Raudhaugene body.

Due to the extensive mapping of the Ugelvik and Raudhaugene peridotite bodies, making up the simplified geological map by Spengler (2006, and references therein), also displayed in a structural geological map (Spengler & Haker, 2006), the author evaluated the peridotite borders within these geological maps as the most reliable. When concerning the surrounding bedrocks, both the N250 map and simplified geological map could be correct. However, the N250 map displays differentiation between gneiss lithologies as well as defining the amphibolite body south of the Raudhaugene body. The author therefore evaluates this map as the map with the highest level of detail when concerning the bedrocks constricting the peridotite bodies.

By comparing the simplified geological map, the structural geological map and the N250 map with the anomaly map (Figure 14.1-2) some correlation between magnetic anomalies and lithology can be observed. Concerning the Ugelvik body, the N250 map (dashed lines) correlates quite good with observed negative anomaly indicated by green and blue colour, corresponding to negative anomalies of mostly -200 to -500nT. Within this area there is also an anomaly low of -500 to -940nT located at the western-central part of the mapped body. The structural geological map (dotted and solid lines) displayed a much bigger body which included areas, especially at the east side of the Ugelvik body, which displayed positive anomalies in the anomaly map. This is indicated by mostly orange and red values corresponding to anomalies of 50 to 100nT. However, right at the mapped border of the Ugelvik peridotite, the positive anomalies, displayed in pink, are as high as 500 to 600nT.

For the Raudhaugene body, the anomaly maps (Figure 14-2 and Figure 14.1-2) also displayed mostly green and blue colours indicating negative anomalies ranging from -200 to -500nT. In addition, a positive anomaly can be observed within the mapped body (for all of the geological maps) at the north border. This anomaly consists of orange to red colours indicating a slight positive contribution ranging from 30 to 150nT. A small pink anomaly can additionally be observed at the north east side of this positive anomaly, indicating a high of 250 to 350nT. Furthermore, the anomaly map indicated a narrow and long low of approximately -300 to -200nT located at the south east side of the "main" Raudhaugene body.

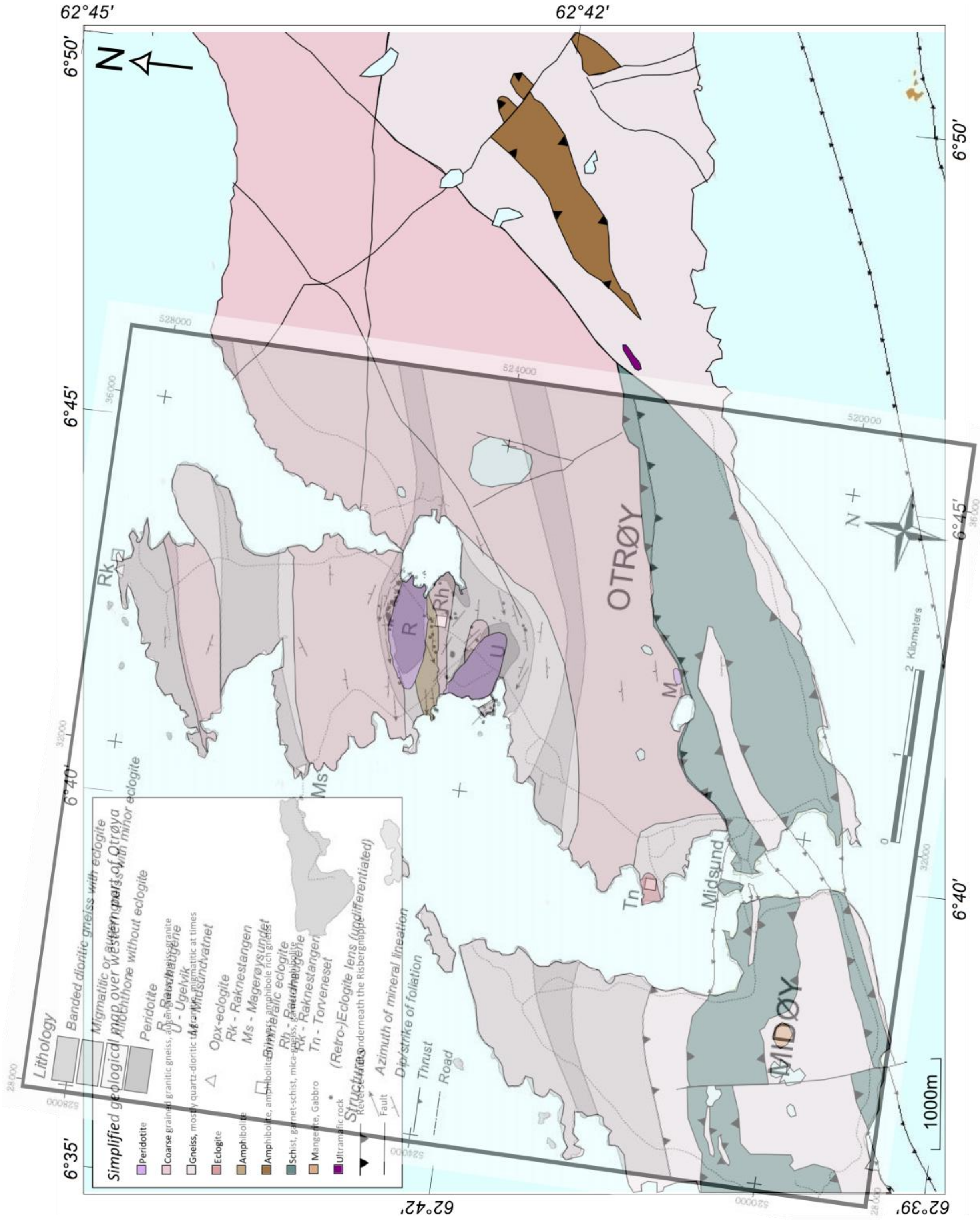

Figure 14.1-1: Simplified geological map of western Otrøya after Spengler (2006, and references therein) superimpose a geologcial map in colour modified after N250 (NGU, n.d.). These maps can be viewed separately in Figure 3.3-1 and Figure 3.3-2.

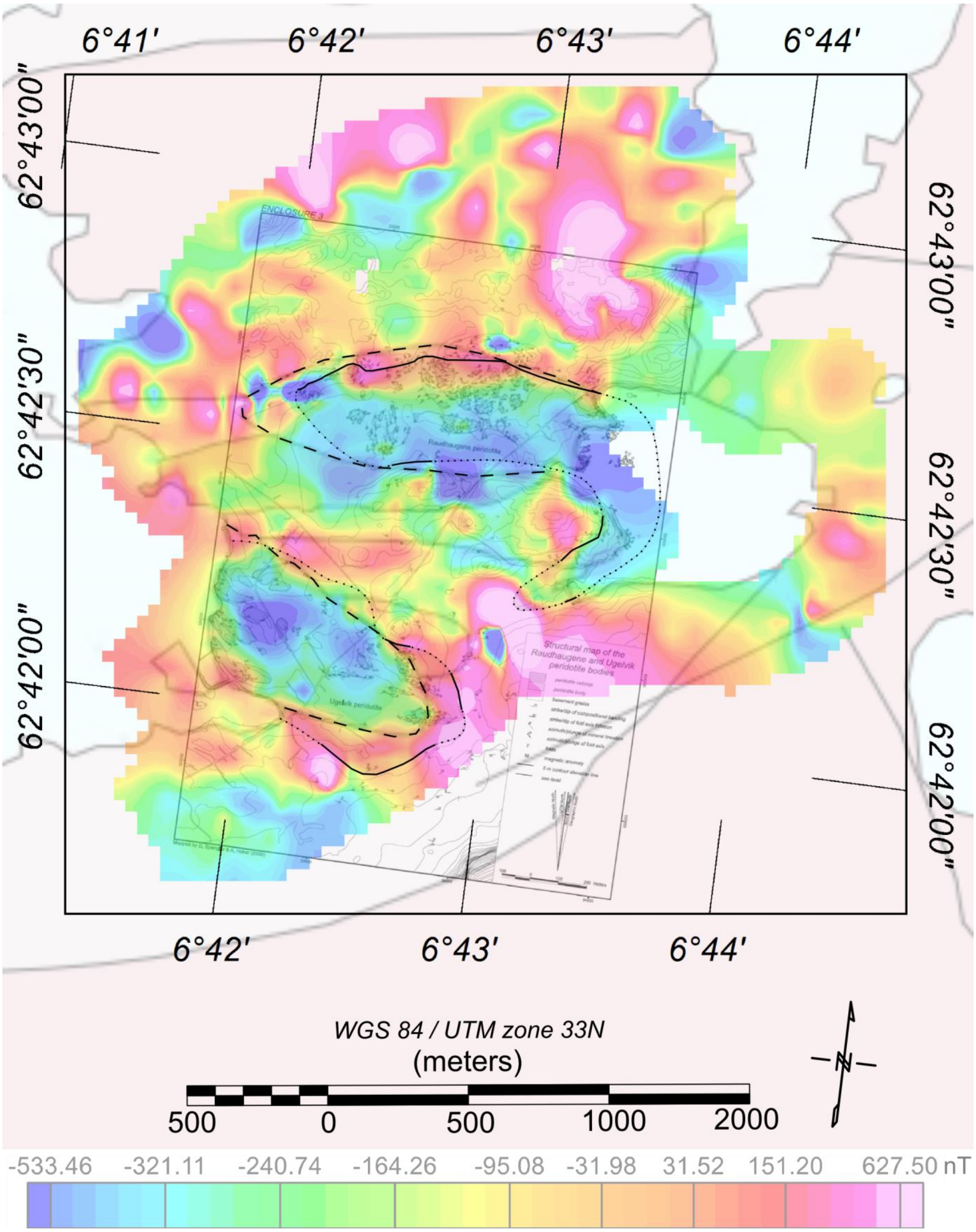

Figure 14.1-2: Magnetic anomaly map overlayed previously mapped geology. Dashed lines indicate the borders of the peridotite defined by the N250 map (NGU, n.d.), whilst the dotted and solid lines indicate the peridotite bodies displayed within the structural geological map (Spengler & Haker, 2006). The dotted lines indicate interpreted border of body, whilst solid lines indicate observed border of bodies. Orange indicates normal magnetic intensities. Blue, green and yellow indicate negative anomalies. Red and pink indicate positive anomalies. The peridotite body at the south-west is the Ugelvik body, whilst the peridotite body at the north-east is the Raudhaugene body.

The location of this anomaly is displayed as part of the Raudhaugene body in the structural geological map. However, this part of the Raudhaugene body is not indicated by the N250 map (Figure 14.1-2). Due to observations in field, this part was verified as existing, and therefore correlates quite well with the negative anomaly observed in the anomaly map. Furthermore, two large negative anomalies associated with the general anomaly area can be observed outside of the mapped Raudhaugene body for all of the geological maps. One can be displayed to the immediate south of the central part of the body, as a broad negative anomaly of approximately -550 to -740nT (Figure 14-2). In the N250 geological map this anomaly is located at an area mapped as amphibolite, while this area is displayed as migmatitic or augen gneiss with minor eclogite within the simplified geological map. The other negative anomaly, a distinct narrow negative anomaly at the west border of the Raudhaugene peridotite, displayed a negative anomaly steeply increasing from -500nT at the east side of the border to -2200nT at the west side of the border (Figure 14-2), based on the structural geological map. However, based on the N250 map, this area is displayed within the Raudhaugene body. Additionally, an area extending south-west from the west side of the Raudhaugene body displayed similar negative anomaly values as the rest of the mapped body, displayed by light blue, blue and green colours, in the anomaly map (Figure 14.1-2). However, this area is defined as amphibolite by the N250 map and as migmatitic or augen gneiss with minor eclogite by the simplified geological map.

Based on the above observations, the area mapped as amphibolite by the N250 geological map displayed predominantly negative anomalies in the anomaly map (Figure 14.1-2). With respect to anomaly high and lows within the other surrounding gneisses, no apparent correlation is evident concerning the different lithologies of gneiss bedrocks indicated by the N250 geological map (Figure 14.1-2). However, larger areas of positive anomalies are commonly observed within the gneisses. These are generally displayed by orange to pink anomalies of neutral (0nT) to high anomalies (600nT). However, some areas displayed extreme highs of 1000 to 3900nT, some areas displayed lows of the same order as the lows displayed within the mapped peridotite, as well as one extreme low of -1500nT (Figure 14-2).

14.2 Correlation of anomalies with estimated induced magnetisation

Previous results showed that specimen susceptibilities within the previously mapped peridotite bodies are consistently low, with location averages between 0.0007 and 0.003 SI. Whilst the constricting bedrocks (referred to as gneiss) displayed substantially higher susceptibility averages with location averages between 0.0072 and 0.0548 SI (Table 14.4-1). The expected response on the anomaly map would be of the peridotite bodies displaying low contribution onto the total magnetic field, with the constricting gneisses displaying as a contrast of higher contribution onto the total magnetic field. Based on the average induced magnetisation of the constricting bedrocks (1.0045 A/m) and the magnetic field intensity at location (41.01nT) the average contribution from the gneisses and peridotites in nT was calculated using the relationship of H (in nT) = H (in A/m)*(400*π) (Formula 1, chapter 5.2.1).

This formula gives the magnetic field directly on the rock, assuming an infinite extension of the rock. However, these are not the conditions in field, where the geometries and topography of the rock will lower the field. The measured magnetic field will additionally be affected by the deeper magnetic bodies. However, the calculated magnetic field values provide maximum values of induced magnetisation for the different rock types, and are therefore used for comparison.

The average induced magnetisation of the gneisses was calculated to be 1262.28nT, whilst the average induced magnetisation of the peridotites (0.0622 A/m) would be 78.23nT. This is a difference of almost 1200nT.

Based on the previously described anomalies within the anomaly map (Figure 14-2 and Figure 14.1-2) the mapped peridotite bodies commonly displayed anomalies with a range of -200 to -500nT, whilst the constricting bedrocks commonly displayed anomalies with a range of 0 to 600nT. The difference between the “normal” anomaly low and the “normal” anomaly high, of respectively the peridotites and the constricting bedrocks, would therefore be approximately 1100nT. This is almost the same difference as for the calculated average induced contribution from the gneiss locations and the calculated average induced contribution from the peridotite locations, which displayed a difference of almost 1200nT.

14.3 Estimated intensities at locations

Based on the calculations of real intensity of remanence and the evaluation of real contribution of remanence onto the total magnetic field intensity, the contributions from, and within, the peridotite bodies and the constricting gneisses, displayed some variants.

14.3.1 Peridotite locations

For the Ugelvik body the remanent intensities were low, with an estimated resultant positive total remanent intensity of 96nT, with a direction close to the ambient field direction at Otrøya. The Raudhaugene body displayed estimated resultant NRM intensities ranging from 106nT to 535nT, all of positive directions. However, location 5 displayed shallow inclination, whilst location 6 and 8 had a direction close to the ambient field direction at Otrøya. The gneiss locations displayed average resultant remanent intensities ranging from 1518nT to 2994nT, all with varying directions. Based on the evaluation of impact of remanence onto the total magnetic field, all of the peridotite locations displayed positive contributions.

Based on the intensities of resulting remanence estimated from the Ugelvik peridotite body, the intensity of resultant positive remanent intensity would give an approximate equal contribution onto the total magnetic field intensity compared with the induced magnetisation. This is based on both the direction of the estimated average positive intensity as well as the calculated Q-value (Table 14.4-1). However, these intensities are both very small and would add up to a positive contribution of less than 200nT.

For the Raudhaugene body the remanent contribution was higher, with exception of location 6 which displayed a resultant remanence (106nT) and Q-value (1.63) indicating similar contribution (though slightly higher remanent contribution) compared with the Ugelvik body. The other two locations, 5 and 8, both displayed estimated resultant intensities of approximately 500nT, which were substantially larger than their induced intensities. Especially for location 5, which displayed the lowest susceptibility value of all the peridotite locations, the average Q-value of 14.58 demonstrated this large intensity difference (Table 14.4-1). However, based on the direction of the remanent intensity at location 5 the contribution from remanence could in reality be much less compared with location 8. At location 5 the estimated direction of the remanence was extremely shallow, almost normal to the ambient field, whilst being in the same direction as the ambient field for location 8. Based on these observations, the contribution from remanence and induced intensity at location 5 would probably just be slightly higher than the induced intensity of 33nT, whilst for location 6 the maximum total increase could be close to maximum 160nT, and for location 8 the total increase could give a maximum increase close to 700nT.

14.3.2 Gneiss locations

For the constricting gneisses, location 1, 7 and 9 displayed similar intensities of estimated resultant remanence of approximately 1500nT. However, the locations' respective estimated induced magnetisation, as well as mean direction of estimated remanent intensity, varied.

For location 1 and 7 the estimated resultant remanent intensity was slightly higher, as reflected by the estimated resultant Q-values of 1.47 and 1.12, respectively. For location 1 the resultant estimated remanent intensity would further increase the positive contribution from the estimated induced magnetisation, due to its direction being close to the direction of the ambient field (Figure 11.1-6), possibly giving a maximum contribution of approximately 2500nT. On the other hand, location 7 displayed a shallow negative estimated remanent contribution, possibly decreasing the estimated induced magnetisation of 1360nT, though its shallow direction lessens the remanent intensity impact.

Location 9 (which also displayed an estimated resultant remanent intensity close to 1500nT) displayed an estimated remanent intensity lower than the estimated induced intensity, reflected by the estimated Q-value of 0.56. However, based on the moderate positive direction of the estimated resultant remanence intensity, it would give a minor positive contribution, adding to the estimated induced magnetisation. Due to this moderate intensity of remanence and induced magnetisation displaying the highest value (2822.61nT) of all locations, the expected maximum contribution would probably be above 3000nT.

Location 4, also from the constricting gneisses, displayed an estimated resultant remanent intensity approximately twice as big as the other gneiss locations (on the basis of its directions all being either positive or negative). The calculated mean direction was extremely shallow indicating a minor contribution onto the total magnetic field. Based on this observation the resultant maximum contribution from estimated induced magnetisation and estimated remanence onto the total magnetic field at location would in any case not differ greatly from the location's estimated induced magnetisation of 373nT, but could be either of a positive or negative contribution.

14.4 Correlations and evaluation of measured anomalies and estimated intensities at locations

For each location the measured anomaly at location (Figure 14.4-1) was obtained and is displayed in Table 14.4-1. These displayed an anomaly range of -342.57nT to 24.48nT for the peridotite locations, and an anomaly range of -176.43nT to 182.85nT for the gneiss locations. These observations differ from the estimated contribution at location for all locations. The estimated response from all peridotite locations was not of negative to neutral contribution, as measured, but of a slight positive contribution. For the gneiss locations the estimated response was mostly of positive contributions onto the total magnetic field, however, small negative and positive anomalies were measured. Values can be viewed in Table 14.4-1.

Table 14.4-1: Estimated contribution of remanence (resultant NRM), its direction (NRM dir.), calculated induced magnetisation (induced magn.) based on field intensity of 41.01nT, and the Q-value based on these two values for each location. The conversion from A/m to nT was calculated using the relationship of B (in nT) = H (in A/m)*(400*π). Anomaly at location is taken from the gridded anomaly map (Figure 14.4-1).

Loc.	result. NRM (A/m)	result. NRM (nT)	NRM dir.	Vol. corr. Susc. (SI)	Induced magn. (A/m)	Induced magn. (nT)	result. Q-value	est. max contrib. (nT)	Anomaly at loc. (nT)	est. diff. (nT)
U. 2	0.0948	119.13	+	0.0017	0.07	88.79	1.34	~200	24.48	<170
U. 3	0.0607	76.28	+	0.0010	0.04	52.41	1.46	<150	-309.97	<460
U. all	0.0765	96.13	+	0.0014	0.06	72.30	1.33	<200		
R. 5	0.3926	493.36	+	0.0007	0.03	33.85	14.58	>33.85	10.93	~20
R. 6	0.0846	106.31	+	0.0013	0.05	65.13	1.63	<160	-342.57	<500
R. 8	0.4261	535.45	+	0.0032	0.13	166.76	3.21	<700	-94.18	<800
R. All				0.0016	0.07	84.15	0.00			
G. 1	1.1780	1480.32	+	0.0196	0.80	1009.77	1.47	<2500	-2.98	~2500
G. 4	2.3827	2994.19	+/-	0.0072	0.30	373.06	8.03	~373	-176.43	~200
G. 7	1.2082	1518.27	-	0.0264	1.08	1360.00	1.12	<1000	182.85	<800
G. 9	1.2533	1574.94	+	0.0548	2.25	2822.61	0.56	>3000	-89.52	>3000
G. all				0.0245	1.00	1262.28				

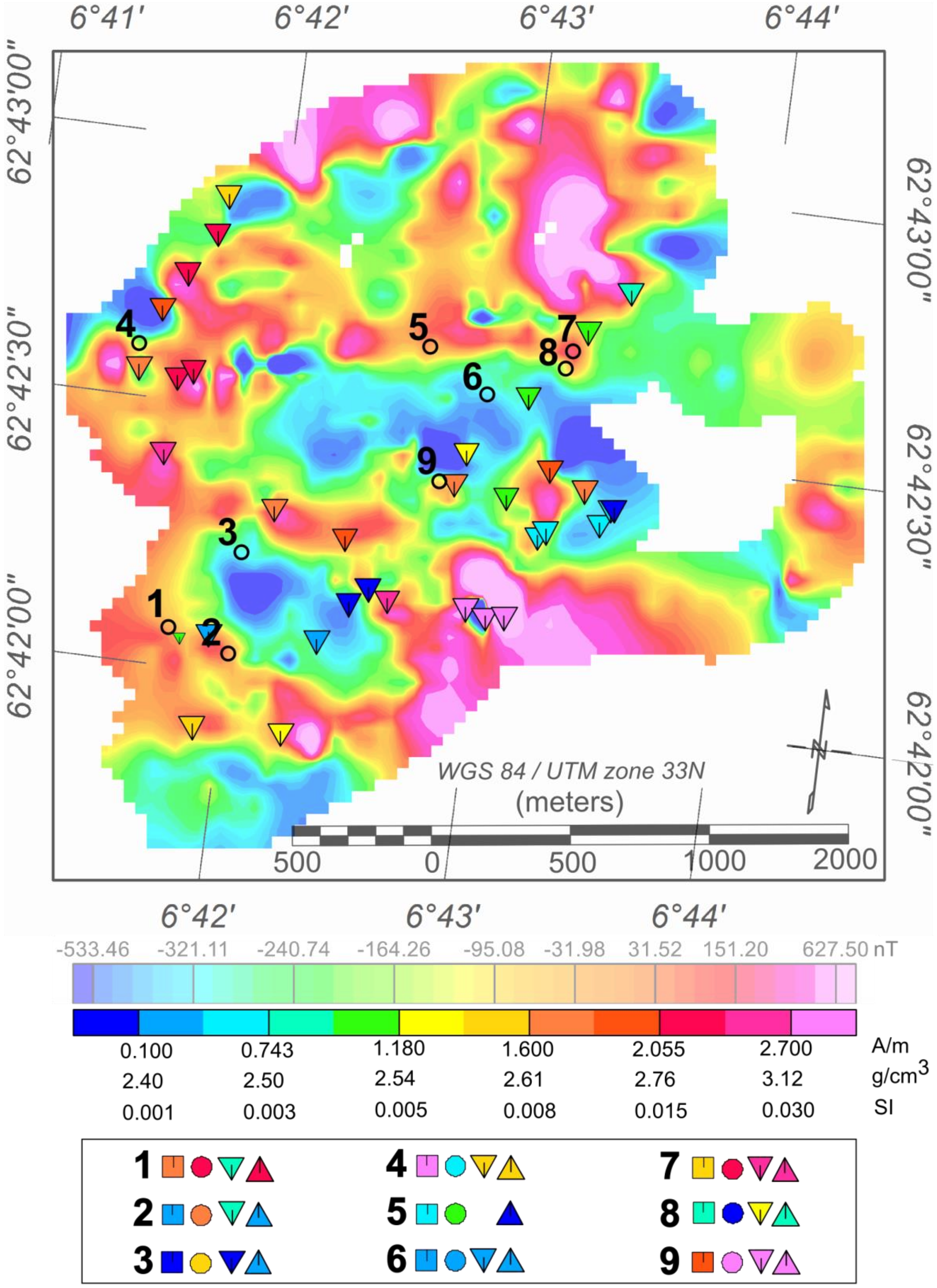

Figure 14.4-1: Field susceptibility (▽), specimen susceptibility (△), specimen density (⬡) and specimen NRM intensity (□) displayed next to their respective location number in the box. Colour coding is displayed in the bar above. Locations indicated by dot (**O**) and number in the anomaly map at the top. Exact values can be viewed in (Table 14.4-1 and Table 12.2-1) Field susceptibility for the rest of the field area is superimposed the anomaly map. Anomaly intensity is displayed in the bar underneath the anomaly map (nT).

14.4.1 Gneiss locations

Location 4 was the only location with estimated possible negative contribution onto the total magnetic field (could be either negative or positive due to extremely shallow inclination). Based on the contribution being negative, this estimate fits quite well with the measured field value of -176.43nT. The impact of the shallow vector was not evaluated, but based on its high intensity (Table 14.4-1) and based on the direction being negative, this measured anomaly (-176.43nT) is plausible for the estimated values. However, this was the only gneiss location with estimated contribution resembling the measured contribution. All the other gneiss locations displayed substantially larger differences between estimated and observed anomaly contributions.

Location 7 also displayed an estimated negative contribution from remanence. However, the estimated total contribution from both remanence and induced magnetisation was estimated to be positive, resulting in a difference from estimated and measured anomalies of less than 800nT. By reviewing the equal area plot of remanent directions for location 7 (Figure 11.1-6) many of the directions displayed as positive had an extreme shallow inclination, and could be of negative directions (previously explained in section 11.3.1). If this is the case, the resultant estimated negative contribution could be greater, decreasing the difference between observed and estimated contribution onto the total magnetic field.

Both location 1 and 9 gave positive estimated contributions from remanence, leading to high estimated contribution to the total magnetic field (>2500nT). However, the measured anomalies were neutral to negative. At both of these locations few specimens (N<6) were measured, this could indicate that these estimates are not representative for the locations and that remanence with negative direction had a greater impact creating the neutral to negative anomalies observed at these locations.

14.4.2 Peridotite locations

For the peridotite locations, the only locations with relatively small differences between estimated and measured contribution were location 2 and 5, respectively within the Ugelvik and Raudhaugene body. In addition, these locations were the only peridotite locations with measured neutral positive anomalies. For location 5 this neutral anomaly corresponds with the estimated neutral positive contribution from remanence and susceptibility. However, the estimated intensity of remanence at this location was relatively high – it was its extreme shallow calculated inclination (I=0.2) which made the estimated positive contribution only slightly contributing. For location 2 the reason for the small estimated difference can probably be explained by the low contribution from both estimated induced and remanent magnetisation coinciding with a neutral positive anomaly. For all of the other peridotite locations the measured anomaly was negative. The largest estimated difference (<800nT) can be observed for location 8, which was estimated to be the most serpentinized location, and with the highest amount of magnetite present in thin section.

Based on the measured anomalies within the areas of mapped peridotite bodies (Figure 14.1-2) displaying neutral to negative anomalies, the estimated remanent contribution of being only positive does not explain these anomalies. However, with exception of location 5, only the positive contribution was taken into account in the estimates of remanent contribution. Based on the large scatter of both negative and positive remanence directions, the negative contribution could be larger than estimated, further lowering the estimated contribution from remanence. However, in exception from location 5, all the peridotite locations displayed dominantly contribution from remanent intensities with positive directions. Based on the peridotite location observations, even with negative directions taken into account the contribution from remanence would still be slightly positive, not negative as observed for locations in the anomaly map (Figure 14.4-1).

14.5 Evaluation of the representability of locations in respect to whole body properties and anomaly response, and probable causes for anomalies

The estimated contributions from remanence used in these comparisons of measured and estimated anomalies at location were mainly based on contribution from the significant vectors in mean vector calculations. In addition, as described, some locations were only represented by a few specimens. These estimates of intensities at locations are therefore somewhat speculative.

A better estimate could have been obtained for the remanent contribution if the intensities of the remanent directions had been taken into account in the vector calculations. This would have made it possible to evaluate a total remanent intensity vector at each location. Additionally, these estimates are only based on specimens collected at the surface; whilst the anomalies measured are based on the total magnetic response measured in field, hence take into account both the surface response as well as the magnetic response at depth. The estimated contribution of remanence and intensity are therefore probably not representative for the anomaly response measured at location. However, the estimated intensities of remanence and intensities of induced magnetisation (Table 14.4-1) give information on the range of possible intensity contributions from the rocks within the field area.

Based on the anomalies observed in the anomaly map, the intensities estimated for both remanent intensities and induced intensities at gneiss locations, can explain both the observed positive and negative anomalies observed within the constricting bedrocks within the anomaly map (Figure 14-2). The local variation displaying negative, neutral and positive anomalies within these bedrocks are probably due to the layered and varying nature of these bedrocks (see section 3.3). However, as mentioned, the estimated remanent intensities and induced intensities at peridotite locations can’t account for the negative anomalies observed within the areas previously mapped as peridotite. However, as previously observed (

Table 11.3-1), the peridotite specimens carrying remanent intensities of negative direction carried higher remanent intensities than the positive ones. In addition, the peridotite locations carried mostly positive remanent intensities (positive>75%) with estimated mean vectors of directions close to the direction of the ambient field. Location 5 was the only exception, carrying almost equal amounts of positive and negative directions (positive=58%), with positive remanent intensities of higher intensities than the negative ones, and a high total estimated remanent intensity of extremely shallow positive direction.

As previously discussed, the magnetite carrying the positive remanent intensities, with the same direction as the ambient field, could be late stage magnetite, while the magnetite within location 5, carrying shallow directions could be earlier forms of magnetite. This indication of an earlier stage of magnetite production leads to the question of whether the remanent intensities of the negative directions, observed at the peridotite locations, also are from an earlier stage of magnetite production. If the positive, weaker intensities are from surface process such as deterioration of NRM carried by magnetite and possible formation of modern CRM, or in other ways not being representative of the remanent directions carried by the whole peridotite bodies, the negative directions could possibly be dominating at depth. Due to the negative intensities being greater than the positive ones for all peridotite locations (except for location 5) this could make a greater impact from remanent contribution then calculated in Table 14.4-1. If this is the case, these earlier created magnetites carrying greater intensities with negative directions could be the reason for the negative anomalies observed within the areas mapped as peridotite within the anomaly map (Figure 14.1-2). However, in this study the specimens were not demagnetized to further investigate this possibility.

Another solution for the observed negative anomalies within areas mapped as peridotite could be the susceptibility contrast between the immediate enclosing bedrocks and the peridotite bodies. As previously investigated, the average calculated intensity from induced magnetisation from the peridotite locations and the gneiss locations display a maximum difference of 1200nT, which is almost the same as the “normal” maximum difference between anomaly highs and lows observed within the peridotites and their enclosing bedrocks within the anomaly map. In addition to the magnetic response these contrasts create, the geometry of the peridotite bodies could further create a negative anomaly. To further investigate this, a 2D profile focusing on the geometry of the peridotite bodies, based on susceptibility being the main contributor to the observed anomalies of the peridotites, was modelled.

15 Modelling of the two peridotite bodies

15.1 Constraints and assumptions

In chapter 8.3 “2D modelling” the structural constraints, constraints of the positioning of the peridotite bodies at surface, and constraints for the magnetic properties are described. In chapter 9.7 “Processing and modelling” restrictions associated with the construction of the models are commented on. In addition, it is assumed that the elevation for data points and topography, based on gridded GPS heights recorded during data acquisition, is correct. A time constraint on the modelling done in this study restricted the modelling to both being simple and in 2D. The resulting studies of the models are brief and further work is suggested to go in depths in these models.

The two rock parameters assigned in the model were peridotite and gneiss. The susceptibility value assigned to peridotite was the average susceptibility value obtained from the specimens collected both for the Ugelvik and Raudhaugene peridotite bodies. The gneiss was assigned the average susceptibility value of the average field measurements and susceptibility measurements. The reason for the different assignations of values was for the peridotites based on the largest dataset being from specimen measurements, and displaying the most consistent values. For the gneisses, due to the large variability in the datasets, both the field susceptibility measurements and specimen susceptibility measurements were included by using the average value of the average field value and the average specimen value. The field dataset was the largest, assumed to provide information covering a larger area of gneiss types, while the specimen susceptibilities were assumed to provide information on the bedrocks close to the peridotite bodies.

An additional assumption was that the gridded anomaly map provided representative data points along the chosen profile line. The quality of the processed data gridded was also assumed to be of a level creating a gridded anomaly map with representative anomaly values for the peridotite and the enclosing bedrocks. The background assigned was the IGRF of 51536nT (model WMM2010) for the Molde region at acquisition time (03.07-11.07.2013), and it is assumed that this is the right background for the field area. The profile data were imported into GM-SYS. Elevation for data points and topography was given by using the gridded GPS heights recorded during the TMI survey. An infinite rock body was defined for susceptibility=0.02 SI. In order to reduce the spiky response, the topography was adjusted to be 1m below sett level, resulting in the acquisition height to be 1m above topography.

15.2 Anomaly response created from the creation of the geometry of the simple peridotite synfold

Figure 15.2-1 displays steps in creating the simple synformal structure connecting the Ugelvik and Raudhaugene peridotite bodies. The solid lines display the magnetic model response, whilst the black dots display the magnetic response from the gridded anomaly map along the given profile line (Figure 8.3-1).

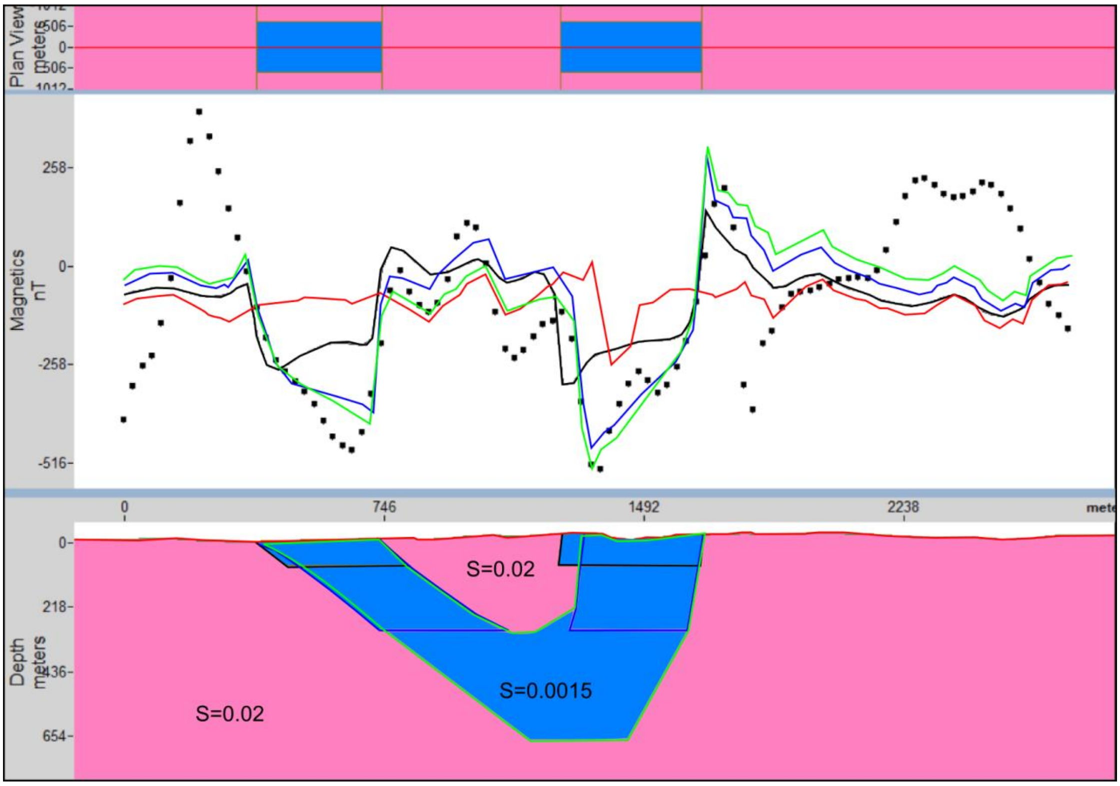

Figure 15.2-1: Solid lines in model displaying: red=the topographic influence made with a rock body of susceptibility of 0.02 SI and infinite length. Black=bodies 75m down. Blue=bodies 300m down. Green=bodies displayed as a syncline extending 675m down. The peridotite bodies (blue) were given a susceptibility of 0.0015 SI. The gneiss (pink) were given a susceptibility value of 0.02 SI. Black dots represent gridded anomaly values along the profile line (Figure 8.3-1).

The red line displays the response created from the gneiss rock with infinitely long extent. This response indicates that topography is creating a magnetic response resembling the gridded anomaly response of the gneiss in the middle of the Ugelvik (left) and Raudhaugene (right) bodies. Additionally, it creates a distinct negative response within the location of the mapped Raudhaugene body.

The black, green and blue solid lines display the response from the peridotite bodies as the synformal geometry is created. The black line displays the response from the peridotite bodies when extending 75m down in the profile. Both of these peridotite bodies creates wide anomalies, displaying lows of [-200,-265nT] for the Ugelvik body, and lows of [-190,-310nT] for the Raudhaugene body. The shape of the anomalies corresponds quite well with the anomalies from the gridded anomaly data, until they reach their minimum value. The anomalies from the gridded anomaly map display lower anomalies with minimums of -480nT for the Ugelvik body and -530nT for the Raudhaugene body. In addition, at the left side of the Raudhaugene body (in the 2D model) the anomaly response created by the model (in black) displays an earlier anomaly low than the anomaly response from the gridded data. The blue line displays the anomaly response from the model with the bodies extending 300m down in the profile. For this model, the left border of the Raudhaugene body was moved 61m to the right, resulting in the anomaly displaying with a response more similar location-wise as the anomaly from the gridded data. The dip of the left side of the Ugelvik body was also slightly adjusted to produce a better fit with the anomaly created by the gridded data. The anomaly response from this model displays anomaly lows of -390nT for the Ugelvik body, and -480nT for the Raudhaugene body. This is -100nT in difference from the maximum anomaly response observed for both bodies along the profile line. The green line displays the anomaly response from the model of a complete synformal structure combining the two peridotite bodies. This model displays minimum anomalies of -420nT for the Ugelvik part of the synfold, and -530nT for the Raudhaugene body of the synfold, indicating just a slightly greater negative anomaly response compared with the anomaly response from the separate bodies extending 300m down (green line).

15.3 Anomaly response created by changing the susceptibility of the rock bodies

Based on the model with a simple synformal peridotite structure with enclosing gneiss, the susceptibility of the rock bodies was changed based on the susceptibility variation observed in the datasets (Table 11.1-1).

Firstly, the susceptibility value of the peridotite was changed based on the standard deviations displayed in Table 11.1-1, both for field and specimen values. Due to the Raudhaugene and Ugelvik bodies displaying different standard deviations, the synform was divided into two sections; Ugelvik at the left, Raudhaugene at the right. For the Ugelvik part both the field and specimen susceptibility values displayed standard deviations resulting in almost similar maximum and minimum values based on one standard deviation up and down from the average value. For the Raudhaugene body the lowest susceptibility value was obtained for one standard deviation away from the average specimen susceptibility value, and the largest susceptibility value was obtained for one standard deviation away from the average field susceptibility value. In Figure 15.3-1 the anomaly response from changing the susceptibility values of the peridotites can be viewed. For the Ugelvik part, the deviation displayed is very little. Due to larger standard deviation observed for the Raudhaugene body, the largest susceptibility value (0.0046 SI) created a smaller anomaly compared with the anomalies created by the average and smallest susceptibility values, which, in addition, do not differ substantially from each other. For these comparisons the gneiss susceptibility was constant at 0.02 SI.

The enclosing gneisses were divided into “middle gneiss” displayed in the middle of the peridotite syncline, and “enclosing gneiss” around the peridotite syncline. To look at variations with varying susceptibility values, the approximate gneiss average values obtained from field and from specimens were used. The varying susceptibility values and their anomaly responses can be viewed in Figure 15.3-2. The middle gneiss displayed the highest anomaly values when assigned the same susceptibility value as the average susceptibility specimen value of 0.025 SI in conjunction with the enclosing gneiss assigned approximately the average field susceptibility value of (0.015) (blue solid line).

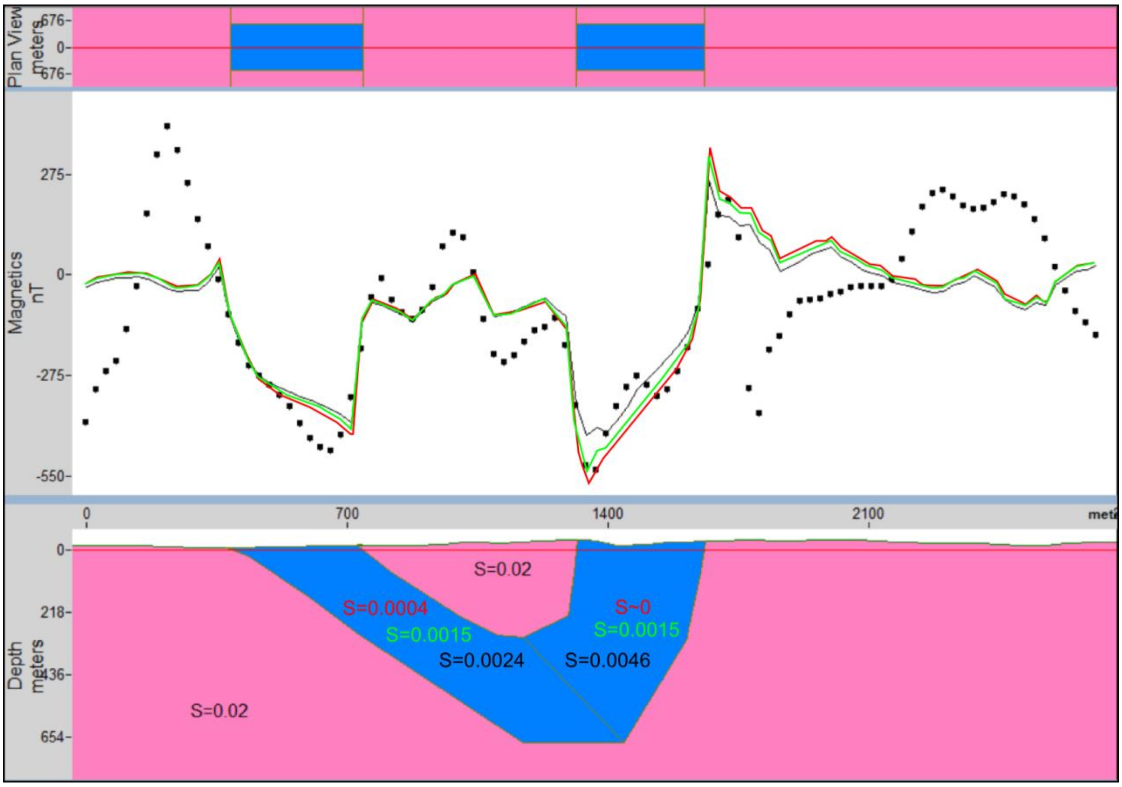

Figure 15.3-1: Model displaying a syncline with changed susceptibility values for the Ugelvik (right part) and Raudhaugene (left part). Changes in susceptibility values can be viewed in figure. Black dots represent gridded anomaly values along the profile line (Figure 8.3-1).

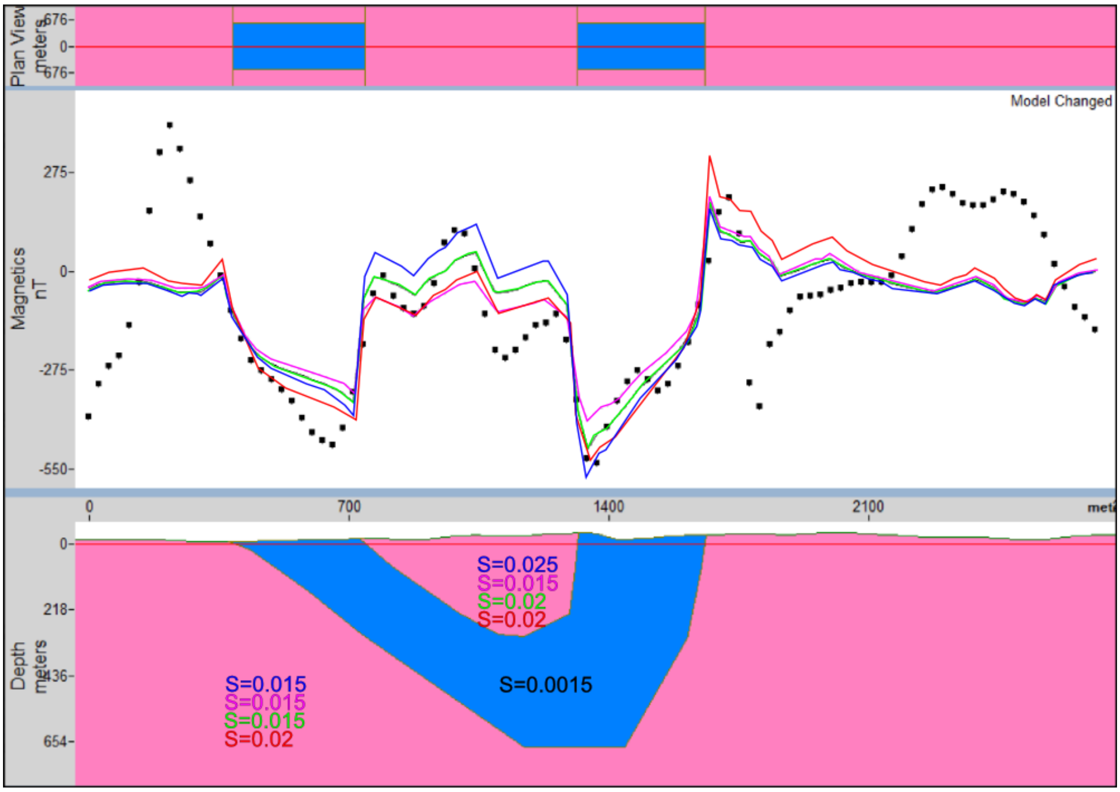

Figure 15.3-2: Model displaying a syncline with changed susceptibility values for enclosing bedrocks and bedrocks displayed within the syncline. Changes in susceptibility values can be viewed in figure. Black dots represent gridded anomaly values along the profile line (Figure 8.3-1).

This setup was the setup providing the minimum anomaly response observed for the Raudhaugene part of the peridotite syncline. The minimum anomaly response for the Ugelvik body was obtained with the middle and enclosing gneiss assigned the average susceptibility value from both the field and specimen susceptibilities (red solid line). Additionally, this setup provided the second minimum anomaly for the Raudhaugene body, and almost the smallest anomaly response from the middle gneiss. When concerning the middle gneiss anomaly response, the other setups displayed variations between the two setups already described, and are displayed in green and pink solid lines within Figure 15.3-2. The lowest anomaly response for the peridotite was observed for both the middle gneiss and enclosing gneiss assigned a susceptibility value of 0.0015 SI, which is approximately the same as the average field susceptibility value (Table 11.1-1).

15.4 Best fit based on susceptibility variation

Based on the given geometry and susceptibility variations of the peridotite syncline, the only substantial deviation was observed for the Raudhaugene part when assigned the largest susceptibility value of 0.0046 SI (black line Figure 15.3-1). This susceptibility value gave the smallest anomaly response of the peridotite susceptibility values, and cannot account for the largest negative anomaly value created by the gridded anomaly values. Apart from this observation, the maximum and minimum susceptibility anomaly responses only slightly varied, indicating that the large variation in gneiss susceptibility values (Table 11.1-1) are the controlling factor of the resultant anomalies. When concerning the anomaly responses created by changing the susceptibility of the gneiss, the largest negative anomalies created were for the setups displayed in red and blue colour in Figure 15.3-2. Of these two the author evaluates the setup with both gneiss divisions with susceptibility set to 0.02 SI (red) as the best fit. This is based on this anomaly response displaying the best fit for the Ugelvik part of the peridotite body and almost the same fit as the blue setup for the Raudhaugene body, creating a large negative anomaly. For the given model geometry, a simple susceptibility variation cannot explain the small amplitude variations of the middle gneiss part. Nor can a simple susceptibility variation explain the small amplitude variation observed within the larger anomaly response of the Raudhaugene part of the syncline and the largest negative anomaly response of the Ugelvik body.

15.5 Best fit based on geometry variation

Based on the susceptibility value of the peridotite being 0.0015 SI and the susceptibility value of the gneiss being 0.02 SI, variations in anomaly response with change in geometry of the peridotite bodies was further investigated. Based on previous observations in Figure 15.2-1, both the model with the Ugelvik and Raudhaugene bodies displaying as two separate boudins extending 300m down (blue anomaly response), and the model of the two bodies creating one simple synformal structure (green anomaly response), creates approximately the same negative anomaly response for the peridotites, with the synfold model creating a slightly larger response. Though, neither of them created the same anomaly shape as

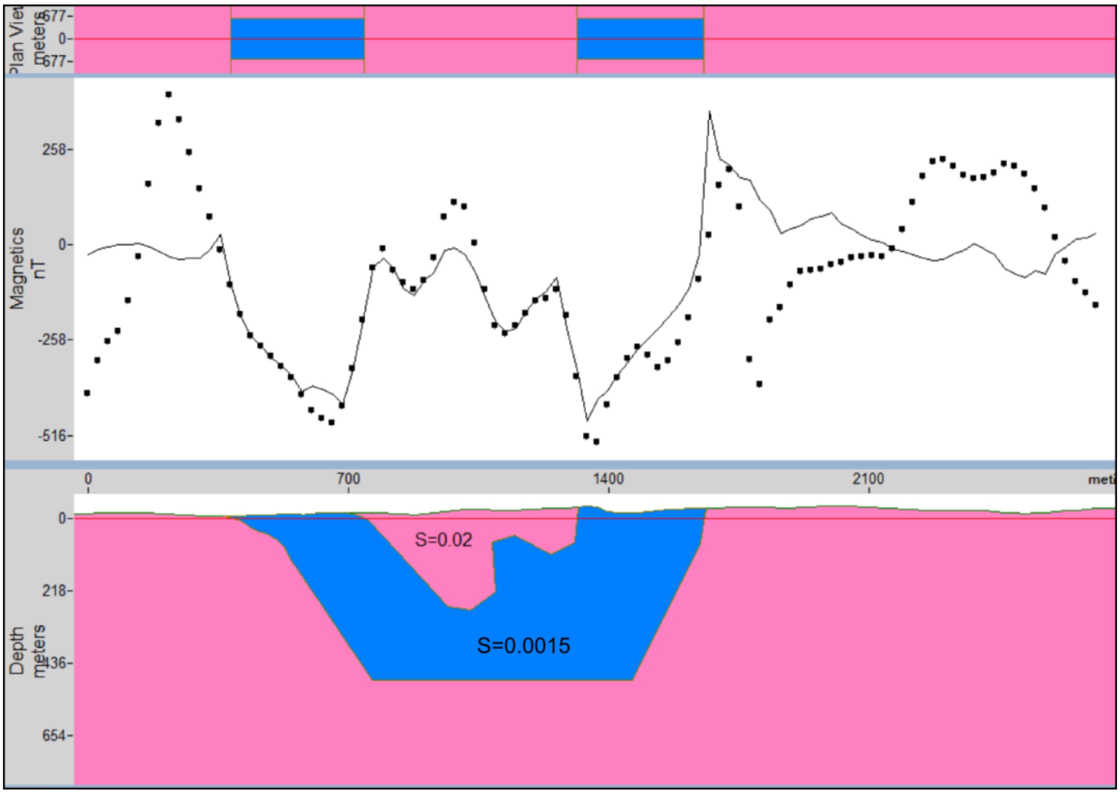

Figure 15.5-1: Model displaying a peridotite synform with its inner part forming two synforms and one antiform. Solid line displays model respons. Black dots represent gridded anomaly values along the profile line (Figure 8.3-1).

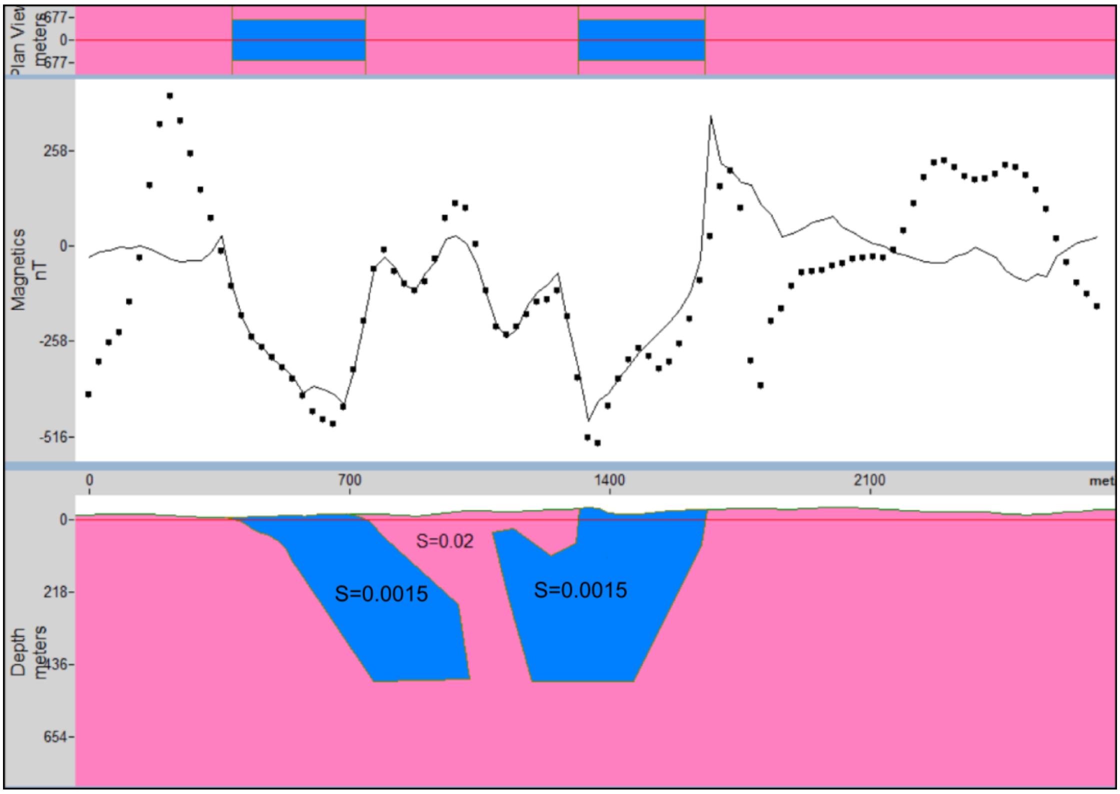

Figure 15.5-2: Model displaying two peridotite boudins. Solid line displays model respons. Black dots represent gridded anomaly values along the profile line (Figure 8.3-1).

displayed for the Ugelvik and Raudhaugene parts of the peridotite, and neither of them made a good fit with the middle gneiss anomaly response. However, the simple syncline model seems to have a better fit with the anomaly of the middle gneiss closest to the Ugelvik part of the peridotite syncline. Based on these observations further modelling of the geometry of both the simple syncline and the peridotite as two boudins were investigated to create a best fit based on geometry variation. The models created were still based on the structural constraints from the structural data and interpretation of the peridotite bodies provided by Spengler (2006). However, some slight modifications on dip were done to create a better fit. The two models created with the best fits can be observed in Figure 15.5-1 and Figure 15.5-2.

Both the best fit syncline model (Figure 15.5-1) and the best fit boudin model (Figure 15.5-2) provides almost the same anomaly response. They both can to a large degree explain the anomaly response of the Ugelvik body, with only the most negative anomaly response not being explained by these models. Additionally, both of the models can to a large degree explain the anomaly response of the middle gneiss area, with only the highest positive anomaly response in the middle differing largely from the anomalies created by these models. However, both of the models can only to some degree explain the “main” character of the anomaly response of the Raudhaugene part. Neither of the models can create the short wavelength signature within the main negative anomaly response of the Raudhaugene part, and none of them creates the minimum anomaly response observed for the Raudhaugene body along this profile.

The simple synformal peridotite model (Figure 15.3-2) gave a response which could explain the minimum anomaly response of the Raudhaugene part of the profile, while the “best fit” models syncline model and the best fit boudin model gave better fits for the middle gneiss part and the Ugelvik part. However, nor the simple synformal peridotite model or the “best fit” models could explain the short wavelength signature within the main negative anomaly response of the Raudhaugene part of the modelled profile.

16 Discussion of the anomalies created in the anomaly map and in the 2D profile

Based on the 2D models, geometry of the peridotite bodies and susceptibility contrast between the constricting bedrocks and the peridotites can to a certain degree explain the observed anomaly lows in the anomaly map (Figure 14.1-2). Based on the 2D model results the geometry of the peridotites could be several. In this study three possible models have been presented as either of a simple synformal structure, a synformal structure displaying two synforms and one antiform in the middle, or being of two boudins. Without several constraints on the models these three model geometries explain to the same degree the anomaly response, differing some in the fit of the modelled anomalies compared with the anomalies from the gridded anomaly map along profile. However, they displayed anomaly lows of an approximate minimum value of -500nT. This indicates that the susceptibility contrast and geometry of the peridotite bodies probably can explain the “normal” negative anomalies observed within areas mapped as peridotite, but cannot account for greater minima. This is based on the structural constraints and proposed peridotite geometries of Spengler (2006) as well as the susceptibility values obtained in this study. However, the anomaly map (Figure 14-2 and Figure 14.1-2) display anomalies within the mapped peridotite areas with negative anomalies much greater than these “normal” negative anomalies.

In chapter 11, 12 and 13, susceptibility values, remanent intensities and Q-values estimated for peridotite indicated possible contribution from remanence onto the total magnetic field. The investigation of remanent direction with intensity additionally indicated that remanent intensities with negative directions commonly displayed with greater intensities than the positive ones and could be earlier stage magnetite. As previously discussed, if these negative directions are more representative for the bulk of the peridotite bodies, these remanent contributions could possibly create the “un-normal” negative lows within the peridotite bodies. However, the possible earlier magnetites possibly being accountable for the negative remanent directions has not been demagnetised, hence their intensities and their directions has not been investigated in this study.

Further, the assumption of the surrounding bedrocks displaying isotropic intensities is only a largely simplified approach. With that in mind, the short wavelength responses in the middle gneiss part could be due to difference in both susceptibility values and remanent intensities and directions within these bedrocks. With more data on the immediate enclosing bedrocks, a better model of the profile could be obtained. Possibly this can give further constraints leading to a better understanding of the geometry of the peridotite bodies. Additionally, Figure 15.2-1 indicates that some of the anomaly response could be due to topography, especially for the middle gneiss part and within the Raudhaugene part of the profile. Furthermore, the spiky nature of the anomalies created by the models indicates that the topography may need corrections. Errors could be due to the gridding of GPS data possibly resulting in topography different from the real topography.

Based on Figure 8.3-1, the investigated profile is positioned where line data are close by, indicating that the anomaly data should be representative of the investigated profile. However, based on the anomaly map (Figure 14-2) the observed “extreme” anomalies with short wavelength could possibly indicate that the quality of the processed gridded data does not hold the assumption of creating a gridded anomaly map with representative anomaly values for the peridotite and the enclosing bedrocks. These types of extreme anomalies with short wavelength can also be indicative of cultural noise. Due to minimum curvature gridding (section 8.1.1) these anomalies could be enhancements of high-frequency parts of the data, such as cultural noise. Such an area could probably be the extreme low of -2200nT (Figure 14-2) located the west side of the Raudhaugene body.

The modelling shows that susceptibility contrast between the peridotite rocks and their constricting bedrocks can create negative anomalies due to the geometry of the peridotites. However, as observed, areas mapped as peridotites also displayed positive anomalies. This can be explained by the peridotite bodies only being a shallow cover on top of the constricting bedrocks. As observed, the mapped Ugelvik body displayed anomaly highs at the east side of the body, and the Raudhaugene body displayed anomaly highs at the north border of the body. These observations could possibly be due to shallow peridotite covers. However, this has not been further investigated due to little structural data obtained and time restrictions.

Another observation was of the constricting bedrocks mapped as amphibolite in the N250 map (NGU, n.d.) displaying predominantly anomaly lows on the same order as the peridotite bodies. The only sample from this area (9.1) displayed both high induced- and remanent magnetisation. If the remanent intensities at these observed locations are of such direction and intensity swamping the contribution from the induced magnetisation, anomalies of this order could be produced.

The most distinct anomaly low mapped as amphibolite was at the immediate south of the mapped Raudhaugene border. It displayed a broad negative anomaly of -750nT, which was approximately -200nT less than the largest negative anomaly within the mapped Ugelvik body. Based on topography, this area is indicated as lower than the other areas mapped as amphibolite (Figure 14.1-2). Additionally, the southern border of the Raudhaugene body is displayed with dotted lines, indicating that the border is interpreted, and not observed. Based on these observations, another possibility for the creation of this anomaly low could be due to peridotite with remanent magnetisation contributing to the anomaly. The two “fitted” models (Figure 15.5-1 and Figure 15.5-2) could indicate that the peridotites could create a negative contribution if they reside shallowly underneath the bedrocks in the middle between the outcropping Ugelvik and Raudhaugene bodies. The magnetic anomaly map superimposed previously mapped geology (Figure 14.1-2) also indicates that the anomaly low observed at the west side of the Raudhaugene body also is topographically lower than the other constricting bedrocks mapped as amphibolite. As at the southern border, this western border of the peridotite is also interpreted and not observed. Due to the anomaly low seemingly naturally extending south-westwards out from this interpreted border, this could indicate that the Raudhaugene peridotite body is extending south-westward with this anomaly low. However, none of these theories has been investigated in this study.

Future studies are suggested to obtain more knowledge on what exactly is creating the anomaly lows associated with the Raudhaugene and Ugelvik peridotite bodies, 3D modelling using gridded data more extensively processed, topographical data with higher accuracy, and contribution from both varying susceptibility as well as remanence taken into account, could be investigated. In addition, the bedrocks surrounding the peridotites, as well as the peridotites itself, could be further sampled to gain more information on induced and remanent magnetisation and how these properties vary with lithology, and should be incorporated into the modelling.

17 Discussion

The study in question was based on the need to obtain more information on the magnetic character of both metamorphic and deep crustal igneous rocks. The peridotites of Otrøya and their immediate enclosing bedrocks (mostly consisting of gneiss) satisfy to these needs, having a proven history of great depth and a proven history of several (U)HP metamorphic events. Additionally, within an aeromagnetic map over Otrøya, the peridotites of Otrøya are displaying within an area of anomaly low with its immediate constricting bedrocks displaying within areas of flat field to anomaly highs. These observations indicate that these rocks inhabit magnetic minerals which differ in properties and characters. Previous studies state that peridotites are mostly paramagnetic, whilst gneiss rocks commonly display ferromagnetic minerals. However, the peridotites of Otrøya are known to have undergone serpentinization, an alteration process with magnetite as product.

The investigated peridotite bodies of Otrøya, and their immediate enclosing bedrocks, have shown that some of the minerals within these rocks contribute magnetically. The main magnetic mineral observed within both the peridotites and the constricting bedrocks was magnetite. Within the constricting bedrocks hemo-ilmenite was additionally observed, known to possibly contribute with a strong remanent magnetisation. Additionally, Cr-spinel and chromite were observed within the peridotites – minerals that are, under certain compositional terms (see chapter 5.6.5), known to be slightly contributing due to remanent magnetisation. However, the magnetic contribution of the Cr-spinels and chromites was not studied.

Several morphologies of magnetite were observed in thin section. Amongst the peridotites, variation in magnetic intensities together with observed magnetite morphologies indicated variation in magnetic characters and properties with morphologies. The location with almost complete estimated serpentinization (location 8) displayed several morphologies of magnetite, displaying SD, PSD and MD sizes, with a mixed MD and SD signature indicating the greatest SD signature of all the peridotite locations, the highest remanent and induced intensities of peridotite locations corresponding to the highest amount of magnetite present, and displaying the lowest densities of all the peridotite locations. All of these observations confirm the presence of a peridotite rock with high degree of serpentinization. The other peridotite locations were estimated to be of substantially lower degree of serpentinization, mostly displaying SD to PSD sizes of magnetite. They all displayed higher density and lower susceptibility values, corresponding to their lower degree of serpentinization. Within these, locations with slightly higher susceptibility values correspondingly displayed discrete dendritic morphologies of magnetite of PSD sizes. However, the location with the lowest susceptibility value (location 5) displayed the second highest remanent intensity almost as high as the location displaying the highest estimated degree of serpentinization (location 8). This does not confirm with expected response of both increasing remanent and induced magnetisation with increasing degree of serpentinization due to expected increased amount of magnetite. Additionally, the morphology of the observed magnetite was not discrete, as mostly observed within the other locations, but as well-defined rims of magnetite around chromites. Due to this morphology and due to reported presence of Cr-spinels prior to serpentinization, these rims could possibly indicate an earlier creation of magnetite. Due to this, as well as high remanent magnetisation and low induced magnetisation in conjunction with low magnetite content, differing from the observed and anticipated behaviours and observations of the other serpentinized peridotite locations, these rims could possibly be of either a very early stage of serpentinization, or possibly of another magnetite creating event, such as decompression.

Further studies on the remanent magnetisation of the peridotites indicated that the location displaying magnetite as well-defined rims around chromites (location 5) additionally differed in intensity and direction of remanence compared with the other locations. This location displayed almost equal amounts of positive and negative directions of remanence, both plotting shallowly in an equal area plot. The other peridotite locations displayed dominantly remanence with positive directions plotting steeply, close to the ambient field vector of the area. A direction close to the ambient field of the area is commonly diagnostic of late stage magnetite creation, thus the location with magnetite rims with shallow plotting directions displayed directions diagnostic of an earlier stage of magnetite creation than the rest of the locations. For all peridotite locations, except of the location with well-defined rims of magnetite, the remanence displaying positive directions displayed lower intensities than the remanence displaying negative directions. This could also be indicative of the remanence with positive directions being carried by late stage magnetite, possibly due to deterioration of NRM and/or possible formation of modern CRM or VRM. Location 5, with well-defined rims of magnetite, displayed positive directions with higher remanent intensities than the remanent intensities with negative directions. However, whether one or the other, or both of the directions, are due to the magnetite rims was not investigated.

The observed morphologies of magnetite, as well as difference in direction and intensity of remanence, indicate several events of magnetite creation. This confirms with previous studies indicating several serpentine generations and growth forms, thus probably leading to magnetite growth. These could be further studied on the basis of magnetite creation timing. The intensities and direction of remanence for the magnetite created from different serpentine generations could also be investigated.

The bedrocks inhabited magnetite of MD size and displayed corresponding MD signatures and high intensities of induced magnetisation. Additionally, the bedrocks inhabited hemo-ilmenite, which possibly account for the high remanent intensities. However, the magnetic contribution from the hemo-ilmenite was not studied.

The remanent directions of the bedrocks were both of negative and positive directions. Whether one or the other was due to magnetite or hemo-ilmenite was not investigated. However, the anomaly map created in this study displayed both distinct positive and negative anomalies within areas of these bedrocks, which can be accounted for by the estimated intensities of contributing remanence and induced magnetisation from these bedrocks. However, they generally displayed neutral to anomaly highs and displayed as a contrast to areas of wide anomaly lows, previously mapped as peridotite.

Compared with the peridotites, the constricting bedrocks displayed substantially higher intensities of both remanence and susceptibility. By evaluating the Q-value, hence the intensity of remanence versus the induced magnetisation, it became apparent that for the peridotites the remanent intensity was the controlling factor of the Q-value, and the susceptibility displayed little or no variance. For the bedrocks the remanence was the main controlling factor of the Q-value, while some variation in susceptibility with Q-value was observed.

By 2D modelling of the peridotite bodies within the constricting bedrock, the controlling factor of average susceptibility onto the observed anomalies in the anomaly map was investigated. The susceptibility values were set as constant for respectively both the peridotites and the constricting bedrock. They were therefore treated as isotropic rock bodies. By conducting the 2D modelling it became apparent that the inferred geometry of the peridotites (based on previous studies, see chapter 8.3 “2D modelling” for references) and the susceptibility contrast observed between the peridotites and the constricting bedrocks could create anomaly lows corresponding in shape and amplitude compared with the measured anomalies, along the chosen profile. However, the minimum anomaly responses of the peridotites could not be modelled properly. In addition, short wavelength anomalies observed for the peridotites could not be accounted for by this modelling.

The reasons for these short wavelength anomalies could be many. The bedrocks displayed a large variance in remanence intensities, and some variance in susceptibility values. These susceptibility variations were not taken into account in the modelling. Additionally, both the bedrocks and the peridotites displayed remanence which by its direction and intensity could swamp the contribution of the induced magnetisation. The peridotite bodies were predominantly displaying remanence of positive directions, which therefore cannot explain the negative anomalies observed in the anomaly map. However, if these positive directions are due to surface processes leading to deterioration of the NRM, or in other ways are created at surface, thus not being representative of the whole body, the bulk contribution of remanence could be negative, thus explaining the negative anomalies of the peridotites.

Based on the interpretation of the magnetic properties of the peridotites and its immediate surrounding bedrocks, the wide anomaly lows within the ground magnetic map are largely due to the susceptibility contrast of the peridotite and the bedrocks, as well as the geometry of the peridotite bodies. However, remanence is contributing both within the bedrocks as well as within the peridotites. The anomalies associated with the peridotites also indicated possible geometries of the peridotites with depth, but also how they possibly could extend in length. Areas mapped as peridotite, but displaying flat to slightly positive anomalies could be consisting of a shallow cover of peridotite upon bedrock, thus the susceptibility of the bedrock being the main contributor to the magnetic response. However, areas of magnetic lows in immediate vicinity of the peridotite bodies also indicated areas where the peridotite possibly could extend in length, longer than previously inferred.

The two wide anomaly lows within the anomaly map created by the ground magnetic survey of this study (Figure 14.1-2) coincide with the anomaly low displayed in the aeromagnetic map of Otrøya (Figure 1.2-1). This indicates that for conditions similar of the magnetic properties of peridotite and enclosing bedrocks in this study, as well as similar geometries of these rocks, could create negative anomalies which are possible to view in an aeromagnetic map. This study also indicates that remanence could be a factor of importance in magnetic modelling of peridotite rocks. The study also indicates that magnetite could possibly be present within the peridotites prior to serpentinization. However, this has not been studied in detail.

17.1 Recommendations for further work

Within this study, the Day-plot contributed to information about the domain state of the magnetite present in the samples. Due to microscopy and backscatter electron microscopy it became evident that several magnetic minerals were present. To further investigate the magnetic domain state of magnetite, magnetic separates should be conducted.

The previous lithological mapping of the peridotite bodies of Otrøya (Spengler, 2006) displays a banded and varying composition. These could be further investigated on how lithology controls serpentinization, and how this effects the development of magnetite.

By investigating the Al-mg versus Fe modal ratios of the chromite and Cr-spinels its contribution to remanent magnetisation could be investigated.

To further investigate if the NRM of the samples have experienced deterioration, AFD (alternating field demagnetization) could be conducted to investigate different stages of magnetite formation, and whether earlier magnetite carries intensities with other directions than the latest magnetites.

Magnetite morphologies, such as the magnetite rims on Cr-spinel and chromites, could be investigated on whether they existed prior to serpentinization.

Based on Oud (2010) serpentine mesh growth were from 530-180*C, which is below the Tc of magnetite. The different stages of mesh formation and fracture filling could be investigated on possible different formation of magnetite product. These could be investigated on different growth types/morphologies of magnetite, hence also if they would contribute to SD, PSD or MD signatures. These could also be investigated on whether these carry different strengths of remanent and induced magnetisations.

Density measurements of all the samples could be conducted to compare degree of serpentinization with weight, as well as obtaining more accurate values for susceptibility and remanence due to better volume estimation of specimens.

A proper statistical analysis of the data could be conducted to investigate correlation between magnetic properties, densities and, if possible, mineralogy.

The data from the ground magnetic study should be more extensively processed to obtain a gridded anomaly map reflecting the lithology of the area with as little contribution from topography and cultural noise as possible.

The obtained intensities of remanence can be incorporated in the 2D modelling. Remanence can be the explanation to the observed magnetic lows within the peridotite bodies, which could not be explained only by susceptibility contrast and geometry. Further modelling can also be done by including variation in both remanent contribution as well as susceptibility variation, to investigate how this would affect the resulting anomalies. To get as much information as possible, a 3D model could be developed.

18 Conclusions

Magnetic minerals within the peridotites and their immediate enclosing bedrocks

The peridotites of Otrøya display magnetite of mostly SD to PSD sizes, but were also observed for MD sizes. MD sizes were commonly observed within heavily serpentinized samples. Several morphologies of magnetite were observed, with either discrete appearance, or as well as defined rims around chromites. These several morphologies are possibly due to several periods of growth. Chromites and Cr-spinels were additionally observed, but their compositions have not been studied, hence their magnetic contribution is unknown.

The enclosing bedrocks display large magnetite grains of MD sizes, and hemo-ilmenite.

The magnetic properties of the peridotites and their immediate enclosing bedrocks

The peridotites displayed low remanent and induced magnetisations, with slightly higher intensities, slightly higher contribution from remanence, and more magnetite at locations with a high grade of estimated serpentinization. The magnetite present within the peridotites displayed consistent susceptibility values, while the intensity and directions of NRMs were varying. Remanent intensities of negative directions were commonly greater than intensities with positive directions, additionally positive directions were commonly observed with the same direction as the ambient field direction. This could be indicative of late stage magnetite formation, deterioration of NRM and/or possible formation of modern CRM or VRM. The peridotites commonly displayed PSD signatures, with locations of high degree of serpentinization displaying mixed signatures with higher contribution from SD than for locations with lower degree of serpentinization.

The enclosing bedrocks displayed substantially higher intensities of remanent and induced magnetisations compared with the peridotites, commonly displaying induced magnetisation as the dominant contributor. Both its induced and remanent intensities were varying, as well as the directions of its remanent intensities. Based on hysteresis data, the magnetic signature was interpreted as MD.

The response of the peridotites and their enclosing bedrocks on a ground magnetic anomaly map

The peridotites could be viewed on the anomaly map as wide anomaly lows, while the enclosing bedrocks commonly displayed as neutral to anomaly highs. On a minor scale, both extreme anomaly lows and highs were observed within the bedrocks. The observed anomalies could be explained by the magnetic properties obtained in this study.

Modelling of the peridotites and their enclosing bedrocks based on geometry and susceptibility constraints

The peridotites and their enclosing bedrocks could be modelled on the basis of average susceptibility and published geometry being the controlling factors of the anomaly response. However, some short wavelength responses, as well as the most negative anomaly responses of the peridotites could not be explained. These could probably be due to susceptibility differences within the enclosing bedrocks as well as contribution of remanence, both for the bedrocks and the peridotites.

19 Bibliography

Agico. (2004). *SPINNER MAGNETOMETER JR6/JR6A: User's Manual – Instrument for measuring remanent magnetization (Ver. 2)* Downloaded from: http://www.agico.com/manuals/jr6-man.pdf

Allmendinger, R. W., Cardozo, N., and Fisher, D. (2012) *Structural geology algorithms: Vectors and tensors in structural geology*. Cambridge University Press

Briggs, I. C., (1974). Machine contouring using minimum curvature. *Geophysics, Vol. 39, No. 1, pp.39-48.*

Brueckner, H. K. & Medaris, L. G. (2000). A general model for the intrusion and evolution of 'mantle' garnet peridotites in high-pressure and ultra-high-pressure metamorphic terranes. *Journal of Metamorphic Geology 2000,* volume 18, pages 123-133. DOI: 10.1046/j.1525-1314.2000.00250.x

Bruckner, H.K., Carswell, D. A., Griffin, W. L., Medaris Jr., L. G., Van Roermund, H. L. M. & Cuthbert, S. J. (2010). The mantle and crustal evolution of two garnet peridotite suites from the Western Gneiss Region, Norwegian Caledonides: An isotopic investigation. *Lithos 2010, v. 117; p1-19. Downloaded:* http://www.sciencedirect.com/science/article/pii/S002449371000023X

Butler, F. R. (2004). *PALEOMAGNETISM: Magnetic Domains to Geological Terrains (Electronic edition).* Oregon: University of Portland: Department of Chemistry and Physics. Downloaded: http://www.pmc.ucsc.edu/~njarboe/pmagresource/ButlerPaleomagnetismBook.pdf

Cardozo, N.& Allmendinger, R. W. (2013). Spherical projections with OSXStereonet. *Computers & Geosciences*, v. 51, no. 0, p. 193 - 205, doi: 10.1016/j.cageo.2012.07.021

Carrey, J., Mehdaoui, B., & Respaud, M. (2011). Simple models for dynamic hysteresis loop calculations of magnetic single-domain nanoparticles: Application to magnetic hyperthermia optimization. *Journal of Applied Physics. Vol. 109.* doi: 10.1063/1.3551582

Carswell, D. A. (1968) Possible primary upper mantle peridotite in Norwegian basal gneiss. *Lithos 1968, v. 1; p322-355.* Doi: 10.1016/S0024-4937(68)80014-3.

Carswell, D.A. (1973). Garnet pyroxenite lens within Ugelvik layered garnet peridotite. *Earth and Planetary Science Letters 1973, V. 20; p 347-352.* doi: 10.1016/0012-821X(73)90009-5.

Christensen, R. U. (2011) Geodynamo models: Tools for understanding properties of Earth's magnetic field. *Physics of the Earth and Planetary Interiors. V. 187.* pp 157-169. doi:10.1016/j.pepi.2011.03.012

Clark, D.A. (1997). Magnetic petrophysics, and magnetic petrology: aids to geological interpretation of magnetic surveys. *Journal of Australian Geology and Geophysics V. 17*, pp. 83–103.

Deer, W. A., Howie, R. A., & Zussman, J. (1992). *An Introduction to the Rock-Forming Minerals (second edition).* Essex: Person Education Limited

Drury, M. R. et al. (2001). Emplacement of deep upper mantle rocks into cratonic litosphere by convection and diapiric uppwelling. *J. Petrology 2001, v. 42;* p131-140.
doi: 10.1093/petrology/42.1.131

Dunlop, D. J. & Özdemir, Ö. (1997). *Rock Magnetism: Fundamentals and frontiers.* The Untited Kingdom: Cambridge University Press

Dunlop D. J., Özdemir, Ö. & Costanzo-Alvarez, V. (2010). Magnetic properties of rocks of the Kapaskasing uplift (Ontario, Canada) and origin of long-wavelenght magnetic anomalies. *Geophys. J. Int. V. 183.* pp. 645-658. doi:10.1111/j.1365-246X.2010.04778.x

Dunlop, D. J. (2002) Theory and application of the Day plot (M_{rs}/M_s versus H_{cr}/H_c) 1. Theoretical curves and testing using titanomagnetite data. *Journal of Geophysical Research, V. 107.* Doi:10.1029/2001JB000486

Evans, B. W., Dyer, M. D., & Kuehner S. M. (2012). Implications of ferrous and ferric iron in antigorite. *American Mineralogist, Vol. 97*, pp. 184-196. Downloaded: http://www.minsocam.org/MSA/AmMin/TOC/2012/Jan12.html

Evans, B. W., Hattori, K. & Baronnet, A. (2013). Serpentinite: What, why, where? *Elements, Vol. 9*, pp. 99-106. DOI: 10.2113/gselements.9.2.99

Fichler, C., Odinsen, T., Rueslåtten, H., Olesen, O., Vindstad, J. E. & Wienecke, S. (2011). Crustal inhomogeneities in the Northern North Sea from potential field modeling: Inherited structure and serpentinites? *Tectonophysics, Vol. 510*, pp. 172-185. DOI: 10.1016/j.tecto.2011.06.026

Ferré, E. C., Friedman, S. A., Martín-Hernández, F., Feinberg, J. M., Conder, J. A. & Ionov. D. A. (2013). The magnetism of mantle xenoliths and potential implications for sub-Moho magnetic sources. *Geophysical Research Letters, Vol. 40*. pp. 105–110. doi:10.1029/2012GL054100.

Ferré, E. C., Friedman, S. A., Martín-Hernández, F., Feinberg, J. M., Till, J. L., Ionov, D. A., & Conder, J. A. (2014). Eight good reasons why the uppermost mantle could be magnetic. *Tectonophysics.* doi: 10.1016/j.tecto.2014.01.004

Geometrics (n.d.). G-859 Magnetimeter. Downloaded from: http://www.geometrics.com/geometrics-products/geometrics-magnetometers/g-859-magnetometer/

Geosoft (2012a) Oasis montaj help. Retrieved from software.

Geosoft (2012b) Topics in gridding. Retrieved from software.

Guillot, S. & Hattori, K. (2013). Serpentinites: Essential Roles in Geodynamics, Arc Volcanism, Sustainable Development, and the Origin of Life. *Elements, Vol. 9*, pp. 95-98. DOI: 10.2113/gselements.9.2.95

MacKenzie, W. S., Donaldson, C. H., & Guilford, C. (1982). *Atlas of igenous rocks and their textures.* Longman.

Marcon, P., & Ostanina, K. (2012). Overview of Methods for Magnetic Susceptibility Measurements. *Session 1P8,* 200.

Marshall, D. D., Anglin, C. D., & Mumin, A. H. (2004). *Ore mineral atlas.* Geological Association of Canada, Mineral Deposits Division.

McEnroe, S. A. & Brown, L.L. (2000). A closer look at remanence-dominated aeromagnetic anomalies: Rock magnetic properties and magnetic mineralogy of the Russel Belt microcline-sillimanite gneiss, northwest Adirondack Mountains, New York. *Journal of Geophysical Reasearch. Vol. 195.* pp. 16,437-16,456.

McEnroe, S. A., Harrison, R., Robinson, P., Golla, U., Jercinovic, M. J. (2001). The effect of fine-scale microstructures in titanohematite on the acquisition and stability of NRM in granulite-facies metamorphic rocks from southwest Sweden. *Journal of Geophysical Research. Vol. 106.* pp. 30,523-30,546.

McEnroe, S. A., Brown, L. L. & Robinson, P. (2004a). Earth analog for Martian magnetic anomalies: remanence properties of hemo-ilmenite norites in the Bjerkreim-Sokndal intrusion, Rogaland, Norway. *Journal of Applied Geophysics, Vol. 56.* pp. 195-212. Doi:10.1016/j.jappgeo.2004.07.002

McEnroe, S. A., Langenhorst, F., Robinson, P., Bromiley, G. D. & Shaw., C. S. J. (2004b). What is magnetic in the lower crust? *Earth and Planetary Science Letters. Vol. 226.* pp. 175-192. doi:10.1016/j.epsl.2004.07.020

McEnroe, S. A., Brown, L. L. & Robinson, P. (2008). Remanent and induced magnetic anomalies over a layered intrusion: Effects from crystal fractionation and magma recharge. *Tectonophysics. Vol. 478.* pp. 119-134. doi:10.1016/j.teto.2008.11.021

McEnroe, S. A., Fabian, K., Robinson, & Brown, L. L. (2009a). Remanent Magnetization in Crustal Rocks. Downloaded: http://www.researchgate.net/publication/242557587_REMANENT_MAGNETIZATION_IN_CRUSTAL_ROCKS/file/60b7d52af57a16b79d.pdf

McEnroe, S. A., Fabian, K., Robinson, P., Gaina, C. & Brown, L. L. (2009b). Crustal Magnetism, Lamellar Magnetism and Rocks That Remember. *Elements, Vol.5.* pp. 241-246. Doi:10.2113/gselements.5.4.241

Moskowitz, B. M. (n.d.). Hitchhiker's Guide to Magnetism. Downloaded from: http://www.irm.umn.edu/hg2m/hg2m.pdf

Musset, A. E. & Khan,M. A. (2000). *LOOKING INTO THE EARTH: An Introduction to Geological Geophysics.* The Untited States of America: Cambridge University Press

Natural Resources Canada (20.08.2013). *Secular variation.* Downloaded from: http://geomag.nrcan.gc.ca/mag_fld/sec-eng.php

NGU (n.d.) N250. Retrieved from: http://geo.ngu.no/kart/berggrunn/

Norge i bilder (n.d) Norge i bilder [map]. Retrieved from: http://www.norgeibilder.no/

Oud, K. (2010). Serpentinization and fracture formation in peridotites on Otrøy, Western Gneiss Region, Norway: Late stage PT-conditions and implications for tectonic decompression. Faculty of Geosciences Theses (2010). Downloaded: http://dspace.library.uu.nl/handle/1874/179058

Philpotts, A. A. (2003). *Petrography of Igneous and Metamorphic Rocks.* The United States of America: Waveland Press, Inc.

Purucker, M. E. (2007). Magnetic anomalies, long wavelength. In Gubbins, D. & Herrero-Bervera, E. (Editors). *Encyclopedia of Geomagnetism and Paleomagnetism*. (1. Edition, pp. 481-483.) The Netherlands: Springer

Reeves, C. & Korhonen, J. V. (2007) Magnetic anomalies for geology and resources. In Gubbins, D. & Herrero-Bervera, E. (Editors). *Encyclopedia of Geomagnetism and Paleomagnetism*. (1. Edition, pp. 477-480.) The Netherlands: Springer

Reynolds, J. M. (2011). *An Introduction to Applied and Environmental Geophysics* (2nd Edition). Oxford: Wiley-Blackwell

SatisGeo, s.r.o. (n.d.). *KAPPAMETER: KT-6 – Instruction Manual.* Downloaded from: http://users.monash.edu.au/~rjarmit/Mag_sus_meter_instructions/KappaMeter_KT6/KT6manSG.pdf

Scambelluri, M., Pettke, T. & Van Roermund, H. L. M. (2008). Majoritic garnets monitor deep subduction fluid flow and mantle dynamics. *Geology, Vol. 36.* pp. 59-62. doi: 10.1130/G24056A.1

Shive, P. N. (1989) Can Remanent Magnetization in the Deep Crust Contribute to Long Wavelength Magnetic Anomalies? *Geophysical Research Letters, Vol. 16.* pp. 89-92.

Spengler, D. (2006). Origin and evolution of deep upper mantle rocks from Western Norway. Utrecht University. Geologica Ultraiectina, Vol. 266 (2006). Downloaded from: http://dspace.library.uu.nl/handle/1874/13831

Spengler, D., Carswell, D. A., van Roermund, H. L. M., Drury, M. R., Wiggers de Vries, D. F., van Straaten, B. I., and Haker, A. (2006). Simplified geological map of western Otrøya. [map] In Spengler. Origin and evolution of deep upper mantle rocks from Western Norway. Utrecht University. Geologica Ultraiectina, Vol. 266 (2006). Downloaded from: http://dspace.library.uu.nl/handle/1874/13831

Spengler, D. & Haker, A. (2006). Structural map of the Raudhaugene and Ugelvik peridotite bodies [Map]. In Spengler, D. Origin and evolution of deep upper mantle rocks from Western Norway. Utrecht University. Geologica Ultraiectina, Vol. 266 (2006). Downloaded from: http://dspace.library.uu.nl/handle/1874/13831

Spengler,D., Van Roermund, H. L. M., Dury, M. R., Ottolini, L., Mason, P. R. D. & Davies, G. R. (2006) Deep origin and hot melting of an Archean orogenic peridotite massif in Norway. *Nature 2006,* v.440; p.913-917. doi:10.1038/nature04644

Swain, C. J. (1976). *A FOTRAN IV program for interpolating irregularly spaced data using the difference equations for minimum curvature. Computers & Geosciences*, Vol. 1, pp. 231-240.

Sørensen, B. E. (2013). A revised Michel-Lévy interference colour chart based on first-principles calculations. *European Journal of Mineralogy, V. 25*(1), pp. 5-10

Tauxe, L., Bertram, H. N., & Seberino, C. (2002). Physical interpretation of hysteresis loops: Micromagnetic modeling of fine particle magnetite. *Geochemistry, Geophysics, Geosystems, Vol. 3.* pp. 1-22. Doi:10.1029/2001GC000241

U. S. Geological Survey [USGS] (05.05.1999). *Inside the Earth.* Downloaded from: http://pubs.usgs.gov/gip/dynamic/inside.html

Van Roermund, H. (2008). Occurrence and interpretation of garnet peridotites in the northernmost UHPM domain of the WGR, Otrøy. In Robinson, P. & Roberts, D. (Editors). *A tectonostratigraphic transect across the central Scandinavian Caledonides Part II*. *Excursion guide in Norway.* 33rd NGU Report 2008.064, Day 7, p.1-17. International Geological Congress, Oslo, Norway

Van Roermund, H. (2009). Recent progress in Scandian ultrahigh-pressure metamorphism in the northernmost domain of the Western Gneiss Complex, SW Norway: continental subduction down to 180-200km depth. *Journal of the Geological Society 2009, Vol. 166*. pp. 739-751. doi: 10.1144/0016-76492008-020

Van Roermund, H. L. M. & Drury, M. R. (1998). Ultrahigh pressure (>6 GPa) garnet peridotites in western Norway: Exhumation of mantle rocks from more than 185km. *Terra Nova 1998*, *Vol. 10.* pp. 295-301. Doi: 10.1046/j.1365-3121.1998.00213.x

Wasilewski, P. J., Thomas, H. H. & Mayhew, M. A. (1979). The Moho as a Magnetic Boundary. *Geophysical Research Letters. Vol. 6.* pp. 541-544

Wasilewski, P. J. & Mayhew, M. A. (1992). The Moho as a Magnetic Boundary Revisited. *Geophysical Research Letters. Vol. 19.* pp. 2259-2262

Williams, M. C., Shive, P. N., Fountain, D. M. & Frost, B. R. (1985). Magnetic properties of exposed deep crustal rocks from the Superior Province of Manitoba. *Earth and Planitary Science Letters. Vol. 76.* pp. 176-184.

World Data Centre for Geomagnetism. (n.d.) *Magnetic North, Geomagnetic and Magnetic Poles.* Retrieved from http://www.geomag.nrcan.gc.ca/mag_fld/sec-eng.php

Worm. H.-U. (1989). Comment on “Can Remanent Magnetization in the Deep Crust Contribute to Long Wavelength Magnetic Anomalies?” by Peter N. Shive. *Geophysical Reaserch Letters. Vol. 16.* pp. 595-597.